Morphology, Physical and Tensile Properties of Quench-cooled Isotactic Polypropylene Films and Spunbonded Fabrics

Victor Caldas

Department of Chemistry
McGill University
Montreal, Canada.

August 1995

A Thesis Submitted to the Faculty of Graduate Studies and Research
in Partial Fulfillment of the Requirements of the Degree of
Doctor of Philosophy

National Library of Canada
Acquisitions and Bibliographic Services Branch
395 Wellington Street
Ottawa, Ontario
K1A 0N4

Bibliothèque nationale du Canada
Direction des acquisitions et des services bibliographiques
395, rue Wellington
Ottawa (Ontario)
K1A 0N4

Your file Votre référence

Our file Notre référence

ISBN 0-612-19696-8

Chemistry Ph.D.

Morphology, Physical and Tensile Properties of Quench-cooled Isotactic Polypropylene Films and Spunbonded Fabrics

Victor Caldas

Abstract

The room temperature morphology of quench-cooled isotactic polypropylene (iPP) films and its development were investigated by scanning transmittance electron microscopy (STEM) and differential scanning calorimetry (DSC). STEM dark field images revealed that within an amorphous matrix there exist microcrystalline regions, 160 Å in size on the average, having the α-monoclinic crystal form. Regions of lower crystalline order were also observed which have an α-monoclinic crystal form that has a substantially longer *b* crystallographic axis. DSC studies indicate that during quench-cooling to the glassy state iPP samples attain a low degree of crystalline order to an extent that depends on sample mass. Upon heating from the glassy state, an exothermic transition is observed following the glass transition temperature which corresponds to the formation of the room temperature morphology.

Cross polarization/magic angle spinning (CP/MAS) nuclear magnetic resonance (NMR) spectroscopy was used to monitor morphological changes in the purely crystalline phase of quench-cooled iPP films and spunbonded fabrics during annealing. The spectra were obtained using a pulse sequence that incorporates a delay period with a reduced spin locking field prior to cross polarization. Morphological changes occurring within the purely crystalline phase of iPP were related to observations made by DSC. Upon annealing, the CP/MAS NMR spectrum of the purely crystalline phase of both iPP samples changed by a redistribution in the intensity of the various peaks within a given carbon resonance. This redistribution of intensity was found to reflect the conversion from the α_1 to the α_2 monoclinic crystal forms. It is shown that the double melting endotherm observed by DSC for the spunbonded fabrics is due to the exothermicity which is associated with this conversion. It is concentrated in the temperature region between 156 and 163 °C.

The tensile properties of the spunbonded iPP fabrics and fibers were enhanced by the dispersion of a silica/silicone additive and by changing the resin characteristics. This additive acts as a nucleating agent for iPP under isothermal crystallization conditions. This nucleating ability manifests itself in smaller crystal sizes and higher nucleation densities in the iPP fibers and bond points. The improved tensile properties are attributed to the smaller crystal sizes which form a more homogeneously dispersed crystalline phase in the amorphous phase as well as to increase the number of load-bearing tie molecules.

Chemistry Ph.D.

Morphologie, Propriétés Physiques et d'Étirement des Films de Polypropylène Isotactique Trempé et des Tissus à Liaison de Fibres

Victor Caldas

Résumé

La morphologie à la température ambiante des films de polypropylène isotactique (iPP) trempé et leur développement ont été étudié par microscopie électronique à balayage et transmission (STEM) ainsi que par calorimétrie différentielle à balayage (DSC). Les images obtenues par STEM à champ obscur indiquent que dans une matrice amorphe, il existe des régions microcrystallines de 160 Å en moyenne ayant la forme α-monoclinique. Des régions de crystallinité inférieure, possédant également une forme monoclinique mais où l'axe crystallographique *b* est plus long, ont aussi été observées. L'étude de la calorimétrie différentielle à balayage indique que l'iPP soumis à un refroidissement rapide jusqu'à l'état vitreux atteint un bas degré de crystallinité qui dépend de la masse de l'échantillon. En réchauffant l'échantillon à partir de l'état vitreux, une transition exothermique est observée suivant la température de transition vitreuse, ce qui correspond au développement de la morphologie de l'iPP à température ambiante.

La résonance magnétique nucléaire (RMN), par la technique de polarisation croisée et rotation à angle magique (CP/MAS), a été utilisée dans le but d'observer les changements morphologiques des films d'iPP trempés et des tissus à liaison de fibres dans la région purement crystalline. Les spectres ont été obtenus en utilisant une séquence de pulse où un délai au champ de découplage réduit est incorporé avant la polarisation croisée. Les changements morphologiques se produisant dans la région purement crystalline ont été reliés à des observations faites par DSC. En observant le spectre obtenu

par CP/MAS RMN pour les deux échantillons, il est possible de remarquer une redistribution de l'intensité des signaux pour chaque résonance. Cette redistribution de l'intensité indique la conversion de la phase monoclinique α_1 à la phase α_2. Il est montré que la double transition endothermique observée par DSC pour les tissus à liaison de fibres est due à l'exothermicité associée à cette conversion. L'exothermicité est présente à des températures variant entre 156 et 163 °C.

Les propriétés d'étirement des fibres d'iPP et des tissus à liaison de fibres ont été améliorées par la dispersion d'un additif silice/silicone et en changeant les caractéristiques de la résine. Cet additif agit comme agent de nucléation pour l'iPP sous des conditions de cristallisation isothermalle. Cette habileté de nucléation se manifeste dans l'observation de plus petits cristaux et d'une plus haute densité de nucléats dans le fibres d'iPP et dans les points de liaison. Ces propriétés accrues d'étirement sont attribuées à la réduction de la dimension des cristaux, formant une phase crystalline de meilleure homogénéité dans la phase amorphe, ainsi qu'à l'accroissement du nombre de points d'attachements moléculaires.

ACKNOWLEDGMENTS

This study was performed under the supervision of Prof. G.R. Brown, to whom I wish to express my sincerest appreciation for his guidance, support, and valuable advice during the course of the experimental work and in the preparation of this thesis.

I wish to thank Drs. R.S. Nohr and J.G. MacDonald of Kimberly-Clark Corp. for supplying the various iPP fibers and spunbonded fabrics as well as for the analysis of the tensile properties of the spunbonded fabrics. It is my understanding that Drs. Nohr and MacDonald are the discoverers of the phenomenon described in Chapter 5.

I would also like to express my gratitude to Mr. Louis Raboin of the University of Massachusetts for performing the electron microscopy investigations and for the analysis of the tensile properties of the iPP single fibers, all at the behest of Drs. Nohr and MacDonald; Dr. F.G. Morin for his help in developing the NMR pulse sequence used in Chapters 3 and 4 as well as for many helpful and illuminating discussions; Dr. Brisse and Nathalie Jourdan of the University of Montreal for the computer program used in the analysis of the crystal structures of the quench-cooled iPP films as well as to Dr. Anne-Marie Lebuis for all her help in performing this analysis; Dr. F. Bossé and Mr. H. Martins for their help in translating the Abstract to french; Mr. F. Kluck, G. Rolland, R. Rossi and G. Kopp whose expertise facilitated my research in ways too numerous to mention.

Special thanks to Mr. Theodore Radiotis for his friendship, encouragement and for many knowledge-sharing discussions throughout the course of these studies. My colleagues and friends, past and present, deserve many thanks for their friendship, helpful discussions and for creating a pleasant and warm working environment.

The Natural Sciences and Engineering Research Council (NSERC) of Canada and Fonds pour la Formation de Chercheur et l'Aide à la Recherche (Fonds FCAR) of Quebec for postgraduate research scholarships.

Finally, I am greatly indebted to my family, especially to my wife Terry, for their immense love, support, patience and understanding.

TABLE OF CONTENTS

CHAPTER ONE

CHAPTER TWO

CHAPTER THREE

CHAPTER FOUR

CHAPTER FIVE

CHAPTER SIX

APPENDICES

List of Figures

CHAPTER ONE

CHAPTER TWO

CHAPTER THREE

CHAPTER FOUR

CHAPTER FIVE

List of Tables

CHAPTER TWO

CHAPTER THREE

CHAPTER FOUR

CHAPTER FIVE

List of Abbreviations and Symbols

a, b, c, β	unit cell constants
a, b	interlayer distances in the α-monoclinic crystal form
A0/100	Exxon 3445 with 0.3% of (5% Silica in Silicone)
A45/55	45%/55% Blend of PP5/PP34 with 0.3% of (5% Silica in Silicone)
A50/50	50%/50% Blend of PP5/PP34 with 0.3% of (5% Silica in Silicone)
A55/45	55%/45% Blend of PP5/PP34 with 0.3% of (5% Silica in Silicone)
A60/40	60%/40% Blend of PP5/PP34 with 0.3% of (5% Silica in Silicone)
B_o	external magnetic field
B_1	spin locking field
B_1^H	spin locking field at the proton resonance frequency
B_1^C	spin locking field at the carbon resonance frequency
C60/40	60%/40% Blend of PP5/PP34
ΔC_p	measured change in heat capacity at the glass transition
ΔC_p^o	change in heat capacity of the pure amorphous glass
C.D.	cross direction
CP	cross polarization
CSA	chemical shift anisotropy
CTEM	conventional transmittance electron microscopy
d	d-spacing of a measured reflection
DSC	differential scanning calorimetry
DD	dipolar decoupling
eqn	equation
ΔE	energy separation of the upper and lower Zeeman energy states
FID	free induction decay
G	radial growth rate

GPC	gel permeation chromatography
h	Planck's constant
h, k, l	Miller indices
h_l^i	local magnetic field produced at nucleus i
HPLC	high performance liquid chromatography
HTP	high temperature peak
ΔH	heat of fusion
iPP	isotactic polypropylene
I	nuclear spin
IR	infrared
k	Boltzmann's constant
K	overall rate constant
L	camera length
LTE	low temperature endotherm
LTP	low temperature peak
MAS	magic angle spinning
M.D.	machine direction
MDD	minimum dose device
M_o^I	magnetization of nucleus I
MFI	melt flow index
MWD	molecular weight distribution
N	number of observed reflections
NMR	nuclear magnetic resonance
n	integer (Avrami parameter)
Δn	birefringence (difference of refractive indices)
n_r	radial refractive index
n_t	tangential refractive index

n_u	population of the upper Zeeman energy level
n_l	population of the lower Zeeman energy level
OD	outer diameter
PP	polypropylene
PP34	Exxon 3445
PP5	Exxon 1052
PET	poly(ethylene terephthalate)
ppm	parts per million
r	radius of a measured diffraction
r_{ij}	internuclear separation between nuclei i and j
rf	radio frequency
R	order parameter
sPP	syndiotactic polypropylene
STEM	scanning transmittance electron microscopy
SAXS	small angle x-ray scattering
t	time
t_c	time interval
$t_{\frac{1}{2}}$	half time of crystallization
T_g (L)	lower glass transition
T_g (U)	upper glass transition
T_g	glass transition
T_m	melting temperature
T_c	crystallization temperature
T	temperature
T_l	lattice temperature
T_s	spin temperature
T_1	spin lattice relaxation time

T_2	spin spin relaxation time
T_{CH}	cross relaxation time
$T_{1\rho}$	spin lattice relaxation time in a rotating frame
$T_{1\rho}$ (^1H)	proton spin lattice relaxation time in a rotating frame
TMS	tetramethylsilane
TEM	transmittance electron microscopy
w_c	weight fraction crystallinity
WAXS	wide angle x-ray scattering
WAXD	wide angle x-ray diffraction
θ	diffraction angle
θ_{obs}	observed diffraction angle
θ_{calc}	calculated diffraction angle
θ_{ij}	angle between the vector r_{ij} and the external magnetic field
μ_j	dipole moment of nucleus j
μ_s	dipole moment of species s
ξ	deviation between calculated and observed values
λ	wavelength
ω_o	resonance frequency
ω_l	resonance frequency due to local magnetic field
τ	delay period prior to cross polarization
σ_{11}, σ_{22}, σ_{33}	three principle values of the chemical shift tensor
γ	magnetogyric ratio
γ_H	proton magnetogyric ratio
γ_C	carbon magnetogyric ratio
$\nu_{½}$	line width of a particular resonance at half height
χ_t	volume fraction of crystalline material

CHAPTER ONE

Introduction

Crystalline polypropylene (PP) is a polymorphic thermoplastic that has been the source of innumerable investigations which, in the main, concentrate on the many aspects of its structural organization in the solid state. While this enormous interest in these fundamental issues is based partly on the fact that PP is one of the simplest of the nontrivially stereoregular polymers, it results primarily from the commercial versatility and viability of PP. This versatility arises from the fact that the structure and properties of PP can be tailored to meet specific requirements. PP can be modified during the polymerization of the resin by the copolymerization with different co-monomers or by the production of a syndiotactic homopolymer, during compounding by the manufacturing of filled or reinforced resins, or in subsequent processing steps. This variety has been demonstrated in a three volume compilation that describes many aspects of the structure-performance relationships relevant to polypropylene homopolymers, copolymers, blends and composites.[1]

Many fundamental studies have been performed on PP in various areas of research that include crystallization, nucleation, melting, morphology, transformations between crystalline phases and supermolecular structures which have contributed to the present state of knowledge in polymer science. Some of these investigations will be discussed not only in this Introduction but also in other sections throughout this thesis. However, before discussing topics that pertain specifically to PP, a general background on semicrystalline polymers is presented.

1.1 Background on Semicrystalline Polymers

1.1.1 Requirements for Crystallization

The development of crystallinity in polymers depends on the regularity of structure along the polymer backbone, *i.e.*, the configuration of the polymer chain as produced during polymerization. A polymer will crystallize if its structure allows packing of its chains in a parallel array. This requires nearly complete chemical and stereochemical regularity.

Chemical regularity is achieved during polymerization when the monomer units attach themselves in an orderly head-to-tail fashion. Occasionally a head-to-head or tail-to-tail attachment will occur that presents a flaw in the chain regularity. If in sufficient quantity, these irregularities can jeopardize crystallization. Other chemical imperfections arise from the production of branching or side chains in an otherwise linear polymer. In the synthesis of polyethylene, for example, the introduction of paraffin side chains reduces the crystallinity to one half when the number of pendent groups is increased from 3 to 30 per 1000 chain units.[2]

In addition to chemical regularity, polymeric chains that have asymmetrical side groups also require stereochemical regularity to crystallize. Pendent groups can be arranged in different ways along the chain of the polymer, giving rise to three different stereoisomers; namely, isotactic (*i.e.*, same side of the vinyl backbone when the chain is in a planar zig-zag conformation), syndiotactic (*i.e.*, alternate sides) and atactic (*i.e.*, random arrangement). Isotactic and syndiotactic polymers will crystallize provided the side chain is not too bulky.

Complete chemical and stereochemical regularity is an idealized situation since polymeric chains include various types of disorder. Therefore, for a large number of reasons, polymers are generally not completely crystallizable and a conglomerate is obtained of crystalline and amorphous regions.[3,4] The fraction of crystalline regions in a sample defines the degree of crystallinity of the polymer.

1.1.2 The Concept of Chain Folding

X-ray diffraction studies, in the 1920's, indicated that some polymers are partially crystalline and, based on x-ray line broadening, the crystals were found to be either very small or imperfect. Based on the known high molecular weight of the polymeric chains and the small size of the crystalline entities, it was established that the chains passed in and out of many crystallites. These findings led to the fringed micelle model that was proposed by Herrmann, *et al.*[5] and is illustrated schematically in Figure 1.1.

This model suggests that the crystalline regions, 50 to 500 Å in size, consist of polymer chains that are crystallographically aligned and are embedded in an amorphous matrix. A single polymeric chain can then extend through a crystalline region, out through a more or less diffuse boundary to an amorphous network and possibly back into another crystalline region. This model was used with great success to explain the mechanical behavior of semicrystalline polymers. However, one of its problems is that as the crystals grow in size an accumulation of strain is expected at the ends of the crystal. This effectively limits the final crystal size. In addition, the observation of the spherulitic morphology by Bunn and Alcock[6] and Bryant[7] could not be accounted for by the traditional model.

Departure from the fringed micelle model came about in the mid 1950's with the successful preparation of polyethylene single crystals by Keller.[8] Electron diffraction analysis of these 100 to 140 Å thick diamond-shaped crystals indicated that the polymer chain axes in the crystal body were essentially perpendicular to the flat face of the crystal. Since the polyethylene chains were known to be thousands of angstroms long and the thickness of the crystals were in the vicinity of 100 to 140 Å, Keller[8] concluded that, in

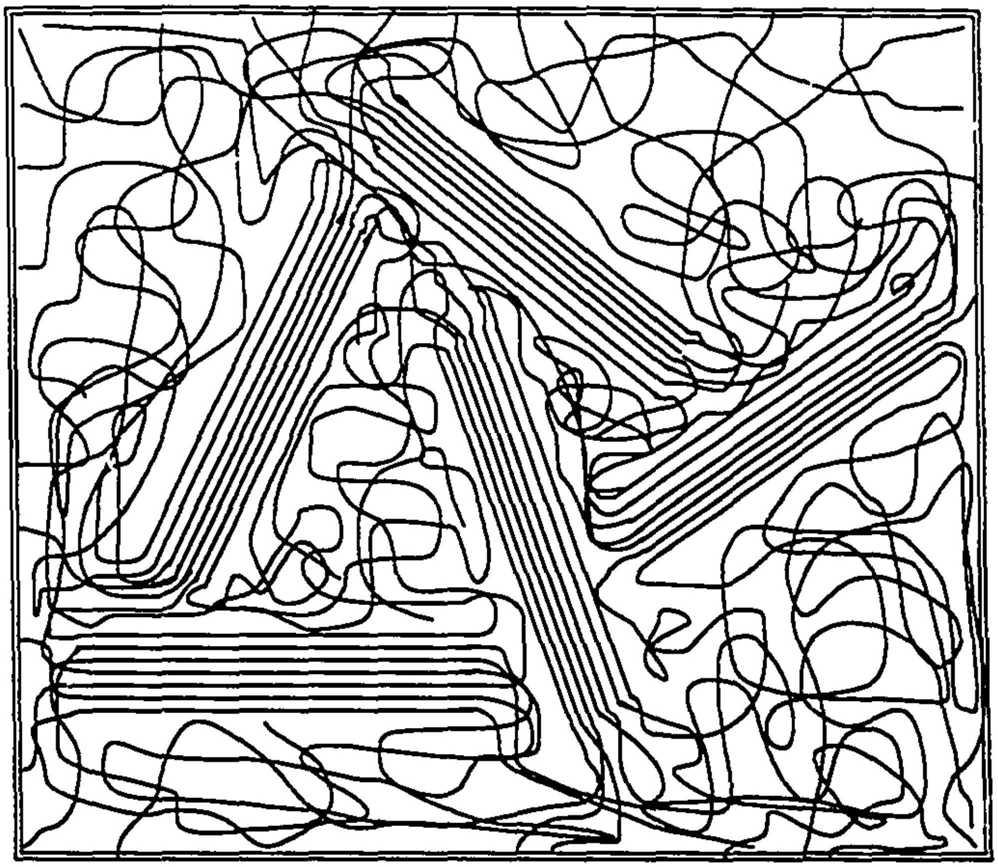

Figure 1.1 Schematic representation of the fringed micelle model showing crystalline and amorphous regions.

the crystals, the polymer chains had to be folded back upon themselves and thus traverse the lamellae many times. These observations were confirmed by Fischer[9] and Till.[10] It is of interest that the possibility of chain folding was first invoked in 1938 by Storks[11] who suggested that the macromolecules of gutta percha were folded back and forth upon themselves. The report of Storks remained unnoticed for almost 20 years, possibly due to the general acceptance, at that time, of the fringed micelle model.

The experimental evidence obtained from solution-grown crystals supports the concept of chain folding which is now universally accepted. However, controversy exists about exactly how the polymeric chains fold in the lamellae. The first model that was proposed is based on adjacent re-entry which was suggested by Keller[8] and Fischer.[9] As illustrated in Figure 1.2a, the chains that exit from a crystal surface re-enter, or fold back, into the crystal at the next possible position in the growth plane by a hairpin turn. This leads to the development of a very smooth and ordered surface, with no amorphous phase. However, it should be noted that although crystallization is essentially complete, the crystal must accommodate certain defects, such as a small degree of atacticity in the molecular body or ends.[12]

At the other extreme is the model that was proposed by Flory[13] in which it was postulated that chain folding occurs by the chain re-entering the crystal at random, non-adjacent locations. The fold surface would be very rough due to the loops of various lengths that are formed in the process of random re-entry. A single loop with non-adjacent re-entry is illustrated in Figure 1.2b. Increasing the number of these loops results in a surface that resembles an old telephone switchboard with its entangled and overlapping leads. For this reason, this model has been termed the "switchboard" model. Hybrid models, illustrated in Figure 1.2b, have been suggested previously[14,15] in which adjacent re-entry predominates with the occurrence of non-adjacent re-entry and dangling chain ends.

Many investigators have used a variety of techniques in an attempt to conclusively demonstrate the true nature of the formation of the fold surface in both single crystals and in bulk crystallized samples. Some of the techniques used in these investigations included infrared spectroscopy,[16-19] carbon-13 NMR[20-22] and small angle neutron scattering.[23-26] Infrared and carbon-13 NMR investigations of single crystals indicate

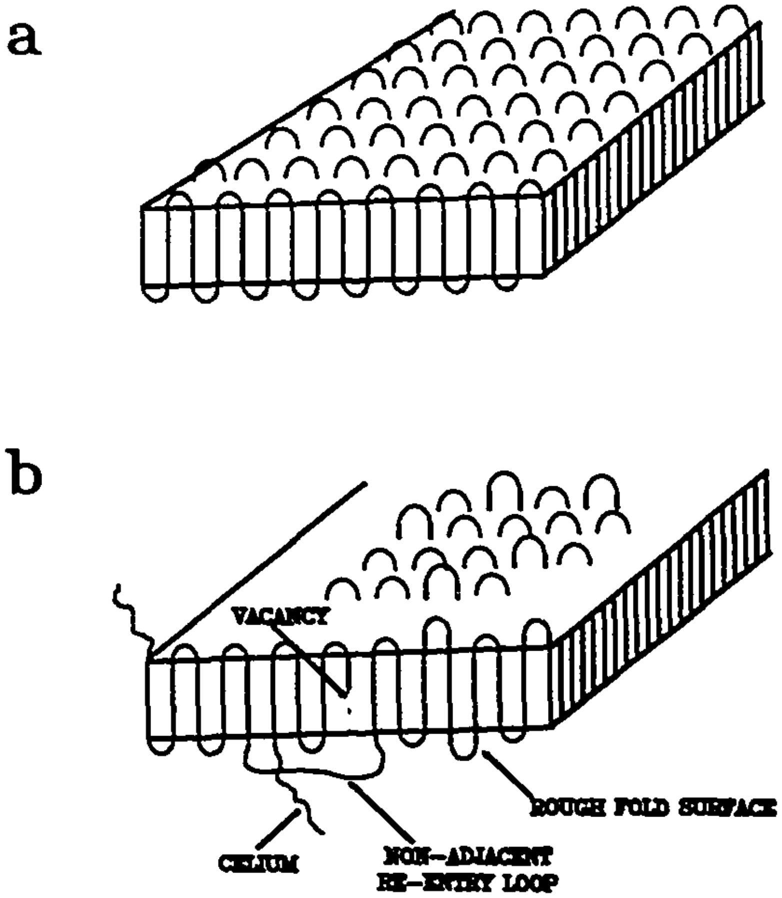

Figure 1.2 (a) Illustration of a regularly chain-folded crystal with adjacent re-entry. (b) Illustration showing possible departures from the strictly regular folding of adjacent re-entry; namely, cilia, non-adjacent re-entry loop and rough fold surfaces.

that the fold surface of the lamellae is more consistent with the occurrence of adjacent re-entry.[27] However, small angle neutron scattering investigations of deuterated and protonated polyethylene single crystals suggest the occurrence of both adjacent and non-adjacent re-entry where the latter occurs after skipping one or two nearest neighbor sites.[25] In melt crystallized samples, the lamellae are found to be organized differently. Experiments by Sadler and Keller[23-26] indicated that nearly random stem re-entry was most likely, *i.e.*, similar to the switchboard model that was proposed by Flory.[13] Adjacent re-entry would occur but only infrequently.

1.1.3 Spherulitic Structure

Crystallization of polymers from dilute solution results in the formation of lamellar-shaped single crystals that, as discussed in the previous section, exhibit a folded chain habit and are of the order of 100 to 200 Å thick. When polymers are crystallized from more concentrated solutions, various branched multilayered structures are observed with a tree-like morphology in which the overall shape of the single crystal is often retained (*i.e.*, dendritic morphology). Finally, when a polymer is crystallized from the molten state or bulk, in the absence of significant flow or stress, the dominant structure that is observed is the spherulite (Figure 1.3a).

Spherulites, as the name suggests, are sphere-shaped crystalline structures. However, this spherical symmetry is maintained only in the initial stages of crystallization from the bulk due to the impingement that occurs in the latter stages. In addition, when spherulites are grown from thin films, the thickness is usually substantially smaller than the diameter of the spherulite such that a cross-section along the diameter of the spherulite is usually being studied. The size of the spherulites generally ranges from 0.5 to 100 μm and is known to decrease as the undercooling is increased. In addition, when viewed on a microscope with crossed polars, each spherulite exhibits an extinction cross, *i.e.*, a Maltese cross, with arms oriented parallel to the vibration directions of the analyzer and polarizer of the microscope.

As illustrated in Figure 1.3b, spherulites are composed of arrays of fibrillar structural units that radiate outward from the central nucleus. In addition, the fibrillar

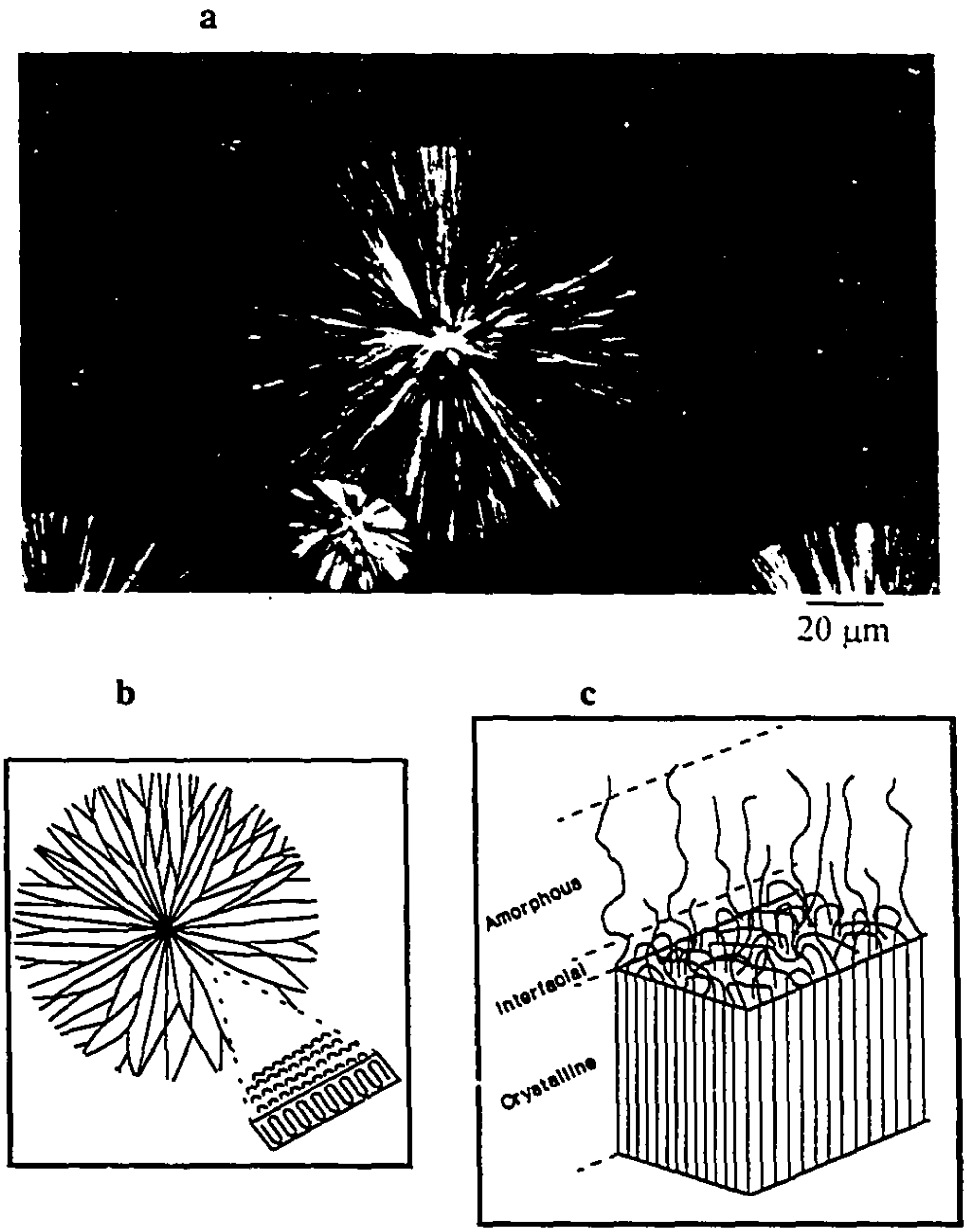

Figure 1.3 (a) Spherulites of isotactic polypropylene, as observed through crossed polarizers. (b) Illustration of the spherulitic structure and the orientation of the chain folded surface with respect to the fibrillar habit. (c) Simplified representation of the crystalline, interfacial and amorphous regions that constitute the fibril morphology of spherulites.

development proceeds by low-angle branching which generates a uniform space filling of the spherulitic structure. These fibrils may also exhibit twisting during the development of the spherulite.

Electron microscopy investigations of the spherulitic structure indicates that the fibrillar structural units of the spherulites are composed of individual lamellar crystalline plates of equal thickness.[28] Further examination by x-ray[29] and electron[30] diffraction indicates that the chain axis of polymer molecules is oriented tangentially to the radial direction of the spherulite (Figure 1.3b). This molecular axis is perpendicular to the flat surface of the lamellae and resembles very closely the structure of single crystals, as discussed previously. However, in the fibrils that make up the spherulites, the structure is better visualized as stacks of elongated lamellae where the molecular chains are oriented at right angles to the long axis of the fibrils (Figure 1.3b).

While the lamellar structure in spherulites is very similar to that of single crystals, the folding of the chains is much more irregular, as discussed in the previous section. As defined by Yoon,[31] there are three regions of importance which constitute the fibrillar morphology: the crystalline lamellar region which is approximately 100 Å thick, an interfacial region about 5 to 15 Å thick and an amorphous region about 50 Å thick. These three regions are illustrated in Figure 1.3c. A nearby re-entry model constrains the chain within the interfacial layer during the irregular folding process. In between the lamellar structures lies amorphous material. This region is composed primarily of less stereoregular polymer chains, low molecular weight material and/or impurities of various kinds.[27] The properties of this region are very similar to those of the molten state.

The individual lamellae in the fibrils that make up the spherulite are bonded together by "tie" molecules which reside partly in more than one crystalline region. These long, thread-like structures serve to tie the entire structure together by passing through many crystalline regions and are thought to be important in the development of greater toughness in semicrystalline polymers.

1.1.4 Structure and Morphology of Fibers

The crystallization of polymers under quiescent conditions is quite different from that which is observed in a dynamic environment which is encountered during the processing of polymers. Crystallization under the influence of stress or flow, as is the case in the process of fiber spinning, invariably affects the morphology that develops. The spherulitic morphology that is observed under quiescent crystallization conditions is not expected to be formed under the influence of stress or flow.

The morphology of fibers that are produced from linear flexible-chain polymers is segregated into regions with different degrees of order.[32] These semicrystalline fibers are mostly viewed as two phase structures consisting of crystalline and non-crystalline regions. This is consistent with their wide angle x-ray scattering which shows discrete reflections assigned to the crystalline material as well as diffuse scattering that is due to a non-crystalline phase. In addition, the physical structure of the fibers is also characterized by a certain degree of chain extension.[33,34]

The structure of the crystalline phase is also thought to be far from perfect. The conformation of the chains as well as their packing differs from that which is expected when the specimen is crystallized under optimum conditions.[35] In addition, in some fibers, the structure is further complicated by polymorphism, where stable and metastable crystal modifications may exist simultaneously.[36-38]

The fine structure of most fibers is a complex combination of long-chain molecules in crystalline and non-crystalline regions which may be aggregated into fibrils or other supermolecular structures.[39] A polymeric chain in the non-crystalline phase may be anchored in two different crystallites thus forming a "tie" molecule. It may re-enter the same crystallite at an adjacent or non-adjacent position thus forming a chain fold or may end in the non-crystalline phase to form the so-called cillium. The formulation of a structural model that describes the structural features of the crystalline and non-crystalline phases of a given fiber is difficult. The diversity of models in the literature, as reviewed by Hearle,[40] suggests the lack of precise knowledge about the fiber structure.

Early models[41-43] of the structure of the fibers resembled very closely the fringed micellar model that is illustrated in Figure 1.1. The structure was viewed as a network of crystalline regions in an amorphous matrix with the molecular axes of the polymeric chains essentially aligned with the fiber axis. Subsequently, various lamellar models have been suggested that describe the fiber structure as alternating layers of crystalline and non-crystalline material.[40]

The fiber structure has also been described in terms of a microfibrillar morphology.[44-49] The microfibrils, as described by Prevorsek, *et al.*,[44] are composed of a series of crystalline and intrafibrillar disordered regions while the areas between these microfibrils are noncrystalline and consist primarily of extended chains. Hearle and Greene[49] suggested a similar model but describe this fibrillar morphology as a modified fringed micelle structure, containing pseudo-fibrils due to the stacking of micelles. Finally, Dees and Spruiell[50] suggested that the morphology of fibers may be due to the formation of row nucleation during the development of the crystalline phase. Lamellar crystals are nucleated by, and grown epitaxially on, fibril nuclei that are generated from the elongational straining of the melt during processing.

1.2 Polymorphism in Isotactic Polypropylene

Isotactic polypropylene (iPP) has been the source of innumerable investigations since the late 1950's, concentrating on the many aspects of its organization in the solid state. The polymorphism in iPP has been reviewed at the supermolecular level (*i.e.*, spherulitic, *etc.*) by Varga[51] while Brückner and co-workers[52] reviewed the many aspects of its crystal structures and morphologies. An overview of this diversity in morphology will be presented with particular emphasis on the α-monoclinic crystal structure since it is the most pertinent to the remainder of this thesis.

1.2.1 Spherulitic Morphologies

Through the use of an optical microscope that is equipped with crossed polarizers, several types of spherulitic structures can be distinguished in iPP. Depending on the features of the fibrils, these spherulites can be either radial or banded and possess different optical characteristics. Radial spherulites are obtained when the fibrils radiate straight from the nucleus as illustrated in Figure 1.3b. Banded spherulites, on the other hand, occur due to periodic twists in the longitudinal direction of the fibril which appear as dark concentric rings whose spacing corresponds to the pitch of the twist.

The optical characteristics of a spherulite are characterized by its birefringence which is defined as the difference between the refractive index, Δn, that is observed in the radial, n_r, and in the tangential, n_t, directions of the spherulite.

$$\Delta n = n_r - n_t \tag{1.1}$$

The structure of a spherulite, as discussed previously, is composed of molecular chains that are folded into fibrils. The chains in these fibrils are oriented essentially perpendicular to the longitudinal direction of the fibril or to the radius of the spherulite. Since the refractive index is higher in the chain direction than in the perpendicular direction, fibrils have a negative birefringence.[51] Therefore, polymer spherulites are expected to be only optically negative.

The different types of spherulites that are observed in iPP were first reported by Padden and Keith[53] in 1959 and were classified as Types I to IV. These spherulites were found not only to differ in the crystal structure (*i.e.*, α-monoclinic or β-hexagonal) but also in their optical characteristics and architecture (*i.e.*, radial or banded spherulites). In addition, the observation of each of these spherulitic morphologies was found to be dependent on the crystallization temperature.

The occurrence of three different types of spherulites that are composed of the same α-monoclinic modification but differ in their optical characteristics was demonstrated by Padden and Keith[53] (*i.e.*, Types I, II and mixed). Positive and negative radial α-monoclinic spherulites were observed at crystallization temperatures below 134 and above 137 °C, respectively. In the intermediate temperature range, a third type of radial α-monoclinic spherulites was observed and found to have a mixed birefringence, *i.e.*, the spherulite has no certain optical character (Figure 1.3a).

In certain temperature regions two types of β-hexagonal spherulites were found to form sporadically among the α-monoclinic modification (*i.e.*, Types III and IV).[53] Negative radial (Type III) and negative banded (Type IV) β-hexagonal spherulites are observed at crystallization temperature below 128 and between 128 and 132 °C, respectively. When viewed under the optical microscope, these spherulites appear highly birefringent compared to the α-monoclinic modification. The observations of Padden and Keith[53] were supported in subsequent investigations[54,55] but other temperature ranges were suggested for the formation of the various types of spherulites.

The optical characteristics of the α-monoclinic spherulites (*i.e.*, positive and mixed birefringence) appear to contradict the negative birefringence that is expected to be produced in polymer spherulites. However, it was demonstrated by electron microscopy[54,56] that the fibrils of the α-monoclinic spherulites are branched with angles as large as 80° to the radius of the spherulite. Therefore, the radial growth is accompanied by a great number of tangential growth forming a "cross-hatched" structure.[54,56,57] The optical characteristics of the spherulite are, thus, controlled by the ratio of radial to tangential fibrils. This ratio increases as the crystallization temperature is increased and this causes, at higher crystallization temperatures, a transition from positive to negative birefringence in the spherulite.[54]

1.2.2 Crystal Structures

The various crystal structures of iPP are based on the development, during crystallization, of two enantiomorphic chain conformations, *i.e.*, right- and left-handed three-fold helices with a periodicity of 6.5 Å.[58,59] In addition, the right- and left-handed helices are further distinguished, in an absolute reference frame, by the orientation of the methyl groups. The covalent bond that joins the methine and methyl carbon atoms will have either an "up" or a "down" orientation with respect to the chain axis.[52] It should be noted that the "up" and "down" orientations differ only by a 180° rotation about an axis perpendicular to the chain direction. Therefore, the combination of these possibilities leads to four distinguishable chain conformations which pack in different geometries to give rise to the four well-known crystal forms of iPP; namely, the α-monoclinic,[59] the β-hexagonal,[59-62] the γ-triclinic[59,60,63] and the quench-cooled (smectic) form.[59] The quench-cooled morphology of iPP is discussed in Chapter 2. The β-hexagonal and γ-triclinic crystalline modification of iPP are not considered in this Introduction.

The structural characterization of the α-monoclinic crystalline phase of iPP was performed by Natta and co-workers in the years 1955 to 1960.[58,59,64] Based on the x-ray diffraction pattern of an oriented iPP fiber, a monoclinic unit cell was proposed with constants $a = 6.65(5)$, $b = 20.96$, $c = 6.50$ Å, and β=99.3°.[59] The unit cell was found to contain four three-fold helices for a total of 12 monomer units per unit cell and a density of 0.936 g/cm^3. According to the analysis of Natta and co-workers,[59] the unit cell of this modification contains both left- and right-handed helices that are arranged as depicted graphically in Figure 1.4. In addition, systematic absences of all odd h+k reflections

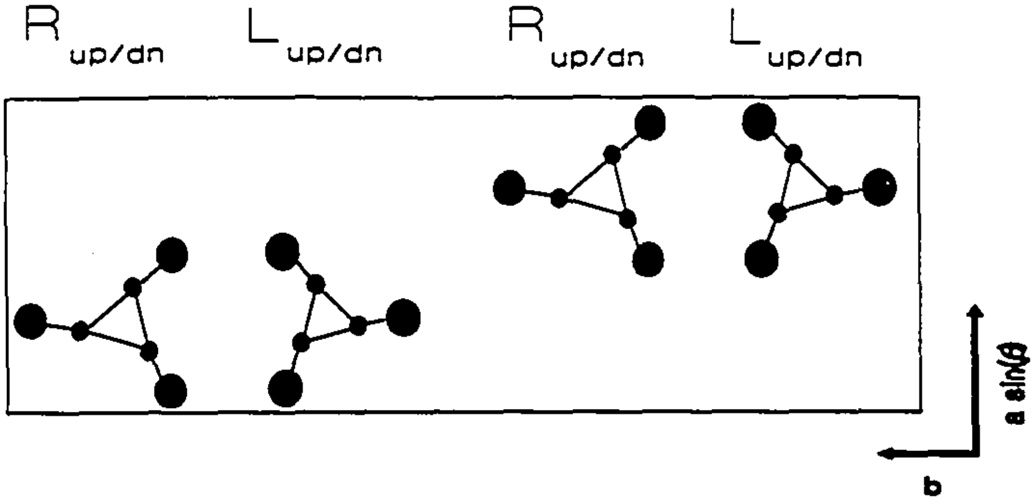

Figure 1.4 Illustration of the packing of the right-and left-handed helices, R and L, respectively, in the α-monoclinic unit cell of iPP.

were noted which suggested a centered crystal lattice. The C2/c space group was suggested with the assumption that a random distribution of "up" and "down" chains occurs (*i.e.*, with equal frequency) so that the average chain has no preferred direction.

Following the report of Natta and co-workers,[59] Mencik[65] observed some odd h+k reflections in the x-ray diffraction pattern of certain iPP samples and proposed that the α-monoclinic crystalline phase is consistent with $P2_1/c$ symmetry. Similarly, Turner-Jones, *et al.*[60] observed odd h+k reflections in unoriented and annealed iPP samples. However, these reflections were not observed in oriented α-phase fibers. The authors suggested that the space group of oriented and unoriented iPP samples in the α-phase might be different. Mencik,[66] in a subsequent investigation, attempted to describe the crystal structure of the α-modification of iPP by assuming $P2_1/c$ symmetry. This space group does not impose a random distribution in the "up" and "down" orientation of the chains, as does the C2/c symmetry, but it requires that bilayers of an "up" orientation be followed by a "down" orientation (*i.e.*, the R_{up}-L_{up}-R_{dn}-L_{dn} sequence in Figure 1.4). The odd h+k reflections were found to be substantially weaker than expected for a perfectly ordered $P2_1/c$ symmetry and, therefore, Mencik[66] invoked partial variation (25%) in the "up" and "down" orientation.

The crystal structure of the α-modification of iPP was also re-examined by Hikosaka and Seto.[67] The authors investigated two oriented fibers that were annealed for 2 hours at 140 and 171 °C, respectively. The sample annealed at the lower temperature did not show any odd h+k reflections while these were present in the sample annealed at the higher temperature. The intensities of the odd reflections were found to be lower than expected for $P2_1/c$ symmetry and the authors, in agreement with Mencik,[66] proposed partial up/down order. It was suggested that regions of ordered $P2_1/c$ symmetry co-existed with disordered regions of C2/c symmetry similar to "ordered islands floating in a disordered sea."

Hikosaka and Seto[67] also investigated the influence of annealing conditions on the level of order in the crystalline phase of oriented and unoriented iPP quench-cooled samples. It was found that the odd h+k reflections, which are associated with $P2_1/c$ symmetry, are absent in the samples annealed at lower temperature but are observed and increase in intensity as the anneal temperature is raised. This behavior was found to begin at lower temperatures for unoriented samples. A structural transition from a disordered C2/c state to an ordered $P2_1/c$ state was suggested. The α-phase for which the odd h+k reflections are extinct (C2/c) was designated α_1 while the limiting higher order form that is associated with $P2_1/c$ symmetry was named α_2.

Corradini, *et al.*[68] suggested an alternative model to the one proposed by Hikosaka and Seto.[67] A bilayer was defined as being composed of two ordered *ac* layers of isoclined enantiomorphic helices (*i.e.*, both left- and right-handed helices have the same up/down orientation). In each bilayer, the helices are all isoclined while the helices that belong to two different bilayers may be isoclined or anticlined. The bilayers of enantiomorphic helices are illustrated in Figure 1.5. It was suggested that the disorder in the up/down orientation is limited to the *b* crystallographic direction, since it is the most likely to show irregularities[66] in the ideal $P2_1/c$ sequence of up/down ordering. When a bilayer is juxtaposed to a bilayer of anticlined helices (Figure 1.5), $P2_1/c$ symmetry is observed. Irregularities occur when a bilayer is juxtaposed to a bilayer of isoclined helices which is consistent with Cc symmetry. According to this model, the α_1 and α_2 crystal forms are easily generated as well as any intermediate between these two forms.

The analysis of Mencik[66] and Hikosaka and Seto[67] clearly showed that the α-phase crystalline structure of iPP shows various levels of order in the "up" and "down" positioning of chains. This behavior is directly related to the thermal and mechanical history of the sample.

1.3 The Present Study

In this introductory chapter, the morphology that is observed in iPP samples under controlled crystallization conditions has been discussed in an effort to show the diversity of iPP morphology. Previous investigations that are pertinent to the research of a particular chapter are presented in the Introduction of each chapter.

This thesis is composed of five chapters: Chapter One is an introductory chapter on the morphology of semicrystalline polymers. Chapter Two describes an investigation of the room temperature morphology of quench-cooled iPP films. In addition, the development of this morphology following the sample quench is also considered. This work has been published in Polymer[69] (Reprinted with permission from Butterworth-Heinemann journals, Elsevier Science Ltd., UK). Chapter Three describes a solid state NMR investigation of the annealing behavior of quench-cooled iPP films. In particular, a new NMR pulse sequence is introduced that allows the exclusive observation of the

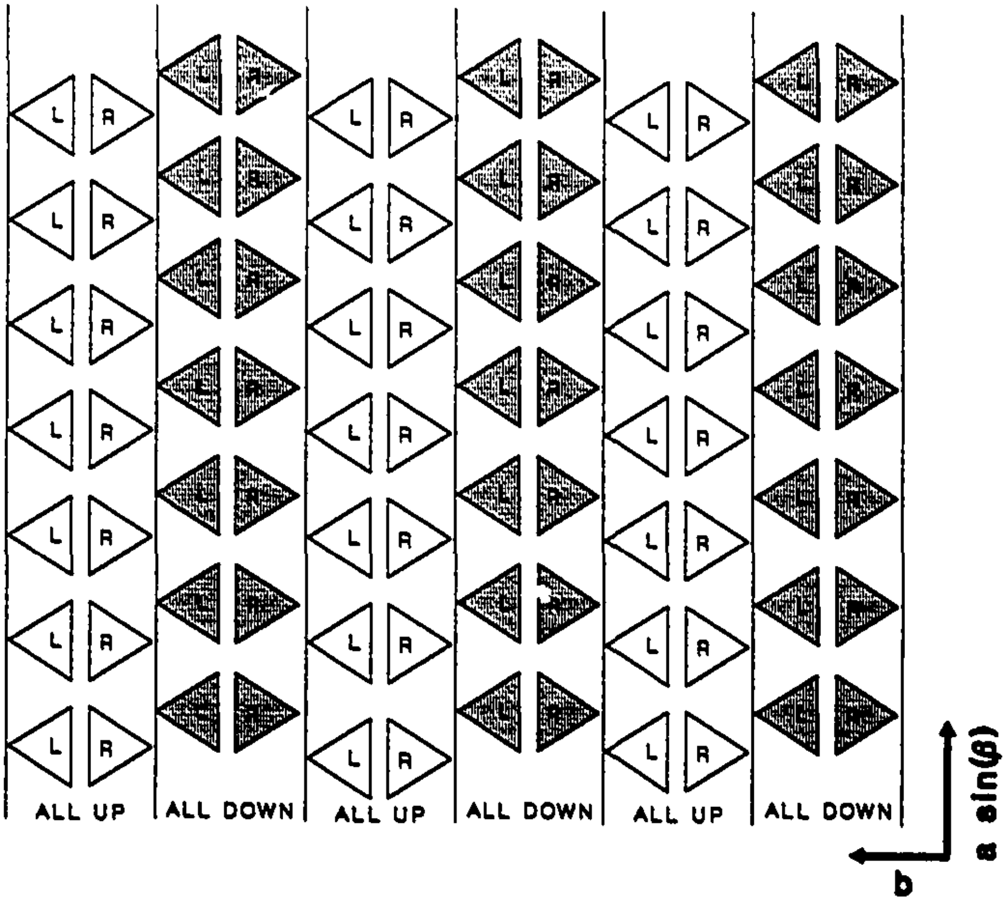

Figure 1.5 Illustration of the packing of the left- and right-handed helices of iPP in bilayers of isoclined helices. A given bilayer is followed by a bilayer of anticlined helices as in the $P2_1/c$ space group.

crystalline phase of iPP and it is used to monitor morphological changes within the crystalline phase of iPP during thermal annealing. This study appeared as an "Invited Paper" in a special issue of the Journal of Magnetic Resonance in Chemistry[70] (Reprinted with permission from John Wiley and Sons Ltd.). Chapter Four describes an investigation of the melting behavior of spunbonded iPP fabrics, with the same NMR characterization method that was used for the work in Chapter Three. In particular, the double melting endotherm of spunbonded iPP fabrics is investigated. Two manuscripts that describe this work have been submitted for publication in the Journal of Polymer Science, Polymer Physics Edition. Chapter Five describes the improvement of the tensile properties of spunbonded iPP fabrics by the dispersion of a surface modified silica/silicone additive. In addition, the melt flow index and molecular weight distribution of the iPP resin is modified by the blending of two iPP resins.

Finally, in Chapter Six, the Contributions to Original Knowledge of this research are summarized and Suggestions for Future Work are outlined.

1.4 References

1 J. Karger-Kocsis (Ed.), 'Polypropylene Structure, Blends and Composites; Vol. 1, Structure and Morphology; Vol. 2, Copolymers and Blends; Vol. 3, Composites' Chapman & Hall, London (1995).

2 E. Passaglia and H.K. Kevorkian, *J. Appl. Polym. Sci.* 7, 119 (1963).

3 F. Khoury and E. Passaglia, *Treatise Solid State Chem.* 3, 335 (1976).

4 B. Wunderlich, 'Macromolecular Physics, Vol. 2', Academic Press, New York (1976).

5 K. Herrmann, O. Gerngross and W. Abitz, *Z. Phys. Chem.* 10, 371 (1930).

6 C.W. Bunn and T.C. Alcock, *Trans. Faraday Soc.* 41, 317 (1945).

7 W.M.D. Bryant, *J. Polym. Sci.* 2, 547 (1947).

8 A. Keller, *Philos. Mag.* 2, 1171 (1957).

[9] E.W. Fischer, *Z. Naturforsch.* **12a**, 753 (1957).

[10] P.H. Till, Jr., *J. Polym. Sci.* **24**, 301 (1957).

[11] K.H. Storks, *J. Am. Chem. Soc.* **60**, 1753 (1938).

[12] G.N. Patel, in 'Methods of Experimental Physics', R.A. Fava (Ed.), Vol. 16, Part B, Academic Press, New York, p. 237 (1980).

[13] P.J. Flory, *J. Am. Chem. Soc.* **58**, 2857 (1962).

[14] A. Keller, *Kolloid-Z. Z.* **165**, 15 (1969).

[15] I.C. Sanchez and E.A. DiMarzio, *J. Chem. Phys.* **55**, 893 (1971).

[16] M. Tasumi and S. Krimm, *J. Polym. Sci., A-2* **6**, 995 (1968).

[17] M.I. Bank and S. Krimm, *J. Polym. Sci., A-2* **7**, 1785 (1969).

[18] S. Krimm and T.C. Cheam, *Faraday Discuss. Chem. Soc.* **68**, 224 (1979).

[19] X. Jing and S.Krimm, *Polym. Lett.* **21**, 123 (1983).

[20] F.A. Bovey, *Org. Coat. Appl. Polym. Sci. Prepr.* **48**, 76 (1983).

[21] F.C. Schilling, F.A. Bovey, S. Tseng and A.E. Woodward, *Macromolecules* **16**, 808 (1983).

[22] R. Kitamarn, F. Horii and S.H. Hyon, *J. Polym. Sci., Polym. Phys. Ed.* **15**, 821 (1977).

[23] D.M. Sadler and A. Keller, *Polymer* **17**, 37 (1976).

[24] D.M. Sadler and A. Keller, *Macromolecules* **10**, 1128 (1977).

[25] D.M. Sadler and A. Keller, *Science* **203**, 263 (1979).

[26] A. Keller, *Faraday Discuss. Chem. Soc.* **68**, 145 (1979).

[27] L.H. Sperling, 'Introduction to Physical Polymer Science', John Wiley, New York, p.192 (1986).

[28] F. Khoury and E. Passaglia, in 'Treatise on Solid State Chemistry, Vol. 3, Crystalline and Noncrystalline Solids', N.B. Hannay (Ed.), Plenum, New York (1963).

[29] Y. Fujiwara, *J. Appl. Polym. Sci.* **4**,10 (1960).

[30] E.J. Roche, R.S. Stein, and E.L. Thomas, *J. Polym. Sci., Polym. Phys. Ed.* **18**, 1145 (1980).

[31] D.Y. Yoon, *J. Appl. Cryst.* **11**, 531 (1978).

[32] J.G. Tomka, 'Polymer Properties in Comprehensive Polymer Science, The Synthesis, Characterization, Reactions & Applications of Polymers', G. Allen (Ed.), Permagon Press, Oxford, p. 494 (1989).

[33] P.J. Lemstra, R. Kirschbaum, T. Ohta and H. Yasuda, in 'Developments in Oriented Polymers, Vol. 2', I.M. Ward (Ed.), Elsevier, London, p. 39 (1987)

[34] P.J. Barnham and A. Keller, *J. Mater. Sci.* **20**, 2281 (1980).

[35] H.M. Heuvel and R. Huisman, *J. Appl. Polym. Sci.* **22**, 2229 (1978).

[36] H.M. Heuvel and R. Huisman and K.C.J.B. Lind, *J. Polym. Sci., Polym. Phys. Ed.* **14**, 921 (1976).

[37] H.M. Heuvel and R. Huisman, *J. Polym. Sci., Polym. Phys. Ed.* **14**, 941 (1976).

[38] H.M. Heuvel and R. Huisman, *J. Polym. Sci., Polym. Phys. Ed.* **19**, 121 (1981).

[39] J.W.S Hearle, in 'Textile Fibers', J.W.S Hearle and R.H. Peters (Eds.), Butterworth, London, p.209-232 (1963).

[40] J.W.S Hearle, 'Polymers and Their Properties, Vol. 1', Horwood, Chichester (1982).

[41] K. Hess and H. Kiessig, *Z. Physik. Chem.* **A193**, 196 (1944).

[42] K. Hess, H. Mahl and E. Gütter, *Kolloid-Z.* **155**, 1 (1957).

[43] J.W.S. Hearle, *J. Polym. Sci.* **28**, 432 (1958).

[44] D.C. Prevorsek, P.J. Harget, R.K. Sharma and A.C. Reimschuessel, *J. Macromol. Sci., Phys.* **B8**, 127 (1973).

[45] D.C. Prevorsek, G.A. Tirpak, P.J. Harget and A.C. Reimschuessel, *J. Macromol. Sci., Phys.* **B9**, 733 (1974).

[46] D.C. Prevorsek, R.H. Butler, Y.D. Kwon, G.E.R Lamb and R.K. Sharma, *Text. Res. J.* **47**, 107 (1977).

[47] A. Peterlin, *Text. Res. J.* **42**, 20 (1972).

[48] A. Peterlin, *Appl. Polym. Symp.* **20**, 269 (1973).

[49] J.W.S. Hearle and R. Greer, *J. Text. Inst.* **61**, 243 (1970).

[50] J.R. Dees and J.E. Spruiell, *J. Appl. Polym. Sci.* **18**, 1053 (1974).

[51] J. Varga, *J. Mater. Sci.* **27**, 2557 (1992).

[52] S. Brückner, S.V. Meille, V. Petraccone and B. Pirozzi, *Prog. Polym. Sci.* **16**, 361 (1991).

[53] F.J. Padden and H.D. Keith, *J. Appl. Phys.* **30**, 1479 (1959).

[54] D.R. Norton and A. Keller, *Polymer* **26**, 704 (1985).

[55] M.O.B. Idrisse, B. Chalbert and J. Guillet, *Makromol. Chem.* **186**, 881 (1985).

[56] F.L. Binsbergen and B.G.M. de Lange, *Polymer* **9**, 23 (1968).

[57] D.C. Bassett and R.H. Olley, *Polymer* **25**, 935 (1984).

58 G. Natta and P. Corradini, *Atti Accad. Naz. Lincei-Memorie* **4**, 73 (1955).

[59] G. Natta and P. Corradini, *Nuovo Cimento Suppl.* **15**, 40 (1960).

[60] A. Turner-Jones, J.M. Aizlewood and D.R. Beckett, *Makromol. Chem.* **75**, 134 (1964).

[61] H.D. Keith, F.J. Padden Jr., N.M. Walker and H.W. Wyckoff, *J. Appl. Phys.* **30**, 1485 (1959).

[62] A. Turner-Jones and A.J. Cobbold, *J. Polym. Sci., Part B, Polym. Lett.* **6**, 539 (1968).

[63] D.R. Morrow and B.A. Newman, *J. Appl. Phys.* **39**, 4944 (1968).

[64] G. Natta, P. Corradini and M. Cesari, *Rend. Accad. Naz. Lincei.* **21**, 365 (1956).

[65] Z. Mencik, *Chem. Prumysl.* **10**, 377 (1960).

[66] Z. Mencik, *J. Macromolec. Sci., Phys.* **B6**, 101 (1972).

[67] M. Hikosaka and T. Seto, *Polym. J.* **5**, 111 (1973).

[68] P. Corradini, G. Giunchi, V. Petroccone, B. Pirozzi and H.M. Vidal, *Gazz. Chim. Ital.* **110**, 413 (1980).

[69] V. Caldas, G.R. Brown, R.S. Nohr, J.G. MacDonald and L.E. Raboin, *Polymer* **35**, 899 (1994).

[70] V. Caldas, F.G. Morin and G.R. Brown, *Mag. Res. in Chem.* 32, S72 (1994).

CHAPTER TWO

The Structure of the Mesomorphic Phase of Quench-cooled Isotactic Polypropylene

2.1 Introduction

Since the initial disclosure by Natta[1] that propylene could be polymerized to yield high molecular weight, isotactic semi-crystalline polymers there have been numerous studies on the structure, morphology, mechanical properties and their inter-relationships. Within this large body of literature there is particular emphasis on the effects of thermal history and mechanical deformations on the crystalline morphologies of polypropylene (PP). The morphology of a partially ordered phase that is attained as a result of quench cooling an isotactic polypropylene (iPP) sample is the focus of this study.

2.1.1 Proposed Levels of Order Within the Quenched Phase

As discussed previously, when crystallized either from the melt or from solution, iPP adopts a 3_1 helical conformation. Depending on the crystallization conditions,[2-8] these helices pack in different geometries giving rise to the three well known polymorphs of iPP,[9] namely the α-monoclinic, the β-hexagonal, and the γ-triclinic crystal forms, which exist in conjunction with an amorphous phase. It was pointed out many years ago[10-13] that a phase possessing order intermediate between the amorphous (atactic) and crystalline states can be obtained by quench cooling. Although the x-ray scattering curve for the quench-cooled sample is very similar to that for atactic polypropylene, the presence of a second scattering maximum at 22.2° (*i.e.*, 2θ) suggests the existence of a somewhat greater degree of order. Infrared studies reported by Natta, *et al.*[10] revealed that, in this quenched phase, for a large fraction of their length the individual chains of iPP maintain the same 3_1 helical conformation that is present in all of the other three polymorphs. In addition, the wide angle x-ray diffraction (WAXD) pattern of a quench-cooled iPP sample that was highly oriented indicated a well-defined identity period of 6.5 Å. It was concluded that the helices have a parallel orientation and the packing perpendicular to their axes is more disordered than along the axes. Since the packing of the helices did not appear to be completely random, Natta, *et al.*[10] referred to this partially ordered phase as a "smectic" form, indicating a degree of order higher than molecular parallelism found in a nematic liquid crystalline phase.

Following the initial description of the quench-cooled phase of iPP as being a "smectic" modification, much work gave evidence that it possesses higher levels of order. Miller,[13] having confirmed the results of Natta, *et al.*,[10] described the quench-cooled iPP morphology as paracrystalline in the sense of Hosemann,[14] *i.e.*, having statistical variations of the edges of the unit cell in both length and direction. Some years later, Zannetti[15] also described the quench-cooled morphology as paracrystalline. Wyckoff[12] performed x-ray analysis on cold drawn quench-cooled samples and pointed out that in the x-ray pattern of this oriented sample the peak belonging to the first layer line was much sharper than expected for an isolated three-fold helix. It was concluded that a certain degree of correlation exists between the positions of adjacent helices suggesting, in addition to chain parallelism, short-range three-dimensional order of a limited nature. Wyckoff did not elucidate the nature of the short-range order but indicated that it must resemble, on a local scale, the order existing in the α-monoclinic phase.

After the β-hexagonal crystal form had been recognized, Gailey and Ralston[16] suggested that the partially ordered phase of iPP is composed of small hexagonal crystals that are 50-100 Å in size. This proposal was based solely on the observation that the two diffraction maxima obtained for the quench-cooled phase coincide with the two most intense diffraction maxima of the hexagonal phase. Farrow[17] agreed with the concept of fine crystals but did not make reference to a hexagonal morphology. Electron microscopy studies on the morphology of the quench-cooled phase, by Gezovich and Geil,[18] revealed "ball-like" structures about 125 Å in size and they suggested that these are defective hexagonal crystals. On the other hand, Bodor, *et al.*[19] assumed the quenched phase to be composed of small crystals of the monoclinic form and suggested that the characteristic x-ray scattering pattern is due to crystal size line broadening. Finally, McAllister, Carter and Hinde[20] proposed that the polymer chains in the quenched phase are arranged in a square symmetry and estimated a crystal size of approximately 30 Å. This was disputed by Guerra, *et al.*[21] who contended that all of the reflection maxima were interpreted as equatorial reflections which does not agree with the x-ray pattern of oriented quench-cooled samples.

To attempt a theoretical elucidation of the structure of the partially ordered phase of iPP, Corradini, *et al.*[22,23] compared the experimentally determined x-ray diffraction intensities for this phase with calculated Fourier transforms for various models of chain aggregates packed in the α-monoclinic and β-hexagonal crystal forms as well as for disordered models possessing character of both phases. The local correlation between chains was found to more closely resemble the crystal structure of the α-monoclinic crystal form than the β-hexagonal, although any correlation between chains appeared to be lost at distances of the order of 30-40 Å.

Although the degree or type of order in the quenched phase of iPP has not been fully determined, through x-ray diffraction and electron microscopy studies Hsu, *et al.*[24] have found that the "smectic" morphology develops as the quench-cooled sample is heated between -20 and 0 °C, *i.e.*, it results due to crystallization from the glassy state. DSC studies confirmed that upon heating a quench-cooled sample of iPP crystallization occurs in the same temperature region where the morphological changes were observed by electron microscopy. Infrared spectra obtained by Glotin, *et al.*,[25] also present evidence that quench-cooled iPP crystallizes from the glassy state.

2.1.2 The Present Study

As can be deduced from the above discussion, the level of order that exists within the quenched morphology of iPP is still in dispute. The goal of this work was to attempt a fuller description of the level of order that exists within the morphology of the quenched phase of iPP. To this end, electron microscopy techniques that offer higher resolution than have been used previously were employed to probe the local order, *i.e.*, areas less than 100 Å^2. A further goal of this study was to investigate the development of order (*i.e.*, crystallinity) during and/or following the sample quench. Detailed DSC studies are presented, which confirm and yield a fuller description on the formation of this phase, *i.e.*, about the crystallization from the glassy state.

2.2 Experimental

The iPP used in this study was obtained from Exxon (Exxon 3445, melt flow index = 34; P_m=0.93, as obtained by NMR). Its weight- and number-average molecular weights, as obtained by gel permeation chromatography analysis, were 144 600 and 50 000, referenced to narrow molecular weight polypropylene standards in 1,2,4-trichlorobenzene at 145 °C. Samples of the mesomorphic form were prepared by melting the iPP sample between microscope slides at a temperature of 225 °C for 15 minutes followed by quench cooling in a cold medium, namely a dry ice/acetone slush (-78 °C) or a pentane slush (-130 °C). An aluminum spacer of 14 µm between the microscope slides controlled the sample thickness. The mesomorphic phase was characterized by electron microscopy, solid state nuclear magnetic resonance (NMR) spectroscopy with cross polarization/magic angle spinning (CP/MAS), and differential scanning calorimetry (DSC).

2.2.1 Electron Microscopy

2.2.1.1 Dark Field Imaging

The previously quench-cooled iPP films were prepared for electron microscopy in the following manner: The film was cut into a square, about 5 mm X 5 mm, and imbedded in Spurr epoxy resin. The epoxy was cured at room temperature for one week, after which the sample was trimmed in preparation for microtoming using the FC4 Reichert-Jung cryo-ultramicrotome set at a temperature of -65 °C. Thin sections, about 400 Å in thickness, were collected and mounted on 3 mm 600 mesh hexagonal grids. The samples were then transferred to the JEOL cryo specimen holder and observed with a JEOL 100cx scanning transmission electron microscope. During the observations the samples were kept at liquid nitrogen temperature to minimize electron beam damage.

To avoid damage to the entire grid sample, the scanning electron beam was controlled using the microscope electron optics to view only specific areas. The scan generator reduced the incident beam to a minimal spot size of 15 Å before the specimen plane, thus allowing the scan width and length on the grid to be controlled by the operator. By using the beam stop below the specimen plane, dark field images (n-beam) of selected specimen areas were obtained using the electrons scattered by the microcrystalline areas. High speed photographic film (400 ASA) was used to record the images. In addition, a beam blanking device, located in the condenser lens beam tilt circuitry, and a minimum dose device (MDD) were used to minimize electron beam damage. The blanking device allows rapid tilting of the beam off and on the optical axis thus accomplishing very fast exposure times. By use of the MDD the beam can be focused on an adjacent area after which it is exposed on a selected new area which has not yet been damaged. In this study, imaging was done near the copper grid bars so that much of the electron beam heating was conducted away from the area of interest. Separate experiments using a thermocouple revealed heating to temperatures no higher than 50 °C in the time required to record the dark-field image.

2.2.1.2 Micro Electron Diffraction

Micro electron diffraction patterns were also obtained using the JEOL 100cx scanning transmission electron microscope, which made it possible to record diffraction patterns of crystalline areas much smaller than could be viewed by conventional transmission electron microscopy (CTEM). Making use of the "spot" mode (15 Å) in selected area scanning, microdiffraction patterns were obtained for selected areas of the quench-cooled film. The condenser and intermediate lenses were controlled manually thus allowing for different camera lengths. To minimize sample beam damage and co-operative molecular rearrangement due to the electron bombardment, Kronex X-ray film was used to record the diffraction patterns which decreased exposure times to the order of 2 seconds. Microdiffraction patterns probing areas less than 100 Å^2 were recorded as a tilt series from 0 to 30°.

In the calculation of the unit cell dimension, the spacings of the various reflections on each of the diffraction patterns in the tilt series were measured as diameters using a micron-drive bar that was attached onto a light box. These measurements were performed under magnification using a 10X magnification eye piece. Three measurements were performed per reflection and averaged.

Calibration of the microscope to obtain the camera length was performed using the polycrystalline ring pattern of a gold standard. The inner-most ring of the gold diffraction pattern, which is the sharpest and most intense, was used for this purpose. This ring is the 111 reflection and is associated with a d-spacing of 2.3545 Å. The camera length, L, was obtained through the use of the following geometric relationship:

$$L = \frac{r}{\tan(2\theta)} \qquad (2.1)$$

where r is the radius of the ring measured from the x-ray film, in mm, and θ is the diffraction angle obtained by implementing the well known Bragg diffraction equation.

$$2\,d\,\sin(\theta) = \lambda \qquad \text{or} \qquad \theta = \sin^{-1}\left(\frac{\lambda}{2d}\right) \tag{2.2}$$

where λ is the incident electron wavelength (*i.e.*, λ=0.0375 Å at a voltage of 100 KV) and d is the d-spacing, in Å, of the measured reflection. Upon obtaining the camera length, the measured radii of the iPP reflections can be converted to d-spacings by a simple reorganization of eqn. (2.1) to obtain the diffraction angle followed by the use of Bragg's Law (*i.e.*, eqn. (2.2)).

The derivation of the unit cell dimension was performed using a Fortran program obtained from Dr. Brisse of the University of Montreal. A listing of the program is shown in Appendix A. Through a least squares analysis, the program derives a unit cell dimension based on proposed Miller indices for each of the observed reflections. It should be noted that this program required the location of a given reflection to be entered as a diffraction angle that is based on Cu K_α (*i.e.*, λ=1.54178 Å) as the incident radiation. Therefore, all measured d-spacings were converted to x-ray diffraction angles by use of Bragg's Law and substituting the electron wavelength with that for Cu K_α.

The assignment of a Miller index to each of the observed reflections was aided by two Turbo Pascal programs that are also listed in Appendix A. The first program listed possible Miller indices for a given d-spacing under an assumed unit cell dimension while the second program proposed a unit cell dimension based on a set of observed d-spacings with possible Miller indices. However, it should be noted that these two programs were only applied to obtain a listing of possible indices for each of the reflections. The final unit cell dimension was obtained with the least squares deviation Fortran program obtained from Dr. Brisse under the constraint that, for a set of given d-spacings and Miller indices, a minimum deviation was observed between calculated and observed diffraction angles. This deviation, ξ, is reported by the Fortran program, in terms of the following relation:

$$\xi = \sqrt{\frac{\sum_{i=1}^{N} \left| \sin^2 \theta_{obs} - \sin^2 \theta_{calc} \right|}{N-1}} \tag{2.3}$$

where N is the number of observed reflections.

2.2.2 Solid State NMR Experiments

CP/MAS ^{13}C NMR spectra were recorded at room temperature with a Chemagnetics CMX-300 spectrometer operating at a static field of 7.1 T. The samples were spun at the magic angle at a frequency of about 3.8 kHz in a 7.5 mm outer diameter (OD) zirconia rotor. A contact time of 1 ms was used in the cross polarization, with a pulse delay of 3 seconds. A 62.5 kHz rf decoupling field was used with a decoupling period of 200 ms. All spectra were referenced to tetramethylsilane (TMS) in a spectral window of 30 kHz by setting the methyl resonance of hexamethyl benzene to 17.40 ppm. Prior to Fourier transformation, the FID was zero-filled to 4K. Spin-lattice relaxation times in a rotating frame, $T_{1\rho}$ (^1H), were measured for the methylene, methine and methyl carbons by varying an interval, τ, prior to cross polarization. The relaxation times were obtained by fitting the intensity data on a double exponential decay curve using a computer program (Peakfit, obtained from Jandel Scientific).

2.2.3 Differential Scanning Calorimetry

Thermal analysis was performed with a Perkin Elmer DSC-7C by heating the sample at 20 °C/min from -60 to 220 °C under a nitrogen flow. Calibration of the DSC for temperature and enthalpy was accomplished by running two high purity standards, namely indium and octadecane. All of the annealing experiments were performed by heating the sample to the appropriate temperature, at a rate of 20 °C/min, and maintaining this temperature for the desired time. The sample was then cooled at 100 °C/min (nominal) to -45 °C and allowed to come to thermal equilibrium prior to thermal analysis.

To describe the crystallization process from the glassy state, the iPP sample in the aluminum DSC pan must be quench-cooled and maintained cold until thermal analysis. This was accomplished by the following technique: The DSC pan containing the iPP sample was heated to 220 °C and maintained for 15 minutes. It was then transferred into a Dewar flask containing a pentane (HPLC grade) slush, thus quench cooling the sample to -130 °C. The sample pan was then transferred to a small flat-bottomed glass vessel containing a small amount of pentane kept at -78 °C by immersing the glass vessel in a dry ice/acetone slush. The vessel, which was maintained at -78 °C, was then attached to a vacuum line where it was pumped by a mercury diffusion pump for at least four hours to remove the pentane. It was then flushed with cold, dry nitrogen, removed from the vacuum line, and the clean DSC pan was quickly transferred into a Dewar flask containing fresh liquid nitrogen. The sample were then transferred to the DSC sample holder, that was maintained at -60 °C by the Perkin-Elmer intracooler accessory, allowed to come to thermal equilibrium and subsequently analyzed as described above.

2.3 Results and Discussion

2.3.1 Differential Scanning Calorimetry

2.3.1.1 Quench-cooled samples maintained at room temperature

The DSC thermogram for the heating of an iPP sample at a heating rate of 20 °C/min which has been allowed to warm to room temperature after it was quench-cooled in a dry ice/acetone slush at -78 °C is shown in Figure 2.1. In addition to the large endotherm between 120 and 165 °C, which corresponds to the melting of the developed crystalline morphology, two distinct regions characterize the thermal behavior of this quench-cooled phase. The first is a small endotherm, of area corresponding to 4.4 J/g, in

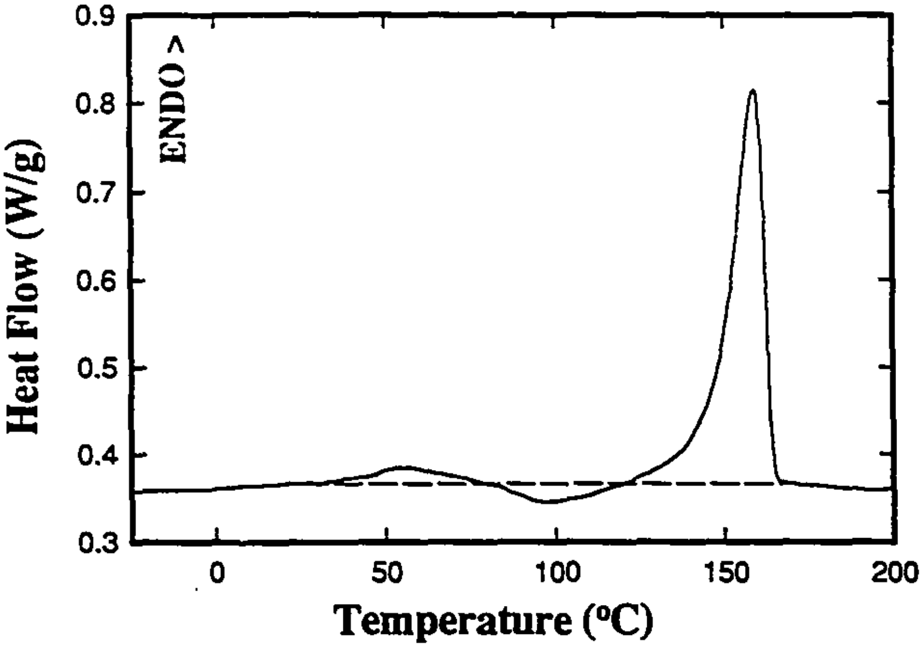

Figure 2.1 DSC thermogram of an iPP sample quench-cooled in a dry ice/acetone slush at -78 °C and allowed to return to room temperature. (The dashed line represents the baseline used in the separation of endothermic and exothermic regions.)

the interval between 30 and 75 °C that is very similar to that observed previously by Fichera and Zannetti[26] for quench-cooled iPP samples subjected to a low temperature anneal. They ascribed it to the melting of small crystals formed during annealing. Grebowicz, *et al.*[27] confirmed the existence of this endothermic transition in annealed quench-cooled samples but demonstrated that it also occurs for a quench-cooled sample that has not been annealed. They also attributed it to the melting of small crystals formed during the quenching process. The nature of this endotherm will be discussed further once the morphology of this phase has been described.

As reported previously[26-29], the low temperature endotherm is followed by an exothermic transition in the interval between 80 and 120 °C that has been attributed to a transition from a quenched phase morphology to the stable α-monoclinic crystalline phase. This interpretation was based on x-ray evidence[30] which showed a transformation from two broad diffraction maxima, the characteristic diffraction pattern of the quench-cooled phase, to the usual diffraction pattern of the crystalline α-monoclinic phase that becomes evident for samples annealed at temperatures ≥60 °C. The heat of conversion is -8.8 J/g (-2.1 cal/g), or approximately 50% that reported by Fichera and Zannetti.[26] It is similar, but slightly greater than that obtained by Grebowicz, *et al.*[27] who reported a value 25-33% that reported by Fichera and Zannetti. The discrepancy with the value of Grebowicz, *et al.* may reflect different quenching techniques, which could result in differences in the morphology. In the work of Fichera and Zannetti, the thermograms begin at 50 °C which, as seen in Figure 2.1, is well into the low temperature endotherm and consequently results in a misplaced baseline. This exotherm will also be discussed further in light of new electron microscopy results as well as DSC experiments presented below.

The DSC thermograms for various quench-cooled iPP samples which have been annealed subsequently for 40 minutes at different temperatures are shown in Figure 2.2. The low temperature endotherm (LTE) that begins near 40 °C for the unannealed quench-cooled sample shifts to higher temperature with increasing anneal temperature, as shown in Figure 2.3. Although previous studies[26-27] reported that the onset of this endotherm corresponds to the anneal temperature, deviations from such a linear relationship are observed at anneal temperatures below 60 °C and again at the higher temperatures, *i.e.*,

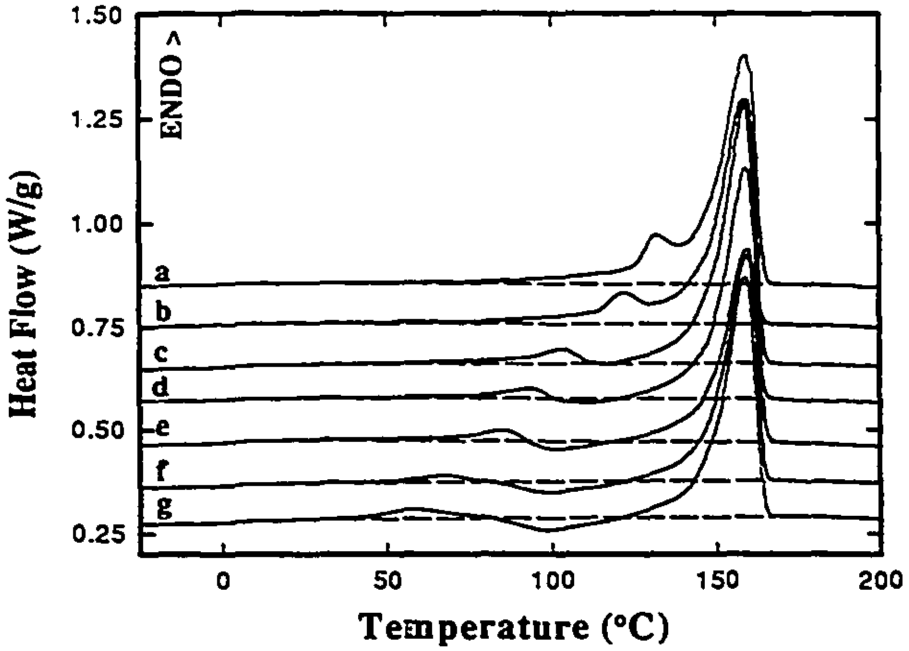

Figure 2.2 DSC thermogram of iPP samples quench-cooled in a dry ice/acetone slush and subsequently annealed for 40 minutes at a) 120 b) 110 c) 90 d) 80 e) 70 f) 50 g) 30 °C. (The dashed line represents the baseline used in the separation of endothermic and exothermic regions.)

above 100 °C. For the quench-cooled sample which has not been annealed the onset temperature of the endotherm (indicated by the inverted open triangle in Figure 2.3) occurs at 42 °C. In keeping with the non-linear relationship represented in Figure 2.3, this onset temperature for the LTE corresponds to an anneal temperature of 27 °C. Therefore, the quench-cooled sample which was allowed to return to room temperature has a

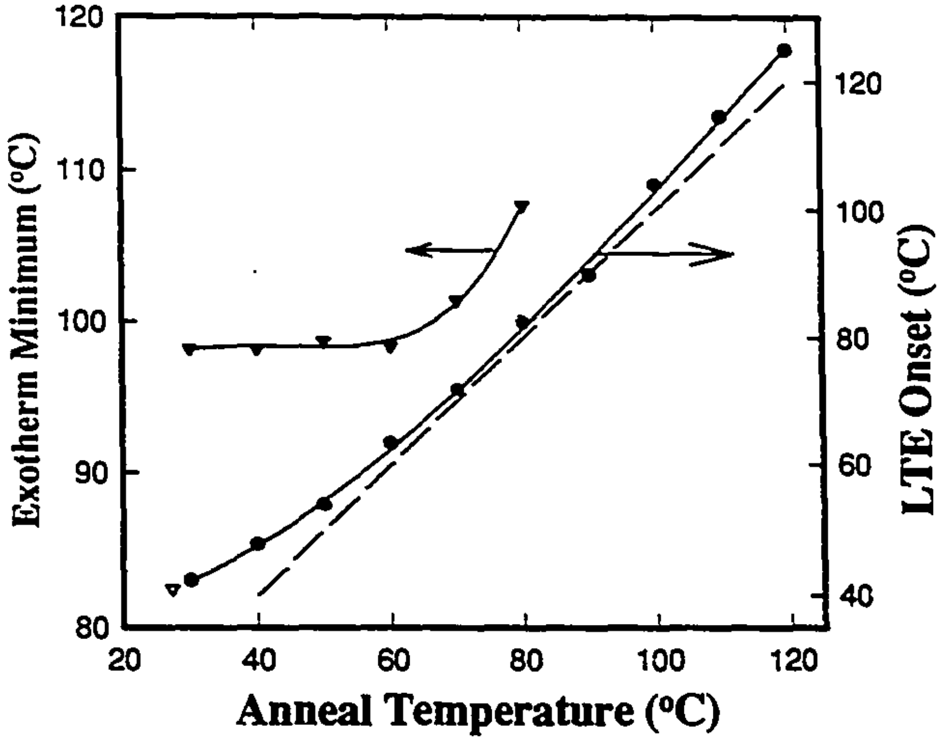

Figure 2.3 Effect of anneal temperature on the onset of the low temperature endotherm (LTE) as well as on the exothermic transition. (The dashed line reflects the relationship $T_{Onset} = T_{Anneal}$.)

crystalline morphology which is consistent with that expected for a sample annealed at room temperature. If this endotherm represents the melting of an imperfect crystalline morphology, as suggested previously, such crystals must develop at a lower temperature during the quenching process, as concluded by Hsu, *et al.*[24]

This endotherm remains approximately constant in area, varying randomly between 3.6 to 5.2 J/g, for anneal temperatures between 30 and 80 °C. It is difficult to accurately determine the ΔH for samples annealed at temperatures above 100 °C, because the LTE coalesces into the onset of the main melting endotherm. Fichera and Zanneti[26] reported an increase in the size of this low temperature endotherm with increase in temperature, between 70 and 120 °C, as well as with anneal time. However, as described above, those areas are in doubt because of the misplaced baseline.

The exothermic transition at about 100 °C can be discerned only for samples that have received thermal treatments at 90 °C or lower, as seen in Figure 2.2. The minimum of this peak remains at 98 °C for anneal temperatures ≤60 °C (Figure 2.3) and the magnitude of its area remains constant at about -8.0 J/g. Higher anneal temperatures result in a small shift to higher temperature as well as a rapid decrease in its magnitude until it disappears at anneal temperatures ≥ 90 °C.

2.3.1.2 Quench-cooled samples maintained at low temperature

DSC thermograms of "as-quenched" iPP samples, *i.e.*, samples which have been quench-cooled and maintained at low temperature until analysis, are shown in Figure 2.4. In each case the baseline represented by a dashed line, used in the separation of exothermic and endothermic regions, is an extension of the baseline obtained for the melt back to the point where it intercepts the thermogram at about -16 °C, *i.e.*, at the end of the glass transition. Upon heating the samples exhibit a glass transition at -19±1 °C followed by an exothermic peak, with an onset at about -14 °C, due to crystallization from the glassy state. The thermogram remains exothermic up to 120 °C in keeping with the occurrence of crystallization or recrystallization processes. Although Hsu, *et al.*[24] also detected a crystallization peak upon heating the quench-cooled iPP sample, the exothermic region of the thermogram between room temperature and 120 °C was not detected, possibly due to baseline curvature that is evident in their thermogram.

The weight normalized DSC thermograms shown in Figure 2.4 for the two

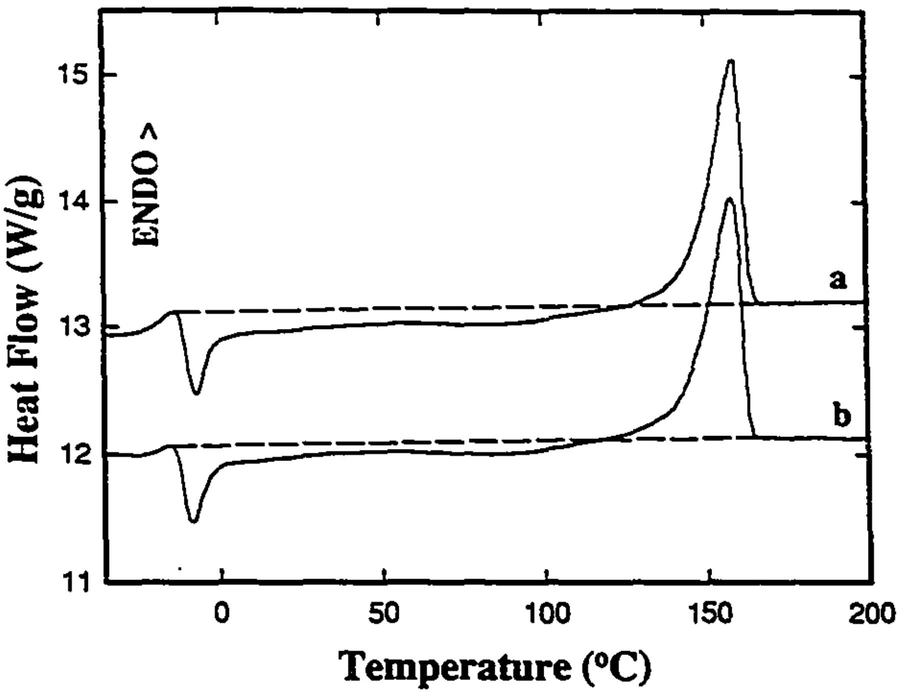

Figure 2.4 DSC thermograms of iPP samples of weights corresponding to a) 1.96 mg and b) 4.22 mg quench-cooled in a pentane slush (-130 °C) and maintained cold until thermal analysis. (The dashed line represents the baseline used in the separation of endothermic and exothermic regions.)

samples of iPP weighing 1.96 and 4.22 mg have identical glass transition, crystallization, and final melting temperatures as well as final heats of fusion. However, the sample of lower mass has a substantially larger change in heat capacity at the glass transition as well as a larger heat of crystallization as measured in the region between -15 and 120 °C.

The degree of crystallinity that develops during quench cooling can be estimated from the excess energy (defined as the difference between the heat of fusion in the region between 120 and 170 °C and the heat of crystallization measured between about -15 and 120 °C) as well as from the change in heat capacity at the glass transition using the relationship

$$w_c = 1 - \frac{\Delta C_p}{\Delta C_p^o} \qquad (2.4)$$

where ΔC_p is the measured change in heat capacity at the glass transition, ΔC_p^o is the corresponding change in heat capacity of the pure amorphous glass ($\Delta C_p^o = 0.559$ J/g°C)[31] and w_c is the weight fraction crystallinity. The degrees of crystallinity derived by these two methods as well as some of the transition temperatures are given in Table 2.1 for iPP samples of weights ranging from less than 1 to 8 mg.

As seen in Figure 2.5, for sample weights >4 mg, the heat of fusion exceeds the heat of crystallization by about 30 J/g. This corresponds to the formation of about 18% crystallinity during sample quenching, based on 165 J/g as the heat of fusion for a 100% crystalline iPP sample.[32] As the sample weight is reduced the excess endothermic energy decreases and approaches zero for sample weights <1 mg. Similarly, the ΔC_p for samples of low mass approaches the accepted value for a 100% amorphous glass (represented by a dash line in Figure 2.5) but decreases with an increase in sample weight, in keeping with higher crystallinity for the larger sample weights. These observations suggest that quench cooling iPP samples of low mass at rates accessible to these experiments results in essentially amorphous glasses, while samples with higher weights develop some crystallinity. The total sample crystallinity, as judged from the final melting peak, at 158± 1 °C, is constant at 76±2 J/g, which corresponds to a sample crystallinity of 46±2 %. This total developed crystallinity is consistent with the results of Fichera and Zannetti,[26] who also reported an ultimate heat of fusion of 75 J/g but slightly higher than a crystallinity of 38±2% reported by Grebowicz, *et al.*[27]

Table 2.1: Transition temperatures and percent crystallinity as obtained from excess endothermic energy and change in heat capacity from DSC thermograms for "as-quenched" iPP samples of various weights

	Transition Temperatures (°C)			% Crystallinity			
Weight (mg)	T_m	T_c	T_g	Excess Energy (J/g)	% Cryst.	ΔC_p (J/g°C)	% Cryst.
7.85	157.5	-7.0	-18.6	31	19	0.22	60
5.25	160.6	-6.4	-16.9	29	18	0.23	58
4.22	157.5	-8.5	-19.2	30	18	0.27	52
2.80	158.6	-7.4	-19.3	20	12	0.36	36
1.96	158.7	-7.5	-19.0	11	6.5	0.50	11
1.30	157.3	-8.4	-20.4	1.6	1.0	0.50	11
0.92	158.8	-7.2	-20.3	0.2	0.1	0.61	—

As developed above, samples of higher mass show significantly larger excess energies with a concomitant decrease in ΔC_p, reflecting the development of some crystallinity in these samples during quench cooling, while those of low mass show essentially no excess energy and exhibit the ΔC_p expected for a 100% amorphous sample.

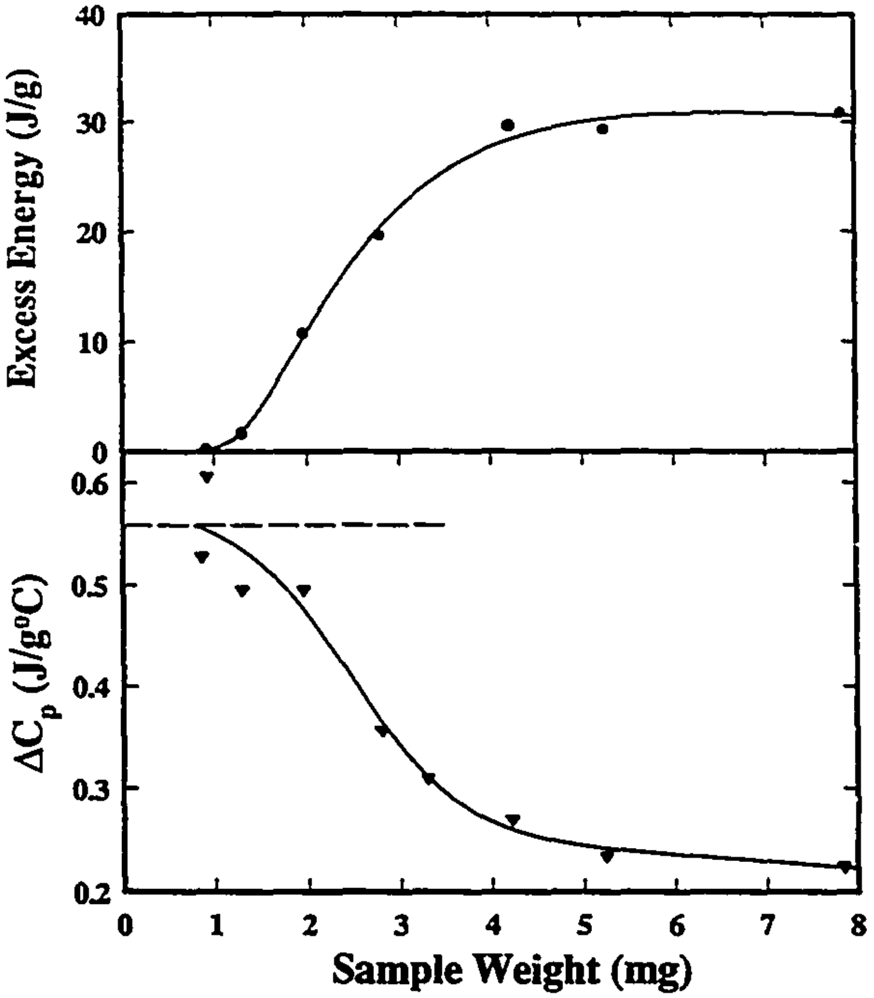

Figure 2.5 Excess energy between the exothermic and endothermic regions as well as ΔC_p for quench-cooled iPP samples of different weights.

However, as seen in Table 2.1, the degree of crystallinity obtained from ΔC_p for samples of higher mass is significantly larger than that derived from the excess energy. In fact, the degree of crystallinity estimated from the change in heat capacity exceeds the crystallinity estimated from the final melting peak, which is unrealistic. Two explanations are offered for these discrepancies.

During the quench cooling of samples of higher mass, appreciable crystallinity is developed and, as predicted by equation (2.1), this diminishes the measured ΔC_p. However, not all of the non-crystalline portion experiences this low temperature glass transition and as a result the degree of crystallinity is overestimated. Indeed, there is much evidence[33-36] from thermal expansion, specific heat, and mechanical loss data for two glass-like transitions in bulk crystallized iPP. For iPP samples possessing very low crystallinity, the first or lower glass transition, $T_g(L)$, was reported to lie between -20 and -12 °C, while a second or upper glass transition, $T_g(U)$, has been reported to occur from 20 °C up to temperatures as high as 100 °C. It was suggested that the $T_g(L)$ is associated with amorphous material rejected by the crystallites as well as cilia while loose loops from chain-folded crystals as well as tie molecules exhibit $T_g(U)$. The unrealistic crystallinities inferred from ΔC_p at $T_g(L)$ suggest that a portion of the amorphous content of the high mass samples passes through the glass transition at higher temperatures and is undetected because of the other exothermic processes that occur simultaneously. A similar observation was also made by Grebowicz et al,[27] who reported that only 10-20% of the amorphous content shows an identifiable T_g in the vicinity of the lower glass transition region.

The second plausible explanation for the discrepancies observed in the estimated crystallinities obtained on quench cooling is based on the nature of the crystalline order obtained when the sample is quench-cooled to the glassy state. If quench cooling results in the formation of a state of poor crystalline order, the eventual melting of this morphology may require less energy than that for a perfect α-monoclinic crystal (*i.e.*, < 165 J/g). Such a situation would result in an underestimation of the crystallinity on quench cooling as measured from the excess energy. STEM dark field and electron diffraction results presented below reveal the existence of such a poor crystalline fraction.

2.3.2 Solid State NMR

The ^{13}C CP/MAS NMR spectra and relaxation data presented in this section are included to establish that the quench-cooled films under investigation possess a morphology identical to previous investigations. A more detailed solid state NMR analysis of the quench-cooled morphology will be presented in the following chapter.

The solid state NMR CP/MAS spectrum of the quench-cooled phase of iPP that has been warmed to room temperature, shown in Figure 2.6b, exhibits resonances for the methylene, methine and methyl carbons at 44.6, 26.7, and 22.1 ppm, respectively, consistent with previously reported spectra for such samples.[37-39] In annealed or isothermally crystallized iPP (*i.e.*, at high temperature), the methylene and methyl resonances show a double peak separated by about 1 ppm, as seen in Figure 2.6a for a quench-cooled sample which was annealed at 161 °C for one hour. It has been postulated that this resonance splitting is a consequence of inequivalent distances within the α-monoclinic unit cell which results from regular packing of right and left handed helices. In the case of the quench-cooled iPP, neither the methylene nor the methyl resonance show the type of splitting that is observed for the α-monoclinic crystalline phase. This suggests that the quench-cooled morphology either is not comprised of the α-monoclinic crystal form or it is composed of an α-monoclinic phase where the inequivalent distances within the unit cell do not exist. The latter explanation requires that the inter-helical distances in the unit cell be larger than in the stable α-monoclinic crystal form so that inequivalent local sites are not observed.

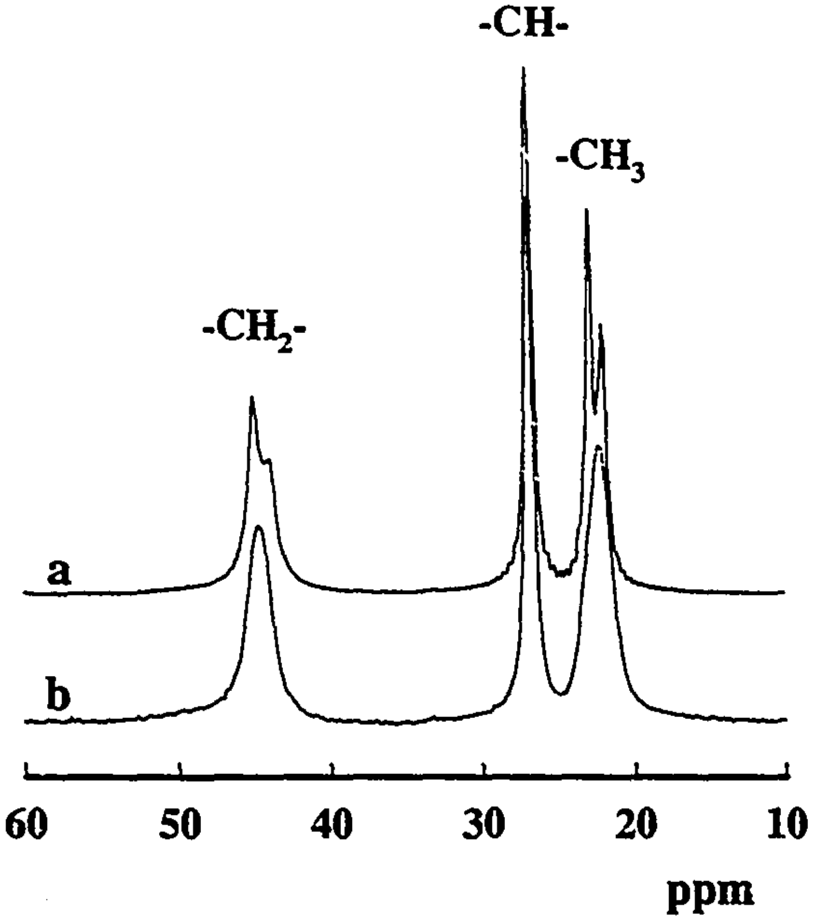

Figure 2.6 Solid state ^{13}C CP/MAS spectrum for a quench-cooled iPP sample which was a) annealed at 161 °C for one hour and b) allowed to return to room temperature.

The measured ^{13}C spin-lattice relaxation times in a rotating frame, $T_{1\rho}$ (^1H), of the quench-cooled morphology consist of two components; a long component of 14.2, 14.8, and 14.1 ms for the methylene, methine, and methyl carbons, respectively, and 2.5, 3.7, and 1.8 ms for the short component. This is in keeping with previous reports by Tanaka[39] who attributed the long component to the relaxations in the crystalline phase while the short component was assigned to the amorphous regions. By comparison, the relaxation times for an α-monoclinic crystalline phase annealed at 161 °C for one hour consist of a long component relaxation time of 126, 121, and 123 ms and a short component of 19, 18, 18 ms. It is well known[37,40] that $T_{1\rho}$ (^{1}H) is dominated by low frequency motions and that the shorter relaxation times can be ascribed to the more mobile phase. The shorter relaxation times measured for the quench-cooled phase indicate that it possesses higher mobility, hence much lower crystallinity, than the stable α-monoclinic crystalline phase. It is rather interesting that the short relaxation times of the annealed α-monoclinic crystals are rather similar to the long relaxation times for the quench-cooled sample.

The solid state NMR data for this phase, as well as its thermal behavior, are consistent with previous reports and indicate that the samples used in this study possess the same morphology as those studied previously by other authors. In addition, it has been shown that the metastable morphology develops on heating quench-cooled iPP to room temperature, as evidenced by the exothermic nature of the "as-quenched" thermogram that results on further heating (Fig. 4). New information about the nature of this morphology, obtained through the use of electron microscopy techniques offering higher resolution than used previously, will now be presented.

2.3.3 Electron Microscopy

2.3.3.1 STEM Dark Field Imaging

The STEM dark field image of n-beam reflections of the quench-cooled iPP sample which has been returned to room temperature is shown in Figure 2.7. In this micrograph there appears to be three distinctly different phases. As indicated by the bright white regions, a microcrystalline phase consisting of crystalline entities that range in size from 100 to 200 Å, with an average of approximately 160 Å, is clearly evident. These

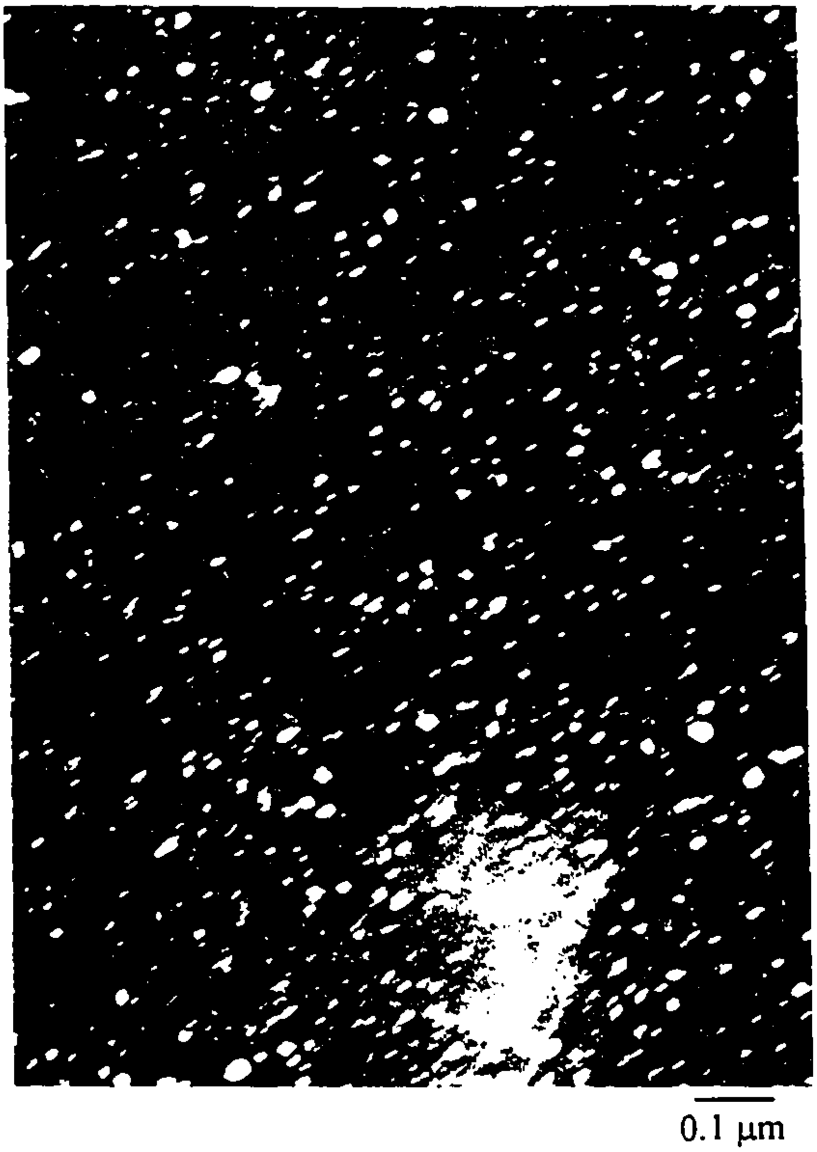

Figure 2.7 STEM dark field image of n-beam reflections of a quench-cooled iPP sample. Magnification: 100,000X

crystal sizes were determined through direct measurement on the negative as well as by the Scherrer method[41] where the breadth at half-height of a given reflection is related to the crystal size by a geometry-dependent constant. The black areas in this micrograph give evidence of a second phase which is due to amorphous material between the bright microcrystals. In addition, certain regions of the micrograph exhibit behavior that suggests the presence of a third phase. This region is seen as the gray areas between the bright microcrystals and suggests the existence of a poorly developed crystalline phase (*i.e.*, regions of a low level of crystalline order). It is noted that this gray area could be due to a decrease in diffracted intensity if the crystalline fraction in that particular region is tilted away from the Bragg angle. However, through micro electron diffraction, it will be possible to ascertain whether these regions are indeed indicative of the presence of a third phase within the morphology of quench-cooled iPP. For the remainder of this chapter, this region will be referred to as intercrystalline.

In previous transmission electron microscopy studies, Gezovich and Geil[18] observed large spherulite-like structures, about 1 μm in diameter, in surface replicas of thick quench-cooled films, while nodular structures about 125 Å in diameter were seen in very thin quench-cooled films. The latter morphology was interpreted as being the "smectic" structure and it was suggested that the nodules are defective hexagonal crystals. Similar nodular structures 75-100 Å in size, were reported for the smectic morphology by Hsu, *et al.*[24] although they did not detect the spherulitic structures. They suggested that the main reason for the discrepancy with the previous study was the difference in the iPP. To determine if these nodular structures are small crystals, dark-field images were attempted; however, the authors were unsuccessful in obtaining such images, which was taken as a confirmation of the small and imperfect nature of the quench-cooled morphology. Using transmittance electron microscopy, Grubb and Yoon[42] also observed a nodular morphology, about 200 Å in diameter, in permanganate-etched surfaces of quench-cooled iPP films. This nodular morphology was found to become better defined, with clearer limits and boundaries, when the samples were annealed at 60 °C. The microcrystalline regions evident in Figure 2.7 are consistent in size with the nodular structures that were observed previously in these investigations and identified as the "smectic" morphology.

Although it is evident that the iPP quench-cooled morphology is composed of small crystals, it is still not known if these entities are small crystals of a hexagonal phase as proposed by Gezovich and Geil[18] or of a monoclinic phase. Micro electron diffraction was performed on both the microcrystalline and intercrystalline regions to identify the type and level of order existing within these phases.

2.3.3.2 Micro Electron Diffraction

Typical micro electron diffraction patterns probing areas less than 100 Å^2 in size are presented in Figure 2.8 for the microcrystalline region, *i.e.*, the bright white regions seen in the STEM dark field image (Fig. 2.7). In this region the various reflections are characterized by arcs rather than diffraction spots or rings indicating that the diffraction area is composed of several crystals that differ in orientation. However, a random crystal orientation is not likely since this would give rise to diffraction rings rather than arcs. Similarly, these diffraction patterns are not consistent with a single crystal since a regular array of diffraction spots would be observed. Therefore, from the diffraction patterns it appears that the bright white regions in the STEM dark field image represent a cluster of crystals differing slightly in orientation.

The positions of the various reflections in each of the diffraction patterns were measured and their corresponding d-spacings as well as diffraction angles are presented in Table 2.2. To assess a possible crystallographic form for this phase, the d-spacings corresponding to the most intense reflections were compared to expected d-spacings for

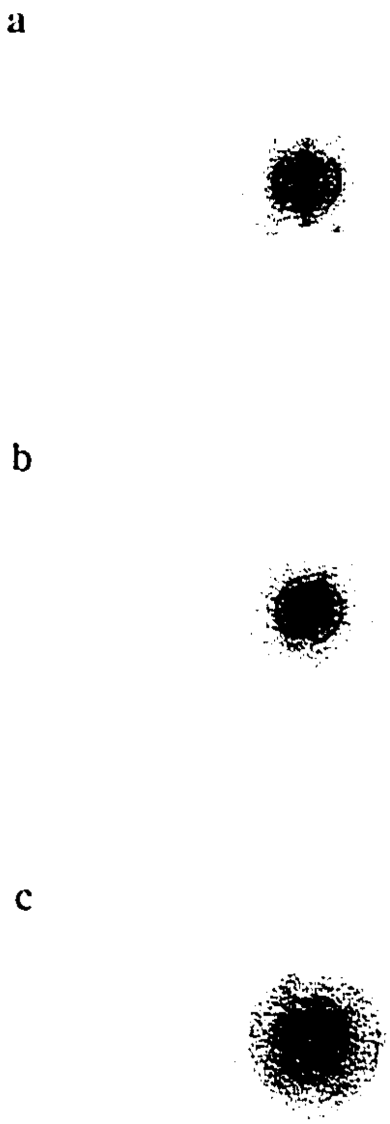

Figure 2.8 Micro electron diffraction patterns for the microcrystalline phase of quench-cooled iPP at (a) 0°, (b) 10° and (c) 25° tilt angles.

Table 2.2 Observed spacings for the microcrystalline and intercrystalline regions of quench-cooled iPP as obtained through micro electron diffraction.

Microcrystalline Region			Intercrystalline Region		
d-spacing (Å)	Diffraction Angle, θ (λ=0.0375 Å)	Diffraction Angle, θ (λ=1.5418 Å)	d-spacing (Å)	Diffraction Angle, θ (λ=0.0375 Å)	Diffraction Angle, θ (λ=1.5418 Å)
6.10	0.176	7.26	4.16	0.258	10.671
5.14	0.209	8.63	4.15	0.259	10.712
4.71	0.228	9.42	3.71	0.290	12.004
4.17	0.258	10.65	3.19	0.337	13.983
4.07	0.264	10.96	2.52	0.426	17.797
3.64	0.295	12.23	2.47	0.435	18.171
3.47	0.310	12.85	2.39	0.449	18.794
3.23	0.333	13.83	2.21	0.486	20.427
3.15	0.341	14.18	2.14	0.502	21.123
2.74	0.392	16.34	2.09	0.515	21.695
2.36	0.456	19.08	2.08	0.517	21.758
2.17	0.496	20.83	1.86	0.578	24.524
1.82	0.591	25.10	1.65	0.650	27.820
			1.64	0.656	28.087
			1.53	0.704	30.323

the three predominant morphologies of iPP; namely, the α-monoclinic, β-hexagonal and γ-triclinic crystal forms. The published hk0 electron diffraction patterns[43,44] and the available x-ray spectra[44-47] of the β-hexagonal crystalline form are all characterized by a very intense reflection at a d-spacing of 6.36 Å. In addition, a very strong reflection is observed at 5.50 Å. Neither of these reflections is observed in the diffraction pattern of the microcrystalline region (Table 2.2) indicating that this phase is not composed of the β-hexagonal form. The γ-form is characterized[45] by five strong x-ray reflections at d-spacings of 6.37, 5.29, 4.42, 4.19, and 4.05 Å. Four of these five d-spacings are very close to four of the five most intense reflections of iPP in the α-monoclinic form,[48] *i.e.*, 6.24, 5.20, 4.76, 4.16, and 4.06 Å. The reflection at a d-spacing of 4.76 Å in the α-monoclinic crystalline form is completely absent in the γ-form and is replaced by the reflection at 4.42 Å. A comparison of the four d-spacings that are common to both of these phases with the ones presented in Table 2.2 indicates a greater similarity between the observed reflections and those of the α-monoclinic phase. In addition, a reflection with a d-spacing of 4.71 Å is also noted in Table 2.2 corroborating that the d-spacings are in agreement with the α-monoclinic crystalline form. Therefore, the diffraction patterns obtained for the microcrystalline region appear to be consistent with the α-monoclinic crystal form.

Analysis of the electron diffraction patterns obtained for the microcrystalline region was based on the α-monoclinic crystal structure under the assumption that the iPP helices are arranged with C2/c symmetry. This assumption is justified by several investigations[9] which indicated that fast growth of α-monoclinic iPP crystals (*i.e.*, large undercoolings) lead to a crystalline phase with C2/c symmetry. With such symmetry systematic absences of several reflections are noted. All reflection in which (h+k) are odd are absent. In addition, the 0k0 and h0l reflections require the non-zero index (*i.e.*, h, k or l) to be even. These absences were applied in indexing the weaker reflections to yield the assignments reported in Table 2.3. It should be noted that three reflections in this table were assigned two different Miller indices. This is simply due to the fact that both indices yielded as good a fit for the observed d-spacing without affecting the derived unit cell dimension. Unit cell constants *a*, *b*, *c*, and β equal to 6.62, 20.69, 6.51 Å, and 98.7° were obtained for this phase with an agreement factor, ξ, of 0.0217 (eqn. (2.3)). These unit cell constants are in very good agreement with previously reported values[9,11,49] for the α-monoclinic crystal form. Based on 12 monomer units per unit cell, the density of this phase corresponds to 0.95 g/cm^3, which is also consistent with previously reported values.[42] Therefore, the bright spots that are observed in the STEM dark field image are primarily due to small α-monoclinic crystals that are between 100 and 200 Å in size.

Table 2.3 Observed and calculated diffraction angles (λ=1.54178 Å) as well as corresponding Miller indices for the various reflections of the diffraction pattern obtained for the microcrystalline region of quench-cooled iPP.

Miller Indices (h,k,l)	Diffraction Angle	$10^2 \sin^2\theta$ (Observed)	$10^2 \sin^2\theta$ (Calculated)	10^3 Difference
1.1.0	7.26	1.594	1.524	0.70
0.4.0	8.63	2.246	2.218	0.28
1.3.0	9.42	2.676	2.633	0.43
1.1.1	10.65	3.411	3.385	0.26
0.4.1	10.96	3.610	3.653	0.43
1.3.1	12.23	4.483	4.494	0.11
1.5.0, 0.6.0	12.85	4.936	4.851, 4.991	0.85, 0.55
0.0.2	13.83	5.705	5.738	0.33
2.2.0	14.18	5.995	6.094	0.99
0.4.2	16.34	7.904	7.957	0.53
0.6.2	19.08	10.671	10.729	0.58
3.1.0, 1.9.0	20.83	12.624	12.603, 12.615	0.21, 0.09
2.6.2, 0.6.3	25.10	17.972	17.976, 17.902	0.04, 0.70

In Figure 2.9 are presented typical micro electron diffraction patterns probing areas less than 100 Å^2 in size for the intercrystalline region, *i.e.*, the gray areas between the microcrystals seen in the STEM dark field image (Fig. 2.7). It is of interest that the diffraction patterns for the intercrystalline region are composed of a regular array of diffraction spots suggesting that each diffraction pattern is due to one or possibly two crystals. The diffraction patterns are composed of four high intensity reflections and as many as twelve very weak reflections detected throughout the tilt series.

The positions of the various reflections in each of the diffraction patterns were measured and their corresponding d-spacings as well as diffraction angles are also presented in Table 2.2. The assessment of a possible crystallographic form for this phase is more difficult than for the microcrystalline phase since the most intense reflections associated with each of the three polymorphs of iPP are not observed in the diffraction pattern of this intercrystalline region (Table 2.2). However, amidst the more intense reflections that are observed for the intercrystalline region, the two reflections occurring at d-spacings of 4.16 and 4.15 Å almost superimpose onto the diffraction pattern for the microcrystalline region. In the diffraction pattern of the β-hexagonal phase, only one and not two intense reflections are observed in the above region (*i.e.*, at a d-spacing of 4.20 Å) suggesting that the intercrystalline region is not consistent with this morphology. In the diffraction patterns of both the α and γ-forms, two intense reflections are noted in this region which suggests that the intercrystalline region may be composed of either of these forms. The intensity ratio of the two reflections is reversed between the two crystallographic forms. The intensity ratio of the two reflections observed for the intercrystalline phase (*i.e.*, 4.16 is less intense than 4.15 Å) is consistent with the intensity ratio observed for the α-monoclinic phase. In addition, the thermal analysis investigation of the quench-cooled morphology, which was discussed in the previous section, does not

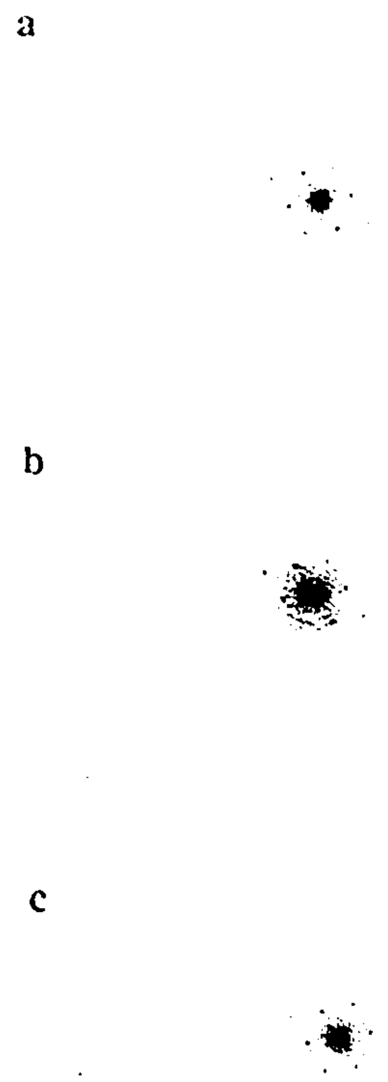

Figure 2.9 Micro electron diffraction patterns for the intercrystalline phase of quench-cooled iPP at (a) 0°, (b) 10° and (c) 20° tilt angles.

give evidence of any melting endotherms in the temperature range between 120 and 145 ° C, that would be expected for the existence of either the β-hexagonal or γ-triclinic crystal forms. Therefore, the diffraction patterns for the intercrystalline phase appear to be more consistent with the α-monoclinic crystal form and will be analyzed under this assumption. In addition, the same assumptions that were applied to the interpretation of the diffraction patterns of the microcrystalline region (*i.e.*, $C_{2/c}$ symmetry) will be used in this analysis.

To index the various reflections of the intercrystalline diffraction pattern, the most intense reflections (*i.e.*, larger d-spacings) were given the same index as for the microcrystalline phase. Using the third computer program that is listed in Appendix A, the d-spacing of each of these reflections with their respective Miller indices were used to obtain a starting unit cell dimension. This unit cell dimension, in conjunction with the second program listed in Appendix A, was used to obtain suggested indices for all of the other reflections. The least squares program was then used to obtain the final unit cell dimension. The analysis indicated that this phase possesses the following unit cell dimension: $a = 6.71$, $b = 22.28$, $c = 6.36$ Å and $\beta = 99.1°$. An agreement factor, ξ, between observed and calculated diffraction angles of 0.0160 (eqn. (2.3)) was obtained for this phase. The Miller index assignment for each reflection as well as the observed and calculated diffraction angles are presented in Table 2.4.

These results indicate that the packing of the helices in the *b* crystallographic direction is substantially larger than for the microcrystalline region. However, all other unit cell constants remain essentially unchanged. Based on 12 monomer units per unit cell, a substantially lower density of 0.89 g/cm^3 is calculated for this phase. It should be noted that the calculated density of the intercrystalline phase lies midway between the densities of the crystalline and amorphous phases. Therefore, an appropriate linear combination of the density of the three phase noted in the quench-cooled iPP morphology can easily yield the observed bulk density of 0.883g/cm^3.[28]

Table 2.4 Observed and calculated diffraction angles (λ=1.54178 Å) as well as corresponding Miller indices for the various reflections of the diffraction pattern obtained for the intercrystalline region of quench-cooled iPP.

Miller Indices (h,k,l)	Diffraction Angle	$10^2 \sin^2\theta$ (Observed)	$10^2 \sin^2\theta$ (Calculated)	10^3 Difference
0.4.1	10.671	3.423	3.414	0.09
1.1.1	10.712	3.449	3.435	0.14
0.6.0	12.004	4.319	4.299	0.20
0.6.1	13.983	5.830	5.802	0.28
1.3.2	17.797	9.327	9.356	0.29
2.6.0	18.171	9.710	9.721	0.11
0.6.2	18.794	10.363	10.311	0.52
2.6.1	20.427	12.162	12.138	0.24
1.9.1	21.123	12.966	12.989	0.23
0.8.2	21.695	13.644	13.655	0.11
2.2.2	21.758	13.719	13.740	0.21
0.12.0	24.524	17.201	17.197	0.04
2.0.3	27.820	21.746	21.691	0.55
2.2.3	28.087	22.131	22.169	0.38
0.10.3	30.323	25.450	25.468	0.18

Thus, the quench-cooled iPP morphology is composed of α-monoclinic microcrystals and the intercrystalline component embedded in an amorphous matrix. The typical diffraction patterns obtained by wide-angle x-ray scattering (WAXS) and by conventional transmission electron microscopy (CTEM) therefore reflect a combination of contributions from the three phases of the quench-cooled morphology. Calculations by previous authors,[16,20] based on the half-width of the most intense wide-angle x-ray diffraction (WAXD) peak, indicated that the "smectic" morphology contains crystals ranging in size between 30 to 100 Å. This study shows, by direct measurement, larger crystals having dimensions of the order of 160 Å. Since the crystals are not as small as reported previously, it must be concluded that the sample possesses a great deal of disorder which is causing further WAXD line broadening. The intercrystalline regions which give rise to a different diffraction pattern with a substantially longer *b* crystallographic axis can further broaden the WAXD reflections. A typical WAXD pattern[9] for the quench-cooled morphology is presented in Figure 2.10. Superimposed onto this diffraction pattern are the observed reflections from both the microcrystalline (full lines) and intercrystalline (dashed lines) phases. The intensity of each reflection was evaluated by visual inspection. The intercrystalline region yields different d-spacings from those of the microcrystals primarily due to different unit cell constants in this region. Convolution of the diffraction patterns from the intercrystalline and microcrystalline regions as well as line broadening effects due to small crystal sizes can account for the observed WAXD pattern. Annealing at temperatures greater than approximately 60 °C perfects both crystalline regions. Eventually a sufficient level of order is attained so that the line broadening effects are negligible and a transformation from the quench-cooled phase WAXD pattern to that of the α-monoclinic crystal form is observed.

2.3.4 Re-evaluation of Observed Behavior

Based on the above analysis of the morphology of quench-cooled iPP, the discrepancy between the exothermic and endothermic transitions observed in the thermogram for the "as-quenched" sample, described above, can be attributed to the development of low crystalline order *during* the quenching process. It is probably of the type seen in the intercrystalline regions in Figure 2.9. This proposal is in accord with the

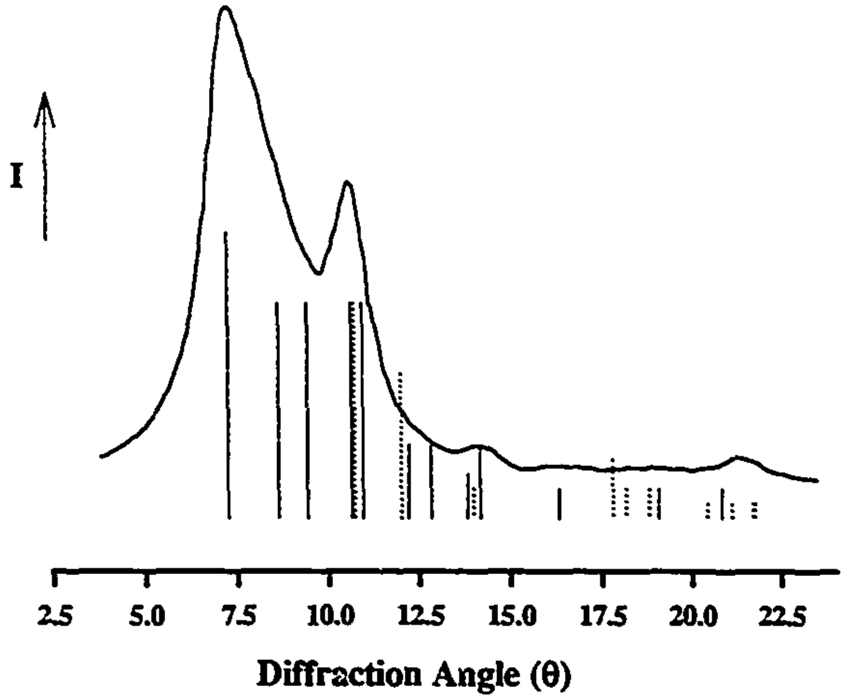

Figure 2.10 Typical WAXD pattern[9] for the quench-cooled iPP morphology with a superposition of the various reflections arising from the microcrystalline (solid lines) and intercrystalline (dashed lines) phases as obtained from micro electron diffraction.

results of Zerbi, *et al.*[50] who, on the basis of evidence from infrared studies, reported the presence in iPP melts of segments at least five repeat units in length having a helical conformation. Such structure would be "frozen in" with some additional ordering during the quench-cooling of the sample, and would result in some low level structure such as is observed in the intercrystalline regions (Fig. 9). Heating the sample to room temperature is accompanied by crystallization from the glassy state. This crystallization, which releases about 18 J/g between -15 and 25 °C, reflects the formation of additional microcrystals observed in the STEM dark field image.

Based on the above considerations, it is unlikely that the low temperature endotherm that was observed in Figure 1 is due to melting of small crystals formed during the quenching or subsequent annealing of the iPP sample, as proposed previously by others. The thermogram of the as-quenched sample (Fig. 4) reveals that about 18 J/g of crystallinity has developed as the temperature of the sample is raised to room temperature, ignoring any crystallinity that develops during quench-cooling. By comparison, the area of the low temperature endotherm in Figure 2.1 corresponds to 4.4 J/g, or only 23% that required to melt the microcrystals. Therefore, the total heat of melting is insufficient to account for the crystallinity which has been developed. It seems more reasonable that the low temperature endotherm reflects some form of pre-melting transition that occurs prior to recrystallization. Such a transition may involve expansion in one or both dimensions of the crystal lattice in a direction perpendicular to the molecular chain direction. Such an expansion may be a requirement prior to sample recrystallization, which occurs at slightly higher temperatures and results in an increase in such factors as chain-fold length and crystal perfection. It is of interest that this transition is not detected in the thermogram of the "as-quenched" sample.

The partially ordered phase of iPP has been shown to be composed of microcrystalline as well as intercrystalline regions possessing an α-monoclinic crystal form. Consequently, the small exotherm observed in Figure 2.1 certainly does not represent the transformation from a quench-cooled phase morphology to the more stable α-monoclinic crystal form. Rather, it must be regarded as perfection of the existing α-monoclinic crystal form to higher levels of order.

In a high resolution solid state ^{13}C NMR study of iPP polymorphs, Gomez, *et al.*,[38] inferred the local chain packing structure of the smectic form through comparisons with the spectra of the well known α and β crystal forms. The chemical shifts, as well as the spin-lattice relaxation times, for the smectic form were found to be similar to those of the β-phase. This similarity led to the suggestion that the packing of the helices in the quench-cooled phase, at least on a very local scale, is similar to the packing in the β-form. In this study, it was shown that the quench-cooled iPP morphology includes a small portion of small crystals of the α-phase which possess the same unit cell dimensions as usually reported in the literature. However, the NMR spectrum of the quench-cooled phase does not show the expected characteristics of the well-developed α-phase (Fig. 6). It is likely that due to the presence of the intercrystalline phase which possesses a substantially longer *b* crystallographic axis, the inequivalent distances are not being resolved in the NMR experiment. Substantially longer interhelical distances in the intercrystalline phase would obscure the inequivalent distances which are found in the microcrystalline regions. Through annealing, and thus, perfection of both phases, it becomes possible to resolve these small differences in interhelical distances and the resonances begin to show the expected splitting observed for an α-phase.

2.4 Summary

A detailed DSC and electron microscopy investigation is presented in this chapter that elucidates the room temperature morphology of quench-cooled iPP. In addition, through a detailed DSC study the development of this morphology as well as some of its annealing behavior was investigated. It has been demonstrated that the morphology of a previously quench-cooled iPP sample that has been heated to room temperature is composed of three phases. (1) Microcrystalline regions that range in size between 100 and 200 Å having the α-monoclinic crystal form. (2) Regions of lower crystalline order also composed of the α-monoclinic crystal form. The helical packing in this region was found to be much less compact than in the microcrystalline region as evidenced by a significantly longer *b* crystallographic axis. (3) An amorphous phase.

The bulk x-ray or electron diffraction patterns that are generally obtained for this morphology are consistent with the occurrence of line broadening effects primarily due to the small nature of the crystalline phase (*i.e.*, α-monoclinic crystals approximately 160 Å in size). However, additional broadening effects arise from the convolution of the diffraction pattern of the microcrystalline region with that of the intercrystalline regions. Annealing samples with this morphology at temperatures above room temperature perfects the crystalline structure in the microcrystalline as well as in the intercrystalline regions, so that the α-monoclinic form is detectable by conventional diffraction techniques due to suppression of the line broadening effects.

The formation of regions of lower crystalline order of the type observed in the intercrystalline regions of the room temperature annealed sample, occurs *during* the quench cooling of the iPP sample. This is evidenced by the difference in ΔH between the exothermic and endothermic transitions as well as by the changes in ΔC_p observed in Figure 2.5. Quench cooling of an iPP sample of low mass appears to yield an amorphous glass, while larger masses form a glass possessing a low degree of crystallinity (*i.e.*, up to 18%). Raising the temperature of the quench-cooled iPP sample results in crystallization from the glassy state, where the kinetics of crystallization are controlled by chain transport. This crystallization results in the formation of the microcrystals observed in the STEM dark field image. The resultant morphology is metastable, as evidenced by the fully exothermic DSC thermogram in the region between -15 and 120 °C, such that raising the temperature within this region results in the generation of a new crystalline morphology having a higher level of order.

2.5 References

1 G. Natta, P. Pino, P. Corradini, F. Danusso, E. Mantica, G. Mazzanii and G. Moriglio, *J. Amer. Chem. Soc* 77, 1708 (1955).

[2] D.R. Morris, *J. Macromol. Sci., Phys.* **B3(1)**, 53 (1969).

[3] H.D. Keith, F.J. Padden, Jr, N.M. Walker and H.W. Wyckoff, *J. Appl. Phys.* **30**, 485 (1959).

[4] E.J. Addink and J. Beintema, *Polymer* **2**, 185 (1961).

[5] K.D. Pae, J.A. Sauer and D.R. Morrow, *Nature* **211**, 514 (1966).

[6] J.L. Kardos, A.W. Christiansen and E. Baer, *J. Polym. Sci. (A-2)* **4**, 777 (1966).

[7] B. Lotz and J.C. Wittmann, *J. Polym. Sci., Polym. Phys. Ed.* **24**, 1541 (1986).

[8] B. Lotz, S. Graff and J.C.Wittmann, *J. Polym. Sci., Polym. Phys. Ed.* **24**, 2017 (1986).

[9] S. Brückner, S.V. Meille, V. Petraccone and B. Pirozzi, *Prog. Polym. Sci.* **16**, 361 (1991).

[10] G. Natta, M. Peraldo and P. Corradini, *Rend. Accad. Naz. Lincei.* **26**,14 (1959).

[11] G. Natta and P. Corradini, *Nuovo Cimento, Suppl.* **15**, 40 (1960).

[12] H.W. Wycoff, *J. Polym. Sci.* **62**, 83 (1962).

[13] R.L. Miller, *Polymer* **1**, 135 (1960).

[14] R. Hosemann, *J Appl. Phys.* **34(1)**, 25 (1963).

[15] R. Zanneti, G. Celotti and A. Armigliato, *Eur. Polym. J.* **6**, 879 (1970).

[16] J.A. Gailey and P.H. Ralston, *SPE Trans.* **4**, 29 (1964).

[17] G. Farrow, *J. Appl. Polym. Sci.* **9**, 1227 (1965).

[18] D.M. Gezovich and P.H. Geil, *Polym. Eng. Sci.* **8**, 202 (1968).

[19] G. Bodor, M. Grell and A. Kallo, *Faserforsch. Textil-Tech.* **15**, 527 (1964).

[20] P.B. McAllister, T.J. Carter and R.M. Hinde, *J. Polym. Sci., Polym. Phys. Ed.* **16**, 49 (1978).

[21] G. Guerra, V. Petraccone, C. De Rosa and P. Corradini, *Makromol. Chem., Rapid Commun.* **6**, 573 (1985).

[22] P. Corradini, V. Petraccone, C De Rosa and G. Guerra, *Macromolecules* **19**, 2699 (1986).

[23] P. Corradini, C. De Rosa, G. Guerra and V. Petraccone, *Polym. Commun.* **30**, 281 (1989).

[24] C.C. Hsu, P.H. Geil, H. Miyaji and K. Asai, *J. Polym. Sci., Polym. Phys. Ed.* **24**, 2379 (1986).

[25] M. Glotin, R.R. Rahalkar, P.J. Hendra, M.E.A. Cudby, and Willis, H.A. *Polymer* **22**, 731 (1981).

[26] A. Fichera and R. Zannetti, *Die Makromol. Chem.* **176**, 1885 (1975).

[27] J. Grebowicz, S.-F. Lau and B. Wunderlich, *J. Polym. Sci., Polym. Symp.* **71**,19 (1984).

[28] V. Vittoria, *J. Macromol. Sci.* **B28**, 489 (1989).

[29] F. De Candia, R. Russo and V. Vittoria, *J. Appl. Polym. Sci.* **34**, 689 (1987).

[30] R. Zannetti, G. Celotti, A. Fichera and R. Francesconi, *Die Makromol. Chem.* **128**, 137 (1969).

[31] U. Gaur and B. Wunderlich, *J. Phys. Chem. Ref. Data* **10(4)**, 1051 (1981).

[32] B. Wunderlich, 'Macromolecular Physics, Vol. 3, Crystal Melting', Academic Press, New York (1980).

[33] R.F. Boyer, *J. Macromol. Sci., Phys.* **B8(3-4)**, 503 (1973).

[34] D.L. Beck, A.A. Hiltz and J.R. Knox, *SPE Trans.* **3**, 279 (1963).

[35] Y. Wada, Y. Hotta and R. Suzuki, *J. Polym. Sci., Part C* **23**, 583 (1968).

[36] M. Jarrigeon, B. Chabert, D. Chatain, C. Lacabanne and G. Nemoz, *J. Macromol. Sci., Phys.* **B17(1)**,1 (1980).

[37] A. Bunn, M.E.A. Cudby, R.K. Harris, K.J. Packer and B.J. Say, *Polymer* **23**, 694 (1982).

[38] M.A. Gomez, H. Tanaka and A.E. Tonelli, *Polymer* **28**, 2227 (1987).

[39] H. Tanaka, *Eur. Polym. J.* 27(7), 565 (1991).

[40] J. Schaeffer, E.O. Stejskal and R. Buchdahl, *Macromolecules* **8**, 291 (1975).

[41] P. Scherrer, *Nachr. Ges. Wiss. Gottingen* **98**, (1918): in 'Kolloid-Chemie', Spamer, Leipzig (1920).

[42] D.T. Grubb and D.Y. Yoon, *Polym. Comm.* 27, 84 (1986).

[43] P.H. Geil, *J.Appl. Phys.*, **33**, 642 (1962).

[44] A. Turner-Jones and A.J.M. Cobbold, *J. Polym. Sci.*, **6**, 539 (1968).

[45] A. Turner-Jones, J.M. Aizlewood and D.R. Beckett, *Makromol. Chem.*, **75**, 134 (1964).

[46] Y. Fujiwara, *Kolloid* Z.-Z. *Polym.*, **226**, 135 (1969).

[47] R.J. Samuels and R.Y. Yee, *J. Polym Sci., A-2*, **10**, 385 (1972).

[48] Z. Mencik, *J. Macromolec. Sci., Phys.*, **B6**, 101 (1972).

[49] J. Brandrup and E.H. Immergut (Eds), 'Polymer Handbook, Third Edition', John Wiley and Sons, New York (1989).

[50] G. Zerbi, M. Guzzoni and F. Ciampelli, *Spectrochimica Acta* **23A**,301 (1967).

CHAPTER THREE

^{13}C CP/MAS NMR Studies of Morphological Changes During Annealing of Quenched Isotactic Polypropylene Films

3.1 Introduction

The development of multinuclear Fourier transform nuclear magnetic resonance (NMR) spectrometers as well as line narrowing and sensitivity enhancement techniques has led to high resolution NMR approaches that make possible the study of polymer morphology in the solid state at the molecular level. It should, however, be noted that the definition of "high resolution" in reference to the solid state must differ from that for the liquid state. In NMR studies of liquid samples, high resolution is attained when the magnitude of the (J) spin-spin coupling constants are larger than the natural line widths of resonance lines. However, in the solid state these J couplings are obscured by the line widths that are attainable with available solid state techniques. Thus, high resolution in the solid state must be defined as the ability to distinguish resonances with reasonably different chemical shifts.

The techniques presently available to obtain high resolution spectra in the solid state were developed to circumvent adverse line broadening effects. NMR spectra for randomly oriented crystalline solids are generally broad and featureless as a result of four possible interactions: dipolar coupling, chemical shift anisotropy, electric field gradients in nuclei with quadrupole moments, and scalar anisotropy. The electric quadrupole interaction is a manifestation of the fact that nuclei with spin ≥ 1 possess an electric charge distribution that is not spherically symmetric. Therefore, the nuclear spin has an orientation dependence with its local electronic environment and with the main field and this generates large line broadening effects. Since the focus of this chapter is on the ^{13}C nucleus, which possesses a spin of ½, the quadrupolar line broadening effect is not considered further. These solid state interactions as well as the line narrowing techniques to obtain high resolution spectra in the solid state have been previously discussed by many authors.[1-9] A brief overview is given below specifically centered around semicrystalline polymers with particular emphasis on dilute nuclei, such as ^{13}C.

3.1.1 Solid State Interactions and Line Narrowing Techniques

The interactions that broaden NMR lines in the solid state are also operative in nonviscous liquids but due to the rapid, random, isotropic reorientational and translational motions of molecules in liquids they are being averaged to zero or to a single non-zero value that is representative of the average interaction. As will become evident, the internal dipolar fields possess a spacial orientational dependence that, in the liquid state, molecular motions are able to modulate efficiently such that any reference spin "sees" only the average of the dipolar fields of its neighbors. This phenomenon of "motional averaging" is much less effective for polymers in the solid state for which the chain mobilities vary over many orders of magnitude in time. Therefore, averaging must be induced by artificial means to minimize the line broadening effects and to obtain high resolution spectra.

3.1.1.1 Dipolar Coupling

The dipolar interaction between nuclear spins is the dominant broadening mechanism in solid state NMR spectra (for spins I=½) of crystalline or glassy polymers. The major source of line broadening in a natural abundance ^{13}C spectrum is the dipolar interaction between carbons and protons which results in a single, broad, featureless line. Carbon-13 atoms are sufficiently dilute to render the ^{13}C-^{13}C dipolar interactions negligible. For protons, the major portion of this dipolar interaction occurs among the protons themselves.

The local magnetic field produced at a nucleus *i*, h_i^l, by a magnetic nucleus *j* with an internuclear separation r_{ij} is given by [10]

$$h_i^l = \pm \mu_j \left(\frac{3\cos^2\theta_{ij} - 1}{r_{ij}^3}\right) \tag{3.1}$$

where μ_j is the dipole moment of nucleus *j* and θ_{ij} is the angle of the vector r_{ij} relative to the external magnetic field, B_o. The magnitude of the local magnetic field is seen to be strongly dependent on the internuclear separation and the angle between this separation and the applied magnetic field but independent of the strength of the applied field. Whether the local magnetic field augments or detracts from the external applied field, indicated by the plus and minus sign in equation (3.1), depends on the orientation of the dipole moment, μ_j, that is, the spin state of nucleus *j*. Therefore, dipolar coupling of a set of magnetically isolated ^{13}C-^{1}H pair at a given angle to the applied field results in a splitting (*i.e.*, a Pake doublet) of the ^{13}C resonance equivalent to $\pm\omega_1$ $(=\mu_s h_1)$ from the resonance frequency, ω_o, that is obtained when the dipolar interaction is zero. Each dipolar interaction in a solid sample produces such a characteristic splitting. However, in an unoriented crystalline or glassy polymer, a nucleus does not experience an isolated dipolar interaction. Neighboring nuclei at different internuclear distances, r_{ij}, and angular relationships to the external magnetic field yield many such interactions (and splittings) to produce a so-called inhomogeneously broadened line which tends towards a Gaussian line shape. Such a spectrum is termed inhomogeneously broadened due to the fact the various parts of the broad line are composed of sharp resonances arising independently from the different nuclear separations and angles. Carbon-13 dipolar interactions with protons, therefore, result in ^{13}C NMR line widths in organic solids of the order of 20 kHz.

3.1.1.2 Dipolar Decoupling

To obtain high resolution spectra in the solid state, it is necessary to remove the effects of these dipolar interactions. In principle, this can be achieved by imparting a suitable average such as that observed in nonviscous liquids. As can be deduced from equation (3.1), the local magnetic field produced at a given nucleus, h^{i}_{j}, is due to the product of a spacial with a spin term. Therefore, appropriate action on either of these terms can result in averaging the dipolar interaction to zero. One possibility is to reduce the $(3\cos^2\theta_{ij} - 1)$ term to zero by physically spinning the sample at 54°44', the magic angle. However, to remove proton-proton and proton-carbon dipolar interactions, spinning speeds between 10 to 50 kHz are required (*i.e.*, the spinning speed must exceed the dipolar linewidth). Although the lower limit can be achieved, the upper limit is impractical. Therefore, magic angle spinning is of limited utility in the removal of such strong interactions. The physical spinning of a sample about the magic angle will be discussed further below in connection with the removal of another broadening interaction operative in the solid state.

The alternative approach operates on the spin term and is particularly effective in the removal of the ^{13}C-^{1}H dipolar interaction. The technique, which is analogous to the decoupling of ^{13}C-^{1}H scalar spin-spin interactions (J coupling) in solution, involves high power radiofrequency (rf) irradiation at the proton frequency and is referred to as "dipolar decoupling".[11] Irradiation modulates the orientation of the proton spins with respect to the main magnetic field, *i.e.*, it forces the spins to change states. If the rate of exchange is large compared to the frequency of the interaction, the effective field from the proton that is seen by the ^{13}C nucleus is averaged and the dipolar interaction is decoupled.[12] However, it should be noted that a decoupling field of 40 kHz or greater is required to remove the 10-40 kHz dipolar coupling which exists in the solid state. Because of the heating that results from rf fields of this magnitude, they are generally not left on continuously for more than 200 ms.

3.1.1.3 Chemical Shift Anisotropy

The resonance frequency of a particular nucleus is not only dependent on the type of nucleus but also on its magnetic environment. The chemical shift is produced by the electrons that shield the nucleus from the applied magnetic field. In general, the electron distribution will have a definite directional character (*i.e.*, the distribution will not be spherical or cubical) which will infer a directional dependence on the chemical shift. In solution, the directional dependence is averaged due to the random isotropic motions of molecules to yield single-valued chemical shifts from anisotropic shieldings. Due to the lack of motional freedom in the solid state, the nucleus experiences different levels of shielding in different directions with respect to the external magnetic field and hence has a different chemical shift in different directions. Therefore, a ^{13}C nucleus oriented at a given angle to the external field will give a sharp signal at a specific chemical shift which is characteristic of that particular orientation. In an unoriented crystalline or glassy polymer, all orientations with respect to the external field are possible. Therefore, the NMR spectrum of such a material will consist of a superposition of sharp lines encompassing the frequency range between the maximum and minimum values of the shielding. Such a spectrum is a result of the line broadening mechanism known as chemical shift anisotropy (CSA) and is referred to as the CSA powder pattern. The isotropic chemical shift observed in solution is the motionally averaged value of all of these sharp lines observed in the powder pattern.

The line shape of the CSA powder pattern is described[13] by three principle values of the chemical shift tensor (σ_{11},σ_{22},σ_{33}) which contain information about the asymmetry of the electronic distribution around a given nucleus. Many different types of powder pattern line shapes have been observed although the most general shape can be described[3] as "tentlike" where σ_{11} and σ_{33} define the extremes of the tent while σ_{22} defines the apex of the tent that is generally located off center. Therefore, a typical solid with a variety of different carbons will yield a ^{13}C spectrum that is the sum of different CSA patterns having somewhat different line shapes and isotropic centers. Overlapping CSA patterns destroy the resolution which was hoped to be gained from dipolar decoupling. Therefore, to perform high resolution NMR spectroscopy in the solid state, a technique is required that reduces this anisotropy to the isotropic chemical shift observed in solution.

3.1.1.4 Magic Angle Spinning

The directional dependence of the chemical shift in solid state NMR, which arises from restrictions placed on molecular motion, must be appropriately averaged to remove this line-broadening effect. The required averaging can be induced by operating on its spatial dependence by utilizing the magic angle spinning (MAS) technique (introduced in connection with the dipolar interaction) independently introduced by Lowe[14] and Andrew, *et al.*[15]

The magic angle spinning technique involves physically spinning the sample at an angle of 54°44' to the external magnetic field with a rotation rate that is fast compared with the CSA. Under these conditions, the spacial dependence (*i.e.*, $(3\cos^2\theta_{ij} - 1)$ is averaged to zero. Therefore, overlapping CSA patterns reduce to their isotropic averages and the result is a high resolution spectrum (*i.e.*, with dipolar decoupling). It should be noted that the rotation rate must be fast compared to the anisotropy, *i.e.*, to the frequency range encompassed by the powder pattern since otherwise peaks known as spinning side bands will appear in the spectrum. For ^{13}C NMR of solids at typical magnetic fields, rotation rates between 1 and 6 kHz are required to reduce the CSA pattern to its isotropic value. Since the nuclear shielding is field-dependent, the width of the CSA pattern increases with the static field strength so that higher MAS speeds are required at higher field strengths to overcome the line broadening phenomenon. If the rate of sample rotation is less than about half of the width of the CSA, spinning side bands will appear at multiples of the spinning speed on both sides of the isotropic chemical shift. The number, intensity and position of the side bands is strongly dependent on the CSA and the spinning speed.

It should be noted that, in principle, MAS removes any solid state interaction that possesses a $(3\cos^2\theta_{ij} - 1)$ dependence. As mentioned previously, strong interactions such as ^1H-^1H dipolar coupling are not efficiently eliminated due to the impractical spinning speeds (*i.e.*, 10 to 50 kHz) that must be achieved. However, weaker interactions such as CSA, natural abundance ^{13}C-^{13}C dipolar coupling and long-range ^{13}C-^1H interactions are totally eliminated by MAS.

3.1.2 Signal Generation and Sensitivity Enhancement

Although high power dipolar decoupling and MAS reduce NMR line widths to acceptable levels, high resolution ^{13}C NMR of solid polymers still suffers from the problem of low sensitivity. This is due to the small magnetic moment of the ^{13}C nucleus that is, in addition, dilute in the system (1.1% natural abundance). The magnetic moment of the ^{13}C spin is about 1/4 as large as the proton moment, which results in a net magnetization that is 1/4 that of the protons in the same static field for an equal number of nuclei. Furthermore, the time required for the carbon spin system to recover from the perturbation necessary to make the measurement can be 10 to 100 times longer than for the proton spin system in the same molecule. This results in substantially longer times between acquisitions. This sensitivity problem has been overcome through the use of a technique known as cross polarization (CP) which involves an enhancement of the magnetization of the rare spins (*e.g.*, ^{13}C) by transfer from the abundant spins (*e.g.*, ^1H). This CP experiment was introduced by Hartmann and Hahn[16] in 1962, and was first applied to the ^{13}C nucleus by Pines and co-workers[17-19] some twenty years ago. To properly introduce the cross polarization technique, it is necessary to first discuss the concept of an isolated spin system and its spin temperature. In addition, a brief discussion on spin relaxation times is warranted. This discussion will consider a molecule possessing only ^1H and ^{13}C nuclei.

3.1.2.1 Spin Temperature

In NMR spectroscopy, it is useful to view an experimental sample as consisting of two parts, *i.e.*, the spin system and the lattice. The spin system is the ensemble of nuclear magnets (*i.e.*, ^{1}H, ^{13}C) that was discussed in the previous section in connection with various line broadening mechanisms. The lattice consists of the molecules that constitute the sample (either in solid, liquid or gaseous form) characterized by a lattice temperature, T_l, which is the quantity measured by the operator. Similar to the lattice, the spin system is also characterized by a temperature. However, this temperature is a consequence of the distribution of the spin population among the energy states available to the magnetic nuclei. In a magnetic field, B_o, nuclear spins (I=½) will populate their Zeeman energy levels according to the Boltzmann distribution:

$$\frac{n_u}{n_l} = \exp\left(\frac{-\Delta E}{kT_S}\right) \qquad (3.2)$$

where n_u and n_l are the populations of the upper and lower states, $\Delta E = \frac{\gamma h B_o}{2\pi}$ is the energy separation of these two states (γ is the magnetogyric ratio of the nucleus in question and h is Planck's constant), k is Boltzmann's constant, and T_S is the temperature of the spin system (*i.e.*, the spin temperature). Equation (3.2) states that a given population distribution (n_u/n_l) is characterized by a spin temperature (T_S) where a change in this population distribution (*e.g.*, by applying an rf pulse) results in a change in the temperature of the spin system. It should be noted that a large population difference between the two states corresponds to a low spin temperature and to a large polarization. Therefore, to induce a large polarization within a spin system it is necessary to lower the spin temperature or, in other words, generate a large population difference.

An organic solid that only contains ^{1}H and ^{13}C spin nuclei (I=½) has two spin systems. Under equilibrium conditions the spin system temperature, T_S, is equal to the lattice temperature, T_l. However, upon resonant irradiation with an rf pulse, a nonequilibrium state is induced and the temperature of the spin system is raised while that of the lattice remains constant. Through the process of spin diffusion, abundant, nonisolated nuclei such as protons equilibrate in a very short time (<100 μs) at a single T_s. It should be mentioned that the process of spin diffusion is defined as the transport of spin energy within the spin system by mutual energy-conserving flips (*i.e.*, a simultaneous change in orientation of two adjacent protons with antiparallel orientation coupled by a dipolar interaction which again yields an antiparallel orientation). After a much longer time the single spin temperature of the proton spin system thermally equilibrates with the lattice on a time scale defined by the spin-lattice relaxation time.

A dilute spin system such as ^{13}C also equilibrates with a single spin temperature over a time scale which is much longer than that for the abundant nuclei due to larger internuclear distances and different relaxation processes. It should also be noted that the separation of their energy levels is only about 1/4 the separation of the proton levels at the same temperature ($\gamma_H = 4\gamma_C$) thus yielding a different resonance frequency. This difference means that the two sets of nuclei cannot communicate efficiently and are isolated from each other. Therefore, the two sets of nuclei form isolated spin systems which also allows them to have different relaxation times.

3.1.2.2 Relaxation Times

In both liquid state and high resolution solid state NMR spectroscopy, the most fundamental and important relaxation times are the spin-lattice, T_1, and spin-spin, T_2, relaxation times. The spin-lattice time constant describes the return of the magnetization of a particular nucleus back to a state of equilibrium which corresponds to an orientation parallel to the static field, *i.e.*, along the z-direction. The return of the magnetization from a perturbed state involves the release of excess energy to the lattice. This occurs through the modulation of local magnetic fields by molecular motions of the appropriate frequency. In addition, since spin-lattice relaxation involves transitions between different nuclear magnetic energy levels, it is most efficient at or near the resonant frequency, $\omega_o = \gamma B_o$. Therefore, this time constant yields information regarding chain mobility.

The spin-spin time constant describes the loss of observable magnetization, *i.e.*, the component of the magnetization in the x,y-directions or perpendicular to the static field. The observed nuclear signal is the free induction decay (FID) described by T_2. This time constant describes the loss of phase coherence arising from the distribution of Larmor frequencies associated with the distribution of local magnetic fields, h_l (Eqn. 1). This equilibration does not involve energy exchange and is, therefore, purely entropic. For a Lorentzian line, the linewidth of a particular resonance, $\nu_{1/2}$, is related to T_2 by

$$\nu_{1/2} = \frac{1}{\pi T_2} \tag{3.3}$$

A relatively efficient interaction among the spin energies resulting from low molecular mobility (*i.e.*, the essentially static lattice possessing a broad distribution in local magnetic fields) results in a short T_2 and, consequently, a broad resonance line. When molecular motion develops, these couplings among nuclei diminish and T_2 becomes longer (*i.e.*, of the order of tens of milliseconds) with a concomitant decrease in the resonance linewidth.

Different relaxation times are observed for isotopically different nuclei due to differences in Larmor frequencies, motions and available relaxation mechanisms. However, relaxation times are seldom independent since different sets of nuclei are generally coupled to other magnetic nuclei by various interactions. This is particularly true for abundant nuclei, such as protons, for which the process of spin diffusion averages the relaxation times of different chemical types.

In the investigation of polymer motional characteristics by NMR, it is necessary to probe a multitude of motional frequencies. In the solid state, polymers typically possess motions with characteristic fequencies ranging from a few kHz to a few hundred MHz. As mentioned previously, the spin-lattice relaxation time, T_1, is most effective when the frequencies of these motions are near the Larmor frequency, *i.e.*, 5-500 MHz. These effective frequencies are determined by the size of the static field. To probe motional characteristics in the kHz range, T_1 measurements can be performed in a very small static field where the Larmor frequency would correspond to a few kHz. However, in such a small static field the NMR sensitivity is very low. This problem has been overcome by performing the spin-lattice relaxation measurements in a rotating frame[20] using a "spin-locking" sequence.

The application of a 90° rf pulse in the y-direction with a field strength of B_1, tips the magnetization, initially directed along the static direction (z-direction), to the x-direction. The phase of the rf pulse is then shifted by 90° to coincide with the magnetization aligned in the x-direction. This procedure is known as "spin locking". In the rotating frame, the magnetization is then under the influence of only the B_1 field, typically 50 kHz in strength, thus probing low frequency molecular motions (*i.e.*, the kHz region). It should be noted that the size of the magnetization is determined by the larger static field thus maintaining the sensitivity. The decay of the magnetization in this lower field is characterized by another time constant, $T_{1\rho}$, the spin-lattice relaxation time in a rotating frame.

Immediately after the spin locking sequence, the magnetization of nucleus I, M_o^I, in the rotating frame, is proportional to $\exp(\frac{2\mu_I B_1^I}{kT_s})$. A dependence on the rf field is clearly evident. At equilibrium (*i.e.*, under the influence of the static field), the observed magnetization is proportional to $\exp(\frac{2\mu_I B_o^I}{kT_l})$. Since $B_1^I = 10^{-3} B_o^I$, T_s, must be $10^{-3} T_l$ for the condition to hold. Therefore, spin locking in the rotating frame results in a cooling of the I spins (*e.g.*, protons) to near 0 K. The subsequent observed decay in the magnetization through spin-lattice relaxation in the rotating frame therefore stems from a flow of energy from the lattice to the cooler spin system.

3.1.2.3 Cross Polarization

The cross polarization technique involves the transfer of polarization from an abundant species, such as protons, to a dilute system, such as carbons, to enhance the signal of the dilute spin system. As has been developed above, in the static field an organic molecule whose only spin-possessing nuclei are ^{1}H and ^{13}C has two essentially isolated spin systems. This is mostly due to the large difference in resonance frequency between the two species. If this resonance frequency mismatch could be eliminated, communication between the previously isolated spin systems would be possible through energy-conserving flips between the protons and carbons and transfer of polarization would be realized. The coupling of the spin systems was first recognized by Hartmann and Hahn and involves the application of two resonant alternating rf fields, *i.e.*, B_1^H and B_1^C, such that

$$\gamma_H B_1^H = \gamma_C B_1^C \tag{3.4}$$

where γ_H and γ_C are the proton and carbon magnetogyric ratios. The Hartmann-Hahn condition is central to the cross polarization technique. The two resonant rf fields (*i.e.*, the first at the proton frequency and the second at the carbon frequency), set at different power levels such that the condition depicted by Eqn. (3.4) is realized, forces a match of the Zeeman energy level splitting in the rotating frame. Therefore, both spin systems are in frames rotating at the same rate, the energy levels are matched and energy transfer is thus allowed.

The carbon-proton cross polarization (CP) pulse sequence utilizing proton spin locking is depicted graphically in Figure 3.1a. The protons are initially prepared in a state of low spin temperature by spin locking them in a rotating frame. As discussed previously, this is accomplished using a 90° rf pulse followed by a 90° phase shift. The small carbon system, initially at the lattice temperature is brought into contact with the colder proton reservoir by use of the double resonance method that satisfies the Hartmann-Hahn

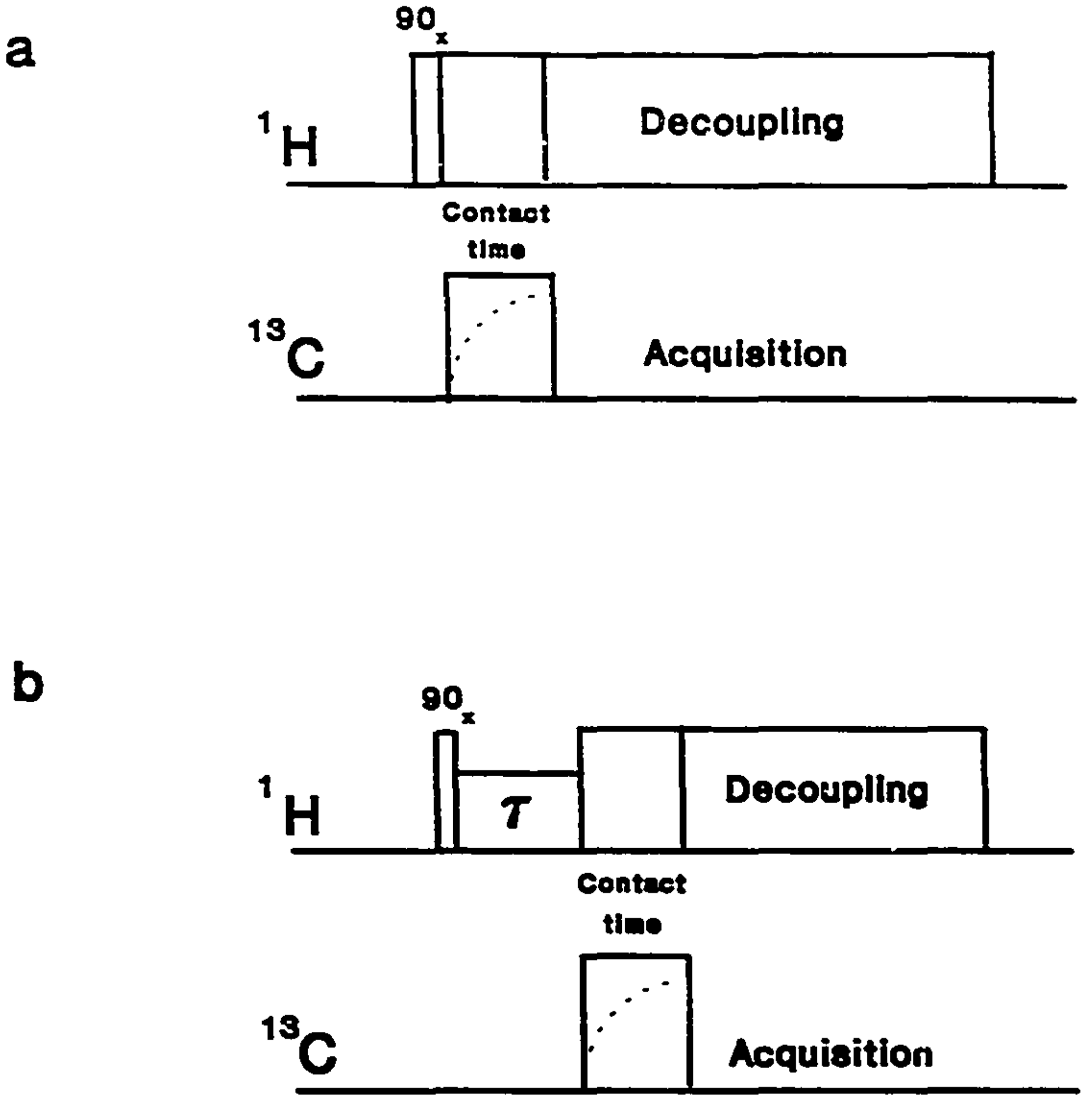

Figure 3.1 a) The carbon-proton cross-polarization pulse sequence utilizing proton spin locking with high power proton decoupling during acquisition of the FID. b) Reduced field, delayed contact cross-polarization pulse sequence utilizing proton spin locking with high power proton decoupling during acquisition of the FID.

condition. In Figure 3.1a, this is depicted by the simultaneous pulses on the proton and carbon channels. This simultaneous irradiation is maintained for a time interval, t_c, necessary to build up the carbon magnetization. Assuming that the thermal connection between the protons and carbons is much better than the connection of each with the lattice, the carbon temperature decreases while that of the protons increases only slightly, thereby establishing a common equilibrium spin temperature. From the definition of spin temperature, a low temperature implies a large polarization of the magnetic moments. The build up of magnetization is represented graphically by the dashed line within the rf pulse of the carbon spin system. After CP the contact between the proton and carbon spin system is broken by removal of the B_1^C field and the FID of the carbons is then observed. High power dipolar decoupling at the proton Larmor frequency is used to remove heteronuclear dipolar interactions between the carbons and neighboring protons thus obtaining high resolution ^{13}C spectra. The cross polarization technique can also be used in combination with MAS for the removal of chemical shift anisotropy.

The transfer of polarization from the proton to the carbon spin system is controlled by a cross-relaxation time, T_{CH}. The rate at which the two spin systems reach thermal equilibrium in the doubly rotating frame, $(T_{CH})^{-1}$, is determined by the effective strength of the dipolar interaction between protons and carbons which is greatly affected by molecular motions and interatomic C-H distances. Different types of carbon spins will also cross polarize at different rates depending on the number of directly attached protons. In addition, the initial polarization of the proton reservoir and the degree to which the Hartmann-Hahn condition is fulfilled alter the cross-relaxation time.

The buildup of carbon magnetization is reduced after some time due to a decay of the proton magnetization in the spin-locked state, *i.e.*, through $T_{1\rho}$ (^1H). The buildup of substantial carbon magnetization requires that the proton spin-lattice relaxation time in a rotating frame be substantially longer than the contact time, t_c, between the carbons and protons. In addition, the contact time must be longer than the cross-relaxation time, T_{CH}. Therefore, for proper polarization transfer to occur, $T_{1\rho}^{H} > t_c > T_{CH}$.

The cross polarization technique yields a substantial increase in sensitivity in the observation of dilute spins. However, a second advantage is also noteworthy. The repetition rate of the cross polarization process is now limited by the proton T_1 rather than the carbon T_1 as would be the case in a single pulse experiment. This is a definite advantage since the proton T_1 is usually less than 1s for polymers while the carbon T_1 is substantially longer, *i.e.*, 10-4000 s. The net result is an increase in the signal-to-noise ratio within a given time interval since it is possible to acquire a larger number of FIDs compared to what can be obtained in the standard one-pulse experiment.

The simple cross-polarization technique described above was developed by Pines, Waugh and co-workers and is currently the most commonly used technique for the observation of dilute spin systems. The first illustrations that a combination of dipolar decoupling/cross polarization/magic angle spinning (DD/CP/MAS) could be used to obtain high resolution ^{13}C spectra of solids are due to Schaefer, Stejskal and Buchdahl[21-23] who reported a series of results on glassy polymers. High resolution DD/CP/MAS spectra have since been obtained on a variety of polymers, including polypropylene, which will now be introduced.

3.1.3 ^{13}C CP/MAS NMR Studies in Polypropylene

The combined techniques of heteronuclear dipolar decoupling, cross polarization and magic angle spinning yield high resolution spectra in polypropylene that reveal fine details about its phase structure. The observations regarding the phase structure of both isotactic and syndiotactic polypropylene (iPP and sPP, respectively) as obtained from solid state spectra will be discussed.

The phase structure of solid sPP was first investigated by Bunn, *et al.*[24] This was one of the early examples of the application of these NMR techniques to polymers. More recently sPP with various thermal and mechanical histories has been studied by Sozzani and co-workers.[25-26] The chemical shifts of all three carbon resonances as reported by both Bunn, *et al.*[24] and Sozzani, *et al.*[26] are listed in Table 3.1 for sPP samples that were either annealed (*i.e.*, labeled 'helix') or cold drawn (*i.e.*, labeled 'stretched'). The chemical shifts of the annealed samples given in these two reports are in good agreement, with the exception that a double methyl carbon resonance was observed by Sozzani and co-workers.[26] This splitting of the methyl resonance will be discussed further below.

Table 3.1 The ^{13}C Chemical Shifts of Syndiotactic Polypropylene in the Solid State.

Sample		**Chemical Shift (ppm)**		
		Methylene	**Methine**	**Methyl**
Bunn, *et al.*[24]	helix	39.6 and 48.3	26.8	21.0
Sozzani, *et al.*[26]	helix	40.2 and 49.0	27.4	21.9 and 22.1
Sozzani, *et al.*[26]	stretched	50.2	28.9	20.8

As seen from the data in Table 3.1, the CP/MAS spectrum of sPP reveals the existence of two methylene resonances with a 1:1 intensity distribution separated by ~8.7 ppm. This resonance splitting suggests the existence of two distinctly different methylene chemical environments in the crystal structure of sPP. Although the level of order within the unit cell (*i.e.*, the space group defining the crystal structure) is still disputed,[27-33] during crystallization sPP is known[34] to adopt a $(ttgg)_2$ helical conformation that packs into an orthorhombic unit cell. This helical conformation supports the existence of two distinct and equally probable sites for methylene groups, *i.e.*, one on the helix axis and the other on either side of this axis. The double methylene resonance was explained by considering the γ-gauche shielding effect[35] which, for polypropylene is predicted[36] to result in a splitting of ~8 ppm between the two resonances. This is close to the observed value of 8.7 ppm. If the γ-effect is the cause of the difference in the chemical shift then the upfield resonance can be assigned to the internal methylene carbons. Therefore, this resonance splitting is due to intramolecular effects. In addition to the above feature, the higher frequency peak showed additional broadening which may be due to interchain effects. However, the atoms on the periphery of the helix should be much more susceptible to perturbations due to interhelical effects, *i.e.*, the packing of helices in a regular array.

The higher structural purity of the sPP samples used by Sozzani and co-workers[25-26] under appropriate thermal and mechanical histories yielded changes in the NMR spectra of sPP which relate directly to the structure of the crystalline phase. Upon cold drawing of a previously quench-cooled sPP sample, the all-trans conformation was obtained. The upfield methylene signal (Table 3.1) described above in connection with the helix crystal structure was absent in the CP/MAS spectrum of that sample.[25] This study clearly demonstrated that the CP/MAS experiment is sensitive to intramolecular conformations in sPP since the difference between the helix and the all-trans conformation was clearly observable. In addition, through an annealing treatment on a previously quench-cooled sPP sample interchain effects associated with helical packing were observed and discussed in a subsequent communication.[26] Details regarding the crystal packing arrangement in sPP were obtained from the observation of a 1:1 methyl split in the solid state spectrum (Table 3.1). The split in the methyl resonance of the annealed sample was interpreted as probing the association of right- and left-handed helices in the crystal structure of this morphology. Therefore, the solid state spectrum is capable of probing not only structure within the helix but also the arrangement of these helices within the crystalline phase of sPP.

The solid state organization of the various morphologies associated with the crystalline phase of iPP has also been investigated by NMR spectroscopy.[37-45] As discussed previously, during crystallization iPP develops both right- and left-handed 3_1 helices that are present in the three distinctly different polymorphs; namely the α-monoclinic, β-hexagonal and the γ-triclinic crystalline forms. In addition to these polymorphs, the quench-cooled morphology described in the first chapter has also been considered in NMR studies.

In the ^{13}C CP/MAS spectrum of iPP, both the quench-cooled (Figure 2.6) and β-hexagonal phases show a single resonance for each of the three carbons. However, for both annealed and isothermally crystallized iPP samples, the methylene and methyl resonances in the α-monoclinic phase show a double peak, separated by *ca.* 1 ppm (Figure 2.6). It has been postulated that this resonance splitting is a consequence of the inequivalent distances within the α-monoclinic unit cell which result from regular packing of right- and left-handed helices. The intensity distribution within these doublets is suggested, from visual observation, to be approximately 2:1, corresponding to a 2:1 carbon ratio at each inequivalent position. The absence of this splitting for the methylene and methyl resonance in quench-cooled iPP suggests that this morphology is either not composed of the α-monoclinic phase or that it is composed of an α-monoclinic phase where inequivalent distances within the unit cell do not exist. The latter explanation, which has also been suggested by Bunn, *et al.*,[36] requires that the inter-helical distances in the unit cell be larger than in the stable α-monoclinic crystal form, which corresponds to the second phase observed by electron diffraction described in the first chapter.

The solid state spectrum of the γ-triclinic crystalline modification was first reported by Brückner, *et al.*[44] As for the α-monoclinic crystal form, the spectrum of the γ-form also reveals the existence of a splitting in the methyl carbon resonance. However, the intensity distribution observed for this phase is opposite to that obtained for the α-monoclinic crystalline phase (Figure 2.6). A reversal in intensity between the upfield and downfield methyl resonance is observed. This splitting in the methyl resonance and the intensity distribution has also been discussed in terms of the packing of helices in the crystal structure of γ-iPP.

High resolution solid state NMR spectroscopy is seen to be extremely sensitive to local environment differences in the various crystalline modifications in both isotactic and syndiotactic polypropylene. This technique is extremely useful as a complementary tool to other solid state characterization techniques.

3.1.4 The Present Work

The second chapter presented a description of the morphology of the quench-cooled phase of iPP as viewed directly by scanning transmission electron microscopy (STEM). It was found to be composed of three phases: 1. Microcrystalline regions that range in size between 100 and 200 Å having the α-monoclinic crystal form; 2. Regions of lower crystalline order also composed of the α-monoclinic crystal form. The helical packing in this region was found to be much less compact than in the microcrystalline region, as evidenced by a larger *b* crystallographic axis; 3. An amorphous phase. The formation of regions of low crystalline order (*i.e.*, phase #2) was found to occur *during* the quench-cooling of the iPP from the melt. The extent of this crystallization depended on sample mass; samples of low mass yielded an amorphous glass while those with larger masses formed a glass possessing a low degree of crystallinity (*i.e.*, $\leq$18%). As the temperature of the quench-cooled iPP sample was raised, further crystallization from the glassy state occurred (observed as an exotherm on the DSC thermogram) which resulted in the formation of the microcrystals that could be observed in the STEM dark field image. The resultant morphology was found to be metastable as evidenced by the DSC thermogram which was fully exothermic in the region between -15 and 120 °C.

The morphology of quench-cooled iPP, although stable at room temperature, transforms to the normal α-monoclinic crystal form upon annealing at temperatures above

60-70 °C. This transformation has been characterized mostly by x-ray diffraction at room temperature of samples previously thermally treated.[46-47484950] Other methods used in the characterization of this transformation include small angle x-ray scattering (SAXS),[51] infrared (IR) and Raman spectroscopy,[52,53] transport properties,[54,55] calorimetry,[56,57] and transmission electron microscopy.[58] IR measurements reveal that the helix conformation begins to form at temperatures as low as -18 °C (*i.e.*, near the T_g) consistent with the DSC findings described in Chapter 2. However, appreciable changes in the WAXS and electron diffraction pattern only appear for samples annealed at temperatures higher than 60 °C. The description of the quenched morphology in Chapter 2 as obtained by scanning transmission electron microscopy, allows for the above apparent discrepancy.

The transformation from the quench-cooled phase morphology to that of the normal α-phase, to date, has not been considered by solid state NMR spectroscopy. As discussed previously, high resolution NMR in iPP reveals fine details regarding the arrangement of helices in the various crystalline forms of iPP. The purpose of this study was to investigate the annealing behavior of samples with this quench-cooled morphology by monitoring changes within the ^{13}C CP/MAS spectra as a function of annealing temperature and thus obtain a fuller understanding of the solid spectrum of the α-monoclinic crystalline phase. A further goal was to develop correlations between these morphological changes, the thermal behavior observed by DSC and the observations made by WAXS.

3.2 Experimental

3.2.1 Sample Preparations

To obtain samples of the mesomorphic form, ~10 mg of iPP was melted between microscope glass slides at a temperature of 240 °C for 5 minutes to form thin films (~25 μm). These melted samples were immediately quench-cooled by immersion in a dry ice/acetone slush (-78 °C). Some of these samples were annealed under a nitrogen flow with a Mettler FP52 hot stage previously calibrated for temperature using high purity standards. The temperature was maintained by a Mettler FP5 temperature controller. The samples were heated to the desired anneal temperature at a heating rate of 20 °C/min and maintained isothermally for the desired time interval. After the annealing treatment, the samples were removed from the hot stage and allowed to cool to room temperature.

3.2.2 Solid State NMR Experiments

The CP/MAS ^{13}C NMR spectra were recorded at room temperature with a Chemagnetics CMX-300 spectrometer operating at a static field of 7.1 T. The samples were spun at the magic angle at a frequency of *ca.* 4.1 kHz in a 7.5 mm OD zirconia rotor. A contact time of 1 ms was used in the cross polarization with a pulse delay of 3 seconds. A 62 kHz rf spin locking field was used with an acquisition time of 68 ms. All of the spectra were referenced to TMS in a spectral window of 30 kHz by setting the methyl resonance of hexamethyl benzene to 17.40 ppm. For all spectra 1024 transients were accumulated and Fourier transformation was performed with no line broadening on an FID which was zero-filled to 8K to obtain sufficient points for peak deconvolution.

The CP/MAS ^{13}C NMR spectra of the purely crystalline phase of iPP were obtained in a delayed contact time experiment by reducing the ^{1}H spin locking field to 39 kHz for a time interval, τ, prior to cross polarization. The pulse sequence is shown graphically in Figure 3.1b. As a result of the relaxation of the spins of the amorphous and interfacial phases during this period with reduced field spin locking, only the signal from the material with the highest crystalline order, which possesses the longest relaxation times, was accumulated. All of the other spectrometer settings remained as given above. The spectra of the more mobile phases, with the shorter relaxation times, were also obtained by subtracting the above mentioned spectra from those having contributions from all phases, obtained with τ = 10 μs. Subtraction of the spectra was performed interactively using the software of a Varian Unity 500 spectrometer.

The ^1H spin-lattice relaxation times in a rotating frame, $T_{1\rho}$ (^1H), were measured at room temperature for the methylene, methine and methyl carbons on a Chemagnetics M-100 spectrometer operating with a static field of 2.35 T by spin locking the protons for various intervals, τ, before cross polarization. It should be noted that a spin locking field of 50 kHz was used in the measurements of the $T_{1\rho}$ (^1H). The $T_{1\rho}$ (^1H) values were obtained by fitting the intensity data (a total of at least 16 τ values) on a double exponential decay curve using a computer program (Peakfit, obtained from Jandel Scientific).

3.2.3 Peak Deconvolution

In the analysis of the solid state spectra of iPP, it became evident that the various peaks could not be represented adequately by either purely Gaussian or Lorentzian line shapes. A close representation of each of the resonances in the overall solid state spectrum, required the use of a Voigt line shape that is a convolution of a Lorentzian with a Gaussian.[59] Peak deconvolution was performed using the computer program, Peakfit. Since the convolution integral describing the Voigt function cannot be evaluated analytically, Peakfit uses the approximation of Puerta and Martin,[60,61] in which the Voigt function is approximated by four generalized Lorentzians using an asymptotical Padé method. Deconvolution of the iPP solid state spectra using the Voigt function always yielded fits with correlation coefficients, $r \geq 0.999$. To minimize the number of fitting variables, deconvolution was performed by forcing the various peaks within a given carbon resonance to share the fitting variable that controls the amount of peak tailing. This procedure essentially forces the same peak shape (*i.e.*, degree of tailing) for all peaks within a given carbon resonance that is being deconvoluted (*e.g.*, methyl resonance).

3.3 Results and Discussion

In the DSC thermogram for the heating of an iPP sample which was quench-cooled in a dry ice/acetone slush at -78 °C, an exothermic transition is clearly evident in the region between 80 and 120 °C (Figure 2.1). Originally this typical exotherm was attributed[56] to a transition from a quench-cooled phase morphology to the more stable α-monoclinic crystalline phase but, in view of the results presented in Chapter 2, it can be viewed as resulting from the perfection and further development of the α-monoclinic crystalline phase that formed during quench-cooling. In addition to the exothermic transition, two endothermic peaks are clearly evident; a small peak between 30 and 75 °C as well as a large peak between 120 and 165 °C. As indicated by the exothermic transition, the latter endotherm does not correspond to the melting of the original morphology but rather of a crystalline phase that has developed during sample heating. To develop a fuller understanding of the changes that occur in the crystalline phase of quench-cooled iPP samples during heating from room temperature, a detailed solid state ^{13}C NMR morphological investigation is presented.

3.3.1 ^{13}C CP/MAS and $T_{1\rho}$ (^{1}H) Analysis

Figure 3.2 shows the ^{13}C CP/MAS NMR spectra of iPP samples which have been quench-cooled in a dry ice/acetone slush before and after high temperature annealing. The spectrum of the sample that has been annealed at 161 °C for one hour (Figure 3.2a) shows methylene (~ 44 ppm) and methyl (~22 ppm) carbon resonances which are split by <1 ppm, in keeping with previously reported spectra.[37,39] In addition, the methine (~26.6 ppm) carbon resonance has a splitting of 0.2 ppm, with an intensity distribution similar to that of the methylene and methyl resonances, as shown in the inset in Figure 3.2. An asymmetrical line shape for the methine peak was observed by Bunn, *et al.*[37] and they suggested that it indicated the presence of an unresolved splitting. However, the spectrum

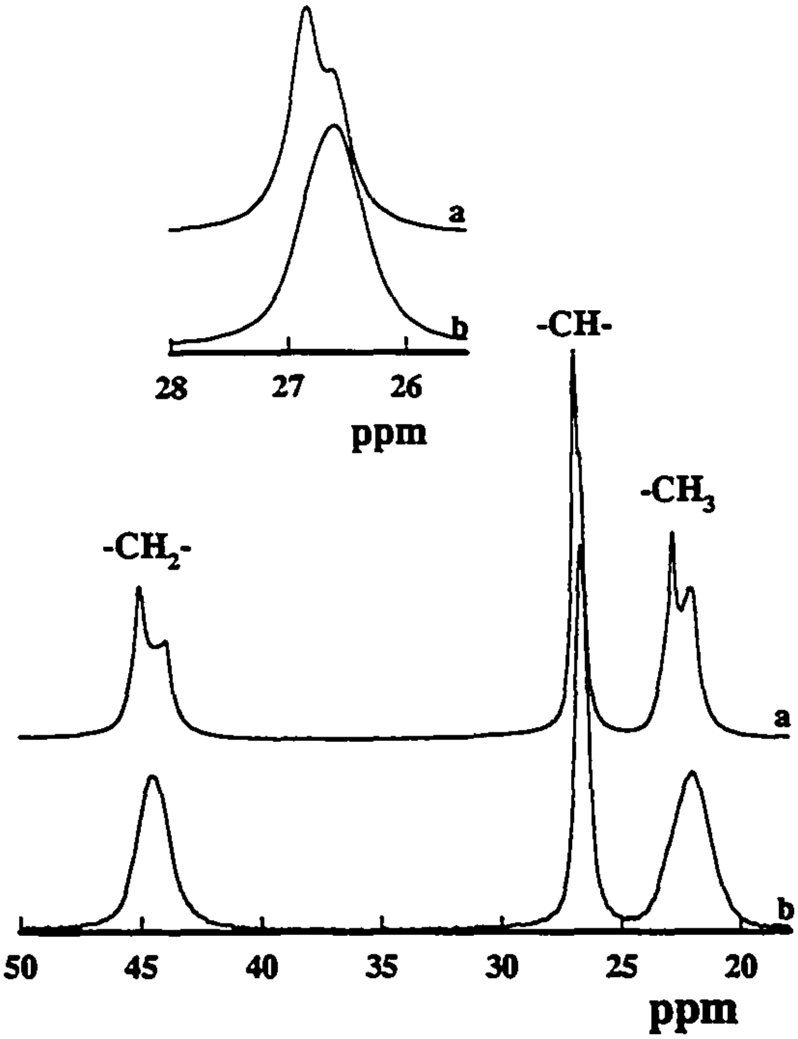

Figure 3.2 ^{13}C CP/MAS NMR spectra of two morphologies of iPP: (a) annealed α-monoclinic and (b) quench-cooled.

given in Figure 3.2 is the first unambiguous identification of the splitting. It should be noted that special conditions are required to detect the splitting of the methine peak: i. a sufficiently long acquisition time of the FID must be used (here 68 ms), ii. no line broadening should be applied, and iii. the FID must be zero-filled to a sufficiently large number (here 8 K).

The ^{13}C CP/MAS NMR spectrum of an unannealed iPP sample, shown in Figure 3.2b, is identical to previously reported spectra for samples having this morphology. The splitting observed for the three resonances of the annealed sample is no longer evident and the peaks appear to be symmetrical, giving no indication of any unresolved splitting. While the chemical shifts of the methyl and methine resonances coincide exactly with those of the most upfield resonances of the spectrum of the annealed sample (Table 3.2), the methylene peak appears at a chemical shift intermediate between the two peaks of the annealed sample. This is consistent with the observations of Gomez, *et al.*[39] but differs from the report by Bunn, *et al.*[37] that all of the carbon resonances of the quenched sample are coincident with the most upfield peaks of the annealed sample.

For both samples the fit of the relaxation data required two $T_{1\rho}$ (^{1}H) components (Table 3.2), in keeping with the existence of at least two phases within the iPP samples as observed by Tanaka.[41] The short relaxation times, which are indicative of the existence of a poorly defined crystalline component, can be ascribed to a more mobile interfacial phase while the long times arise from the highly crystalline portion. As with all semi-crystalline polymers, undoubtedly a third phase must also be present that possesses the mobility of a completely amorphous phase. As pointed out by Tanaka,[41] in this phase essentially all of the magnetization relaxes during cross polarization. *i.e.*, the relaxation time is too short to be measured. Clearly local spin diffusion within the repeat unit is operating effectively in these samples since each of the three carbon resonances of a given sample has the same long and short relaxation times. Both the long and short relaxation times increase significantly with annealing, as expected for the development of a more rigid matrix with larger crystalline regions.

Table 3.2: ^{13}C NMR Chemical Shifts and ^1H Spin Lattice Relaxation Times in a Rotating Frame for iPP at Ambient Temperature.

Sample	Chemical Shifts (a) (ppm from external TMS)			$T_{1\rho}(^1H)$ (b) (ms)		
	Methylene	Methine	Methyl	Methylene	Methine	Methyl
Quenched	44.6	26.6	22.0	19.9	19.9	19.3
				5.4	4.6	3.4
Annealed	45.0	26.8	22.7	109.8	109.7	108.0
161°C/1hr	43.9	26.6	22.0	14.7	14.2	12.7
Interfacial	44.5	26.7	22.3			

(a) Obtained at 75.3 MHz.

(b) Obtained at 25.1 MHz with a 50 KHz spin locking field.

As pointed out above, the ^{13}C CP/MAS spectrum of an iPP sample obtained under conditions such that the magnetization transfer occurs under optimal conditions, *i.e.*, 1 ms, is composed of contributions from at least two phases within the samples: the highly crystalline phase as well as a more mobile phase that possesses more order than the completely amorphous phase, which will be referred to as the interfacial component. In addition, although not representative of the total amount of the amorphous component, some magnetization resulting from this phase is observed. Due to the short ^1H $T_{1\rho}$ of this phase, the majority of the magnetization relaxes during cross polarization and only a small fraction is observed in the CP/MAS spectrum.

To describe the annealing behavior of this quench-cooled morphology, it is desirable that the contributions from the faster relaxing components be eliminated from the solid state spectra so that only that of the purely crystalline component remains. This can be accomplished by allowing the magnetization associated with the fast relaxing components to decay prior to the onset of the acquisition of the FID, which can be accomplished by using the pulse sequence described previously in the Experimental section.

3.3.2 ^{13}C CP/MAS Analysis of the Purely Crystalline Phase of iPP

The ^{13}C CP/MAS NMR spectra of a quench-cooled iPP sample annealed at 161 °C for one hour shown in Figures 3.3a and 3.3b were obtained with periods of reduced spin locking field before cross polarization of 10 μs and 15 ms, respectively. The use of a short 10 μs delay period prior to cross polarization results in the usual ^{13}C CP/MAS spectrum (Figure 3.3a) that has contributions from all of the phases in the iPP sampies. The resonances with a 15 ms delay period (Fig. 3b) are much better resolved, as evidenced by a better separation of the peaks for a given carbon resonance. This reflects the suppression of the signal arising from the shorter relaxing components associated with the more mobile phases. As is described later, the subtraction of these two spectra clearly yields the spectrum of the shorter relaxing component. This method of subtraction was also used in the determination of the value of τ, *i.e.*, the time prior to cross polarization that is required to obtain spectra for which the contributions from the more mobile phases are eliminated. The use of increasingly longer τ values prior to cross polarization eventually resulted in two τ values yielding identical spectra of different intensities which, when subtracted from each other, yielded a null spectrum. In this way, the τ value necessary to eliminate the faster relaxing component from the spectrum was identified.

The ^{13}C CP/MAS NMR spectra of the purely crystalline phase of iPP, obtained in

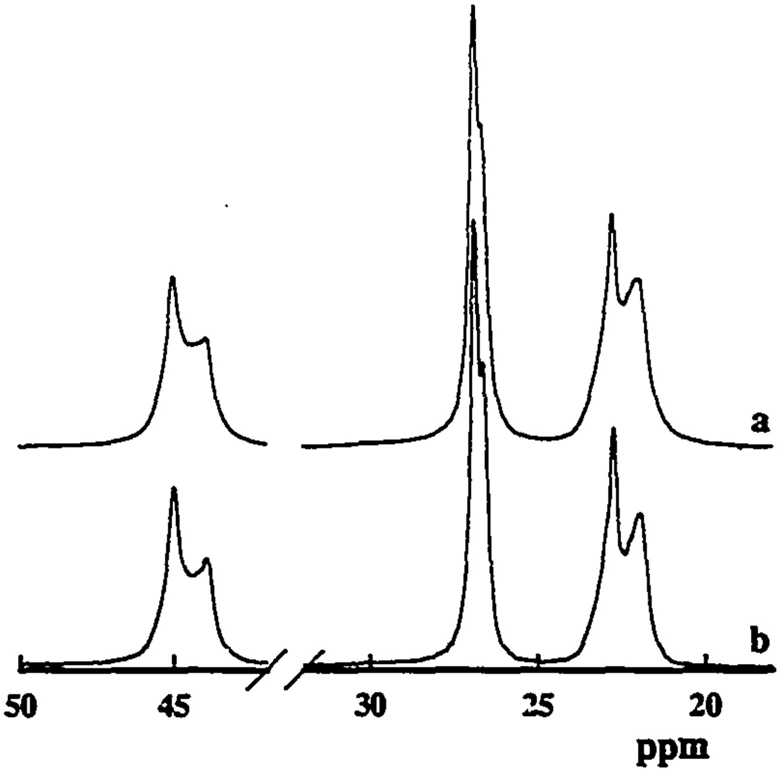

Figure 3.3 ^{13}C CP/MAS NMR spectra of the purely crystalline phase of a quench-cooled iPP sample annealed at 161 °C for one hour. The spectra were obtained by reducing the ^1H spin locking field for a time interval, τ, prior to cross polarization. (a) $\tau = 10$ µs and (b) $\tau = 15$ ms.

the delayed contact time experiment, for a quench-cooled sample subjected to various anneal temperatures between room temperature and 157 °C are shown in Figure 3.4. There is a gradual progression from an apparent single resonance, in the spectra of the samples annealed at low temperatures, to the split resonances in the spectra of those annealed at high temperatures. These changes are marked by an increase in the intensity of the downfield peak associated with each resonance (*e.g.*, the methyl resonance at 22.6 ppm) as well as what appears to be a sharpening of the most upfield peak within each resonance (*e.g.*, the methyl resonance at 21.9 ppm). In addition, in the spectra of samples annealed at temperatures between 115 and 140 °C it is clear that the methyl resonance of the crystalline phase is composed of three resolved peaks, rather than two. The third peak is located at *ca.* 23 ppm or on the downfield side of the methyl resonance. Careful inspection of the downfield side of the methylene resonance for the sample annealed at 130 °C also gives evidence of an unresolved splitting. As shown in the inset in Figure 3.4, the methine resonance is also split and the intensity distribution follows the same pattern as that for the methyl and methylene resonances. These spectra describe the effect of the annealing treatment on the purely crystalline phase of the iPP quench-cooled morphology. It indicates a change from a state of low crystalline order to one with a degree of perfection sufficient to cause the local resonance environments to differ, as evidenced by different chemical shifts within a given carbon signal.

A deconvolution procedure was applied to the various ^{13}C CP/MAS spectra of the crystalline component which, as described in the Experimental section, used a Voigt line shape to obtain the relative areas of the individual lines. Typical peak deconvolutions for the methine and methyl resonances of the spectra of as-quenched and two annealed samples (130 and 157 °C for one hour) are shown in Figure 3.5. The Voigt line shape clearly yields an excellent deconvolution of the solid state spectrum, with correlation

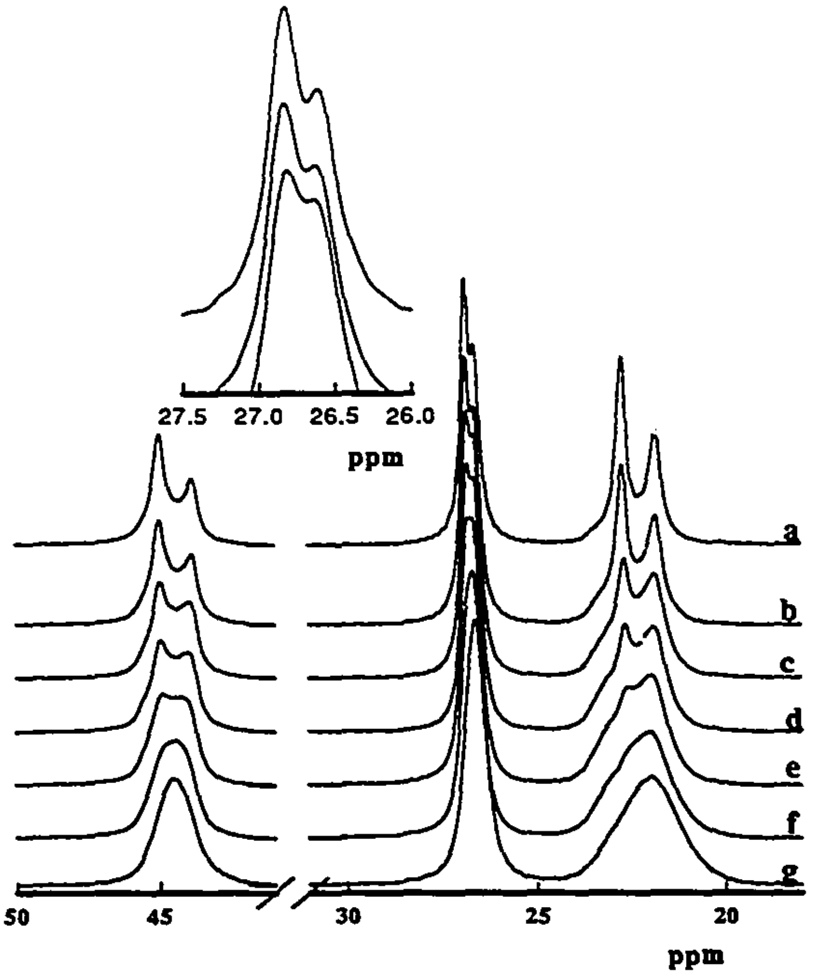

Figure 3.4 ^{13}C CP/MAS NMR spectra of the purely crystalline phase of a quench-cooled iPP sample annealed at various temperatures for one hour. The spectra were obtained by reducing the ^1H spin locking field for a time interval, τ, prior to cross polarization. (a) 157 °C, $\tau = 15$ ms; (b) 150 °C, $\tau = 15$ ms; (c) 140 °C, $\tau = 15$ ms; (d) 130 °C, $\tau = 15$ ms; (e) 115 °C, $\tau = 10$ ms; (f) 100 °C, $\tau = 10$ ms; (g) no anneal, $\tau = 5$ ms.

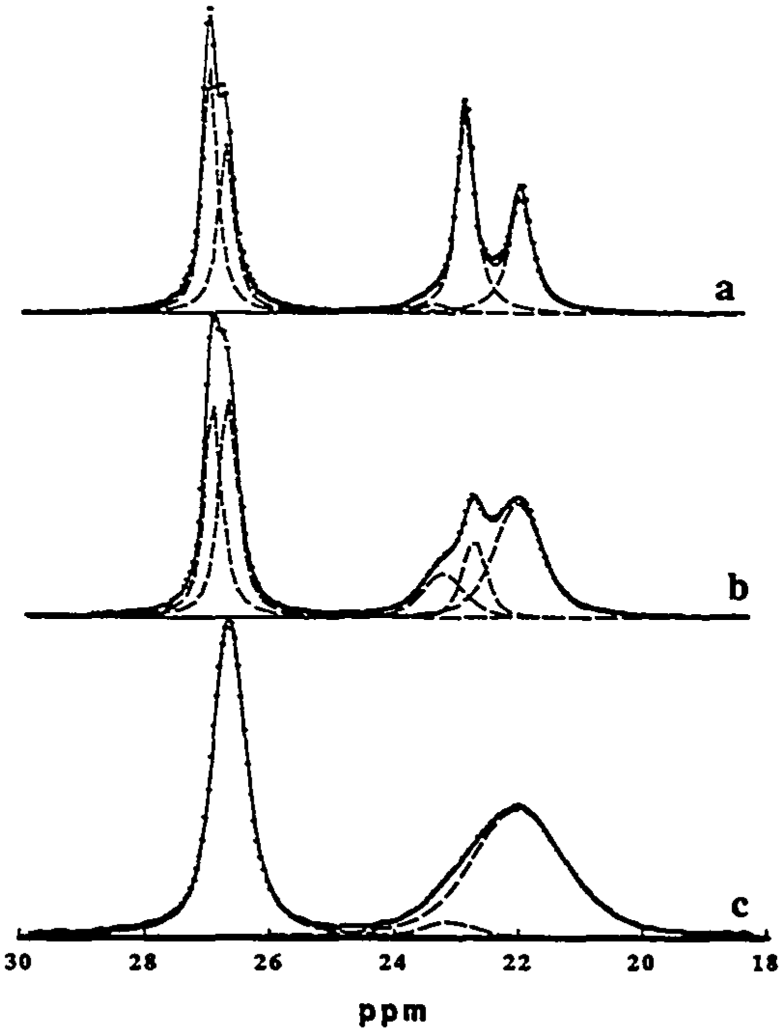

Figure 3.5 Deconvolutions obtained for the methine and methyl resonances of the ^{13}C CP/MAS NMR spectra of quench-cooled and annealed iPP samples. (a) 157 °C for 1 hour, (b) 130 °C for 1 hour, (c) no anneal.

coefficients better than 0.999.

It is apparent in the spectrum of the sample annealed at the intermediate temperature of 130 °C (Fig 3.5b), that the fit of the methyl resonance intensity requires three peaks that are due to inequivalent local environments. The most downfield methyl peak is also present in the resonance of the unannealed sample (Fig 3.5c) but with substantially reduced intensity. In addition, the midfield methyl resonance line is clearly absent. Annealing at a higher temperature (*i.e.*, 157 °C) results in an increase in the intensity of the midfield methyl line with a concomitant decrease in the most downfield component. As shown in Figure 3.5, the intensity distributions of the methine resonance show similar patterns with the downfield peak increasing in intensity while the upfield decreases as the anneal temperature is increased. However, the most downfield methine peak is absent (or at least unresolved) in the spectrum of the unannealed sample. A close inspection of the spectra shown in Figure 3.4, indicates similar trends for the methylene resonance.

The effects of anneal temperature on the relative areas of the methyl peaks as well as their corresponding line widths are shown in Figures 3.6 and 3.7, respectively. Although the deconvolution of the methyl region is discussed here, because it shows the best resolved peaks, similar patterns were noted for the other resonances. Since the methyl group is located furthest away from the helix, it is expected to be most sensitive to differences in the local environments. The relative areas reported in Figure 3.6 are based on a normalization that included the summation of the areas of the methine and methyl resonances. This was required because the close proximity in chemical shift of these two resonances precluded a separate consideration.

As shown in Figure 3.6, the relative peak areas of the methyl group in the crystalline component remain essentially unchanged at anneal temperatures up to approximately 75 °C. Apparently the small endothermic transition detected by DSC

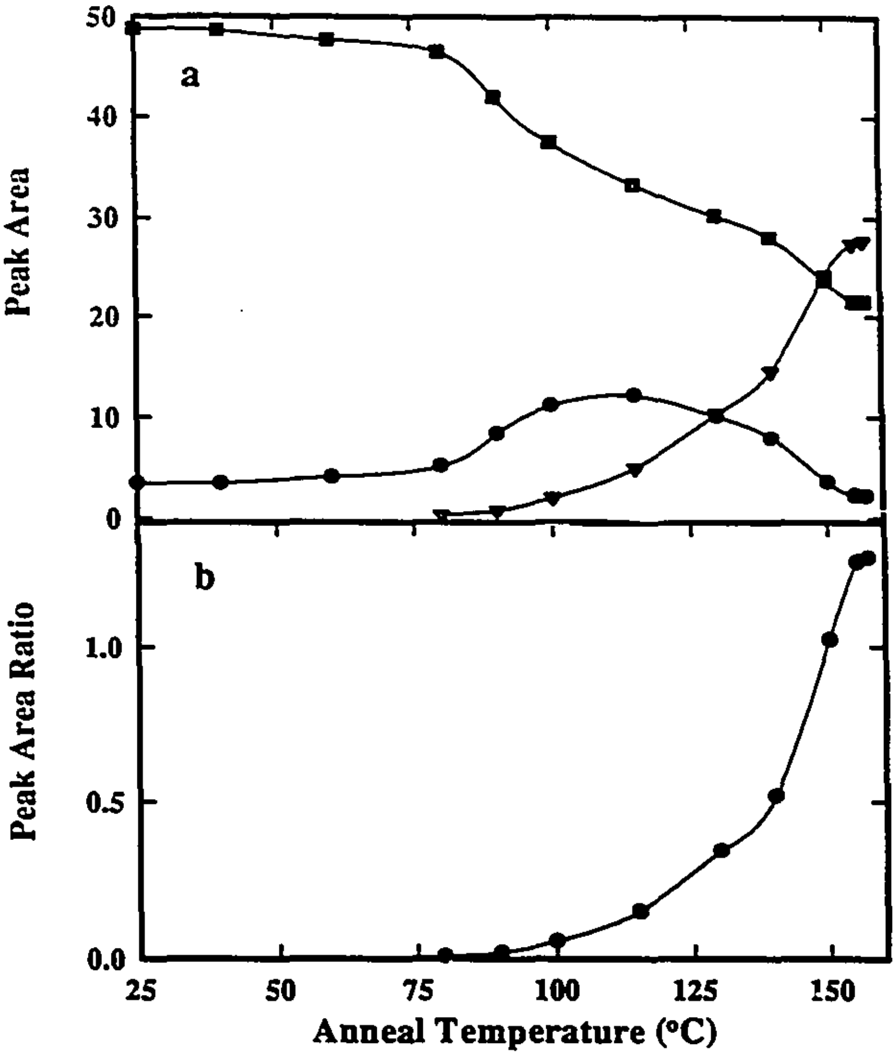

Figure 3.6 (a) Peak area deconvolution results for the methyl carbon of quench-cooled iPP samples annealed at various temperatures; ● downfield resonance; ■ upfield resonance; ∇ midfield resonance. (b) The ratio of the area of the midfield to that of the upfield resonance. The areas are expressed as a percentage of the total methyl plus methine areas (see text).

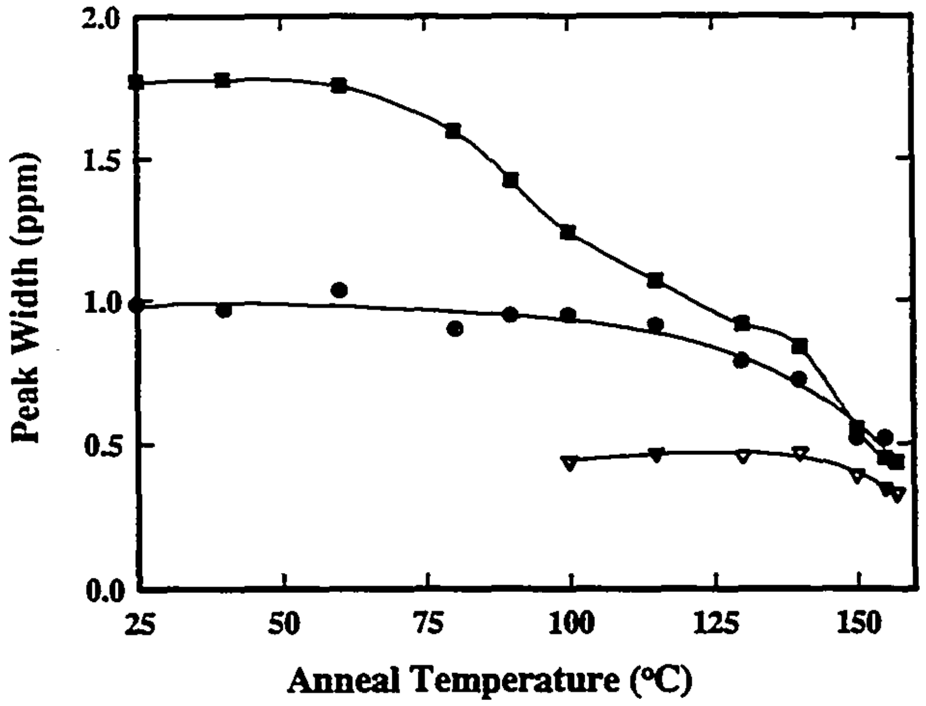

Figure 3.7 (a) Widths of the methyl peaks as determined by deconvolution of quench-cooled iPP samples annealed at various temperatures; ● downfield resonance; ■ upfield resonance; ∇ midfield resonance.

between 30 and 75 °C (Figure 2.1) does not correspond to a concomitant morphological change which can be detected by NMR. As the temperature is raised further, between *ca.* 75 and 120 °C, an increase in the relative areas of both the downfield and midfield methyl resonances is observed with a concomitant decrease in the upfield resonance. This temperature region coincides with the exothermic transition, observed by DSC, that was attributed to the perfection of the existing crystalline fraction. The NMR spectra reveal that this crystallization, or recrystallization, results in the development of three distinctly different local environments in the crystalline component. The midfield resonance continues to increase in intensity at anneal temperatures above 120 °C even though the DSC thermogram indicates the onset of the final melting transition. Thus, while the crystalline population is in a regime tending towards melting, there remains a positive drive towards perfection and development of the crystalline morphology, in keeping with an equilibrium between melting and recrystallization. Meanwhile, the downfield and upfield resonances decrease in intensity for anneal temperatures >120 °C. Clearly, these changes reflect alterations in the local environments within the iPP crystalline fraction as it recrystallizes to a higher degree of order. In addition, the most downfield resonance appears to show the behavior of an intermediate environment which is formed during the initial stages of crystal re-organization and then essentially disappears when the final crystalline state is attained.

The ratio of the areas of the midfield to the upfield methyl peaks is also presented in Figure 3.6. As mentioned above, this ratio is expected to be 2:1 based on the inequivalent sites, hence two distinctly different interhelical distances, that arise from the packing of left- and right-handed helices in the unit cell of the α-monoclinic crystal form, as is currently understood. Instead, the ratio follows closely the curve representing the intensity increase of the midfield resonance and appears to approach a limiting value of only 4:3. Two explanations can be offered to account for the failure of this ratio to attain the predicted value: 1. The ultimate peak ratio of 2:1 cannot be achieved by annealing this quench-cooled iPP morphology. 2. The splitting of these resonances is more complex than has been suggested to date and is possibly reflecting more than simply the association of right- and left-handed helices. The latter suggestion is supported by the fact that three resolved peaks, varying in intensity depending on the anneal temperature, are observed in the methyl resonance. The existence of the most downfield methyl peak, although observed for the first time in this study, was first suggested by Bunn and co-workers[37] in their original discussion of the resonance splitting pattern observed for the α-monoclinic crystaliine form. The occurrence of this splitting in the higher intensity methyl resonance was postulated from x-ray analysis which indicated two minor changes in the positioning of the methyl groups within the α-monoclinic crystalline phase. This difference is due to the way in which the iPP helices traverse the unit cell, *i.e.*, the positioning of the helices depends on the level of symmetry that exists within the unit cell.

As discussed previously, it has been shown by Mencik[62], as well as by Hikosaka and Seto[63], that the crystal form of annealed α-monoclinic iPP is described by the space group $P2_1/c$ which possesses disorder in the distribution of "up" and "down" chain directions. This disorder resembles the situation in the C2/c space group. In fact, it has been suggested that during annealing at high temperatures a structural transition occurs from a disordered state (C2/c) to an ordered state ($P2_1/c$). These space groups reflect differences in the structural arrangements of isoclined and anticlined bilayers of helices along the b crystallographic axis.[64] It is reasonable to suggest that the splittings observed in the NMR spectra of the crystalline portion of the annealed samples are not only reflecting environmental differences that correspond to the packing of right- and left-handed helices but that they are also probing changes that occur in the "up" and "down" ordering of chain position as the sample is annealed. This possibility will be discussed further in the following chapter which investigates the melting behavior of iPP spun fibers and spunbonded fabrics.

The line widths of the various peaks associated with the methyl resonances of the crystalline component range from approximately 0.5 to 1.7 ppm (Figure 3.7). A sharpening of the upfield resonance is clearly evident for the samples annealed at the temperatures corresponding to the onset to crystallization, *i.e.*, ≥75 °C. Meanwhile, the other two lines remain approximately constant in width until anneal temperatures ≥140 °C. All three methyl resonances seem to converge to a single line width at the highest anneal temperatures. These trends suggest that the iPP helices are converging to more singularly defined positions relative to one another which results in the formation of well-defined local environment differences and sharper resonance lines.

In a recent study[65] the melting and recrystallization behavior of a quench-cooled ethylene-propylene block copolymer (~7% ethylene) was investigated as a function of anneal temperature by simultaneous use of small angle x-ray scattering and wide angle x-ray scattering (SAXS/WAXS). A solid state transformation was observed at 65 °C as indicated by a change in the WAXS curve from the pattern characteristic of the quench-cooled phase to that of the α-monoclinic. A concomitant increase in the long range order was revealed by the SAXS. These observations coincide exactly with the exothermic transition in the DSC thermogram of iPP as well as the changes that are seen in the solid state NMR spectra of the crystalline component, as described above. The development of the multiple peaks for each of the carbon resonances, occurring in the same temperature range where morpholgical changes are observed by WAXS/SAXS and DSC, is indicative of the development of the α-monoclinic crystal structure.

3.3.3 ^{13}C CP/MAS NMR Spectra of the Amorphous and Interfacial Phases of iPP

As described above, by subtracting the spectra for the purely crystalline phase of iPP from spectra containing information for all phases (*i.e.*, a CP/MAS spectrum), it is possible to obtain the spectrum of the more mobile phases of iPP. The spectra for the quench-cooled and annealed iPP samples that were obtained by following this subtraction procedure are presented in Figure 3.8. Single resonances are observed for the methylene, methine and methyl carbons. These chemical shifts are also presented in Table 3.2. The peaks appear to be symmetrical and are located at chemical shifts intermediate between the doublets observed for each carbon in the spectra of the purely crystalline phase of the annealed samples. The shorter relaxing components of $T_{1\rho}$ (^{1}H) listed in Table 3.2 are

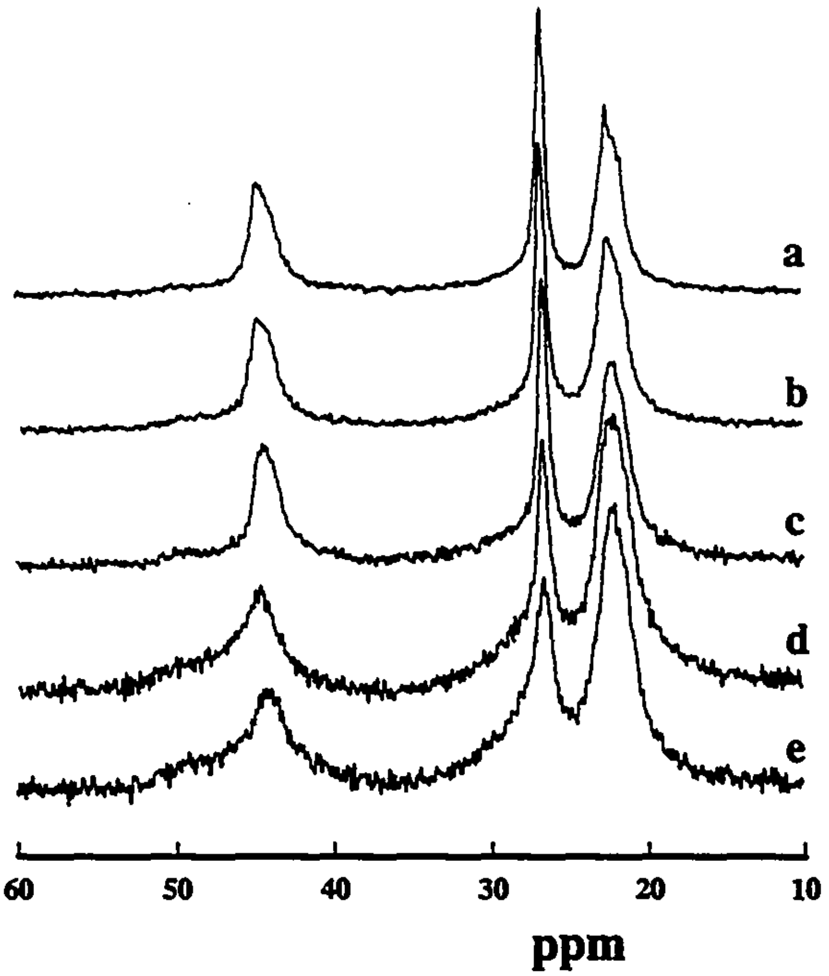

Figure 3.8 ^{13}C CP/MAS NMR spectra for the interfacial and amorphous phases of iPP obtained by subtracting the spectrum of the purely crystalline phase of iPP from one with contributions from all phases. Anneal Temperatures: (a) 157 °C; (b) 140 °C; (c) 100 °C; (d) 60 °C; (e) No anneal.

associated with these resonances. They characterize a phase of increased mobility which corresponds to the interfacial region between the amorphous and crystalline phases. It is of note that a similar interfacial peak, which was also reported by Saito et al,[44] was required for the proper deconvolution of the methylene region in the ^{13}C CP/MAS NMR spectra for the crystalline portion of iPP. It appeared intermediate between the methylene doublet and corresponds with the resonances presented in Figure 3.8. Although the authors described this peak as being due to the interfacial component, they also suggested that it could be a consequence of assuming a Lorentzian line shape in the deconvolution procedure. It becomes evident from the results presented here that this peak does indeed reflect the interfacial component in the iPP.

As discussed previously in connection with $T_{1\rho}$ (^1H) measurements, the signal associated with the fully amorphous phase in these iPP samples is not properly sampled since essentially all of the magnetization relaxes during cross polarization. It is primarily for this reason that only two $T_{1\rho}$ (^1H) values are measured. However, the CP/MAS spectra of the samples annealed at temperatures <80 °C (Fig. 3.8) indicate the existence of very broad peaks below each of the main resonances which is consistent with the signal expected from an amorphous phase. In the case of the methylene resonance this broad peak appears displaced downfield. Therefore, although this peak is not representative of the amount of the fully amorphous phase that is present in these samples, there is a clear indication of its presence. It is noteworthy that a similar peak on the downfield side of the methylene resonance was observed by Saito, *et al.*[44] in a variable temperature NMR investigation of isothermally crystallized iPP samples. The downfield methylene peak was also attributed to the amorphous phase.

As seen in Figure 3.8, the broad peaks associated with the fully amorphous phase appear substantially reduced in samples annealed at temperatures of 100 °C or higher. This trend is entirely expected in view of the recrystallization that occurs in the region between 80 and 120 °C which should substantially reduce the amorphous content. In addition, the amount of interfacial material appears greater for samples annealed at temperatures >100 °C compared to those subjected to the low temperature anneals. This behaviour is consistent with a greater number of crystal interfaces following sample recrystallization.

3.4 Summary

In this chapter, solid state NMR spectroscopy was employed to monitor changes that occur within the crystalline phase of quench-cooled iPP films as the sample is annealed at continuously higher temperature. Although previous investigations have also used solid state NMR spectroscopy to characterize the various polymorphs of iPP, this study is the first to employ this characterization technique as a means of describing the annealing behavior of the quench-cooled iPP morphology. In addition, the characterization of these morphological changes is performed through the use of a modified CP pulse sequence that allows the crystalline phase to be observed exclusively.

The modified CP pulse sequence that was used to observe only the crystalline phase of iPP exploited the differences in ^{1}H $T_{1\rho}$ relaxation times between the crystalline and more mobile phases. The modification involved incorporating into the usual CP pulse sequence a delay period with a reduced spin locking field prior to cross polarization. During this delay period, sufficient time was allocated such that the magnetization associated with the faster relaxing components (*i.e.*, the interfacial and amorphous phases) relaxed and only the magnetization associated with the slower relaxing component (*i.e.*, crystalline phase) was available for cross polarization. This technique allowed a separation of the signal arising from the crystalline phase from that of the amorphous and interfacial components. Furthermore, spectra for the more mobile phases of iPP were obtained by subtracting the spectra of the purely crystalline phase of iPP from those containing information on all three phases (*i.e.*, a CP/MAS spectrum).

In the NMR spectrum for the crystalline phase of iPP, a gradual conversion was observed upon annealing; from single methylene, methine and methyl resonances for the quench-cooled morphology of iPP to split resonances consistent with the fully developed α-monoclinic phase. These split resonances reflect the inequivalent sites within the α-monoclinic unit cell. The onset of this transformation was found to coincide with an exothermic transition observed by DSC at an anneal temperature of 80 °C. For the methylene and methine carbon resonances, this transformation involved an increase in the intensity of the downfield peak with a concomitant decrease in intensity of the upfield peak. It should be noted that, although suggested previously, the spectra reported in this study are the first unambiguous identification of a splitting pattern in the methine carbon resonance. A difference of 0.2 ppm was noted between the two methine peaks. In addition, the methyl carbon resonance was found to be composed of three peaks rather than two. The transformation as observed for this resonance occurred through an increase in intensity of the midfield methyl peak with a concomitant decrease in intensity of the upfield methyl peak.

Deconvolution was performed on the methyl and methine resonances using a Voigt line shape. The area and width of each of the peaks in the methyl resonance were reported as a function of anneal temperature. In the temperature region between approximately 75 and 120 °C, an increase in the area of the downfield and midfield methyl peaks is observed with a concomitant decrease in the area of the upfield peak. At anneal temperatures greater than 120 °C, both the downfield and upfield peaks decrease in area while the midfield methyl peak continues to increase. The downfield resonance appears to show the behavior of an intermediate environment which is formed during the initial stages of crystal reorganization and disappears when the final crystalline state is attained. In addition, simultaneously with the changes in peak area, a narrowing of the various peaks in the solid state spectrum was observed, consistent with a convergence to more singularly defined positions within the crystal structure.

The ratio between the areas of the midfield and downfield methyl peaks was also monitored as a function of anneal temperature. This ratio is expected to be 2:1 based on two inequivalent sites within the α-monoclinic phase arising from a closer association due to the packing of right- and left-handed helices. Instead, this ratio follows closely the curve representing the intensity increase of the midfield methyl peak and approaches a limiting value of only 4:3. The observation of three peaks within the methyl resonance as well as a much lower peak ratio than expected suggests that the splitting observed in the solid state spectrum of the α-monoclinic phase of iPP reflects more than a simple association of right- and left-handed helices. The general behavior suggests that the splitting patterns reflect the level of symmetry that exists within the unit cell of this phase, *i.e.*, the manner in which the helices traverse the unit cell.

Spectra of the more mobile, largely interfacial, phases of iPP were obtained by the subtraction procedure described above. A single peak was observed for each of the carbon resonances at a chemical shift intermediate between the doublet of the crystalline phase. These peaks, which are associated with the short $T_{1\rho}$ (^1H) value, are due to the presence of the more hindered interface between the purely amorphous and crystalline phases. In addition, the low temperature annealed samples indicate the existence of very broad peaks below the signal associated with the interfacial phase. In the case of the methylene resonance, this broad peak appears to be displaced downfield. Although the signal from the fully amorphous phase is not properly sampled in these spectra, the characteristics of these broad peaks are consistent with an expected amorphous phase. Upon annealing at temperatures of 100 °C or greater, the intensities of these broad peaks are substantially reduced. This trend is entirely expected in view of the recrystallization that occurs between 80 and 120 °C and supports the suggestion that these peaks are due to an amorphous phase. It should be noted that an increase in the interfacial component is also observed in this temperature region, indicating the formation of new crystal/amorphous interfaces during recrystallization.

3.5 References

[1] R.A. Komoroski (Ed), 'High Resolution NMR Spectroscopy of Synthetic Polymers in Bulk', VCH Publishers, Florida (1986).

[2] M. Mehring, 'High Resolution NMR in Solids', Springer-Verlag, Berlin (1983).

[3] J.R. Lyerla, in 'Methods of Experimental Physics', **16A**, 241 (1980).

[4] C.A. Fyfe, 'Solid State NMR for Chemists', C.F.C. Press, Guelph (1984).

[5] E. Fukushima and S.B.W. Roeder, 'Experimental Pulse NMR - A Nuts and Bolts Approach', Addison-Wesley, Reading (1981).

[6] J. Schaefer and E.O. Stejskal, *Top. 13C NMR Spectrosc.* **3**, 283 (1979).

[7] F.A. Bovey and L.W. Jelinski, *J. Phys. Chem.* **89**, 571 (1985).

[8] B.C. Gerstein, *Analytical Chemistry* **55**, 781 (1983).

[9] G.E. Maciel, *Science* **226**, 282 (1984).

[10] A. Carrington and A.D. McLachlan, 'Introduction to Magnetic Resonance', Chapter 11, Harper, New York (1967).

[11] J. Schaefer, E.O. Stejskal and R. Buchdahl, *Macromolecules* **10**, 384 (1977), and references therein.

[12] L.R. Sarles and R.M. Cotts, *Phys. Rev.* **111**, 853 (1958).

[13] E.R. Andrew, *Prog. Nucl. Mag. Res. Spectrosc.* **8**, 1 (1971).

[14] I.J. Lowe, *Phys. Rev. Lett.* **2**, 285 (1959).

[15] E.R. Andrew, A. Bradbury and R.G. Eades, *Nature* **182**, 1659 (1958).

[16] S.R. Hartmann and E.L. Hahn, *Phys. Rev.* **128**, 2042 (1962).

[17] A. Pines, M.G. Gibby and J.S. Waugh, *J. Chem. Phys.* **59**, 569 (1973).

[18] A. Pines, M.G. Gibby and J.S. Waugh, *J. Chem. Phys.* **56**, 1776 (1972).

[19] A. Pines, M.G. Gibby and J.S. Waugh, *Chem. Phys. Lett.* **15**, 373 (1972).

[20] T.M. Connor, *NMR, Basic Princ. Prog.* **4**, 247 (1971).

[21] J. Schaefer, E.O. Stejskal and R. Buchdahl, *Macromolecules* **8**, 291 (1975)

[22] J. Schaefer and E.O. Stejskal, *J. Am. Chem. Soc.* **98**, 1031 (1976).

[23] J. Schaefer, E.O. Stejskal and R. Buchdahl, *Macromolecules* **10**, 384 (1977)

[24] A. Bunn, M.E.A. Cudby, R.K. Harris, K.J. Packer and B.J. Say, *J. Chem. Soc., Chem. Commun.* 15 (1981).

[25] P. Sozzani, M. Galimberti and G. Balbontin, *Makromol. Chem., Rapid Commun.* **13**, 304 (1992).

[26] P. Sozzani, R. Simonutti and M. Galimberti, *Macromolecules* **26**, 5782 (1993).

[27] B. Lotz, A.J. Lovinger and R.E. Cais, *Macromolecules* **21**, 2375 (1988).

[28] A.J. Lovinger, B. Lotz and D.D. Davis, *Polymer* **31**, 2253 (1990).

[29] A.J. Lovinger, D.D. Davis and B. Lotz, *Macromolecules* **24**, 552 (1991).

[30] A.J. Lovinger, B. Lotz, D.D. Davis and F. J. Padden, Jr., *Macromolecules* **26**, 3494 (1993).

[31] W. Stocker, M. Schumacher, S. Graff, J. Lang, J.C. Wittmann, A.J. Lovinger and B. Lotz, *Macromolecules* **27**, 6948 (1994).

[32] C. De Rosa and P. Corradini, *Macromolecules* **26**, 5711 (1993).

[33] F. Auriemma, C. De Rosa and P. Corradini, *Macromolecules* **26**, 5719 (1993).

[34] P. Corradini, G. Natta, P. Ganis and P.A. Temussi, *J. Polym. Sci., Part C* **16**, 2477 (1967).

[35] D.M. Grant and E.G. Paul, *J. Am. Chem. Soc.* **86**, 2984 (1964).

[36] F.C. Schilling and A.E. Tonelli, *Macromolecules* **13**, 270 (1980).

[37] A. Bunn, M.E.A. Cudby, R.K. Harris, K.J. Packer and B.J. Say, *Polymer* **23**, 694 (1982).

[38] M.E.A. Cudby, R.K. Harris, K. Metcalfe, K.J. Packer, P.W.R. Smith and A. Bunn, *Polymer* **26**, 169 (1985).

[39] M.A. Gomez, H. Tanaka and A.E. Tonelli, *Polymer* **28**, 2227 (1987).

[40] H. Tanaka, *Eur. Polym. J.* **21**, 673 (1985).

[41] H. Tanaka, *Eur. Polym. J.* **27**, 565 (1991).

[42] H. Tanaka and H. Harada, *Eur. Polym. J.* **27**, 1 (1991).

[43] H. Tanaka, Y. Fujiwara, T. Asano and S. Polizzi, *Makromol. Chem.* **194**, 2279 (1993).

[44] S. Saito, Y. Moteki, M. Nakagawa, F. Horii and R. Kitamaru, *Macromolecules* **23**, 3256 (1990).

[45] S. Brückner, S.V. Meille, P. Sozzani and G. Torri, *Makromol. Chem., Rapid Commun.* **11**, 55 (1990).

[46] J.A. Gailey and R.H. Ralston, *SPE Trans.* **4**, 29 (1964).

[47] G. Bodor, M. Grell and A. Kallo, *Faserforsch. Textil-Tech.* **15**, 527 (1964).

[48] V. Vittoria, *J. Macromol. Sci., Phys.* **B28**, 489 (1989).

[49] P.B. McAllister, T.J. Carter and R.M. Hinde, *J. Polym. Sci., Polym. Phys. Ed.* **16**, 47 (1978).

[50] R. Zannetti, G. Celotti, A. Fichera and R. Francesconi, *Die Makromol. Chem.* **128**, 137 (1969)

[51] R. Zannetti, G. Celotti, A. Fichera and F. Ferrero, *Eur. Polym. J.* **4**,399 (1968).

[52] M. Glotin, R.R. Rahalkar, P.J. Hendra, M.E.A. Cudby and H.A. Willis, *Polymer* **22**, 731 (1981).

[53] P.J. Hendra, J. Vile, H.A. Wills, V. Zichy and M.E.A. Cudby, *Polymer* **25**, 785 (1984).

[54] V. Vittoria, *Polymer* **29**, 1118 (1988).

[55] R. Natale, R. Russo and V. Vittoria, *J. Mater. Sci.* **27**, 4350 (1992).

[56] A. Fichera and R. Zannetti, *Die Makromol. Chem.* **176**, 1885 (1975).

[57] W.K. Busfield and C.S. Blake, *Polymer* **21**, 35 (1980).

[58] D.T. Grubb and D.Y. Yoon, *Polym. Comm.* **27**, 84 (1986).

[59] P.A. Jansson (ed.), 'Deconvolution With Applications in Spectroscopy', Academic Press, p. 40 (1984).

[60] J. Puerta and P. Martin, *Appl. Optics* **20**, 3923 (1981).

[61] P. Martin and J. Puerta, *Appl. Optics* **20**, 259 (1981).

[62] Z. Mencik, *J. Macromolec. Sci., Phys.* **B6**, 101 (1972).

[63] M. Hikosaka and T. Seto, *Polym. J.* **5**, 111 (1973).

[64] P. Corradini, G. Giunchi, V. Petraccone, B. Pirozzi and H.M. Vidal, *Gazz. Chim. Ital.* **110**, 413 (1980).

[65] W.J. O'Kane, R.J. Young, A.J. Ryan, W. Bras, G.E. Derbyshire and G.R. Mant, *Polymer* **35**, 1352 (1994).

CHAPTER FOUR

^{13}C CP/MAS NMR Investigation of the Annealing and Melting Behavior of Spunbonded Isotactic Polypropylene Fabrics

4.1 Introduction

In the previous two chapters, the morphology and annealing behavior of quench-cooled isotactic polypropylene (iPP) films were thoroughly investigated. An understanding of the quench-cooled state is of the utmost importance not only from a fundamental but also from an industrial point of view as many processes involve quench-cooling of the molten polymer. Spun iPP fibers are one such example. The process of fiber spinning involves a rapid decrease in temperature to solidify the molten polymer in the fiber form. The quench-cooling of fibers is performed with room temperature air and is, thus, considerably less rapid than the quenching medium used to form the quench-cooled films described in Chapters 2 and 3. The quenching medium used in the formation of the fibers is not only much warmer than the dry ice/acetone slush but it also has a much lower heat capacity thus reducing the quenching efficiency. However, the substantially reduced size of the sample increases the surface area and allows for a rapid rate of heat loss. At this cooling rate the resulting morphology of spun fibers is expected to possess many similarities with the quench-cooled films.

In the previous chapter, the annealing behavior of quench-cooled iPP films was investigated by solid state NMR spectroscopy. This technique proved to be an excellent method of studying morphological changes that occur at the molecular level within the crystalline phase of iPP. The changes within this crystalline fraction were monitored well into the endothermic transition associated with crystal melting. In addition, excellent correlations were noted with observations made by differential scanning calorimetry (DSC) as well as x-ray and electron diffraction analysis.

The solid state NMR techniques used in the analysis of the annealing behavior of the quench-cooled films will be utilized to investigate the morphology of spun iPP fibers as well as the morphological changes that occur to the crystalline phase as the sample is annealed. It will be shown in this chapter that, unlike the quench-cooled films, a double endothermic transition is observed in the DSC thermogram of iPP spun fibers. Multiple endothermic transitions have been observed previously not only for iPP but also for a variety of other polymers. A brief review of the observations and explanations considered for this phenomenon will be presented.

4.1.1 Multiple Melting Endotherms

The phenomenon of multiple melting endotherms appears to exist with most polymers and to be dependent on the thermal and mechanical history of the sample. Isothermal and non-isothermal crystallization as well as annealing of the existing crystalline morphology of a polymer, under certain conditions, will generate multiple melting behavior. Mechanical deformation as obtained by sample drawing is also known to drastically affect the melting behavior of the resultant morphology.

The phenomenon of multiple melting endotherms has been investigated under various experimental conditions and several well-defined characteristics have been observed. A strong temperature and area dependence of the various peaks on the crystallization temperature has been noted. Furthermore, annealing a sample whose melting behavior is associated with a double melting endotherm affects both the transition temperature and the area of the peaks. The high temperature peak tends to increase in area and possibly shift to higher temperature. The low temperature peak will either decrease in area and shift to lower temperature or increase in area and shift to higher temperature until it joins the high temperature peak.

In the analysis of multiple melting endotherms, a variety of explanations have been proposed that encompass a range of molecular level mechanisms.[1-8] Undoubtedly for specific cases one particular mechanism will be favored over all others. These explanations, however, either deal with the amount of order existing within the crystalline phase of the polymer or with reorganizational processes. The latter either involves perfection of the lamellae during sample heating without melting or lamellar melting and subsequent recrystallization. A brief review of each explanation considered for the phenomenon of multiple melting endotherms is given below.

4.1.1.1 Secondary Crystallization

In semicrystalline polymers, molecular motion in the temperature range between the glass transition temperature and the melting point results in increased structural order through primary and secondary crystallization. Primary crystallization is the formation of the first set of crystals from the melt while secondary crystallization, occurring towards the end of the main process (*i.e.*, primary), refers to changes in the existing structure that produce larger and more perfect crystallites. This process is thought to be the cause of multiple melting endotherms in some polymers under certain thermal conditions.

Mandelkern and co-workers[1] investigated isothermally (at 130 °C) crystallized linear polyethylene that was slowly cooled to room temperature over 24 hours. Upon heating, in addition to the main melting endotherm a small peak was observed at lower temperature due to the melting of crystals formed during the cooling of the samples (*i.e.*, secondary crystallization). In melt crystallized isotactic polystyrene, Lemstra and co-workers[9,10] also observed multiple peaks and the lower temperature peak was thought to originate from secondary crystallization. Similar observations were made by Hybart and Platt[11] for drawn and annealed nylon 6,6.

In a recent investigation of the crystalline order and melting behavior of isotactic polypropylene, samples subjected to an annealing treatment above 160 °C followed by a cooling at 10 °C/min to room temperature also melted with a double endotherm.[12] By recording the annealing, cooling, and subsequent melting thermograms, Guerra, *et al.*[12] clearly showed that the low temperature peak arises from material crystallized during sample cooling. Analogous experimental observations were made previously by Pae and Sauer.[13]

4.1.1.2 Crystallization in Two Different Lattice Structures

As discussed in previous chapters, in iPP several crystalline modifications are known to exist. In addition, these crystalline modifications can co-exist within a given iPP sample, depending on the crystallization conditions and the presence of certain heterogeneities[14-20], and these are known to cause multiple melting behavior. Four melting peaks were found by DSC studies of extruded iPP.[21] It was postulated that the low temperature endotherm was due to the melting of the β-hexagonal crystalline phase which subsequently recrystallized and melted again, giving rise to the second endotherm. The two remaining endotherms were assigned to the melting of the α-monoclinic phase. Others[22,23] have also attributed the multiple melting behavior of iPP to the existence of two different crystal forms.

The mechanism by which β→α conversion occurs in iPP was recently investigated by Fillon and co-workers[24] using thermal analysis as well as optical and electron microscopy. Multiple melting endotherms were interpreted in terms of melting and recrystallization occurring within the β-phase as well as the generation of latent α-phase nuclei within the β-phase from which the β→α conversion occurs.

4.1.1.3 Partial Melting, Recrystallization and Complete Melting

In the analysis of multiple melting endotherms, several authors have described this phenomenon as being due to melting of the existing crystalline morphology followed by recrystallization into a more perfect form that melts at a higher temperature. Partial melting followed by reorganization has been invoked to explain the melting behavior in polyethylene,[4,25] annealed or drawn poly(ethylene terephthalate),[26-29] polystyrene (*i.e.*, melt crystallized[30] and single crystals[31]), some polyamides[32], and isotactic polypropylene.[33-38]

Recrystallization was shown to occur in polyethylene single crystals by cross-linking by γ-irradiation so as to suppress lamellar reorganization during sample heating.[4] Indeed, irradiated samples melted with a single endotherm while unirradiated samples had a pronounced multiple peaked melting pattern attributed to a lamellar thickening process. It was suggested that the annealing process in the temperature range between 118 and 126 °C resulted in crystal thickening without true melting while recrystallization of melted crystals occurred above 126 °C. Mandelkern and Allou[25] also performed differential calorimetric studies of the fusion of single crystals of polyethylene. Upon heating an exothermic process was observed between two endotherms and it was suggested that partial melting followed by recrystallization was the major process that was occurring. Sample cross-linking by γ-irradiation was also performed by Todoki[39] on nylon 6, nylon 6,6, poly(ethylene terephthalate), and polypropylene to show that crystal reorganization is responsible for the double melting endotherms observed in these samples.

High temperature, isothermally crystallized iPP samples were investigated by Petraconne, *et al.*[33] and, through a nitric acid etch[40] of the amorphous phase and the fold surface of crystals, it was shown that recrystallization is the primary reason for the occurrence of a double melting endotherm. After the etching treatment, the melting endotherm presented only one narrow peak whose position was intermediate between that of the two peaks observed before etching. Recrystallization phenomena were conclusively demonstrated to be the reason for the double melting endotherm for samples isothermally crystallized in the temperature range between 135 and 150 °C. The low temperature peak was attributed to the fusion of the original crystals with the actual melting temperature being determined by a competition between melting and recrystallization. The high temperature peak was thought to be due to melting of the recrystallized crystals.

The occurrence of multiple melting endotherms in systems composed of a single distribution of crystal types has been simulated[41,42] under the assumption that melting and recrystallization are occurring as the sample is heated. By combining an initial distribution of melting temperatures with only one maximum and a temperature-dependent crystallization regime, multiple melting endotherms were successfully modeled. Satisfactory agreement between the experimental and simulated curves was found for the melting behavior of poly(butylene terephthalate) without considering additional crystallization from the amorphous regions.[43]

4.1.1.4 Differences in Degree of Crystal Perfection

Differences in the level of order that exists within the crystalline phase of a given polymer system has been invoked to explain its melting behavior. Hoashi and Machizuki[6] investigated the melting behavior of melt crystallized or heat treated linear polyethylene. A double melting endotherm was observed for these samples, the appearance of which depended on the crystallization temperature and on the temperature and time of the heat treatment. Further heat treatment on a sample whose melting behavior indicated a double melting endotherm resulted in a splitting of the lower temperature peak into two peaks, one lower and one higher in temperature relative to the original peak. The results were interpreted in terms of development of higher order within the crystalline fraction associated with the lower melting endotherm that resulted in a higher melting temperature. During this process, partial melting occurred and on cooling less perfect crystals formed with a lower melting temperature.

The melting behavior of 1,4-cis-polyisoprene was investigated by Edwards[44] and the observed double melting endotherm was assigned to two different spherulitic lamellar crystals having different growth rates, lamellar thicknesses, and growth planes. Differences in the degree of crystalline perfection were also invoked to explain the melting behavior of cold-drawn high density polyethylene,[45] annealed poly(ethylene terephthalate),[46] and isothermally crystallized natural rubber.[47]

The level of structural order that exists within the α-monoclinic crystalline phase of iPP was also considered by Corradini and co-workers[48] to explain the melting behavior of isothermally crystallized samples observed at a low sample heating rate. The level of structural order that was considered is related to the level of symmetry existing within the unit cell of this crystalline phase (*i.e.*, disordered state: C2/c; ordered state: $P2_1/c$). It was proposed that, at low sample heating rates a double melting endotherm is observed by DSC if the crystalline phase is associated with the less ordered crystalline form while the more ordered crystalline phase melts with a single peak. Reorganization from the less to more ordered state was postulated to occur at low heating rates for samples with an originally less ordered crystalline phase.

The melting behavior of the α-monoclinic phase of iPP was interpreted by Celli and co-workers[49] in terms of the regime of crystallization.[50] Multiple melting endotherms were observed for samples crystallized in regime III while those crystallized in regime II melted with a single endotherm. Regime III crystallization leads to a less ordered crystalline phase that melts and recrystallizes into a more ordered phase giving rise to multiple melting endotherms. Crystallization in regime II induces a predominantly ordered phase that melts in a single stage. Although this description of behavior is different from the analysis of Corradini and co-workers,[48] the underlying explanation presented in both of these studies is based on the level of order that exists within the crystalline phase and suggests a less ordered to more ordered transformation during sample heating as the main cause for the double melting endotherm.

4.1.1.5 Other Considerations

Several others explanations have been put forward to explain the occurrence the multiple melting endotherms in certain polymer systems. In a study on the melting behavior of isotactic polystyrene and nylon 6,6, Bell and Dumbleton[7] suggested one endotherm was due to the melting of extended chains while the second was due to the melting of chain-folded crystals. A similar suggestion was made by Pals and co-workers[51] in the analysis of stretched polypropylene films. It was postulated that one endotherm was due to the melting of "stretched nuclei material" and the other to less oriented crystals. Kardos and co-workers[52] observed four endotherms in the DSC thermogram of high pressure crystallized polyethylene and suggested that two of these are due to melting of chain extended structures and chain-folded crystals.

Molecular weight fractionation has also been proposed for the occurrence of a double melting endotherm in high density polyethylene.[8] It was assumed that a temperature dependent preferential crystallization of lower and higher molecular weight species occurred during sample annealing which gave rise to molecular weight fractionation. Subsequent melting resulted in the observation of a double melting endotherm.

4.1.2 The Present Work

This brief review of the various explanation that have been proposed for the occurrence of multiple melting endotherms in various polymer systems suggests that there is more than one explanation for this phenomenon. More than one event can occur simultaneously and undoubtedly different behavior exists for different polymer types and under different thermal and mechanical histories within a given polymer system. For example, reorganization within the crystalline phase suggests that different levels of order exist within the polymer crystals so that on heating a disorder to order transformation could be the reorganizational process.

The purpose of this investigation was to examine the double melting endotherm of iPP by monitoring changes within the solid state NMR spectrum as the sample is annealed. It was expected that a correlation could be made between the morphological changes observed by NMR and by DSC. Throughout this chapter, a comparison between the behavior of the spun-bonded fabrics and quench-cooled films will be maintained in an effort to gather information regarding similarities and differences between these two morphologies. A fuller understanding of the solid state NMR spectrum of the α-monoclinic phase of iPP will be achieved not only from the investigation of the spunbonded fabrics but also through a comparison with the NMR behavior of the previously analyzed quench-cooled iPP films.

4.2 Experimental

4.2.1 Sample Preparation

The spunbonded iPP fabric that is under investigation is a commercially available product that was obtained directly from the manufacturer. The following information was provided regarding the manufacturing process. The spunbonded fabrics were prepared with iPP, obtained from Exxon (Exxon 3445), having a melt flow index of 34. It contained a stabilization package specifically targeted for the commercial fiber spinning process.

The fibers were prepared by a melt spinning process in which the molten iPP was extruded, with either a single or twin-screw extruder, through a die having a plurality of orifices extending the full width of the machine. The extruded molten polymer was then solidified by cooling in a quenching fluid which is usually low pressure air. While the fibers were in a partially molten or softened state, a stream of heated high velocity air separate from the quenching fluid was used to lightly draw the fibers. The iPP fibers were collected for characterization following this drawing procedure.

A moving porous surface, such as a continuous belt or wire screen, collected the drawn fibers as a web of entangled fibers, *i.e.*, a nonwoven web. The nonwoven web was then pattern bonded by the application of heat and pressure to form a fabric. The entangled fibers passed between two rolls, one of which is customarily embossed with a characteristic bonding pattern. One or both of these rolls is heated at a single temperature, in the range between 80 and 180 °C, such that optimum bonding is obtained. The applied pressure was also controlled to obtain optimum bonding quality. These bonding conditions were chosen so that partial fusion occurred and the fibers were bonded. Patterns used in thermal bonding generally range so as to cover between 5 to about 30% of the surface area of the nonwoven web. The fabrics investigated in this study had a bond point surface coverage of approximately 25%.

Annealing of the spun-bonded fabric was performed by cutting a strip of fabric (approximately 4 X 3 cm), placing it between two microscope slides and heating the samples under a nitrogen flow in a Mettler FP52 hot stage previously calibrated using high purity standards. The temperature was maintained using the Mettler FP5 temperature controller. The samples were heated to the desired anneal temperature at a heating rate of 20 °C/min and maintained for the desired time interval. It should be noted that the samples reported as a "0 minute anneal" were removed from the hot stage immediately upon attaining the anneal temperature. Following the annealing treatment, the samples were allowed to cool to room temperature using ambient temperature. The annealed samples were subsequently cut into small squares for both thermal analysis and solid state NMR spectroscopy.

4.2.2 Sample Characterization

4.2.2.1 Optical Microscopy

A Nikon Optiphot polarizing microscope equipped with a Cohu video camera was used to view the spunbonded fabric and fibers as well as to monitor the shrinkage of the fabrics that occurs during sample heating. The video image was displayed on a secondary monitor by means of a frame grabber board (PCVision Plus) located on an AT computer which translated the video signal to digital format by defining light intensity intervals on a 256 gray level scale through the use of a software program (Java, purchased from Jandel Scientific). To monitor the shrinkage of the fabrics during heating, the fabrics were placed between microscope slides and then heated in the Mettler hot stage, initially set at a temperature of 140 °C, at a heating rate of 2 °C/min.

Photomicrographs of the fibers and bond points were taken at 25X magnification under cross polarized light using the Nikon Optiphot polarizing microscope equipped with a Nikon 35 mm camera.

4.2.2.2 Differential Scanning Calorimetry

Thermal analysis was performed on either the Perkin Elmer DSC-2C or on the DSC-7C by heating the sample at various scan rates in the temperature range between 0 and 200 °C under a nitrogen flow. The DSC was calibrated for temperature and enthalpy with two high purity standards, namely indium and octadecane. The samples of unannealed spunbonded fabrics were prepared for thermal analysis by punching a hole in the fabrics through the use of a hole puncher and placing 1 to 2 mg of sample in the DSC aluminum pans. This method allowed for excellent sample contact with the DSC sensing head. Thermal analysis on the iPP fibers was performed by cutting the continuous fibers into short lengths and placing 1 to 2 mg in the DSC pans. All thermograms are presented in a mass normalized form.

4.2.2.3 Solid State NMR Spectroscopy

The ^{1}H spin-lattice relaxation times in a rotating frame ($T_{1\rho}$ (^{1}H)), cross polarization/magic angle spinning (CP/MAS) NMR spectra of the purely crystalline phase of iPP and CP/MAS NMR spectra of the interfacial phase of iPP were obtained as described previously in Chapter 3.

4.3 Results and Discussion

4.3.1 Optical Microscopy

The optical micrographs presented in Figure 4.1 exhibit the supermolecular structure of the spunbonded fabrics that are under investigation. An array of fibers possessing a random orientation in any given plane within the non-woven fabric is clearly observed. These fibers have diameters ranging between 19 and 22 μm. In addition, in these micrographs the bond points are clearly observed as the bright diamond shape amidst the array of fibers. These bond points, representing approximately 25% of the total area in these fabrics, were formed by thermal bonding which is a hot calendering process. A close inspection of the bond point in Figure 4.1b, reveals that a certain amount of fiber character is retained within the bond points. This suggests that the heat treatment during the bonding process is of sufficient magnitude only to soften the fibers (with possible partial melting) whereafter compression fuses the fibers. Undoubtedly, a certain amount of annealing of the crystalline phase of the fibers occurs during the bonding process.

4.3.2 Differential Scanning Calorimetry

4.3.2.1 Melting Behavior

A DSC thermogram for the heating of an iPP spunbonded fabric at a heating rate of 20 °C/min is presented in Figure 4.2a. The melting behavior of this sample has a characteristic double endothermic transition. The DSC thermogram for the heating of a previously quench-cooled iPP sample, discussed in Chapter 2, has been included in this figure for purposes of comparison. It is of note that these samples were prepared from the same polymer, *i.e.*, Exxon 3445. Therefore, they have the same physical properties (*e.g.*, molecular weights and degree of isotacticity) but differ in thermal and mechanical histories. The melting transition temperatures and corresponding heats of fusion for the

Figure 4.1 Optical photomicrographs of the spunbonded iPP fabrics at 25x magnification. (a) Middle of fabric (b) Thin edge.

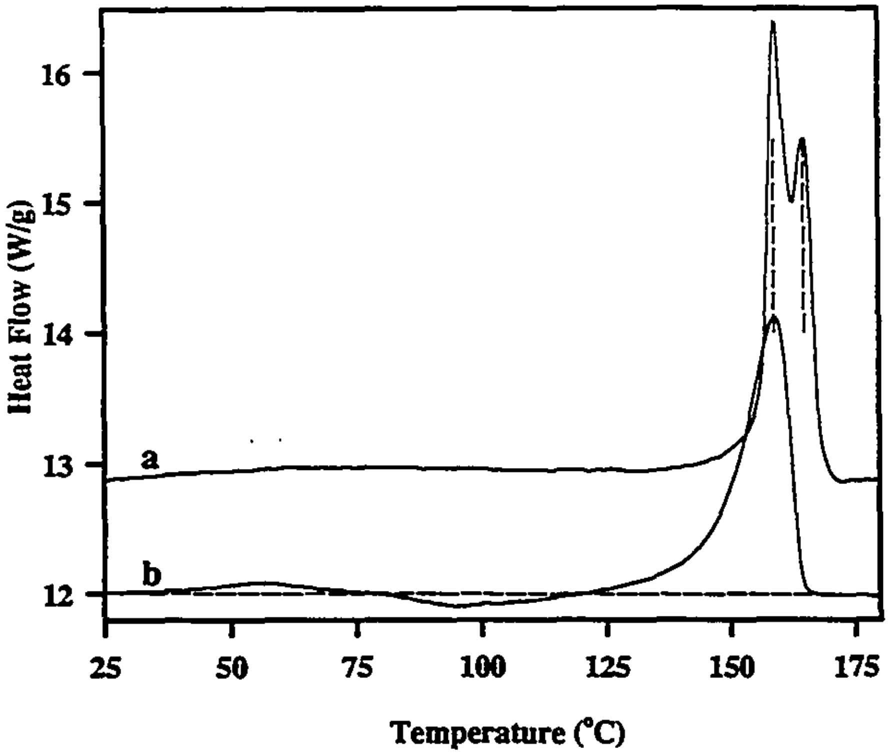

Figure 4.2 DSC thermogram, obtained at a heating rate of 20 °C/min, of (a) a spunbonded iPP fabric and (b) an iPP sample quench-cooled in a dry ice/acetone slush. The horizontal dashed line represents the separation of endothermic and exothermic regions.

above mentioned samples as well as for the quench-cooled films that were maintained at low temperature until thermal analysis, as discussed in Chapter 2, are presented in Table 4.1.

A comparison of these two thermograms (Figure 4.2) reveals that the low temperature peak (LTP) of the double endothermic transition coincides with the melting temperature for the quench-cooled sample as indicated by the vertical dashed line. Although there is agreement in melting temperature between these two samples, the melt transition region for the quench-cooled film is substantially broader than that for the spunbonded fabric as indicated by a somewhat lower peak onset temperature (Table 4.1). This is possibly reflecting a broader distribution in crystal size for the quench-cooled films compared to that of the spunbonded fabric. In addition, there is no evidence of the high temperature peak (HTP) in the thermogram of the quench-cooled film.

Table 4.1: Summary of Endothermic Transitions and Heats of Fusion for Various Polypropylene Samples with Varying Thermal and Mechanical Histories.

Sample	Peak Onset (°C)	Peak Maximum (°C)		ΔH (J/g)
		LTP	HTP	
Quench-cooled Films	146-147	158-160	——	80-83
Quench-cooled Film - Low T	145-147	157-159	——	74-78
Spunbonded Fabrics	153-154	157-159	164-165	92-95

A comparison of the heats of fusion of the various samples listed in Table 4.1 reveals a substantially higher crystallinity of 56±1% in the spunbonded fabrics compared to a crystallinity of 49±1% in the quench-cooled films (46±2% for the quench-cooled films maintained at low temperature prior to thermal analysis). These crystallinities are based on 165 J/g as the heat of fusion for a 100% crystalline iPP sample.[53] This higher level of crystallinity is indicative of the thermal treatment received by the sample during the bonding process. In addition, a substantially higher crystallinity may exist within the iPP fibers themselves compared to the quench-cooled films due to a significant difference in the temperature of the cooling medium. The colder dry ice/acetone slush used in the preparation of the quench-cooled films is more efficient in generating a quench-cooled state.

The exothermic transition between 80 and 120 °C, clearly evident in the thermogram of the quench-cooled film (Figure 4.2), is not observed for the spunbonded fabric. As discussed in Chapter 2, this exothermic transition is associated with recrystallization processes involving perfection of the existing α-monoclinic crystal form to higher levels of order. Since the exothermic transition is not observed for the spunbonded fabric, it would appear that the room temperature crystal structure within the spunbonded fabric is already of a much higher level of order than that of the quench-cooled film. This observation is consistent with the observations regarding crystallinity discussed above.

As discussed in Chapter 2, in the interval between 30 and 75 °C a small endotherm was observed in the thermogram of the iPP quench-cooled films (Figure 4.2b). In the DSC thermogram of the spunbonded fabric, a much broader peak is indicated in the interval between room temperature and approximately 100 °C. However, upon close inspection of the thermogram, it is difficult to determine whether this is simply due to curvature in the baseline or a very broad endothermic peak. In the quench-cooled films, the low temperature endotherm was found to shift to higher temperature upon sample annealing where its onset coincided closely to the anneal temperature. Low temperature annealing of the spunbonded fabric can confirm the existence of this apparent broad peak. Such anneals are reported and discussed further in the following section.

Since the spunbonded fabrics are composed of both bond points and fibers, on first inspection, the double endothermic transition may be attributed to the melting of different crystalline morphologies associated independently with each of these components. However, comparison of the DSC thermogram of the fibers with that for the spunbonded fabric (Figures 4.3 and 4.4) reveals that the melting behavior of the fibers is also characterized by a double endothermic transition which is very similar to that for the spunbonded fabric. This double endothermic transition is observed for both fibers and spunbonded fabrics at heating rates as high as 40 °C/min. Therefore, from the DSC thermograms it becomes evident that the crystal morphologies of the fibers and spunbonded fabric are very similar and that melting of the fibers or bond points is not reflected independently by either of the endothermic peaks.

A comparison of Figures 4.3 and 4.4 indicates that the onset temperature of both endothermic peaks decreases with increasing heating rate. The variation of the observed melting temperature with heating rate has been considered by Miyagi and Wunderlich[54] for several poly(ethylene terephthalate) (PET) samples. In certain PET samples, an increase in the observed melting temperature was noted with increasing heating rate. This behavior was explained on the basis of superheating, *i.e.*, a process whereby a sample is heated faster than the melt-crystal boundary can progress through the sample resulting in unusually high melting temperatures. However, in other PET samples a decrease in the melting temperature was noted with increasing heating rate. This behavior was thought to be consistent with the occurrence of reorganization (*i.e.*, partial melting followed by recrystallization) within the crystalline phase of the PET samples during heating. Since these iPP samples indicate a decrease in melting temperature with increasing heating rate, it appears that reorganization in the crystalline phase is occurring within the time scale of the DSC experiment.

The double endothermic transition observed for these samples may also be due to separate melting of two different lattice structures that co-exist within the crystalline phase

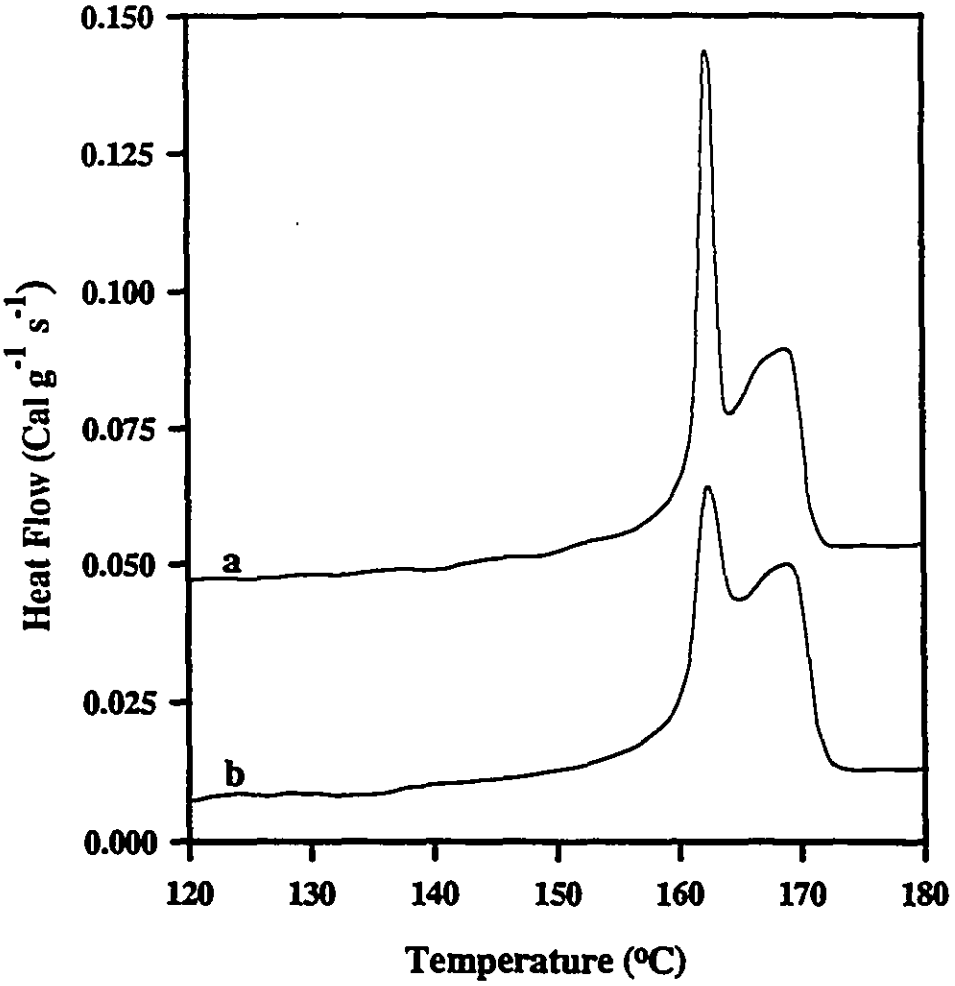

Figure 4.3 DSC thermogram, obtained at a heating rate of 1.25 °C/min, of (a) a spunbonded iPP fabric and (b) spun iPP fibers.

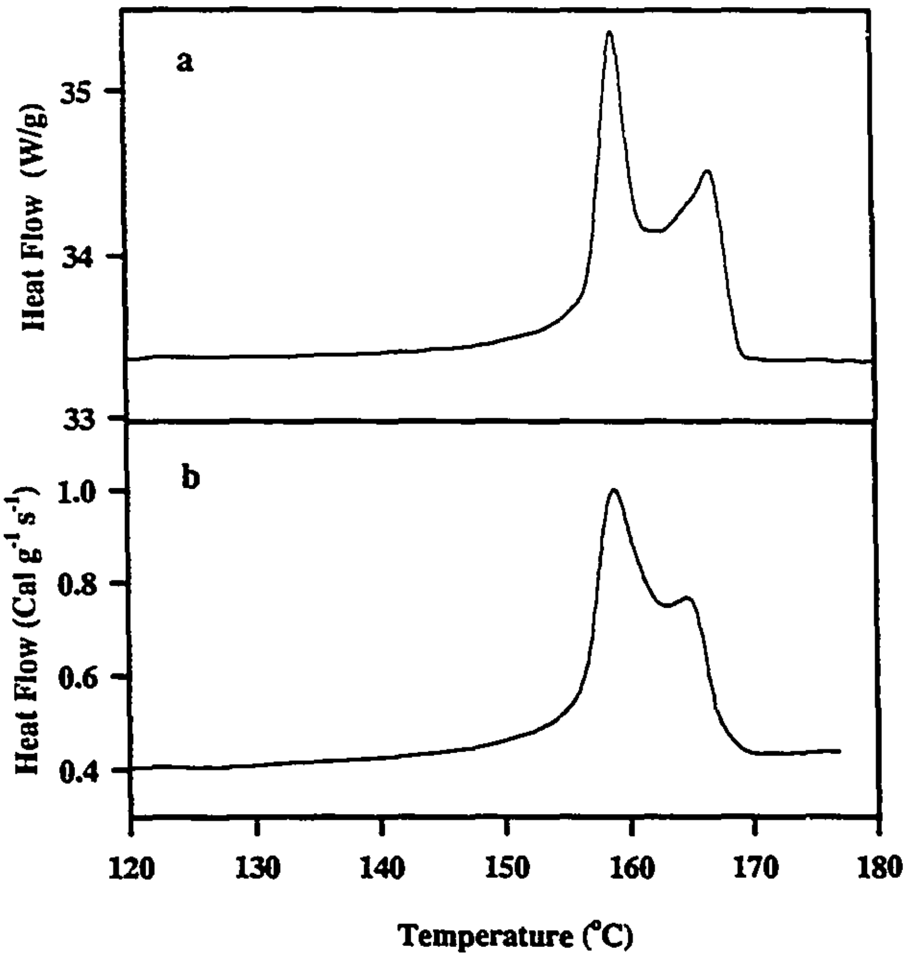

Figure 4.4 DSC thermogram, obtained at a heating rate of 10 °C/min, of (a) a spunbonded iPP fabric and (b) spun iPP fibers.

of the iPP spunbonded fabrics. For example, crystallization during the formation of the iPP fibers or subsequently during thermal bonding could result in the formation of both the α-monoclinic and β-hexagonal crystalline phases. Heating of the iPP samples could then result in melting of the β-hexagonal phase followed by recrystallization into the α-monoclinic phase which melts at higher temperature thus resulting in a double endothermic transition. Such behavior has been investigated by many authors[24,55-60] and the two phases have been shown to have significantly different melting temperatures. However, the β to α growth transition is known to occur at approximately 140 °C while the LTP of the double endothermic transition, discussed previously, occurs at a substantially higher temperature (*i.e.*, 157-159 °C). In addition, the melting temperature of the quench-cooled film, which was shown to be composed of only the α-monoclinic crystalline phase, coincides exactly with the LTP of the spunbonded fabrics suggesting that this melting peak is associated with the α-phase. Therefore, the double endothermic transition observed for this sample is not a consequence of a β to α growth transition.

4.3.2.2 Annealing Behavior

Low temperature annealing of the spunbonded fabric yields changes to the DSC thermogram that are very similar to the effects that were observed for the quench-cooled films following similar thermal treatment. The DSC thermograms obtained upon heating of the spunbonded fabric following low temperature anneals for 40 minutes, in the temperature range between 50 and 120 °C, are presented in Figure 4.5. A small endothermic peak whose position is almost coincident with the anneal temperature is clearly observed. This behavior confirms that the apparently very broad peak in the DSC thermogram of the spunbonded fabric that was not annealed (Figure 4.2a) is not associated with baseline curvature but reflects an endothermic transition. This small peak

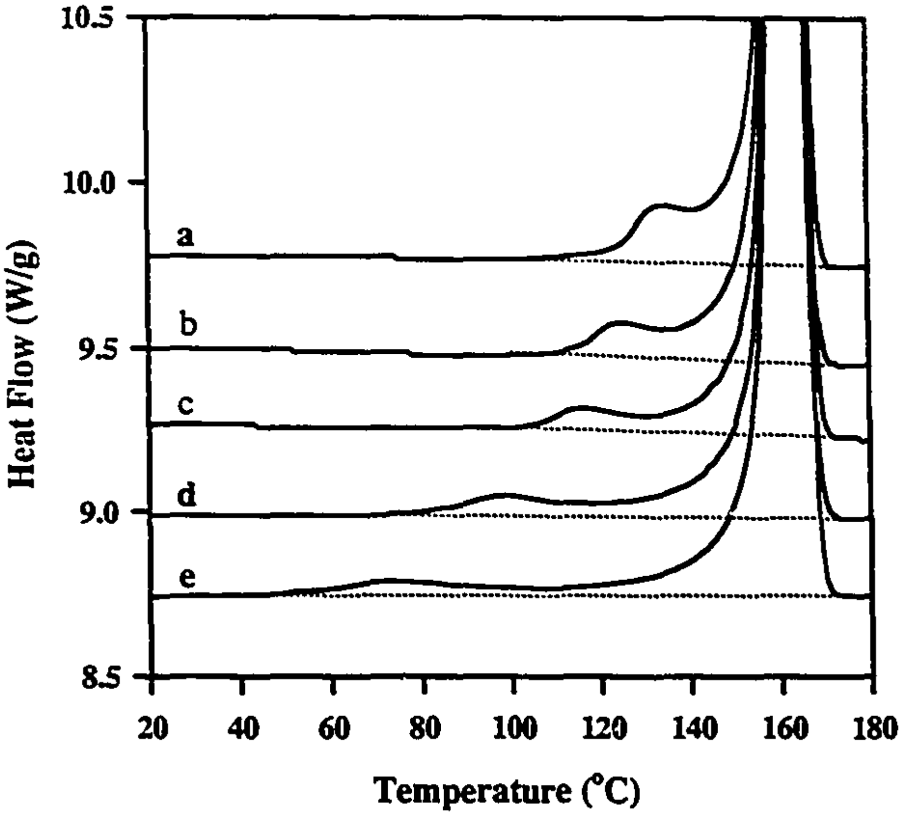

Figure 4.5 DSC thermograms obtained upon heating, at a rate of 20 °C/min, of iPP spunbonded fabrics that were previously annealed for 40 minutes at (a) 120, (b) 110, (c) 100, (d) 80, (e) 50 °C.

behaves similarly to that observed for the quench-cooled films and is clearly associated with the annealing treatment. As mentioned in Chapter 2, this endotherm probably reflects some form of premelting transition.

High temperature annealing of the spunbonded fabric was performed at temperatures between 120 and 165 °C for time intervals between 0 and 60 minutes, as described in the Experimental section. Representative thermograms for samples annealed for 0 and 60 minutes are presented in Figures 4.6 and 4.7, respectively. The former demonstrate, to a certain extent, the changes that occur during sample heating during a typical DSC investigation. Upon annealing, a gradual conversion from a double endotherm to a single melting peak is clearly evident for both 0 and 60 minute anneal times. However, this transformation is characterized by different behavior within three different temperature regions, as seen in Figure 4.8. At anneal temperatures below 140 °C, the endotherms are unaffected, *i.e.*, the low temperature peak (LTP) remains at *ca.* 157 °C while the high temperature peak (HTP) is at *ca.* 164 °C. Annealing at temperatures between 150 and 156 °C, results in a shift of the LTP towards higher temperature while the position of the HTP remains essentially unchanged at 164 °C. For the samples annealed for the longer time the progression of the LTP towards higher temperature occurs at lower temperatures and at any anneal temperature within this region a much higher melting temperature is observed for the LTP. Consequently, the double endotherm character persists until higher anneal temperatures for the samples annealed for 0 minutes. As the LTP moves to higher temperature, the HTP appears as a shoulder on the high temperature side of the endotherm, thus making it difficult to judge not only the actual transition temperature of the HTP but also possible changes in peak area. However, visual inspection suggests that the annealing treatment results in a decrease in the area of the HTP with a concomitant increase in the area of the LTP.

Annealing at temperatures greater than *ca.* 156 °C results in thermograms having a single melting endotherm. When a single endotherm is first observed, the temperature of this transition is very close to that of the HTP in the unannealed sample but this single endotherm then shifts to higher temperature upon annealing. In addition, for a given anneal temperature the melting temperature is substantially higher for the samples

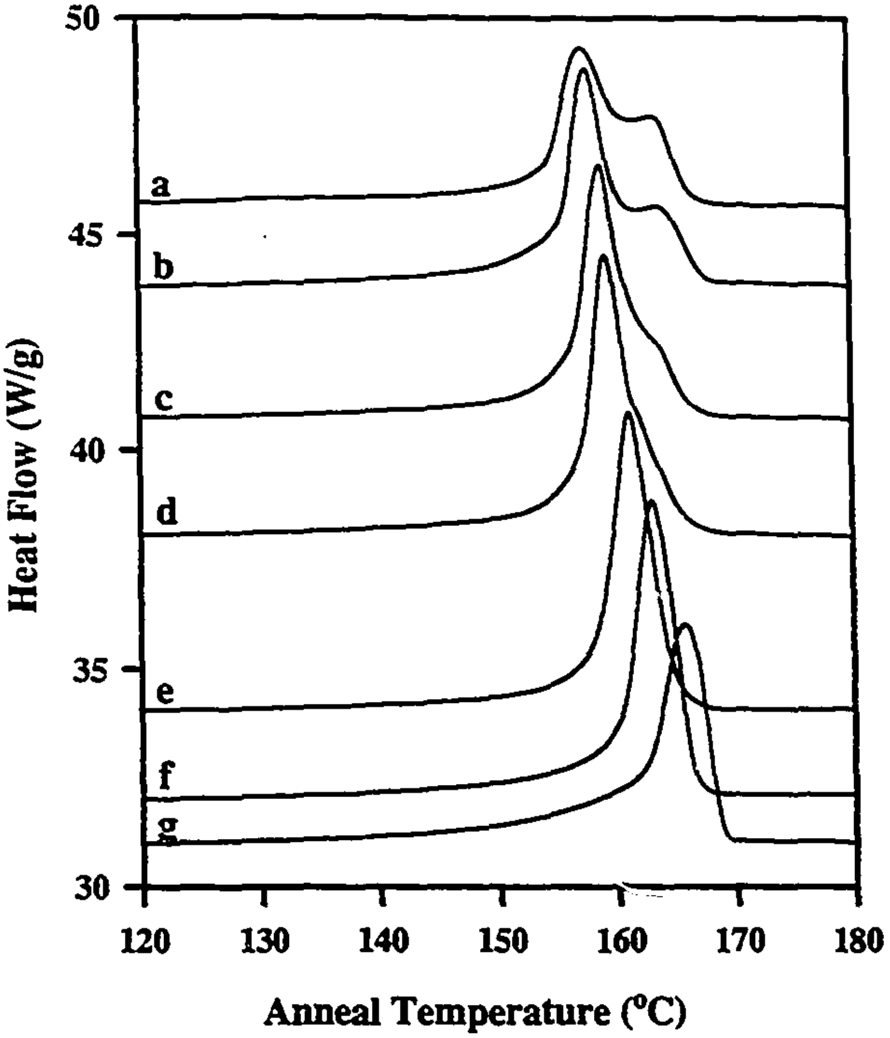

Figure 4.6 DSC thermograms obtained upon heating, at a rate of 20 °C/min, of iPP spunbonded fabrics that were previously annealed for 0 minutes at (a) 130, (b) 150, (c) 152, (d) 154, (e) 156, (f) 158, (g) 159 °C.

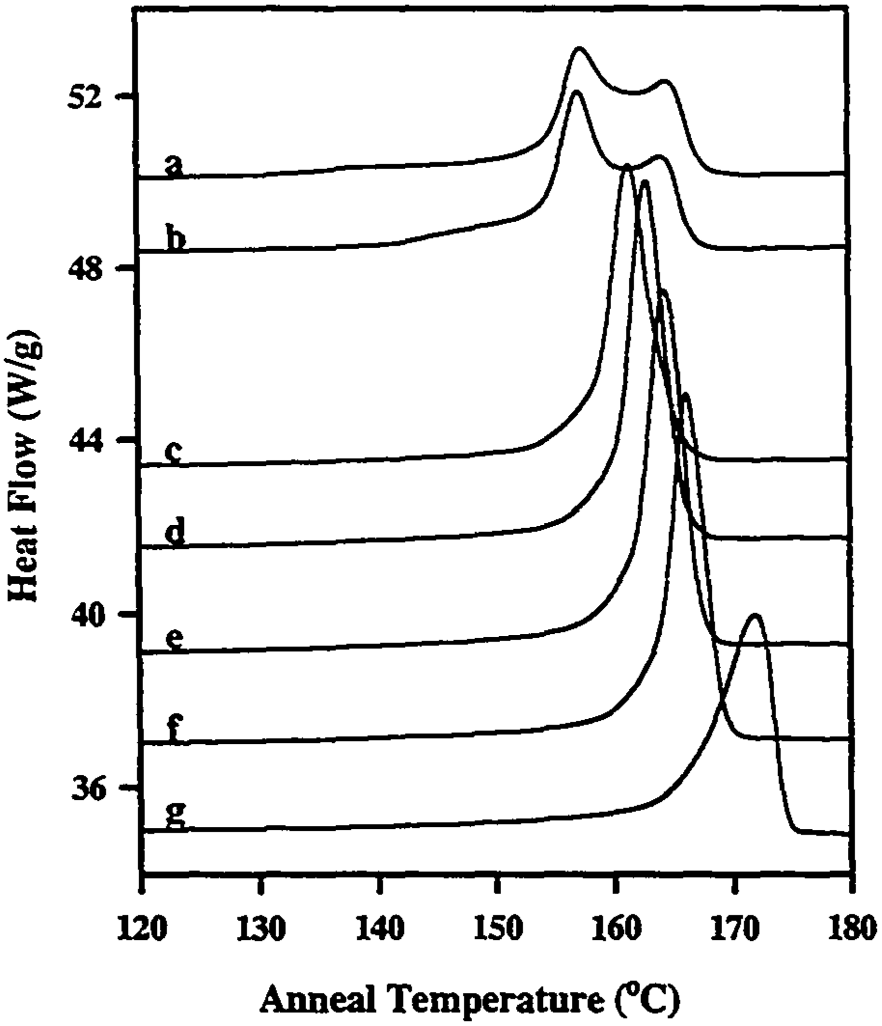

Figure 4.7 DSC thermograms obtained upon heating, at a rate of 20 °C/min, of iPP spunbonded fabrics that were previously annealed for 60 minutes at (a) 130, (b) 140, (c) 152, (d) 154, (e) 156, (f) 158, (g) 161 °C.

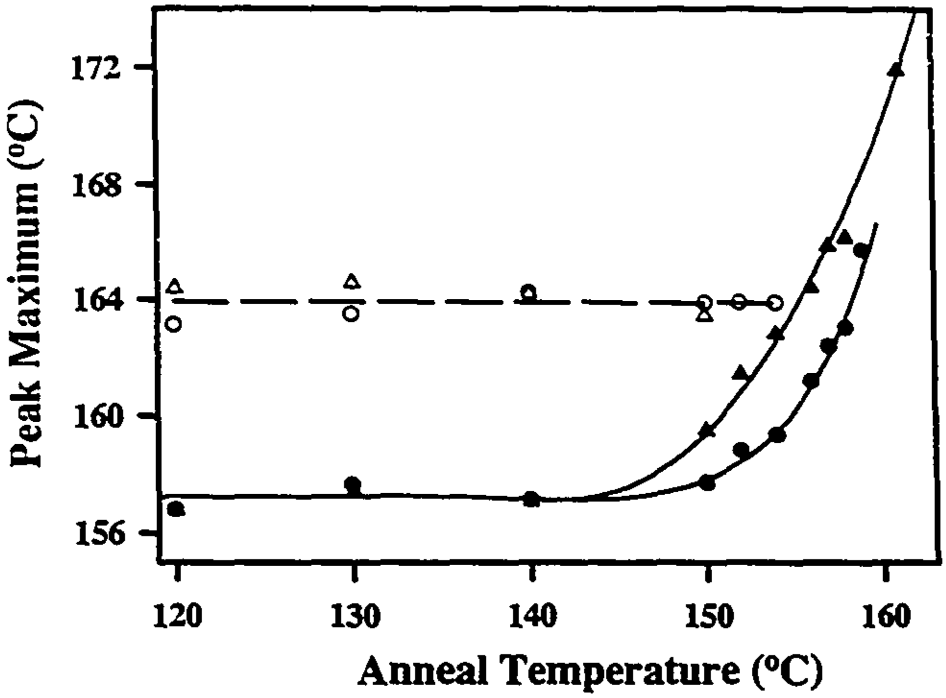

Figure 4.8 Effect of anneal temperature on the position of the low temperature peak (filled symbols) and high temperature peak (open symbols). Circles indicate 0 minute anneals and triangles indicate 60 minute anneals.

annealed for the longer time period. To verify this, an appropriate peak deconvolution would have to be performed on these thermograms. However, since the line shape for a DSC thermogram is unknown this task is presently impossible.

The measured heats of fusion (ΔH) for the spunbonded fabrics annealed at various temperatures are presented in Figure 4.9. A gradual increase in the measured heat of fusion, or sample crystallinity, is observed as a function of anneal temperature. However,

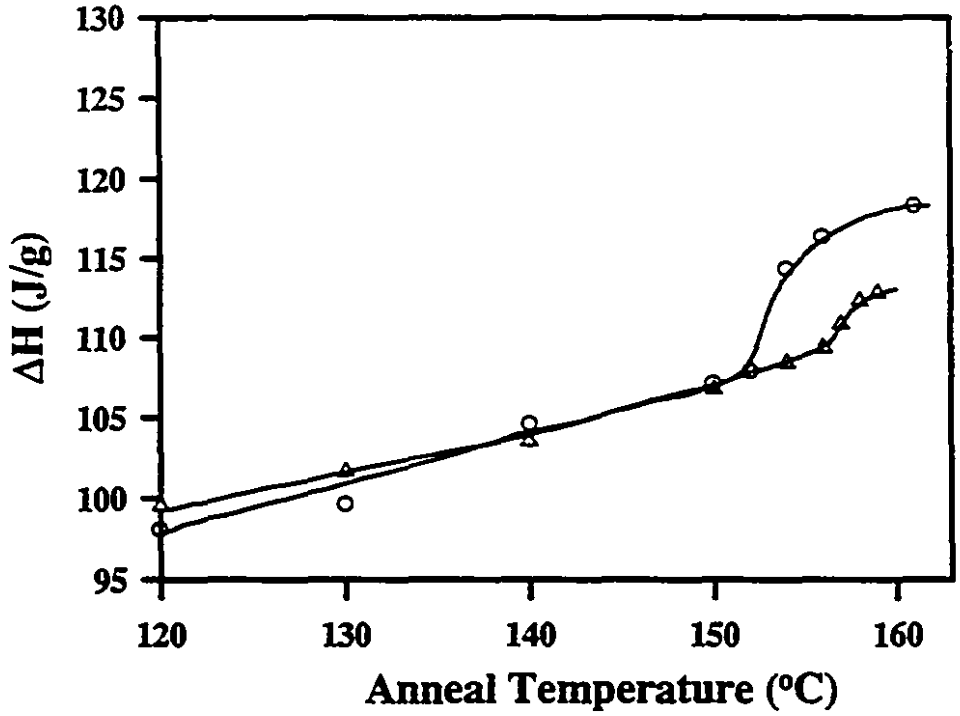

Figure 4.9 Effect of anneal temperature on the measured heat of fusion, ΔH. The circles indicate 60 minute anneals and triangles indicate 0 minute anneals.

at high anneal temperatures a rapid increase in the heat of fusion is observed to an extent that is dependent on the anneal time. This larger heat of fusion suggests that recrystallization has occurred in the samples thus inducing higher sample crystallinities. Indeed, the rapid increase in heat of fusion occurs concomitantly with the observation of a single melting endotherm. In samples annealed for 0 minutes, the sudden change in the heat of fusion begins at 156 °C. This is also the last temperature for which the HTP is discernible as a shoulder on the high temperature side of the LTP (Figure 4.6). The thermogram for the spunbonded fabric annealed at 157 °C represents the first observation of a single endotherm for the samples annealed for 0 minutes, which is consistent with the observation of an increased heat of fusion. In the case of the samples annealed for 60 minutes, the first temperature at which a single endotherm is observed occurs at approximately 154 °C, which is also consistent with the temperature at which there is an increase in the heat of fusion.

4.3.3 Solid State NMR Spectroscopy

In the previous chapter, a ^{13}C cross polarization/magic angle spinning (CP/MAS) NMR pulse sequence was introduced which incorporates a delay period with a reduced spin locking field prior to cross polarization. This pulse sequence exploited the differences in $T_{1\rho}$ (^{1}H) between the various phases of iPP (*i.e.*, crystalline, interfacial and amorphous) for the exclusive observation of the crystalline component. In addition, appropriate subtraction of spectra allowed for the observation of the interfacial and amorphous components. This technique proved to be an excellent method for the study of morphological changes that occur within the crystalline phase of iPP as a function of sample anneal. This solid state NMR technique is further exploited in the following section to investigate the crystalline phase of the iPP spunbonded fabric as well as possible morphological changes that occur within this crystalline fraction as the sample is annealed. The NMR findings will then be correlated with the observations made by DSC to develop an explanation of the double endothermic transition.

4.3.3.1 Sample Morphology

The CP/MAS NMR spectra of only the crystalline phase of both iPP fibers and spunbonded fabric were obtained using the reduced spin-locking field delayed contact time pulse sequence described in Chapter 3. The methine and methyl region of the CP/MAS spectra of the crystalline phase of these iPP samples and that for the quench-cooled films are presented in Figure 4.10. The peak deconvolution of the methine and methyl

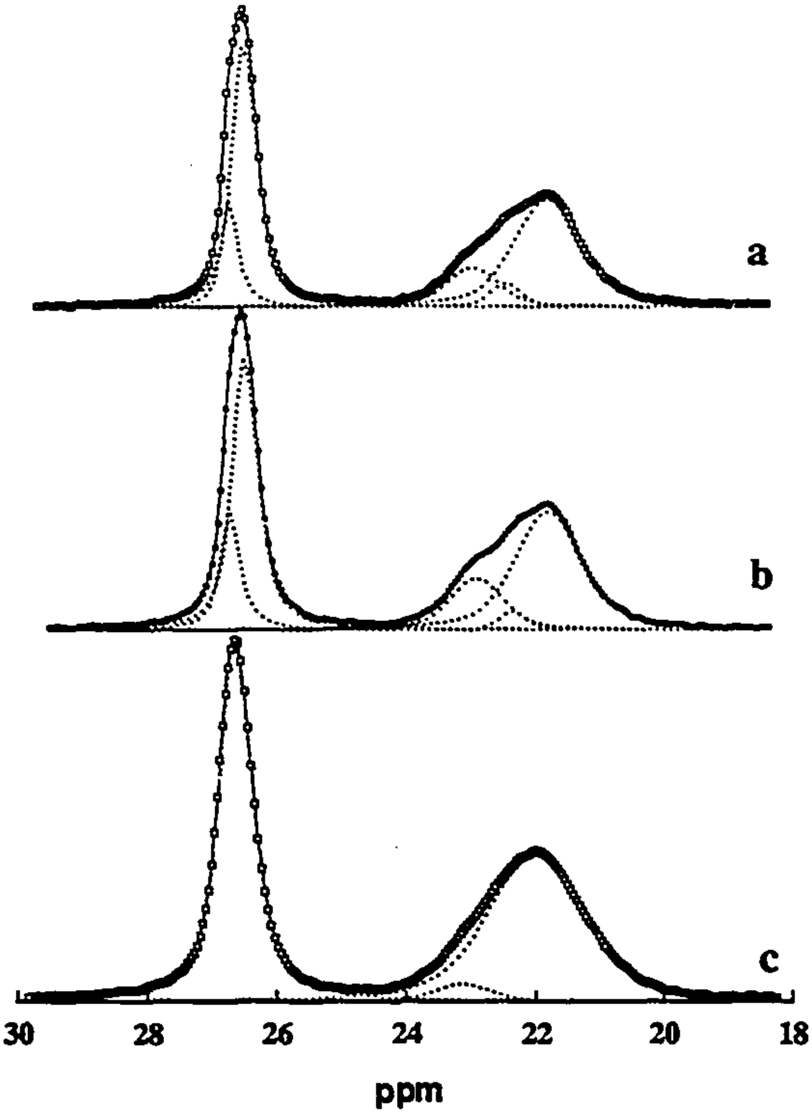

Figure 4.10 Deconvolutions obtained for the methine and methyl resonances of the ^{13}C CP/MAS NMR spectra of the purely crystalline phase of (a) spun-bonded fabrics (b) spun fibers (c) quench-cooled films.

resonances of the three spectra was performed and the results are also presented in Figure 4.10. These deconvolutions were performed using a Voigt line shape to obtain the relative areas of the individual lines, as described in Chapter 3.

It is apparent from Figure 4.10 that the crystalline morphologies of the iPP fibers and spunbonded fabric are substantially better developed than that of the quench-cooled films. Indeed, both the methine and methyl resonances reveal splitting patterns which are similar to those obtained for the quench-cooled films after they were annealed in the temperature range between 100 and 115 °C for one hour. Three peaks were obtained in the deconvolution of the methyl resonance while the methine reveals two peaks with intensity distributions very similar to those for the annealed quench-cooled films (Figure 3.6). This resonance splitting pattern is not only consistent with a more developed crystalline morphology but is also in accord with the DSC thermogram for these samples. Indeed, the exothermic transition in the temperature region between 80 and 120 °C that is associated with the development of improved order within the existing α-monoclinic crystalline phase is not observed for these samples. Both the solid state spectra as well as the DSC analysis concur that the crystalline morphology of the fibers is similar to that of a quench-cooled system thermally treated in the temperature region between 100 and 115 °C.

The chemical shifts, peak widths and peak areas for each of the peaks in the methyl resonance as obtained by peak deconvolution for the three samples as presented in Figure 4.10 are listed in Table 4.2. It is clear from the results presented in Chapter 3 that the unit cell environment associated with the midfield methyl peak is the most sensitive to the level of order which exists within the crystalline phase of iPP. This peak increases in intensity as higher levels of order are attained within the crystalline phase of iPP. The midfield methyl resonance is clearly observed in the iPP fibers and spunbonded fabric while it is

Table 4.2: Results Obtained for the Deconvolution of the Methyl Resonance of the ^{13}C CP/MAS NMR Spectrum of the Crystalline Phase of iPP Fibers, Spunbonded Fabrics and Quench-cooled Films.

Sample and Peak Description	Chemical Shift (ppm)	Peak Width (ppm)	% Area
Spunbonded Fabric			
Downfield Methyl Peak	23.10	0.92	10.5
Midfield Methyl Peak	22.59	0.56	3.8
Upfield Methyl Peak	21.93	1.21	37.2
Fibers			
Downfield Methyl Peak	23.11	0.94	12.6
Midfield Methyl Peak	22.56	0.46	2.2
Upfield Methyl Peak	21.99	1.19	36.1
Quench-cooled Films			
Downfield Methyl Peak	23.12	0.99	3.4
Midfield Methyl Peak	——	——	——
Upfield Methyl Peak	21.99	1.78	48.8

clearly absent in the quench-cooled films. The percent area of this peak is consistent with the results obtained for the quench-cooled films that were annealed at approximately 100 °C. In addition, the midfield methyl resonance for the spunbonded fabric is larger than for the fibers suggesting that, on average, a higher level of order exists within the crystalline phase of the spunbonded fabric. Since the formation of the bond points involves, in part, a thermal treatment of the fibers, higher order is expected and is reflected in the midfield methyl resonance. All of the other parameters listed in Table 4.2 are consistent with previously observed values (*i.e.*, the annealed quench-cooled films discussed in Chapter 3) as well as with the deconvolution results obtained for annealed iPP spunbonded fabrics to be presented in the following section.

The ^{1}H spin-lattice relaxation times in a rotating frame ($T_{1\rho}$ (^{1}H)) for the iPP fibers, spunbonded fabrics and quench-cooled films measured at ambient temperature are presented in Table 4.3. As discussed previously, the fit of the relaxation data requires two $T_{1\rho}$ (^{1}H) components, *i.e.*, a long and a short component. As developed in Chapter 3, the long component arises from a phase that is most hindered in molecular motion (*i.e.*, the crystalline) phase while the short component can be ascribed to a more mobile phase, the interfacial component. A comparison of the long ^{1}H $T_{1\rho}$ component of the various samples reveals a substantially longer relaxation time for the iPP fibers and spunbonded fabrics compared to that of the quench-cooled films. This suggests that the crystalline phase of these samples is more rigid and restricted to molecular motion. A more rigid crystalline phase suggests that a higher level of order exists within these samples. In addition, the relaxation data suggest that the crystalline phase of the spunbonded fabrics is more restricted than that of the fibers only as evidenced by longer relaxation times. However, the difference in mobility within the crystalline phase between these two samples is small. These results are consistent with previous DSC and CP/MAS observations.

The NMR analysis of the crystalline morphology of both the iPP fibers and spunbonded fabrics reveals that, on average, the spunbonded fabrics possess a slightly better developed crystalline phase. However, the differences between these two samples is minor. Therefore, the analysis regarding the morphological changes that occur during sample annealing were performed only for the spunbonded fabrics. All of the morphological data suggest that the iPP fibers should behave in the same manner as the spunbonded fabrics. In addition, since the DSC observations are similar for these samples, the conclusions regarding the double endothermic transition that are reached from the NMR analysis can also be extended to the iPP fibers.

Table 4.3: ^{1}H Spin-Lattice Relaxation Times in a Rotating Frame for iPP Fibers, Spunbonded Fabrics and Quench-cooled Films at Ambient Temperature.

Sample	$T_{1\rho}$ (^{1}H) (ms)					
	Methylene		Methine		Methyl	
	Long	Short	Long	Short	Long	Short
Bonded Fabric	28.7	6.5	28.6	5.2	27.4	3.9
Fibers	25.9	6.0	24.9	4.4	24.6	3.6
Quench-cooled Films	19.0	4.3	19.2	3.9	18.6	2.9

4.3.3.2 Annealing Behavior by $T_{1\rho}$ (^{1}H) Analysis

The ^{1}H spin-lattice relaxation times in a rotating frame ($T_{1\rho}$ (^{1}H)) for iPP spunbonded fabrics thermally annealed at temperatures between 120 and 165 °C for both 0 and 60 minutes (filled and open circles, respectively) are presented in Figure 4.11. The values presented in this figure represent the average of the individual relaxation times measured for the methylene, methine, and methyl resonance since $T_{1\rho}$ (^{1}H) values in solids usually represent an average value of the relaxation behavior over the ensemble of protons. This is due to the strong dipolar coupling between the protons that gives rise to efficient spin diffusion thus creating a mechanism to average nonequilibrium magnetization in any part of the proton spin system. Indeed, essentially the same relaxation time was

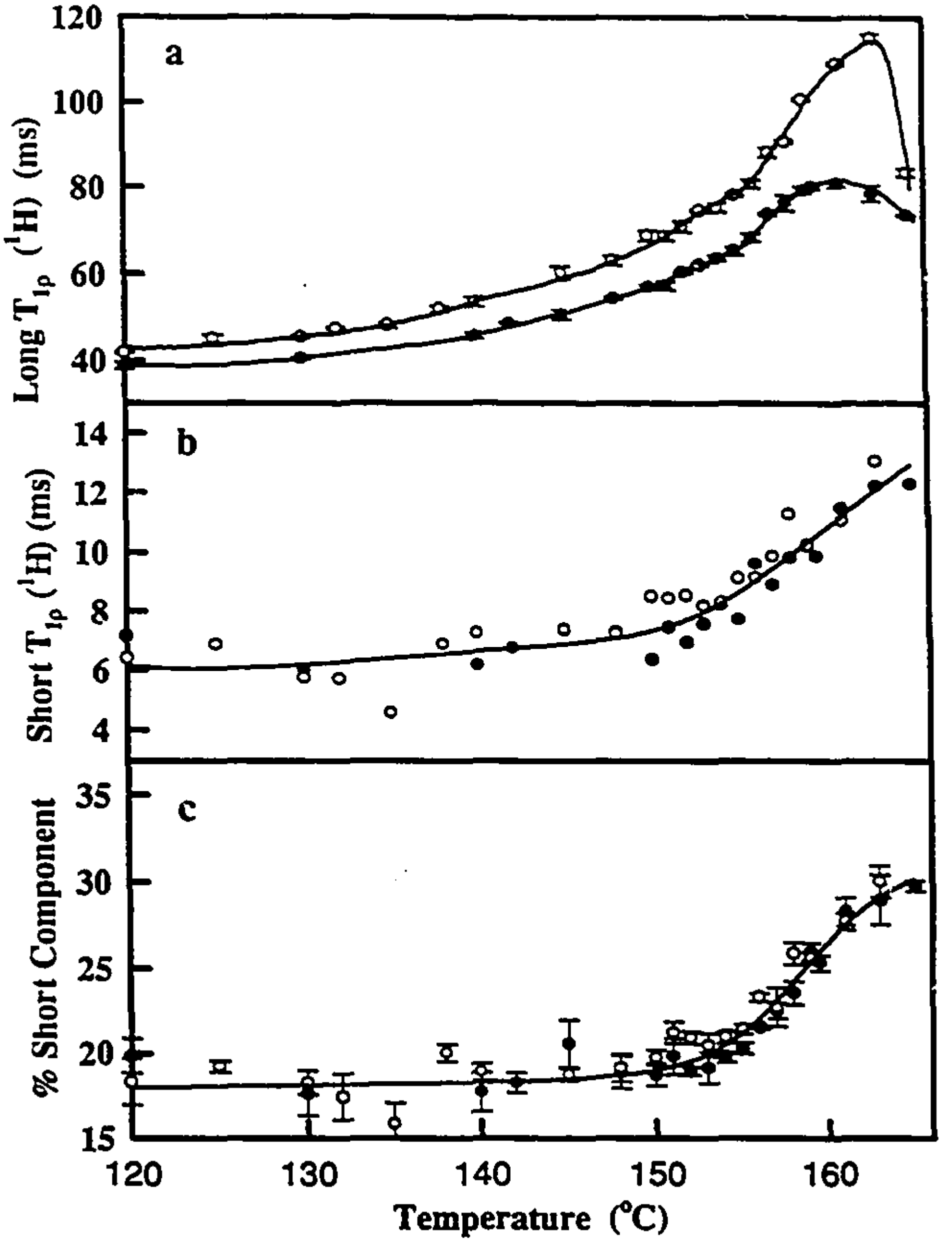

Figure 4.11 The effect of sample anneal on the spin-lattice relaxation time, $T_{1\rho}$ (^{1}H). Open circles indicate 60 minute anneals and filled circles indicate 0 minute anneals. (a) Long component (b) Short component (c) Percent short component.

obtained for each carbon. As was found with previous relaxation data, two relaxation components were measured. The times for both components are presented in Figure 4.11. In addition, the percentages of the phase associated with the short relaxing component in the annealed samples as derived from the amplitude associated with the double exponential decay curve used in fitting the measured intensity, are also presented (Figure 4.11c).

The times associated with the long relaxing component, which is associated with the crystalline phase of iPP, were found to increase with increasing anneal temperature for both anneal times (Figure 4.11a). For the samples annealed for 0 minutes, to a certain extent this increase corresponds to the changes that occur within the crystalline phase when this sample is heated during a typical DSC experiment. Morphological changes occur within the crystalline phase of iPP in the time interval defined by a 20 °C/min heating rate since the sample was cooled immediately after it attained the anneal temperature, as is evident from the relaxation data. It is of note that in certain temperature ranges changes to the crystalline phase occur within the time elapsed in simply raising the temperature by as little as 1 °C. Since the relaxation times measured for this component increase with increasing anneal temperature, it must be concluded that a re-organization occurs within the crystalline phase that results in an increased perfection and, consequently, a more hindered mobility. In addition, for all of the anneal temperatures investigated, the times for the long relaxing component were found to be substantially longer for the samples annealed for 60 minutes than for those annealed for shorter times. Therefore, the re-organization that occurs within the crystalline phase is not only dependent on the anneal temperature but also on the anneal time. This suggests that the re-organization that occurs during a typical DSC experiment should be dependent on the sample heating rate, since slower heating rates allow more time between "anneal" temperatures.

At the highest anneal temperatures, a decrease is observed in the values of the long relaxing component. This decrease in the relaxation time suggests that a significant portion of the crystalline phase has melted during the sample anneal. As the sample is returned to room temperature this molten fraction crystallizes non-isothermally and adopts a less perfect form. This results in a certain percentage of the crystalline phase with a decreased level of order and, therefore, increased mobility which in the subsequent NMR analysis yields a shorter ^{1}H spin lattice relaxation time. While a plateau is observed at temperatures between 159 and 163 °C in the values of the long relaxing component for the samples annealed for 0 minutes, those for the samples annealed for 60 minutes continue to increase. However, at anneal temperatures greater than 163 °C, a very rapid decrease in $T_{1\rho}$ (^{1}H) is observed for the samples annealed for 60 minutes. This anneal temperature coincides with the HTP observed by DSC, *i.e.*, with temperatures associated with the complete melting of the crystalline fraction.

A closer inspection of the increases in the times of the long relaxing component as the sample is annealed at continuously higher temperature reveals an apparent change in the rate of increase at anneal temperatures greater than approximately 156 °C. The values of the long $T_{1\rho}$ (^{1}H) increase more rapidly at the higher anneal temperatures. This is particularly evident for the samples that were annealed for 60 minutes. It should be noted that the temperature at which this apparent change in rate occurs coincides exactly with the temperature for which a single melting endotherm is first observed by DSC in the annealed spunbonded fabrics. In addition, the rate discontinuity occurs at a temperature (156 °C) which is very close to the maximum melting temperature of the LTP as observed by DSC for the spunbonded fabrics that were not annealed. A faster increase in the values of the long $T_{1\rho}$ (^{1}H) suggests that the crystalline fraction within this sample changes more rapidly to a level of higher order at these anneal temperatures.

The variation in the short relaxing component with anneal temperature is presented in Figure 4.11b. As with the long relaxing component, the values reported for these relaxation times are also an average of the individual relaxation times obtained for the methylene, methine, and methyl carbons. Although a substantial uncertainty, ranging from 10 to 20%, is associated with the measured values of this short relaxing component, there is no doubt about the increase in this relaxation time at anneal temperatures greater than 152 °C. This increase in relaxation times occurs concomitantly with the changes observed for the long relaxing component discussed above. The mobility of the interfacial phase, which is described by the short relaxing component, is reduced at the higher anneal temperatures. This reduction in mobility occurs in conjunction with an increase in the total fraction of the sample that is in this phase, *i.e.*, in the interfacial phase, since the percentage of the short relaxing component also increases at high temperature (Figure 4.11c). These results indicate an increase in the total amount of interfacial material which suggests an increase in the total number of chain folded crystals within the sample morphology. This increase in the interfacial component must come from the completely amorphous phase or from extended chains since an increase in the percent crystallinity is noted by DSC for samples annealed in this temperature region. A decrease in the mobility of the interfacial component suggests possible segregation of material previously present within the crystalline phase to the interfacial regions.

4.3.3.3 Annealing Behavior of the Purely Crystalline Phase of iPP

The ^{13}C CP/MAS NMR spectra of the purely crystalline phase of the iPP spunbonded fabrics annealed at temperatures between 120 and 163 °C for 0 and 60 minutes are presented in Figures 4.12 and 4.13, respectively. It is evident that upon annealing the intensities of the downfield peak of the methylene and methine carbon resonances increase with a concomitant decrease in intensity of the upfield peak. As observed for the quench-cooled films, three peaks are clearly observed within the methyl

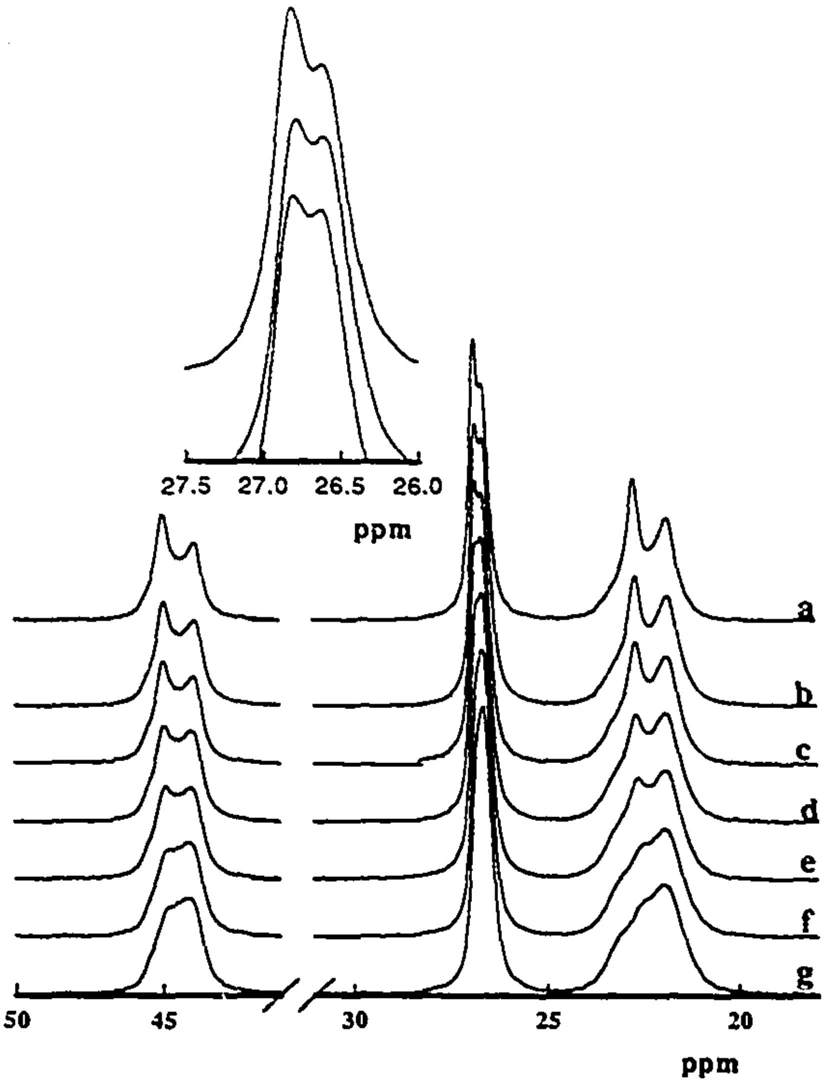

Figure 4.12 ^{13}C CP/MAS NMR spectra of the purely crystalline phase of the spunbonded iPP fabrics annealed for 0 minutes at various temperatures. The spectra were obtained by reducing the ^1H spin locking field for a time interval, τ=15 ms, prior to cross polarization. (a)159 °C, (b)158 °C, (c)157 °C, (d)154 °C, (e)150 °C, (f)140 °C, (g)130 °C.

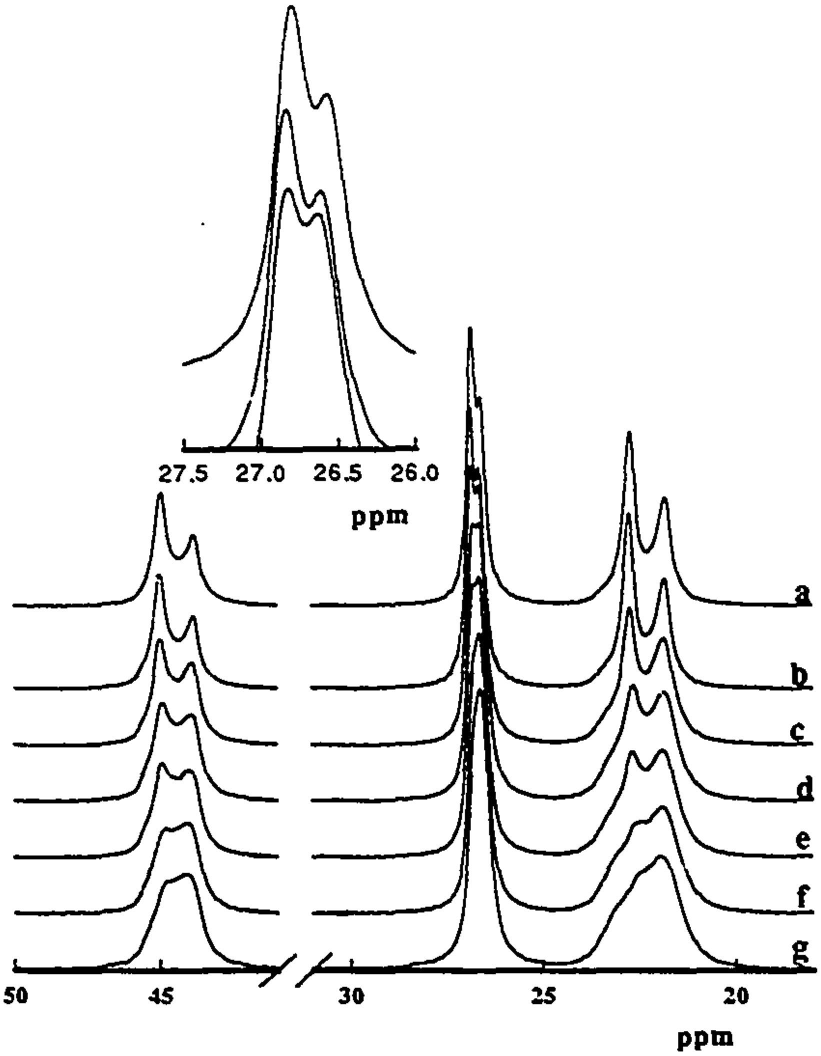

Figure 4.13 ^{13}C CP/MAS NMR spectra of the purely crystalline phase of the spunbonded iPP fabrics annealed for 60 minutes at various temperatures. The spectra were obtained by reducing the ^1H spin locking field for a time interval, τ=15 ms, prior to cross polarization. (a)163 °C, (b)161 °C, (c)158 °C, d)154 °C, (e)150 °C, (f)140 °C, (g)130 °C.

carbon resonance. Upon annealing, an increase in intensity of the midfield methyl resonance is observed with a concomitant decrease in intensity of both the upfield and downfield peaks. The changes that occur to the CP/MAS spectrum of the spunbonded fabric upon annealing are very similar to those that were observed for the quench-cooled films. The distribution of intensities within a given resonance varies in a manner very similar to what was described for the quench-cooled films and tends towards the expected splitting pattern indicative of the α-monoclinic crystalline phase.

As seen in Figure 4.12, morphological changes to the crystalline phase of the spunbonded fabric even occur readily in samples during the time interval required to attain the indicated anneal temperature, *i.e.*, in the samples labeled "0 minutes". Changes within the crystalline phase, as evidenced by multiple peaks within a given carbon resonance, occur simply during the heating of the sample to the desired annealing temperature (*i.e.*, at 20 °C/min). Therefore, changes to the crystalline phase occur within the time elapsed in raising the temperature by as little as 1 °C. Since the annealed samples are developing multiple peaks within a given resonance, which is characteristic of a more developed crystalline phase, it can be concluded that some re-organization is occurring within the crystalline phase which results in increased perfection within this phase while the sample is heated. The changes in the CP/MAS spectra concur with the increased values for $T_{1\rho}$ (^{1}H) discussed previously.

Deconvolution was performed on the methyl and methine resonances of the spectra of the various annealed spunbonded fabrics in the same manner as was described for the spectra of the quench-cooled films. The changes in the area of the three peaks within the methyl resonance for the samples annealed for 0 and 60 minutes are presented in Figures 4.14 and 4.15, respectively. Indeed, an increase in the area of the midfield methyl resonance is clearly observed with a concomitant decrease in the areas of both the

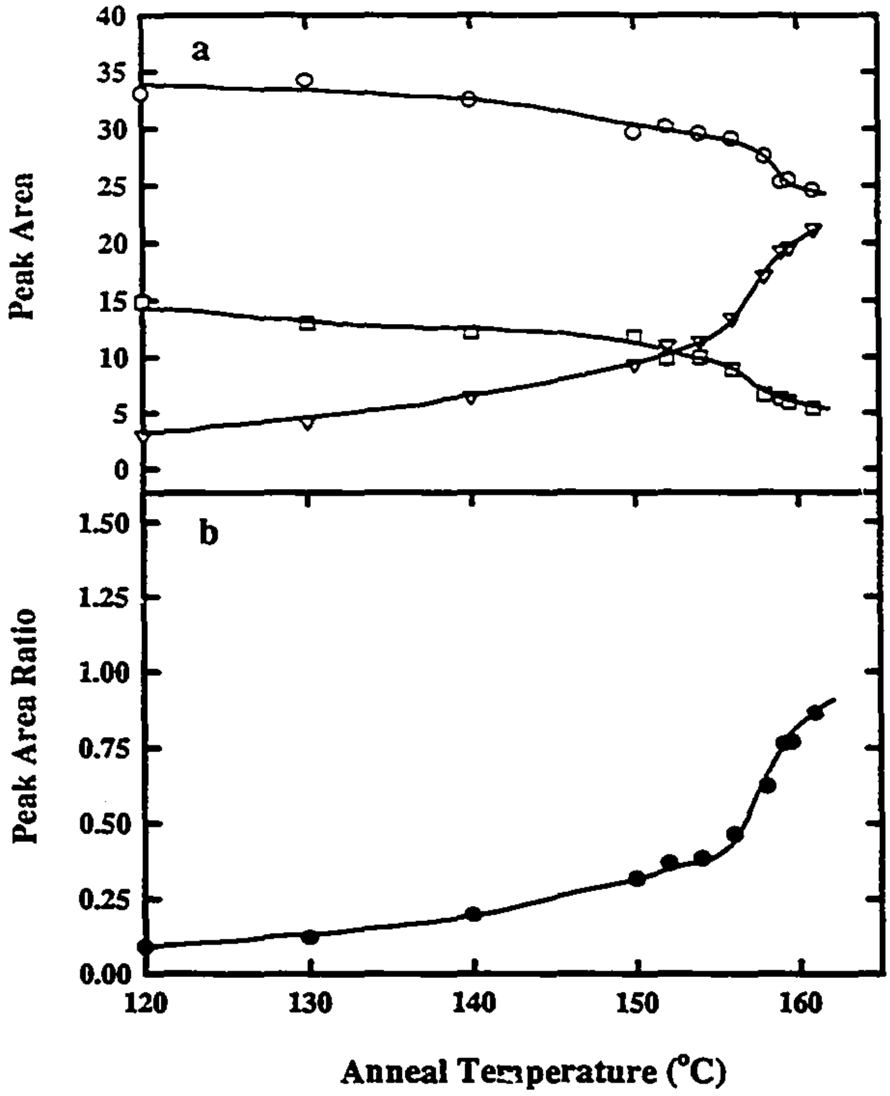

Figure 4.14 (a) Results for the peak area deconvolution of the methyl carbon resonance of the purely crystalline phase of spunbonded iPP fabrics annealed for 0 minutes at various temperatures; (Square), downfield peak; (Circle), upfield peak; (Inverted Triangle), midfield peak. The areas are expressed as a percentage of the total methyl plus methine areas. (b) The ratio of the area of the midfield to the upfield resonance.

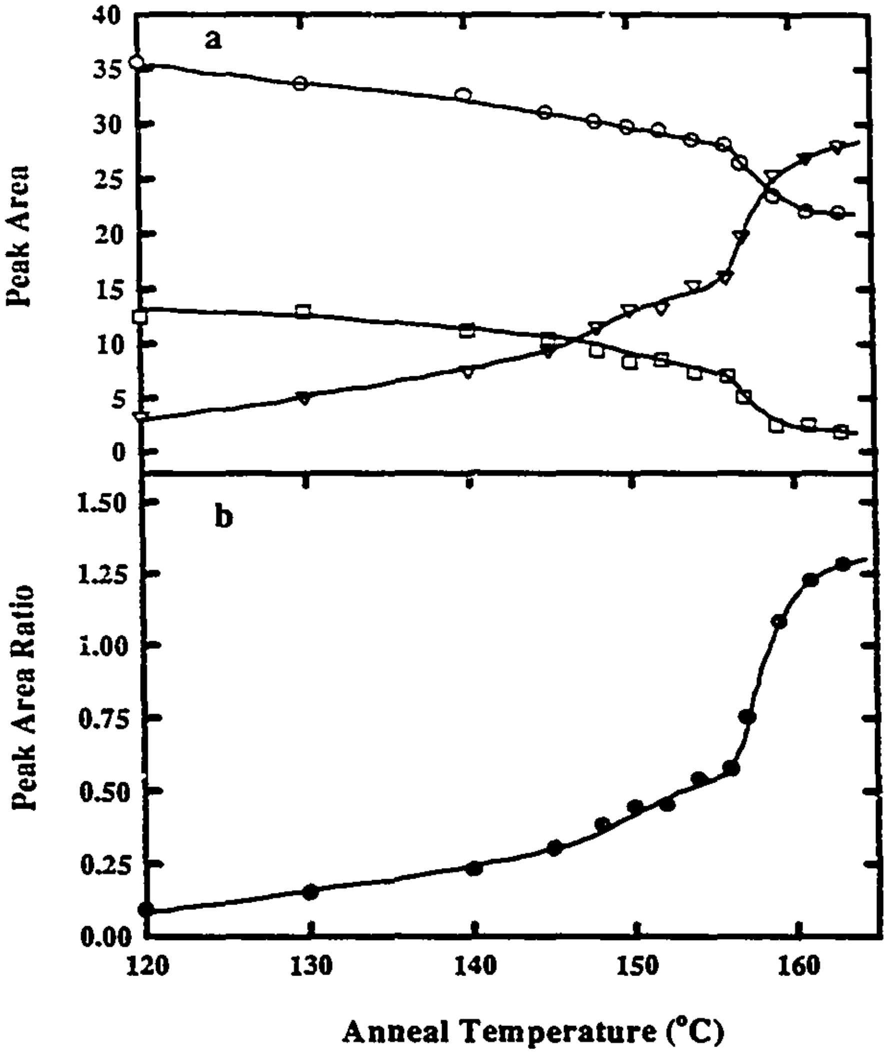

Figure 4.15 (a) Results for the peak area deconvolution of the methyl carbon resonance of the purely crystalline phase of spunbonded iPP fabrics annealed for 60 minutes at various temperatures; (Square), downfield peak; (Circle), upfield peak; (Inverted Triangle), midfield peak. The areas are expressed as a percentage of the total methyl plus methine areas. (b) The ratio of the area of the midfield to the upfield resonance.

downfield and upfield methyl resonances. However, unlike the pattern observed for the quench-cooled films, the redistribution of intensities within the methyl resonance does not increase smoothly as the sample is annealed at progressively higher temperature. A sharp increase in the area of the midfield methyl resonance is observed at temperatures greater than 156 °C while a sharp decrease in area is observed for both the downfield and upfield methyl resonances. This is particularly evident for the samples that were annealed for 60 minutes. This discontinuity in the increase of resonance intensity begins at an anneal temperature that coincides with that for which a faster rate of increase in the values of the $^{1}H\ T_{1\rho}$ was observed. This apparent transition temperature is also the first point at which a single endothermic transition was observed by DSC. The maximum of the LTP on the DSC thermogram of the spunbonded sample that was not annealed also coincides with this anneal temperature. Thus, there is a strong correlation between the observations made by NMR and the DSC investigations.

The ratio of the areas of the midfield to the upfield methyl peak is presented for both 0 and 60 minutes annealed samples in Figures 4.14b and 4.15b, respectively. An ultimate peak ratio of 4:3 is obtained for the samples that were annealed for 60 minutes while the peak ratio for the samples annealed for 0 minutes only attains an ultimate value of 9:10. This difference in the ultimate ratio confirms that the reorganization which occurs at high temperature is anneal time dependent. According to the model which suggests that inequivalent distances exist in the unit cell of the α-monoclinic phase of iPP due to the packing of right- and left-handed helices, this peak ratio should attain an ultimate value of 2:1. However, as with the quench-cooled films, the peak ratio does not attain this expected value. It is of interest that exactly the same ultimate peak ratio was obtained for the quench-cooled films when annealed for the same amount of time, *i.e.*, 60 minutes. This difference between the measured peak ratio and the expected ultimate peak ratio is discussed further in a subsequent section.

The widths at half maximum of the various peaks within the methyl resonance as obtained upon peak deconvolution are presented in Figure 4.16 for 0 and 60 minute anneals, respectively. The peak width decreases only slightly or remains essentially constant until approximately 156 °C. However, for anneals above this transition temperature a definite decrease in peak width is observed for all three peaks within the methyl resonance. Consistent with prior arguments, this change in peak width suggests that structural reorganization is occurring within the existing crystalline phase. The local environments described by each of the three peaks are converging to more singularly defined positions within the crystalline phase. As with prior observations, this change not only occurs within a few degrees (*i.e.*, 156 to 160 °C) but also occurs very rapidly since the samples annealed for 0 minutes also present evidence of re-organization above the transition temperature.

4.3.3.4 Annealing Behavior within the Interfacial Phase of iPP

Through an appropriate subtraction, such as that which was performed for the spectra of the quench-cooled films, the spectra of the interfacial component were obtained (Figure 4.17) for the spunbonded fabrics that were annealed for 1 hour. For each of the carbon resonances a single peak is observed at a chemical shift intermediate between the doublet observed for the crystalline phase. This is in accord with the values reported for the quench-cooled iPP films (Table 3.2). The chemical shifts of each carbon resonance remain unchanged as the sample is annealed at successively higher temperatures. However, upon closer inspection, the intensity of each of the three carbon resonances appears to increase with increasing anneal temperature. The peak intensity for each of the carbon resonances is plotted as a function of the anneal temperature in Figure 4.18. Indeed, a sudden increase in peak intensity is observed for samples annealed at temperatures greater than approximately 154 °C. This increase in the amount of

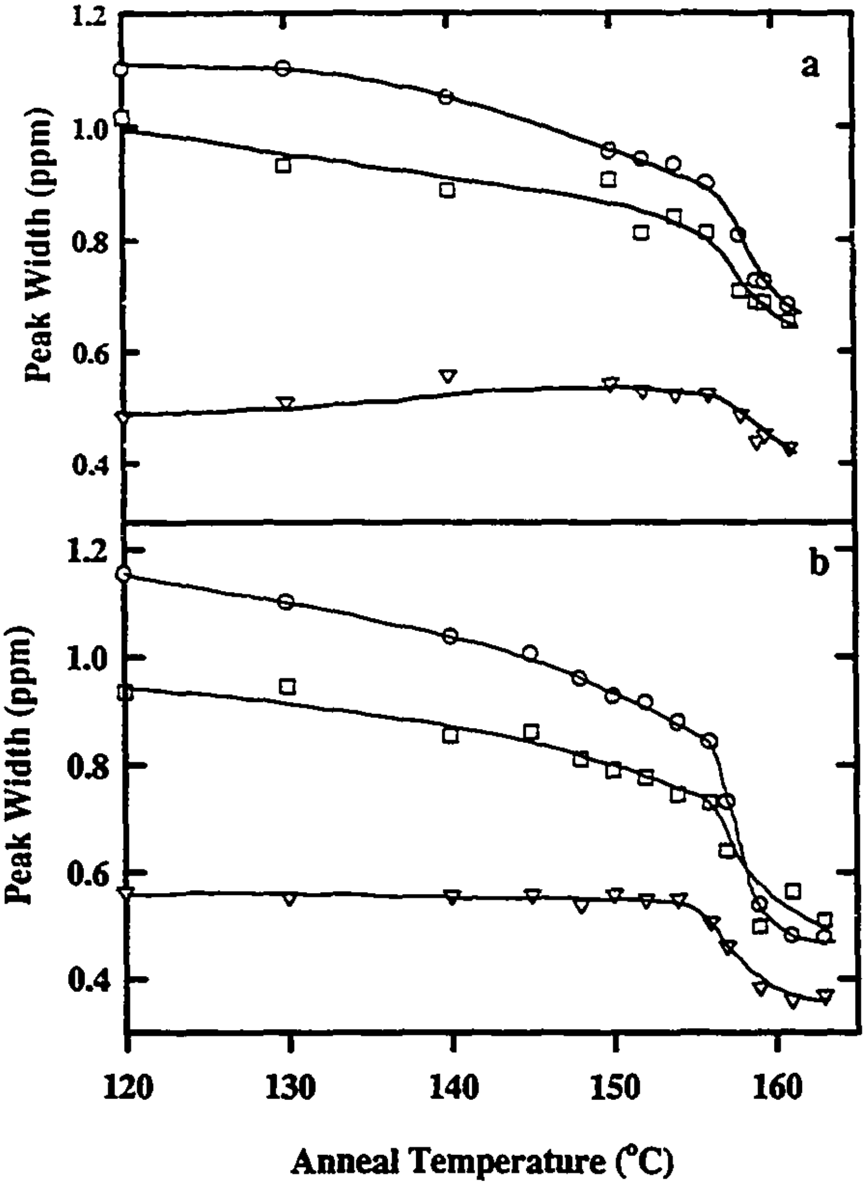

Figure 4.16 Methyl carbon peak width at half height as determined from the deconvolution of the methyl resonance for spunbonded iPP fabrics annealed for (a) 0 and (b) 60 minutes at various temperatures; (Square), downfield peak; (Circle), upfield peak; (Inverted Triangle), midfield peak.

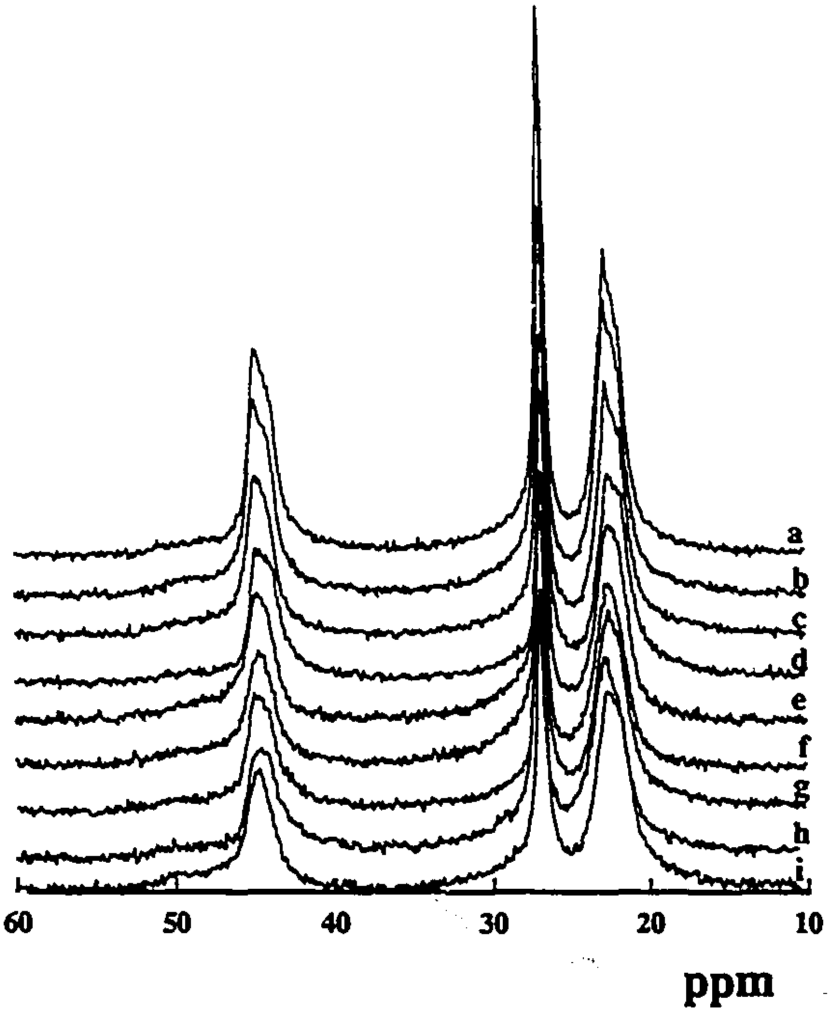

Figure 4.17 ^{13}C CP/MAS NMR spectra for the interfacial phase of iPP obtained from a subtraction of the spectrum of the purely crystalline phase from one with contributions from all phases. (a) 163 °C, (b) 161 °C, (c) 159 °C, (d) 156 °C, (e) 154 °C, (f) 150 °C, (g) 140 °C, (h) 130 °C, (i) 120 °C for one hour.

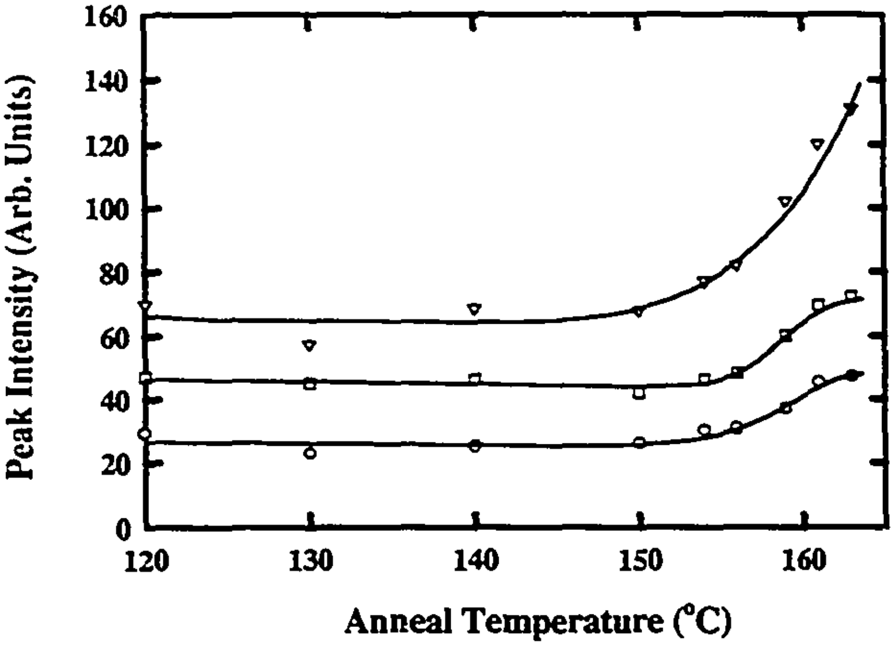

Figure 4.18 Methylene (Circle), methine (Inverted Triangle) and methyl (Square) peak intensity of the interfacial phase of the spunbonded iPP fabrics that were annealed for one hour at various temperatures.

interfacial material occurs concomitantly with the observed changes in the spectra of the crystalline component discussed previously. No change in the amount of interfacial component is detected at anneal temperatures lower than 154 °C. This increase in intensity of all carbon resonances within the spectra of the interfacial component is consistent with the results obtained from the $T_{1\rho}$ (^{1}H) analysis, as discussed previously.

4.3.4 Re-evaluation of the CP/MAS NMR Spectrum of α-phase iPP

As has been discussed previously and presented in this study, the CP/MAS NMR spectrum of the α-monoclinic phase of iPP contains spectral splittings that are intermolecular in origin. The model, originally proposed by Bunn and co-workers[61] and subsequently accepted by others,[62] proposes that this fine splitting is due to the association of right- and left-handed helices within the monoclinic unit cell of iPP. Helices of opposite handedness are able to enmesh more closely thus allowing for a closer association. As a result of this association, there exist two distinctly different environments for the monomer unit. This gives rise to the fine splitting observed in the solid state NMR spectrum.

An illustration of the packing environment within the crystal structure of the α-phase of iPP as viewed down the c crystallographic axis ($P2_1/c$ space group) presented in Figure 4.19, shows the different environments that are referred to above. The vertical direction in this illustration is the *a sin*(β) crystallographic axis while the horizontal direction is the *b* crystallographic axis. Successive vertical layers of left (L) and right (R) handed helices are illustrated. Each left/right association (*i.e.*, those of close proximity) forms a bilayer with respect to the 'up' and 'down' ordering of the chains such that successive bilayers are anticlined (*i.e.*, all 'up' followed by an all 'down' configuration), as discussed in the Introduction. This configuration represents the limiting higher order form, α_2, of the α-monoclinic phase (*i.e.*, the $P2_1/c$ space group) while a similar configuration possessing disorder in the 'up' and 'down' ordering of the chains forms the limiting lower order form, α_1 (*i.e.*, the C2/c space group). Depending on the crystallization conditions, the crystalline morphology of iPP in the α-monoclinic modification is composed of various relative amounts of each form.[64,65]

The discussion regarding the inequivalent environments presented by Bunn and co-workers[61] is best understood by looking at the two left/right handed helices for which all three methyl groups are fully labeled (*i.e.*, environments A and B, at the top, right hand side of Figure 4.19). It was postulated that these right- and left-handed helices form a closer association at the A labeled methyl sites while the third methyl site for each helix, labeled B, is in an environment characterized by a greater separation from any other helix. These two distinct environments for the monomer unit are characterized by four methyl groups at the A labeled site and two methyl groups at the B labeled site, thus forming a 2:1 ratio between sites. These two different sites were postulated to be the cause of the 2:1 peak intensity ratio that has been identified by visual inspection of the NMR spectrum of iPP. Although this discussion has been centered around the methyl carbon, it should be noted that the inequivalent site model also applies to the methine and methylene carbons since the CH-CH_2 bond is almost parallel with the c crystallographic axis.[66]

The peak deconvolution performed on the methyl resonance in this study made possible a more precise evaluation of the peak area ratio of the two more intense methyl peaks than was achieved from the visual inspection[61,62] of the peak intensity. For both the quench-cooled films and spunbonded fabrics that were annealed for 60 minutes (Figures 4.15(b) and 3.6(b)), this peak area ratio was monitored as a function of sample anneal temperature and was found to increase until it reached an ultimate peak ratio of only 4:3.

In Chapter 3, it was suggested that it is possible that the theoretical peak ratio of 2:1 cannot be attained for quench-cooled samples simply by sample annealing. However, based on the presence of another peak downfield from the most intense methyl peak and the fact that the peak area ratio attains an ultimate value of only 4:3 it seems more likely that the model describing the fine splitting does not account adequately for the details of the solid state spectrum. In addition, this model does not account for the reduced peak ratio observed in the spectra of iPP samples that were annealed at lower temperatures or

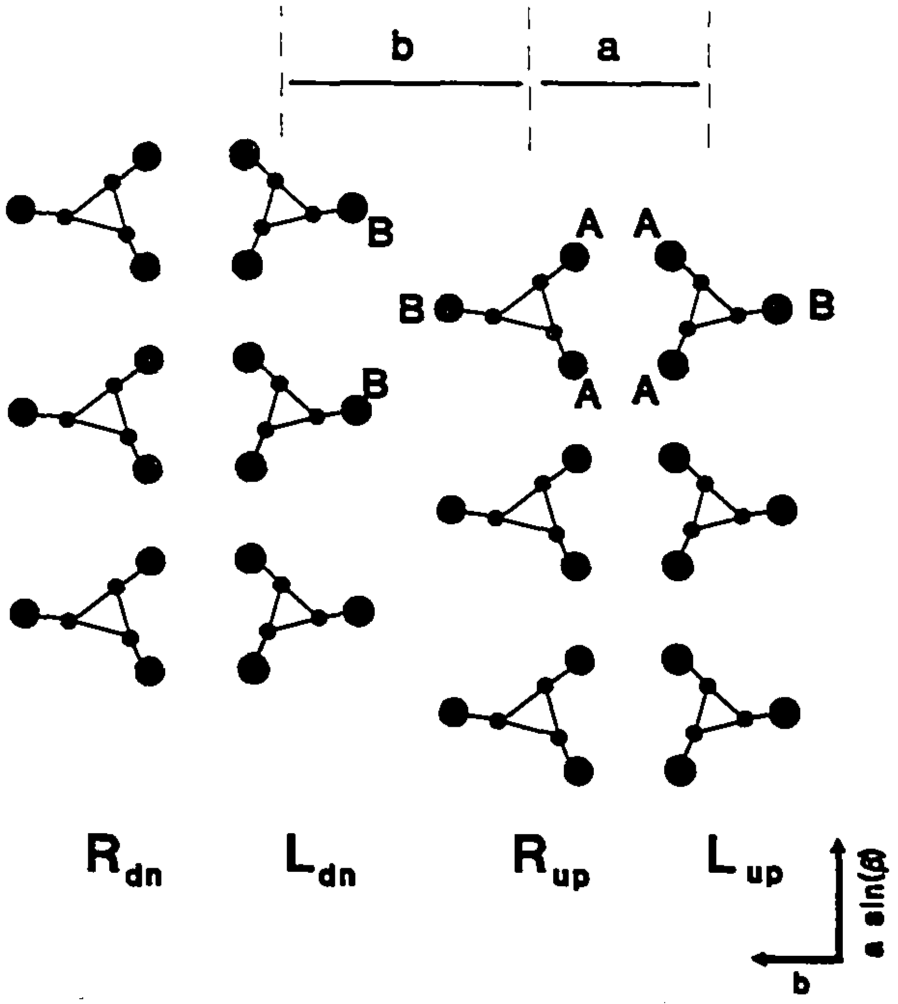

Figure 4.19 Illustration of the crystal structure of the α-monoclinic form of iPP under $P2_1/c$ symmetry as viewed down the *c* crystallographic axis. This illustration is based on the packing diagram presented by Brückner and co-workers.[63]

the single peak observed for quench-cooled films. Thus, this model, which describes the inequivalent environments in terms of distances between helical centers, may be insufficient in describing the fine details regarding the splitting patterns observed in the solid state spectra of iPP.

Recently, Brückner and co-workers[63] investigated the CP/MAS NMR spectrum of the γ-triclinic crystalline modification of iPP. This crystal form was first described by Turner-Jones, *et al.*[14] but has more recently been re-examined and refined by Brückner and Meille.[67] In the γ-phase of iPP, the arrangement of 3_1 helices was found to violate the requirement of chain axis parallelism in that bilayers (*i.e.*, parallel helices two chains wide) present a chain axis orientation with an 80° tilt with respect to the adjacent bilayer. The CP/MAS NMR spectrum of this modification also reveals fine splitting patterns associated with intermolecular phenomena, similar to that obtained for the α-phase. However, in the γ-phase, the intensity of the upfield methyl peak is roughly double the intensity of the downfield methyl peak, reversing the intensity ratio observed for the α-phase. Brückner and co-workers[63] also considered this splitting pattern to be due to inequivalent distances between helical axes. However, due to the chain axis nonparalleiism that exists within the γ-phase, distances between chain axes could not be used as a measure of the overall steric crowding. The authors chose to adopt the interlayer spacing, illustrated by the **a** and **b** distances in Figure 4.19, as a measure of the packing density around a given atomic position.

The **a** and **b** interlayer distances reported by Brückner and co-workers[63] for both the α- and γ-phases of iPP are presented in Table 4.4. It should be noted that the various interlayer distances reported for the α-phase were obtained from the x-ray analysis reported by various authors. The first interlayer distance listed in Table 4.4 considers the original description of the α-phase reported by Natta and Corradini (*i.e.*, C2/c space group) while the following interlayer distances consider subsequent models that attempted a refinement of the original model (*i.e.*, $P2_1/c$ space group). In their analysis of the γ-phase solid state spectrum, Brückner and co-workers[63] averaged all of the α-phase interlayer distances reported in Table 4.4 to obtain **a** = 5.13 and **b** = 5.34. They compared these to the interlayer distance reported for the γ-phase in attempting to develop an explanation for the observed reversal in the intensities of the two methyl peaks. An inversion of the two interlayer distances was noted; **a** being longer than **b** for the γ-phase. It was suggested that this inversion is related to the corresponding inversion of the methyl intensities in the solid state NMR spectrum.

Table 4.4: Interlayer distances **a** and **b** as reported by Brückner and co-workers[63] for both the α- and γ-phases of iPP.

Description of Crystal Structure	Interlayer Distances	
	a (Å)	b (Å)
α-phase (Natta and Corradini)[66]	5.30	5.17
α-phase (Mencik)[65]	5.07	5.41
α-phase(Hikosaka and Seto)[64]	5.10	5.33
α-phase (Immirzi)[68]	5.03	5.45
γ-phase (Brückner and Meille)[67]	5.34	5.24

The interlayer distance reported by Brückner and co-workers,[63] which was based on the x-ray evidence of Natta and Corradini (Table 4.4), refers to an α-phase with C2/c symmetry (*i.e.*, a limiting disordered structure) while all of the other interlayer distances given in Table 4.4 are associated with a crystal form that is closer to $P2_1/c$ symmetry. It is of note that an inversion between the **a** and **b** interlayer distances does not only occur as a result of change in structure, *i.e.*, from the α to the γ phase, but also on perfection of the α-phase from the space group C2/c to $P2_1/c$. Interlayer distances of **a** = 5.30 and **b** = 5.17 Å are reported for the α-phase in the disordered form (*i.e.*, C2/c) while **a** = 5.07 and **b** = 5.40 Å are reported for the ordered $P2_1/c$ form. It might be expected that this inversion in interlayer distances is also related, at least in part, to the corresponding reversal in peak ratio that is observed in lower temperature annealed samples as well as the single peak that is observed in quench-cooled iPP.

The structural arrangement of helices at the two interlayers discussed above (*i.e.*, interlayers **a** and **b** defined in Figure 4.19) has been examined, in part, by Lotz and Wittmann[69-71] in their consideration of the contact faces of epitaxially crystallized iPP in the α-monoclinic and γ-triclinic forms. In agreement with the layer structure description of the α-monoclinic phase of iPP, they identified two possible packing modes in this crystalline phase under $P2_1/c$ symmetry. One type of packing is noted at the contact faces of the interlayer labeled **a** while a completely different packing mode is observed for the interlayer labeled **b** in Figure 4.19. The methyl groups of these contact faces are labeled A and B in Figure 4.19. When the A labeled contact face is viewed from either the *+b* or *-b* crystallographic direction (*i.e.*, perpendicular to the *ac* crystallographic plane), two methyl groups are exposed at the contact face, for both the right- and left-handed helices, while the third methyl group is buried behind the helix and is in the **b** interlayer. The reverse is observed at the B labeled contact face, *i.e.*, one methyl group is exposed while two are buried.

If a helix of at least three monomer units viewed along the *c* crystallographic direction is associated with another helix of the same handedness (*i.e.*, along the *a* crystallographic direction), two different packing geometries are noted at the A and B contact faces. These yield a striking difference in density of exposed methyl groups. The packing of the methyl groups at both of these contact faces is presented graphically in Figure 4.20. The filled circles represent exposed methyl groups while the empty circles indicates a methyl group buried behind the helix. In the **a** interlayer contact face (Figure 4.20a), the methyl groups are arranged in a face-centered geometry or as the "five" face of

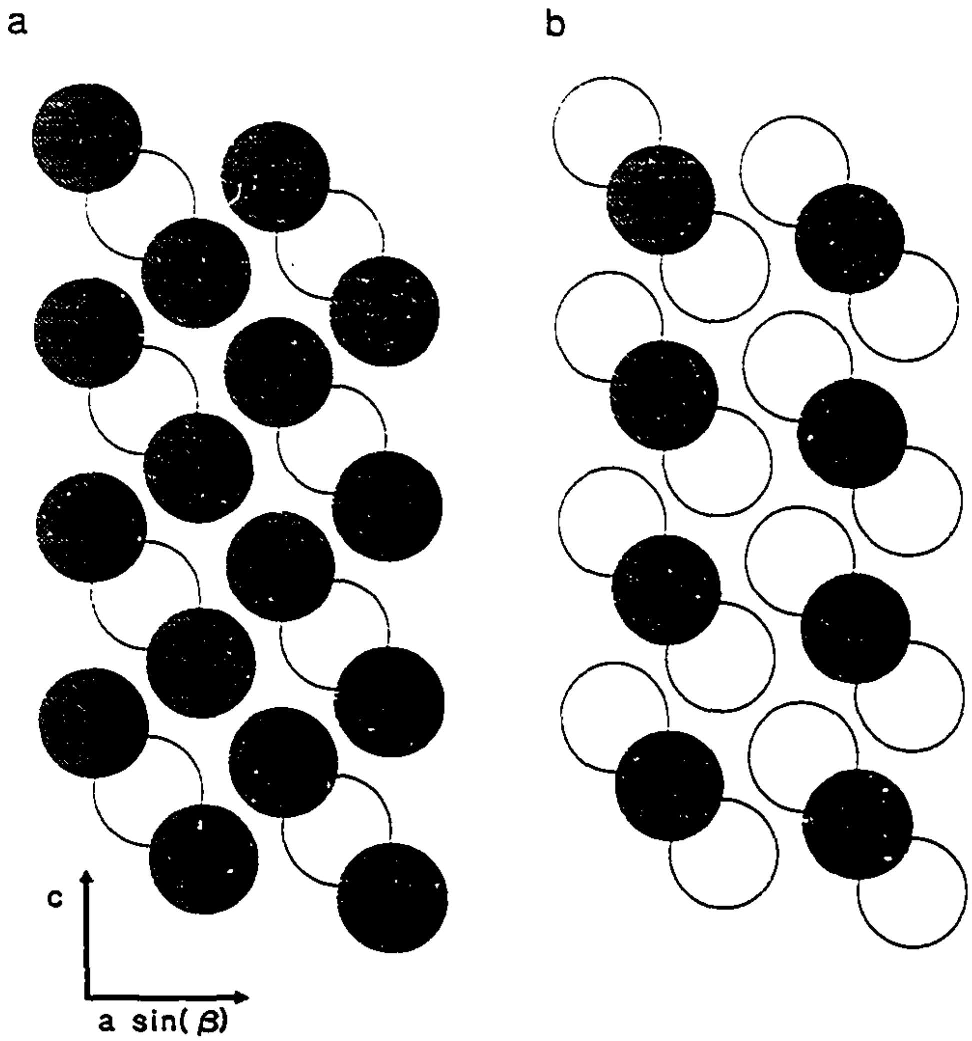

Figure 4.20 Illustration[71] of the positioning of the methyl groups at the contact face (a) at the a interlayer and (b) at the **b** interlayer. The shaded circles represent exposed methyl groups while the hollow methyl groups represent methyl groups that are buried behind the helix. The (a) five and (b) four patterns of dice (*i.e.*, simple and face centered) are easily seen.

a dice while at the b interlayer contact face (Figure 4.20b), the geometry can be illustrated as the "four" face of a dice.[70] Therefore, at the A labeled sites (Figure 4.19), a considerably higher density of exposed methyl groups is noted compared to the B labeled site.

Based on the above considerations, the fine splitting observed in the CP/MAS NMR spectrum of the α-phase of iPP results from the closer association of right- and left-handed helices in the interlayer labeled a (Figure 4.19) as well as from a striking difference in density of exposed methyl groups at this contact face. However, these differences are associated with the α-phase possessing higher order, *i.e.*, that packed according to $P2_1/c$ symmetry. As discussed above, the α-phase possessing lower order (*i.e.*, C2/c space group) has a substantially greater separation at this interlayer, while the interlayer defined by the B sites is substantially smaller. However, it should be noted that the density of exposed methyls at the contact face of interlayer B is much smaller. Consequently, for the unit cell of lower order the methyl groups of the A and B interlayers are observed in the NMR spectrum essentially as a single upfield resonance. For the higher order crystal form, large differences in helical packing and interlayer distances generate inequivalent distances within the unit cell that result in the observation of fine splitting for all of the carbon resonances. A crystal of intermediate order, *i.e.*, one composed of relative amounts of both limiting structures, will result in a splitting pattern of reduced peak ratios consistent with a reduced level of order. Therefore, the changes in the fine splitting patterns observed in the solid state NMR spectrum of iPP characterize the transformation of a crystalline phase existing in a state of low order (*i.e.*, C2/c symmetry or α_1 form) to a limiting higher order form (*i.e.*, $P2_1/c$ symmetry or α_2 form). The midfield methyl resonance reported in Figures 4.14, 4.15 and 3.6 appears to follow the structural transformation from the α_1 to the α_2 modification.

The existence of such a structural transformation was also suggested by Hikosaka and Seto[64] based on x-ray diffraction analysis. In their analysis, the co-existence of both levels of structural order was postulated and, from the x-ray diffraction intensity data, it was shown that the volume fraction of the higher order form in a highly elongated and high temperature annealed sample was 66%. In this NMR study, the area of the midfield methyl resonance, which is now thought to reflect the amount of higher order within the crystalline phase, attains an ultimate value of 56% (Figures 4.15 and 3.6). Considering the different thermal and mechanical histories of these samples, this is in good agreement with the value reported by Hikosaka and Seto.[64] It should be noted that, although attained at different anneal temperatures, both the quench-cooled films and the spunbonded fabrics attain the same ultimate value of 56%.

In previous studies, it was generally agreed that the peak intensity ratio between the downfield and upfield methyl resonances should attain an ultimate ratio of 2:1 due to inequivalent distances within the unit cell. Based on the interlayer arguments presented above, it is predicted that the methyl peak area ratio should attain a value of 4:3, consistent with four methyl carbons at interlayer a and three at interlayer **b** generating the inequivalent distances in the α_2 modification. As noted from Figures 4.15 and 3.6, the methyl peak area ratio does indeed attain this ultimate value of 4:3. Therefore, the inequivalent distances present in the unit cell of α-phase iPP that are generating the fine splitting patterns observed in its solid state spectrum should be interpreted in terms of interlayer spacing and the packing density at the contact faces of each interlayer.

As noted for the annealed quench-cooled films (Figure 3.6), the downfield methyl resonance appears to behave as an intermediate environment since it forms during the initial stages of reorganization and essentially disappears when the final crystalline state is attained. In the spunbonded fabrics, this methyl peak is observed in the spectra for the samples with the original morphology, *i.e.*, prior to the annealing treatment. Its presence suggests that there exists an even closer association of helices than that observed in the final state of higher order. It should be noted that a shorter separation between helices corresponds to a downfield shift of the methyl resonance.[63] In the investigation of the α_2 form of iPP, Mencik[65] calculated the interatomic distances at the interface between a regular region, built with $P2_1/c$ symmetry, and a disordered region, *i.e.*, a chain with the wrong up/down orientation. All shortest distances between regular and defect chains were found to be equal to or larger than 4.04 Å with the exception of one methyl group for which a separation of 3.67 Å was calculated with its counterpart on the defect chain. This smaller separation between methyl groups may give rise to the downfield methyl peak. Mencik pointed out that this short distance can be relieved by a rotation and a small shift of the defect chain in the *c* crystallographic axis. With this small shift, the distance that was previously too short increases to 3.90 Å. Therefore, the environment generated by this too small distance (*i.e.*, downfield methyl peak) would be lost following a shift of the helix along the *c* crystallographic axis. In the solid state NMR spectrum, the downfield peak formed due to a closer association of helices would decrease in intensity as more defect chains are integrated into the α_2 modification. The presence of this peak in the highest order samples (*i.e.*, highest anneal temperatures) is in accord with x-ray evidence which indicated that pure $P2_1/c$ symmetry cannot be obtained in iPP.

4.3.5 The Double Endothermic Transition in iPP Spunbonded Fabrics

As discussed in the previous section, the solid state NMR spectrum of the α-phase of iPP provides information regarding the level of order that exists within the crystalline phase. This in turn reflects its thermal and mechanical history. Thus, the NMR spectra can be used to monitor the conversion of the crystalline morphology from a state of low order to that of a higher level of order (*i.e.*, α_1 to the α_2 crystal form). The area of the midfield methyl resonance appears to be related to the amount of the higher order phase that is present in the sample.

The melting behavior of a given polymer sample reflects the level of order existing within the crystalline phase of the original morphology. In addition, enthalpic contributions associated with any reorganization that occurs within the sample as the temperature is raised will contribute to its melting behavior. In the case of iPP in the α-phase, the reorganization that occurs during sample heating involves conversion to the $P2_1/c$ space group. The melting behavior of various iPP samples possessing different thermal and mechanical histories has been investigated[12,48,72] in terms of the level of structural order that exists within the crystalline fraction of these samples. DSC and x-ray diffraction data were carefully compared for various unoriented and oriented iPP samples with specific thermal histories.

In these investigations, an order parameter, R, was defined which yields semi-quantitative estimates of the degree of order existing within a given sample. This parameter was taken equal to the ratio of the area of the x-ray peak between 34.4 and 36° (*i.e.*, (h+k) even and odd reflections) and 36.4 and 38° (*i.e.*, (h+k) even only). This ratio reaches nearly 2 for the most ordered samples (*i.e.*, $P2_1/c$ space group) while a value of 0.5 is obtained for the disordered state (*i.e.*, C2/c space group). The following observations[12,48,72] were made concerning the effects of structural order on the melting behavior of the samples: (1) Unoriented iPP samples with a thermal history defined by a 10 °C/min cooling from the melt to room temperature and subsequently annealed at 125 °C have a disordered form with R = 0.8. They melt with a single peak at fast heating rates while at slow heating rates a double melting peak is observed (*i.e.*, single peak at heating rates > 10 °C/min; double peak at rates < 2.5 °C/min). Upon annealing at 165 °C they reorganize to a more ordered form with R=1.6 and a single melting peak is observed at all heating rates. It was postulated that when a sample in the disordered form is heated at a slow heating rate it has sufficient time to reorganize into the more ordered form that melts at a higher temperature thereby generating a double melting peak. (2) Upon sample annealing, an increase in the order parameter is observed consistent with the transformation from the disordered to the ordered state. This increase is observed for all samples independent of prior thermal history. However, the onset temperature for this transformation varies between samples and depends on thermal history. The temperature range associated with this transformation was shown to be related to the position and shape of the melting endotherm of the original sample (*i.e.*, prior to annealing treatment). (3) The increase in the order parameter at the α_1 to α_2 transition occurs concomitantly with an increase in the melting temperature of the annealed samples. A linear relationship was observed between the order parameter and the melting temperature of the sample. The reorganization that occurs for all samples increases the temperature of melting and corresponds to increases in the "up/down" degree of order. (4) In the fiber form, the α-phase of iPP is in a disordered state (*i.e.*, C2/c space group) and its melting behavior is always characterized by a double melting peak, even for heating rates as high as 40 °C/min.

The above evidence suggests a strong correlation between the level of structural order that exists within the α-phase of iPP and the melting and annealing behavior of the sample. In Figure 4.21, the area of the midfield methyl resonance is plotted as a function of the melting temperature, for all of the annealed spunbonded iPP samples. Above a certain anneal temperature, a linear relationship is obtained for both the 0 and 60 minute annealed samples. This linearity is similar to the linear relationship observed previously by De Rosa and co-workers[72] based on the order parameter, R, obtained from x-ray diffraction analysis. Therefore, the melting behavior of the iPP samples is dependent on the amount of "up/down" order within the crystalline phase. The linearity between the area of the midfield methyl resonance and the melting temperature indicates further that the solid state NMR spectrum is indeed describing the transformation of the disordered

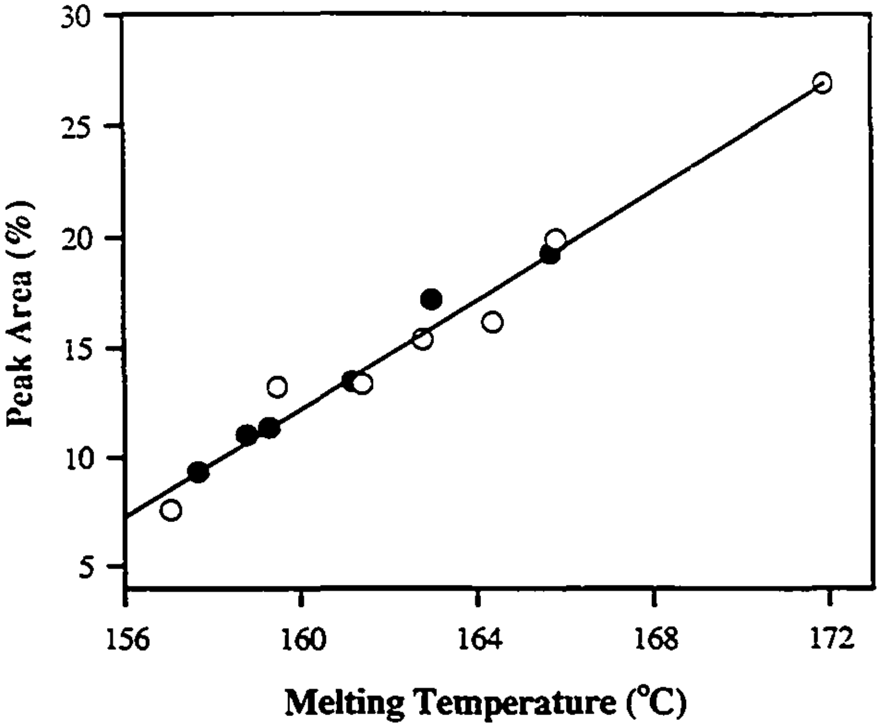

Figure 4.21 Relationship between the peak area of the midfield methyl resonance and the sample melting temperature obtained by DSC. Open circles represent the 60 minute anneals while the filled circles represent the 0 minute anneals.

state to an ordered one. It should be noted that this linear relationship is only observed for anneal temperatures ≥ 150 °C, which is consistent with the fact that no change in the DSC thermogram is observed below this anneal temperature.

The area of each of the three methyl peaks as well as the peak area ratio for both the quench-cooled films (Chapter 3) and spunbonded fabrics that were annealed for 60 minutes are presented together in Figure 4.22 for purposes of comparison. As might be

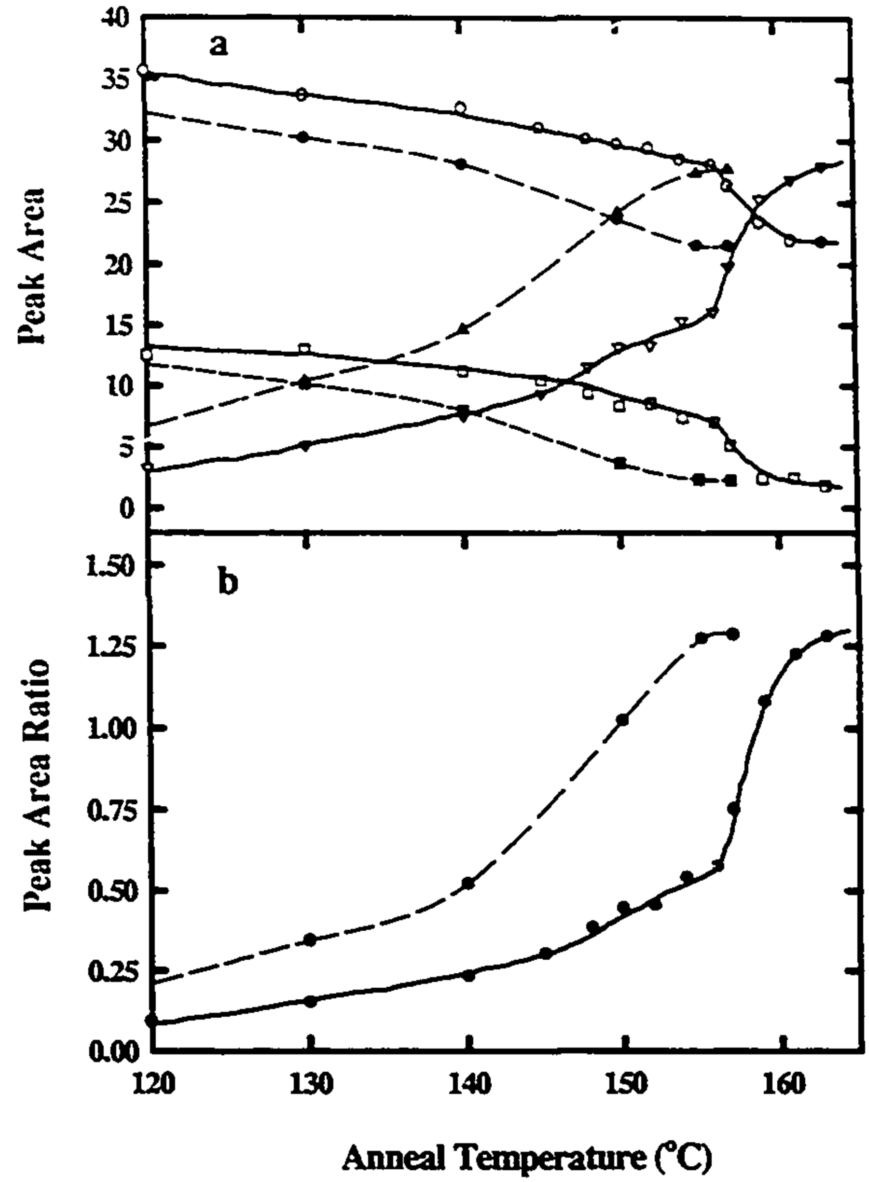

Figure 4.22 Comparison of the peak area deconvolution results for the spunbonded fabrics (solid lines) and the quench-cooled films (dashed lines). Data previously illustrated in Figure 4.15 and 3.6.

expected, distinctly different behavior is observed for these two systems. At the anneal temperature of 156 °C the quench-cooled films have attained their final intensity distribution, consistent with reorganization to the higher order α-phase while, by comparison, the spunbonded fabrics have spectra with a much reduced intensity distribution. The fastest redistribution of intensity for the spunbonded fabrics occurs at anneal temperatures greater than 156 °C, *i.e.*, the temperature that is also associated with significant changes in the spectrum of the interfacial phase as well as in the DSC thermogram, *i.e.*, melting with a single endotherm. However, it should be noted that both samples attain exactly the same intensity distribution at anneal temperatures associated with the maximum melting temperature measured by DSC. The quench-cooled films melt with a broad single endotherm with the temperature of the peak maximum that is consistent with the final state observed by NMR. In the case of the spunbonded fabrics, this temperature is associated with the LTP while the final state observed by NMR, for samples annealed at 163 °C, is coincident with the HTP observed by DSC.

Since the NMR spectrum reflects the amount of higher order within the α-phase crystals, it is clear that although the melting behavior of these samples is drastically different the ultimate levels of order that develop within the crystalline phase are identical. However, the paths by which the final state is attained are strikingly different and this is reflected in the melting behavior of these samples. A gradual conversion from the NMR spectrum with the intensity distribution associated with the disordered state to that of the ordered state is noted for the quench-cooled films (Figure 4.22). In fact, this conversion appears to begin with anneals at approximately 80 °C (Figure 3.6), coinciding with the exothermic transition observed by DSC. The gradual conversion may, in part, be reflected in the broadness of the DSC thermogram for this system (Table 4.1). In the case of the spunbonded fabrics, the extent of conversion is largest for annealing in the temperature range between 156 and 163 °C, *i.e.*, the area between the two DSC endotherms. It is of note that the two peaks in the DSC thermogram for the spunbonded fabrics are comparatively sharp with very little low temperature tailing (Figure 4.2).

Napolitano and co-workers[73] have performed packing energy calculations for both the space groups C2/c and $P2_1/c$ using the values of the axes of the unit cells experimentally obtained at various temperatures. The calculations consistently indicate lower energies for the crystals with $P2_1/c$ symmetry compared to those with C2/c, suggesting that the higher order form is thermodynamically more stable and that the lower order phase forms due to kinetic constraints (*i.e.*, rapid cooling). During the transformation to the form with higher order, this energy difference must be prevailingly of enthalpic character. In the case of the quench-cooled films, this enthalpic contribution to the transformation from the disordered to the ordered state occurs over a large temperature range, as indicated by the gradual conversion that is observed by NMR (Figure 4.22). However, in the case of the spunbonded fabrics, the enthalpic contribution associated with this transformation would be localized in the temperature region between 156 and 163 °C, *i.e.*, the temperature range where a rapid redistribution of intensity is observed in the NMR spectrum. This temperature range coincides exactly with the region between the two melting endotherms suggesting that the main melting transition has been modified by an exotherm. Therefore, for the spunbonded fabrics, the exothermicity associated with the α_1 to α_2 transition is concentrated within a small temperature range that is superimposed on the melting endotherm so the overall process is observed by DSC as a double endotherm. For the quench-cooled films, this exothermicity occurs over a large temperature range and is not detected by DSC. However, it may be possible that at low heating rates, the temperature transition region may be reduced and the exothermicity detected by DSC yielding once again a double endotherm.

From the above arguments, it appears that the melting behavior of iPP in the α-phase is dependent on two variables. The first is the level of order that exists within the original crystalline morphology of the sample. This level of order defines the degree of reorganization that can occur during sample heating. The second variable is the path by which the crystalline fraction reorganizes, *i.e.*, over a small or large temperature range and the rate of transformation within this temperature range. It must be noted that the second variable must be dependent on the conditions of the thermal analysis experiment (*e.g.*, sample heating rate, restrained versus unrestrained thermal analysis).

4.3.6 Crystal Orientation and Sample Shrinkage

In the analysis of the melting and annealing behavior of the spunbonded iPP fabrics, comparisons were made throughout this chapter with the melting and annealing behavior of the quench-cooled iPP films. The double melting endotherm that is observed for the spunbonded fabrics was found to be due to a combination of an originally poorly developed crystalline phase (*i.e.*, C2/c symmetry) and to a transformation of this disordered crystalline phase to an ordered phase (*i.e.*, $P2_1/c$ symmetry) within a small temperature region. By comparison, the quench-cooled films are also composed of essentially the same level of order within the crystalline phase; however, the transformation to a higher order crystalline form occurs over a large temperature span. This difference in the temperature region where the transformation from a disordered to an ordered crystalline form occurs must be related to a difference in the gross morphology of the samples.

A scanning transmittance electron microscopy (STEM) dark field image of n-beam reflections of a longitudinal section of the iPP fibers is presented in Figure 4.23. This image was obtained as described in the Experimental section in Chapter 2. Contrary to the quench-cooled films (Figure 2.7), the crystalline phase of the iPP fibers is highly oriented in the fiber direction, as is clearly seen by the long white regions in the STEM dark field image. Therefore, the difference in the path by which the transformation from the

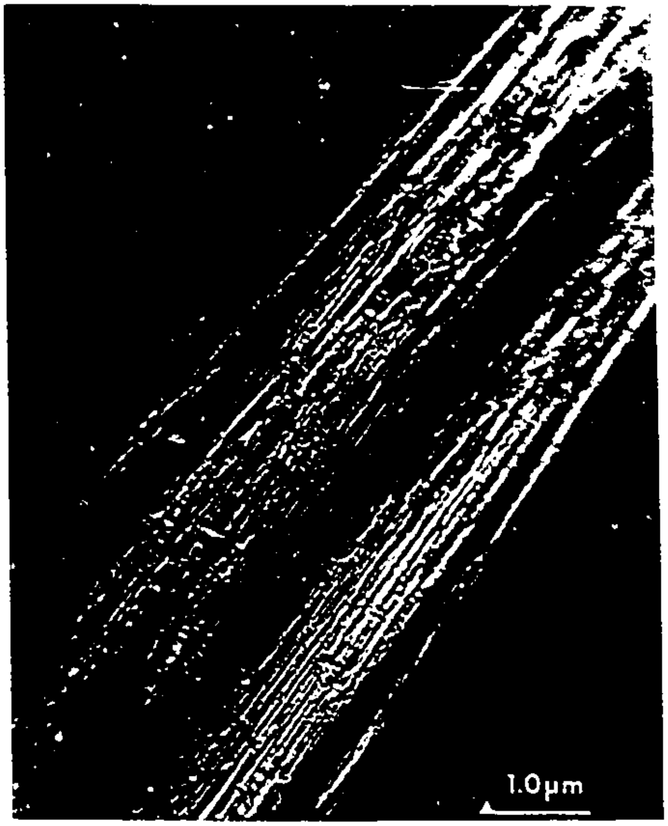

Figure 4.23 STEM dark field image of n-beam reflections of a longitudinal section of the iPP fibers at 10,000X magnification. The fiber was cut longitudinally close to the fiber surface.

disordered to the ordered α-monoclinic crystalline form occurs (Figure 4.22) must be related to the level of orientation that is present in the sample. It is possible that in the oriented fibers, reorganization is restricted due to the orientation in the crystalline phase and occurs only once the fibers begin to soften. This is expected to require the spunbonded fabrics to shrink in the temperature region associated with this transformation.

The heating of the spunbonded iPP fabric was performed at a rate of 2 °C/min under an optical microscope to monitor any changes in the size of the fabric as the temperature was raised. The size of the spunbonded fabric as measured within the microscope viewing area is plotted as a function of temperature in Figure 4.24. Indeed, at a temperature of *ca.* 152 °C, the spunbonded fabric begins to contract. It is of interest that at this temperature changes to the interfacial phase were observed by NMR. A very rapid contraction of the sample is noted in the temperature region between 157 and 163 °C. This temperature region coincides exactly with all prior observations made by DSC and NMR regarding morphological changes within the crystalline phase of iPP. Therefore, it appears that the transformation within the crystalline phase of iPP follows the softening and, thus, loss of orientation in the crystalline phase of the iPP fibers.

4.4 Summary

The melting and annealing behavior of iPP spunbonded fabrics was investigated by solid state NMR spectroscopy and DSC. Changes to the CP/MAS NMR spectrum of the α-monoclinic phase of iPP were monitored as the sample was annealed at continuously higher temperature. As with the quench-cooled films discussed in Chapter 3, splitting patterns developed within all carbon resonances characteristic of a more ordered crystalline form. The methylene and methine carbons revealed split resonances whose intensity distribution depended on the sample anneal temperature. The methyl resonance,

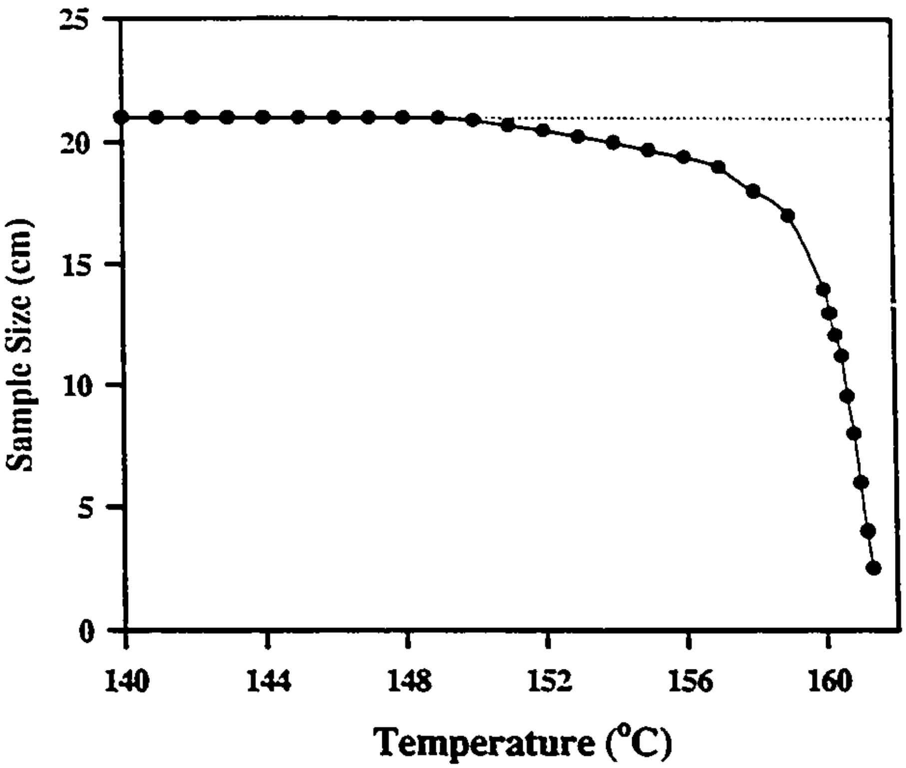

Figure 4.24 Mapping of the shrinkage of the iPP spunbonded fabric as a function of temperature at a heating rate of 2 °C/min.

as observed for the quench-cooled films, was split into three peaks. It was shown that the development of the splitting patterns is consistent with the generation of higher order within the α-monoclinic crystalline phase. In particular, the midfield methyl resonance maps the conversion of the crystalline phase from a disordered state described by C2/c symmetry to a more ordered state that is described by $P2_1/c$ symmetry.

The highest crystalline order attained in this study (*i.e.*, closest to $P2_1/c$ symmetry) results in a split within the methyl resonance characterized by an intensity ratio of 4:3, as was also observed for the annealed quench-cooled films. This splitting pattern is due to inequivalent packing geometries in the $P2_1/c$ symmetry α-phase due to the association of right- and left-handed helices that generate a bilayer. Within a given bilayer that is characterized by the same methyl orientation (*i.e.*, up or down), a smaller interlayer separation and a higher methyl packing density exists than for the interlayer defined by the packing between bilayers of opposite orientation. This distance and density variation generates two different environments at the interlayers yielding two peaks in the solid state spectrum for this higher order form. A 4:3 peak area ratio is borne out of this model and is observed experimentally.

To understand the nature of the double endothermic transition in the spunbonded iPP fabrics, the samples were annealed at high temperature and the changes occurring to the crystalline phase were characterized by DSC and solid state NMR spectroscopy. An apparent transition temperature of 156 °C was identified by both of these characterization methods. DSC analysis indicated a sudden change in crystallinity in samples annealed at temperatures higher than this transition temperature. In addition, the thermograms of these annealed samples did not indicate a double endothermic transition but rather a single peak. NMR characterization of the level of order existing within the crystalline fraction as well as the overall mobility of the polymer chains also indicated a sudden change occurring within the crystalline phase at a temperature of 156 °C. This change was identified as a transition from a disordered phase with respect to the "up/down" orientation of helices within the unit cell to an ordered phase. Proton spin-lattice relaxation times in a rotating frame indicated that above 156 °C, chain mobility decreased more rapidly than below this temperature, which is consistent with the crystallinity observation made by DSC. The CP/MAS NMR spectra of the purely crystalline phase of iPP indicated a rapid re-distribution of peak intensity at temperatures above this apparent transition temperature. The width of the various peaks within a given carbon resonance decreased suggesting that the helices are located at more singularly defined positions, which is consistent with a crystal of higher order. In addition, changes were also noted within the interfacial component. The amount of interfacial component in these samples increased with a concomitant decrease in chain mobility suggesting, respectively, possible crystallization of previously extended chains and/or amorphous material and segregation of polymer chains previously in the crystalline phase to the interfacial component. These observations were confirmed by $T_{1\rho}$ (^{1}H).

The transition temperature of 156 °C is consistent with the peak maximum of the LTP observed by DSC for the spunbonded fabrics and the melting temperature of the quench-cooled films. In addition, the temperature range between the two melting endotherms coincides exactly with the range where drastic changes occur to the crystalline phase of iPP as determined by solid state NMR spectroscopy. Conversion from a state of low to higher order is noted in this region. Therefore, at temperature above 156 °C, the melting endotherm is being modified by exothermic processes from this transformation.

The effect of this transformation on the melting behavior is also thought to be path dependent. The quench-cooled films attain the same level of order as the spunbonded fabrics but melt with a single endotherm. However, the transformation is gradual in comparison to the spunbonded fabrics, and occurs over a large temperature range. Therefore, the exothermicity associated with this conversion occurs over a large temperature range. In the spunbonded fabrics, the conversion is very rapid and is concentrated within a much smaller temperature range and, thus, so is the exothermicity that is modifying the endothermic transition and generating a double melting peak. This difference is thought to be due to orientation of the crystalline phase that is observed for the spun fibers. This orientation restricts reorganization in the crystalline phase until a temperature associated with softening of the fiber form. Shrinkage of the spunbonded fabric is observed in the temperature region where the morphological changes within the crystalline phase are observed through DSC and NMR characterization.

4.5 References

[1] L. Mandelkern, J.G. Fatou, R. Denison and J. Justin, *J. Polym. Sci., Part B* 3, 830 (1965).

[2] H.W. Holden, *J. Polym. Sci. C* **6**, 53 (1964).

[3] J.P. Bell, D.L. Slade and J.H. Dumbleton, *J. Polym. Sci.* **6**, 1773 (1968).

[4] H.E. Bair, R. Salovey and T.W. Huseby, *Polymer* **8**, 9 (1967).

[5] L. Mandelkern and A.L. Allou, *Polym. Lett.* **4**, 447 (1966).

[6] K. Hoashi and T. Machizuki, *Makromol. Chem.* **100**, 78 (1967).

[7] J.P. Bell and J.H. Dumbleton, *J. Polym. Sci., Part A-2* **7**, 1033 (1969).

[8] W.G. Harland, M.M. Khadr and R.H. Peters, *Polymer* **13**, 13 (1972).

[9] P.J. Lemstra, T. Kooistra and G. Challa, *J. Polym. Sci., Part A-2* **10**, 823 (1972).

[10] P.J. Lemstra, A.J. Schouten and G. Challa, *J. Polym. Sci., Polym. Phys. Ed.* **12**, 1565 (1974).

[11] F.J. Hybart and C. Noel, *J. Chim. Phys.-Chim. Biol.* **69**, 874 (1972).

[12] G. Guerra, V. Petraccone, P. Corradini, C. DeRosa, R. Napolitano, B. Pirozzi and G. Giunchi, *J. Polym. Sci., Polym. Phys. Ed.* **22**, 1029 (1984).

[13] K.D. Pae and J.A. Sauer, *J. Appl. Polym. Sci.* **12**, 1901 (1968).

[14] A. Turner-Jones, J.M. Aizlewood and D.R. Beckett, *Makromol. Chem.* **75**, 134 (1964).

[15] F.J. Padden, Jr. and H.D. Keith, *J. Appl. Phys.* **30**, 1479 (1959).

[16] H.J. Leugering, *Makromol. Chem.* **109**, 204 (1967).

[17] D.R. Morrow and B.A. Newman, *J. Appl. Phys.* **39**, 4944 (1968).

[18] R.J. Samuels and R.Y. Yee, *J. Polym. Sci., Part A-2* **10**, 385 (1972).

[19] A.J. Lovinger, *J. Polym. Sci., Polym. Phys. Ed.* **21**, 97 (1983).

[20] D.R. Norton and A. Keller, *Polymer* **26**, 704 (1985).

[21] A.A. Duswalt and W.W. Cox, in 'Polymer Characterization', C.D. Craver (Ed.), Plenum, New York, p. 147 (1971).

[22] J.L. Kardos, A.W. Christiansen and E. Baer, *J. Polym. Sci., Part A-2* **4**, 447 (1966).

[23] K.D. Pal, *J. Polym. Sci., Part A-2* **6**, 657 (1968).

[24] B. Fillon, A. Thierry, J.C. Wittmann and B. Lotz, *J. Polym. Sci., Part B: Polym. Phys.* **31**, 1407 (1993).

[25] L. Mandelkern and A.L. Allou, Jr., *J. Polym. Sci., Part B* **4**, 453 (1966).

[26] P.J. Holdsworth and A. Turner-Jones, *Polymer* **12**, 195 (1971).

[27] R.C. Roberts, *J. Polym. Sci., Part B* **8**, 381 (1970).

[28] G.W. Miller, *Thermochim. Acta* **8**, 129 (1974).

[29] G.E. Sweet and J.P. Bell, *J. Polym. Sci., Part A-2* **10**, 1273 (1972).

[30] J. Boon, G. Challa and D.W. VanKrevelen, *J. Polym. Sci., Part A-2* **6**, 1791 (1968).

[31] P.J. Lemstra, A.J. Schouten and G. Challa, *J. Polym. Sci., Polym. Phys. Ed.* **10**, 2301 (1972).

[32] N. Lanzetta, G. Maglio, C. Marchetta and P. Palumbo, *J. Polym. Sci., Polym. Chem. Ed.* **11**, 913 (1973).

[33] V. Petraccone, C. De Rosa, G. Guerra and A. Tuzi, *Makromol. Chem., Rapid Commun.* **5**, 631 (1984).

[34] C. Passingham, P.J. Hendra, M.E.A. Cudby, V. Zichy and M. Weller, *Eur. Polym. J.* **26**, 631 (1990).

[35] K. Kamide and K. Yamaguchi, *Die Makromol. Chem.* **162**, 205 (1972).

[36] R.J. Yan and B. Jiang, *J. Polym. Sci., polym. Phys. Ed.* **31**, 1089 (1993).

[37] R. Paukkeri and A. Lehtinen, *Polymer* **34**, 4083 (1993).

[38] S.H. Ryu, C.G. Gogos and M. Xanthos, *Polymer* **32**, 2449 (1991).

[39] M. Todoki, *Thermochimica Acta* **93**, 147 (1985).

[40] Y. Maeda, K. Nakajama and H. Kanetsuma, *Polym. J.* **14**, 295 (1982).

[41] M.E. Nichols and R.E. Robertson, *J. Polym. Sci., Polym Phys. Ed.* **30**, 305 (1992).

[42] I.R. Harrison, *Polymer* **26**, 3 (1985).

[43] M.E. Nichols and R.E. Robertson, *J. Polym. Sci., Polym Phys. Ed.* **30**, 755 (1992).

[44] B.C. Edwards, *J. Polym. Sci., Polym Phys. Ed.* **13**, 1387 (1975).

[45] W.G. Harland, M.M. Khadr and R.H. Peters, *Polymer* **15**, 81 (1974).

[46] R.C. Roberts, *Polymer* **10**, 117 (1969).

[47] H.G. Kim and L. Mandelkern, *J. Polym. Sci., Part A-2* **10**, 1125 (1972).

[48] P. Corradini, R. Napolitano, L. Oliva, V. Petraccone, B. Pirozzi and G. Guerra, *Makromol. Chem., Rapid Commun.* **3**, 753 (1982).

[49] A. Celli, A. Fichera, C. Marega, A. Marigo, G. Paganetto and R. Zannetti, *Eur. Polym. J.* **29**, 1037 (1993).

[50] J.J. Janimak, S.Z.D. Cheng, P.A. Giusti and E.T. Hseih, *Macromolecules* **24**, 2253 (1991).

[51] D.T.F. Pals, P. Van Der Zee and J.H.M. Albers, *J. Macromol. Sci.* **B6**, 739 (1972).

[52] J.L. Kardos, E. Baer, P.H. Geil and J.L. Koenig, *Kolloid-Z. & Z. Polym.* **204**, 1 (1965).

[53] B. Wunderlich, 'Macromolecular Physics, Vol. 3, Crystal Melting', Academic Press, New York (1980).

[54] A. Miyagi and B. Wunderlich, *J. Polym. Sci., Part A-2* **10**, 1401 (1972).

[55] W. Ullmann and J.H. Wendorff, *Prog. Colloid Polym. Sci.* **66**, 25 (1979).

[56] J. Varga, *Angew Makromol. Chem.* **104**, 79 (1982).

[57] J. Varga, *J. Thermal Analysis* **31**, 165 (1986).

[58] J. Varga, *J. Thermal Analysis* **35**, 1891 (1989).

[59] G-Y. Shi, B. Huang, Y-H. Cao, Z-Q. He and Z-W. Han, *Makromol. Chem.* **187**, 643 (1986).

[60] G-Y. Shi, X-D. Zhang, Y-H. Cao and J. Hong, *Makromol. Chem.* **194**, 269 (1993).

[61] A. Bunn, M.E.A Cudby, R.K. Harris, K.J. Packer and B.J. Say, *Polymer* **23**, 694 (1982).

[62] M. A. Gomez, H. Tanaka and A.E. Tonelli, *Polymer* **28**, 2227 (1987).

[63] S. Brückner, S.V. Meille, P. Sozzani and G. Torri, *Makromol. Chem., Rapid Commun.* **11**, 55 (1990).

[64] M. Hikosaka and T. Seto, *Polym. J.* **5**, 111 (1973).

[65] Z. Mencik, *J.Macromol. Sci. - Phys.* **B6**, 101 (1972).

[66] G. Natta and P. Corradini, *Nuovo Cimento Suppl.* **15**, 40 (1960).

[67] S. Brückner and S.V. Meille, *Nature* **340**, 455 (1989).

[68] A. Immirzi, *Acta Crystallogr., Sect. B* **36**, 2378 (1980).

[69] B. Lotz and J.C. Wittmann, *J. Polym. Sci., Polym. Phys. Ed.* **24**, 1541 (1986).

[70] B. Lotz, J.C. Wittmann, W. Stocker, S.N. Magonov and H.-J. Cantow, *Polym. Bull.* **26**, 209 (1991).

[71] W. Stocker, S.N. Magonov, H.-J. Cantow, J.C. Wittmann and B. Lotz, *Macromolecules* **26**, 5915 (1993).

[72] C. De Rosa, G. Guerra, R. Napolitano, V. Petraccone and B. Pirozzi, *Eur. Polym. J.* **20**, 937 (1984).

[73] R. Napolitano, B. Pirozzi and V. Varriale, *J. Polym. Sci., Polym. Phys. Ed.* **28**, 139 (1990).

CHAPTER FIVE

Enhancement of the Tensile Properties of iPP Fibers and Spunbonded Fabrics with a Dispersed Silica/Silicone Additive

5.1 Introduction

In the previous chapter, the melting and annealing behavior of a spunbonded iPP fabric that was prepared from a 34 melt flow index iPP resin was investigated. Through a comparison with the melting and annealing behavior of quench-cooled iPP films, it was found that these physical properties are strongly dependent on the structure and morphology of the sample. The degree of orientation that is present in the iPP fibers as well as the level of structural order in the crystalline phase drastically affect its melting behavior which manifests itself as a double endothermic transition in the DSC thermogram. Similarly to the effects on the physical properties, the physical structure of a given fiber influences its mechanical performance.[1,2]

The enhancement of the mechanical properties of spunbonded iPP fabrics is the focus of this investigation. Invariably the evaluation of the mechanical properties of a given fabric starts with the evaluation of its tensile properties. The tensile performance of a spunbonded fabric will be dependent on the tensile properties of the individual fibers as well as on the quality of the bond points. In addition, consideration must be given to the bond point interface.[3-6] To improve the tensile properties of the spunbonded fabrics, the performance of individual fibers is of principal importance. Since the tensile properties of fibers are directly related to their physical structure, the enhancement of their tensile performance requires appropriate modification of the physical structure.

The physical structure of a given polymeric fiber is governed by several features which also influence its mechanical performance.[1,2] The most important features that are associated with the crystalline phase are the degree of order, the orientational order of the crystallites, crystallinity and the distribution of this crystalline phase in the fiber. In the amorphous phase, the degree of chain extension is the most important factor. The modulus of a fiber is known to increase with structural factors such as crystallinity, degree of orientation (amorphous and crystalline), chain stiffness and the level of order in the crystalline phase.[2] Similarly, the tensile strength of a fiber is influenced by factors such as molecular weight, amorphous and crystalline orientation, length and distribution of "tie" molecules and uniformity in thickness and orientation.[2] Therefore, to improve the tensile properties of a fiber, its physical structure must be affected in a manner that promotes beneficial changes in fiber morphology. It should be noted that some of the above features are a consequence of the choice of polymer (*e.g.*, chain stiffness), the characteristics of the resin (*e.g.*, molecular weight) and the processing conditions (*e.g.*, amorphous and crystalline orientation due to sample drawing). However, some of the features can be influenced by acting specifically on the crystalline phase and its development during the process of fiber spinning. The incorporation of additives that alter the overall crystallization kinetics of the polymer, *e.g.*, nucleating agents, can be used to influence the physical structure of the fiber, possibly improving its tensile performance.[7]

Silica particles have been added to several polymers[8-12] and shown to affect their crystallization kinetics under quiescent conditions. The addition of a hydrophilic silica to isotactic poly(propylene oxide) and poly(ethylene oxide) was found to increase the number of primary nuclei during isothermal crystallization.[11,12] Surface modification of the silica particles through a trimethylsilation of its surface silanol groups resulted in a reduction in the number of primary nuclei that formed in both polymers compared to the untreated silica. However, the number of nuclei in the composites prepared with the surface modified silica still exceeded that obtained in the unfilled system.

The influence of the surface treated and untreated silica particles on the crystallization behavior of poly(ethylene terephthalate) and isotactic polystyrene was investigated by Turturro, *et al.*[8-10] An increase in nucleation density was observed in both polymers with the addition of a low concentration of the silica particles. In addition, Turturro[8,10] investigated the effect of silica particle size on the crystallization kinetics of isotactic polystyrene. The concentration of the untreated silica particles in the polymer was maintained constant but its surface area was increased from 50 to 380 m^2/g. Increasing the surface area, by decreasing the size of the silica particles, caused the number of polymer-nucleant interaction sites to increase within a given volume. A greater nucleation density was found in the samples containing the higher surface area, *i.e.*, smaller size, silica particles.

Turturro[8] also demonstrated that the number of silica particles in the filled polymers far exceeded the number of nuclei that were observed in the sample under isothermal crystallization conditions. Therefore, only a very small fraction of the particles that are present in the sample are active nucleating agents. This was also evident in the study of Cole and St-Pierre[12] on heterogeneous nucleation of isotactic poly(propylene oxide). It was suggested by Turturro[8] that individual silica particles group together into clusters, by hydrogen bonding, and this reduces the number of particles that can become effective nucleating sites. Therefore, the efficiency of the silica particles as nucleating agents was found to be dependent not only on the surface characteristics and the particle size, but also on the level of dispersion that can be achieved in the polymer.

The relationship between the quiescent crystallization kinetics of iPP and the structure and properties of the resulting spun filaments was investigated by Lu and Spruiell.[7] The rate of the quiescent crystallization of the homopolymer was increased by the addition of a nucleating agent while slower crystallization was obtained by using a resin that was randomly copolymerized with a small amount of ethylene. It should be noted that the melt flow index (MFI=35) of the iPP resins was maintained constant. Increasing the rate of the quiescent crystallization caused crystallization to occur closer to the spinneret during processing and, thus, at a higher temperature. A filament of lower tenacity and higher elongation-to-break was produced. In addition, the effects were found to be most significant under conditions of low levels of stress (*i.e.*, low "take up" velocities). Similarly, slower quiescent crystallization produced a filament of lower elongation-to-break but higher tenacity. A direct relationship was observed between the quiescent crystallization kinetics and the properties of the spun filaments.

The role of molecular weight distribution (MWD) and MFI of an iPP resin on the structure and properties of melt spun iPP fibers was investigated in detail by Misra and co-workers[13] although their importance had been suggested previously.[14-15][16] Three sets of resins that varied in MFI were investigated where within each of these sets, each containing three resins, the MWD of the individual resins was also varied from a narrow (M_w/M_n=2.8-3.1) to a broad (M_w/M_n=3.8-4.8) distribution. The MFI of the first set of resins ranged from 19 to 22 while the other two ranged from 40 to 45 and 85 to 95. Melt-spun filaments, *ca.* 35 to 45 µm in diameter, were prepared from each of the resins and their tensile properties were evaluated. The following effects were noted on the tensile elastic modulus, tensile strength and elongation-to-break in changing the resin characteristics:[13] Under similar spinning conditions, increasing the weight average molecular weight, *i.e.*, decreasing the MFI, while maintaining the MWD approximately constant produced a filament of higher modulus, tensile strength and elongation-to-break. Similarly, within a given set of MFI resins increasing the MWD produced a filament of higher modulus and elongation-to-break but of lower tensile strength. Therefore, the tensile properties of iPP filaments are strongly affected by the resin characteristics.

Notwithstanding the uses of silica by others as described above, no reported uses in iPP or other polyolefins were found. In fact, studies carried out by Drs. Nohr and MacDonald and other scientists at Kimberly-Clark Corporation demonstrated that silica alone failed to impact improved tensile strength characteristics to iPP. In many cases, the presence of the silica made the spinning of fibers more difficult at best and on occasion plugged die orifices to an extent sufficient to prevent fibers formation.

The purpose of this study was to understand the improvements in the tensile properties of spunbonded iPP fabrics discovered by Drs. Nohr and MacDonald, who used two different approaches. (1) The first method was to specifically target the overall crystallization kinetics of iPP. The nucleating ability, in iPP, of a silica whose surface is modified with polydimethylsiloxane was investigated under quiescent conditions. Particular emphasis was placed on the particle size and level of dispersion. The size of the silica particles was reduced by a ball-milling procedure and attempts were made to generate a better dispersion of the silica particles in the polymer. This was accomplished by dispersing the silica particles in a silicone fluid prior to its incorporation into the iPP. This pre-dispersed, fine-particle surface-modified silica was tested for its ability to enhance nucleation in iPP. It was hoped that a higher nucleation density, under quiescent conditions, would be realized by the addition of this combination and that it would affect the sample morphology and yield improved tensile properties. (2) The second method, also used in conjunction with the first, was to change the MFI and MWD of the iPP resin.

5.2 Experimental

5.2.1 Sample Preparation

The iPP spunbonded fabrics and fibers were prepared by the manufacturing process that was described in Chapter 4. In this investigation, the resin characteristics were changed by blending a 5 melt flow index (MFI) resin with the 34 MFI resin that was used previously in Chapter 4 (*i.e.*, Exxon 1052 and 3445, respectively). The degree of isotacticity for the Exxon 1052 resin, as obtained by NMR, is 94%. In the blend systems, the concentration of the lower MFI resin was varied between 45 and 60 wt %. It should be noted that the fiber denier was maintained constant in this study, between 1.6 and 1.8.

The silica that was used in this investigation was a fumed silica, obtained from Cabot Corporation (Cab-O-Sil TS-720), that was rendered hydrophobic by treatment of the silanol surface with a poly(dimethylsiloxane) fluid. The molecular weight of the poly(dimethylsiloxane) chains on the surface of the silica particles is not known. These silica particles were dispersed in an alkyl poly(dimethylsiloxane) silicone oil. The alkyl substitution on the poly(dimethylsiloxane) backbone was random, ranging from 2 to 11 methylene units.

The silica/silicone additive that was dispersed in the iPP was prepared in the following manner: The size of the surface modified silica particles was reduced by ball milling for three hours per 100 g of silica at room temperature. Steel balls were used in this procedure. This fine particle surface modified silica was then dispersed in the alkyl silicone in an Eiger Mill. Mixing was performed for 15 minutes per liter of silicone in the temperature range between room temperature and 80 °C. The concentration of the silica in the silicone fluid was maintained constant at 5 %.

Twin screw extrusion was used to disperse the silica/silicone additive into the iPP. Extrusion was performed at 70 rpm with several polymer melt zones that ranged in temperature from 190 to 200 °C and a feed rate of 140 kg per hour. The extruded iPP containing the silica/silicone additive was cooled and cut into pellets. These pellets were subsequently used to produce the iPP fibers and spunbonded fabrics. The concentration of the silica/silicone additive in the iPP was maintained constant at 0.3 %.

In addition to the samples that contain the silica/silicone additive, two control samples were considered in this investigation. The first control sample was prepared from only the 34 MFI resin while the second was a 60%/40% blend of a 5 and 34 MFI resins, respectively, neither containing any silica/silicone additive. In subsequent sections, these samples as well as those prepared with the silica/silicone additive will be referred to as described in Table 5.1.

5.2.2 Sample Characterization

5.2.2.1 Tensile Properties

To investigate the tensile properties of single fibers of iPP, they were mounted individually on a previously cut cardboard test pieces. The mounting was performed by gluing the ends of the fibers onto a cardboard form as shown in Figure 5.1. The cardboard mount, containing the single fiber, was clamped onto the Instron tensile tester with a one gram load cell using pneumatic clamps. Once clamped, the cardboard was cut leaving only the single fiber to be tested. The tensile deformation of the single fibers was performed at room temperature using an 8 cm fiber length and a 25 cm/min rate of pull. The reported initial modulus, tensile strength and elongation-to-break are the averages of 25 tensile measurements.

Table 5.1: A Description of the Various Samples that were Investigated.

Sample	Description	
	Polymer	Silica/Silicone Additive
PP34	Exxon 3445	none
PP5	Exxon 1052	none
C60/40	60%/40% Blend of PP5/PP34	none
A0/100	Exxon 3445	0.3% (5% Silica in Silicone)
A45/55	45%/55% Blend of PP5/PP34	0.3% (5% Silica in Silicone)
A50/50	50%/50% Blend of PP5/PP34	0.3% (5% Silica in Silicone)
A55/45	55%/45% Blend of PP5/PP34	0.3% (5% Silica in Silicone)
A60/40	60%/40% Blend of PP5/PP34	0.3% (5% Silica in Silicone)

The grab tensile properties of the spunbonded fabrics were investigated using an Instron with a 50 kg load cell. The fabric was cut into a 4 X 6 inch test piece, with the 6 inch length cut in either the machine or in the cross direction. A 25 cm/min rate of pull at

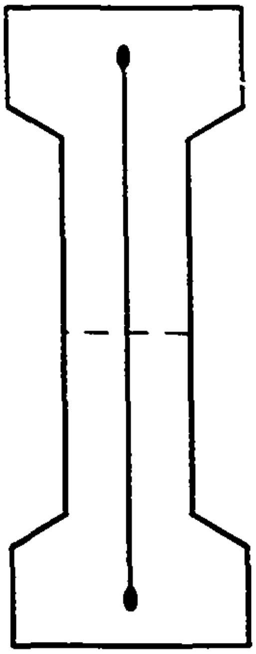

Figure 5.1 Representation of the experimental method used in the analysis of the tensile properties of single fibers. The dashed line represents the cutting of the cardboard piece prior to analysis.

room temperature was also used in these tensile measurements. The reported peak load, peak energy and elongation-to-break are the averages of 10 tensile measurements.

5.2.2.2 Optical Microscopy

A Nikon Optiphot optical polarizing microscope fitted with a Linkam THMS 600 hot stage and a Cohu video camera was used to observe isothermal crystallization at 100 x magnification. The hot stage could be held at constant temperature to within ±0.1 °C of the desired crystallization temperature using the Linkam TMS 91 temperature control unit. Thin slices of the sample were sandwiched between two thin, round glass slides and melted on a hot plate at a temperature of 220 °C while applying pressure. The thickness of the melted film was fixed by a 14 µm aluminum spacer between the glass slides. Films of the order of 15 to 20 µm in thickness were obtained and used to view isothermal crystallization.

The samples were melted in the hot stage at 220 °C for 15 minutes to remove crystallinity. The hot stage was then set to the desired crystallization temperature and cooled at a rate of 130 °C/min. Temperature equilibrium was attained quickly and the growing spherulites were monitored until impingement. The photomicroscopy images of the isothermal crystallization process, as viewed under cross polars, were recorded on a Mitsubishi U80 VCR. The video image was displayed on a secondary monitor by means of a frame grabber board (PCVision Plus) located on an AT computer which translated the video signal to digital format by defining light intensity intervals on a 256 gray level scale through the use of a software program (Java, purchased from Jandel Scientific). The software allowed measurement of the area of any object within a selected region of a frozen image. Area calibration was performed using a pre-recorded scale of known size.

The isothermal radial growth rates, G, were determined by measuring the area of the spherulites as seen in the recorded images as a function of time and converting this area to an average radius. From the average radii, plotted as a function of time, the radial growth rate of the spherulite was determined as the slope of the resulting straight line. For each sample and crystallization temperature, the average radial growth rate was determined from at least four radial growth rate measurements. The experimental error in these growth rates was determined to be less than 5%.

5.2.2.3 Differential Scanning Calorimetry

The crystallization behavior of the various iPP samples was investigated on the Perkin Elmer DSC-7C under isothermal and non-isothermal conditions. The samples were prepared for thermal analysis by cutting thin slices from iPP pellets. Isothermal crystallization was performed by melting 3 to 4 mg of the iPP sample at 220 °C for 15 minutes and quenching the sample at a nominal rate of 300 °C/min to the desired crystallization temperature. Data acquisition was initiated following temperature equilibration. Non-isothermal crystallization of the various iPP samples was performed by first heating the iPP to 220 °C and maintaining this temperature for 15 minutes to destroy all signs of crystallinity and then lowering the temperature at a constant rate of 20 °C/min.

The melting behavior of the spunbonded iPP fabrics was investigated as described in Chapter 4.

5.2.2.4 Solid State NMR Spectroscopy

The ^{13}C and ^{29}Si CP/MAS NMR spectra of the surface modified silica were recorded at room temperature with a Chemagnetics CMX-300 spectrometer operating at a static field of 7.1 T. The samples were spun at the magic angle in the frequency range between 3.8 and 4.5 kHz in a 7.5 mm OD zirconia rotor. A 62.5 kHz rf decoupling field was used in obtaining these spectra which were zero-filled to 4K prior to Fourier transformation. The ^{13}C and ^{29}Si spectra were obtained with a 2 ms and 5 ms contact time, respectively. A 3 second pulse delay was used in obtaining both of the above spectra. The proton spectrum of the surface modified silica was obtained using a single-pulse pulse sequence in a 100 kHz spectral window with a 3 second pulse delay. All spectra were referenced to tetramethylsilane (TMS) by setting the methyl resonance of hexamethyl benzene to 17.40 ppm. In obtaining the ^{13}C, ^{29}Si and proton spectra of the surface modified silica, 736, 16000 and 56 free induction decays (FID) were collected. The ^{29}Si CP/MAS NMR spectrum of the virgin silica, Cab-O-Sil M5, was obtained under the conditions that were described for the surface modified silica and represents the co-addition of 9500 FID.

The measurements of the proton spin-lattice relaxation times in a rotating frame for the spunbonded iPP fabrics and fibers were performed as described in Chapter 3. The thermal annealing of the spunbonded fabrics was performed as described in Chapter 4.

5.2.2.5 Infrared Spectroscopy

The surface modification of the silica particles was identified by infrared (IR) spectroscopy using the Perkin Elmer 1600PC by collecting 128 scans at a resolution of 4 cm^{-1}. The silica particles were dispersed in carbon tetrachloride (CCl_4) to produce a slurry which was placed in a liquid sample holder.

5.2.2.6 Electron Microscopy

The size distribution of the silica particles as well as their dispersion in the silicone fluid and in iPP were investigated by bright field scanning transmittance electron microscopy (STEM) using a Jeol 100cx STEM microscope. The fine particle silica was dispersed in methanol at a concentration of approximately 0.1 %. A drop of the silica slurry was placed onto the surface of carbon coated TEM hexagonal grids. The methanol was allowed to evaporate and the silica particles were observed in bright field. Bright field imaging was performed by placing an aperture in the back of the focal plane of the objective lens to stop all electrons which are scattered above a certain angle. Regions of the specimen that are thicker or of higher density scatter more strongly and appear darker in the image. The absence of a specimen in the path of the electrons produces a bright image.

The dispersion of the silica particles in the alkyl silicone was investigated by cryo-microtoming thin sections of the mixture. A drop of the silica/silicone mixture was placed on a sample holder that was maintained at liquid nitrogen temperature. The liquid solidified immediately on coming into contact with the holder. The sample holder containing the frozen sample was then mounted on the FC4 Reichert-Jung cryo-ultramicrotome set at liquid nitrogen temperature. Thin slices of approximately 500 Å in thickness were collected and placed under vacuum (10^{-7} torr) at liquid nitrogen temperature. Gold was evaporated onto the surface of the thin section at an angle of 30°. The sample was then transferred to the STEM and observed in bright field.

The dispersion of the silica in the iPP was investigated by cryo-microtoming the iPP fibers into thin sections (400 Å) and observing the silica particles in bright field. The method used to microtome thin sections of the iPP fibers was the same as that described in Chapter 2 for the study of quench-cooled iPP films.

The STEM dark field investigation of the crystalline morphology of the iPP fibers and spunbonded fabrics was performed as described in Chapter 2 for the quench-cooled films.

5.3 Results and Discussion

In the Introduction, it was noted that particular emphasis would be placed on the size of the silica particles as well as on the level of dispersion that could be achieved in the polymeric matrix. Therefore, prior to the evaluation of the effect of this additive on the crystallization kinetics and on the tensile properties of spunbonded fabrics, the surface modification of the silica as well as the size and dispersion in the silicone fluid and iPP were investigated.

5.3.1 Characterization of the Chemically Modified Silica

5.3.1.1 Surface Modification

The surface modification of the ball milled silica was characterized by solid state NMR spectroscopy to confirm the type and extent of surface modification produced on the virgin silica. The ^{29}Si and ^{13}C CP/MAS NMR spectra as well as a ^{1}H single pulse NMR spectrum of the ball milled surface modified silica are presented in Figure 5.2. In addition, a ^{29}Si CP/MAS NMR spectrum of CAB-O-Sil M-5, the unmodified silica, is presented in Figure 5.2 as a reference material. The ^{29}Si CP/MAS NMR spectrum of

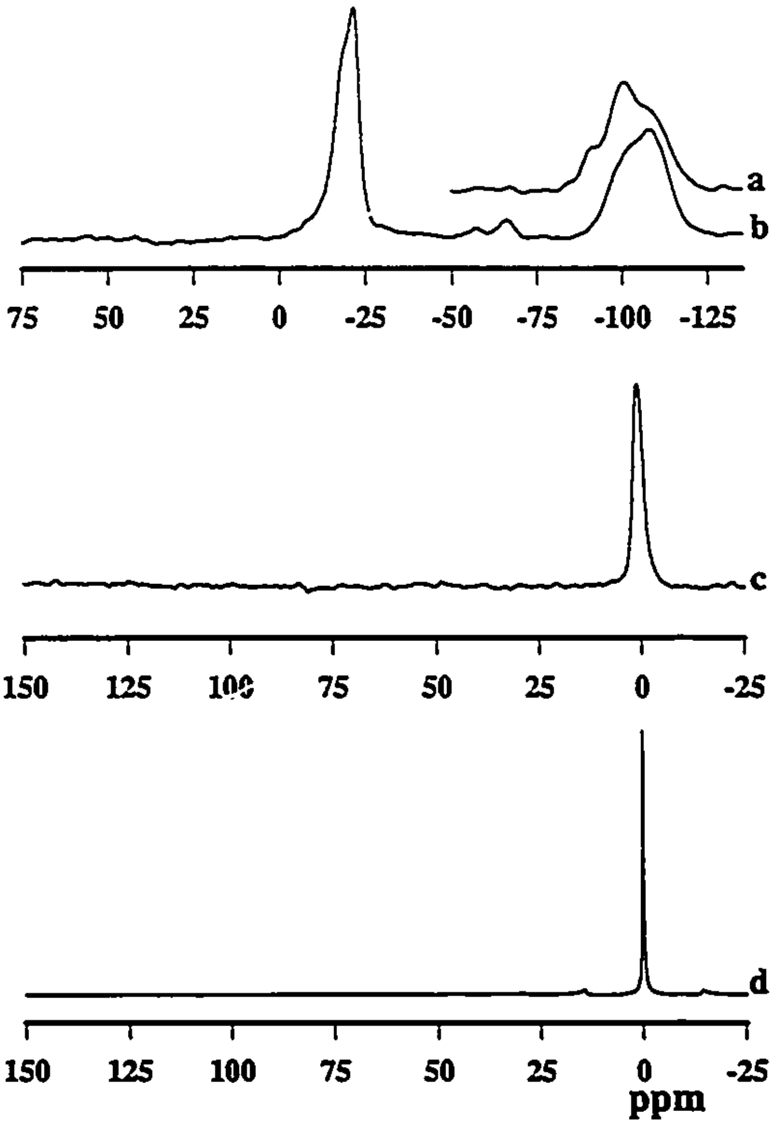

Figure 5.2 (a) ^{29}Si CP/MAS NMR spectrum of Cab-O-Sil M5 hydrophilic silica (b) ^{29}Si CP/MAS NMR spectrum of polydimethylsiloxane surface modified silica (c) ^{13}C CP/MAS NMR spectrum of polydimethylsiloxane surface modified silica (d) ^{1}H single pulse NMR spectrum of polydimethylsiloxane surface modified silica.

virgin silica gel is characterized by three NMR resonances:[17] geminal silanol groups (-91 ppm), silanol groups (-100 ppm) and siloxane groups (-109 ppm) referenced to TMS. The ^{29}Si NMR spectrum of the M-5 virgin silica presented in Figure 5.2a clearly shows these three resonances. It is of interest that, unlike infrared spectroscopy, NMR characterization of a silica gel allows the differentiation between free and geminal silanol groups. However, due to drastically different optimum contact times between the three NMR resonances,[17] signal quantification is a major drawback of this characterization method. This large difference in the optimum contact time for each of these ^{29}Si resonances is due to large differences in relaxation times.

Modification of the silica surface, as discussed by Albert and Bayer,[17] results in additional resonances whose chemical shifts are dependent on the functionality of the added silanes. These surface moieties can be distinguished by ^{29}Si CP/MAS NMR.[18-23] The chemical modification of virgin silica with a monofunctional silane yields a surface species that is observed in the ^{29}Si CP/MAS NMR spectrum at a chemical shift of *ca.* 12 ppm. Similarly, the chemical shift of the surface species obtained upon derivatization of virgin silica gel with a difunctional silane is between -4 and -22 ppm while a silica gel that is derivatized with a trifunctional silane will show resonances between -40 and -70 ppm. In addition, resonances associated with the remaining silanol and siloxane groups of the native silica gel are also observed in the spectrum of the modified silica.

The ^{29}Si CP/MAS NMR spectrum of the surface modified silica gel (Figure 5.2b) reveals two large peaks, at -19 and -23 ppm, consistent with the polydimethylsiloxane surface modification reported by the manufacturer. In addition, two small peaks at chemical shifts of -57 and -66 ppm are present in the region that is characteristic of a silica modification with a trifunctional silane. It should be noted that these two small peaks correspond to only approximately 5% of the total intensity observed for this sample. Finally, the resonances due to the native silica can be seen in the chemical shift region between -100 and -110 ppm. This region no longer shows a resonance for geminal silanol groups at -90 ppm and shows a greatly diminished silanol peak at -100 ppm. In fact, the intensity in this region corresponds mainly to the siloxane groups at a chemical shift of -109 ppm. Therefore, the ^{29}Si solid state NMR spectrum of the surface modified silica indicates that the surface modification of the silica particles is incomplete. However, as discussed previously, signal quantification is a major drawback of this characterization method due to drastically different optimum contact times between the silanol and siloxane groups. While the optimum contact time of the silanol groups is 5 to 8 ms, in the case of the siloxane groups it is 22 to 25 ms.[17] Since a contact time of 5 ms was used in this investigation, the peak that is due to the silanol group (-100 ppm) appears intense with respect to that of the siloxane group which suggests that a large number of surface silanol groups remain on the surface. However, this apparent large intensity for the silanol peak is simply due to a mismatch in optimum contact time for the two groups. Although the surface modification is incomplete, the number of remaining surface silanol groups is not nearly as large as suggested from a visual inspection of the intensity of these two peaks.

In the ^{13}C CP/MAS NMR spectrum of the surface modified silica, presented in Figure 5.2c, only a single sharp resonance is observed at 1 ppm, referenced to TMS, consistent with the occurrence of only methyl substituents in the sample. The ^{1}H spectrum of the modified silica (Figure 5.2d) also only shows one very sharp resonance at 0 ppm which confirms the existence of only methyl modification on the silica surface. The two small peaks on either side of this main resonance are spinning side bands corresponding to a spinning speed of 4500 Hz. Together with the ^{29}Si spectrum of the surface modified silica, these spectra confirm a polydimethylsiloxane surface modification.

The surface modification of the silica particles was also characterized by infrared (IR) spectroscopy (Figure 5.3). The IR spectrum of the virgin silica shows two bands in the frequency range between 2900 and 3900 cm^{-1} due to hydrogen bonded hydroxyl groups (3674 cm^{-1}) and molecular water that is weakly physisorbed onto the silica surface

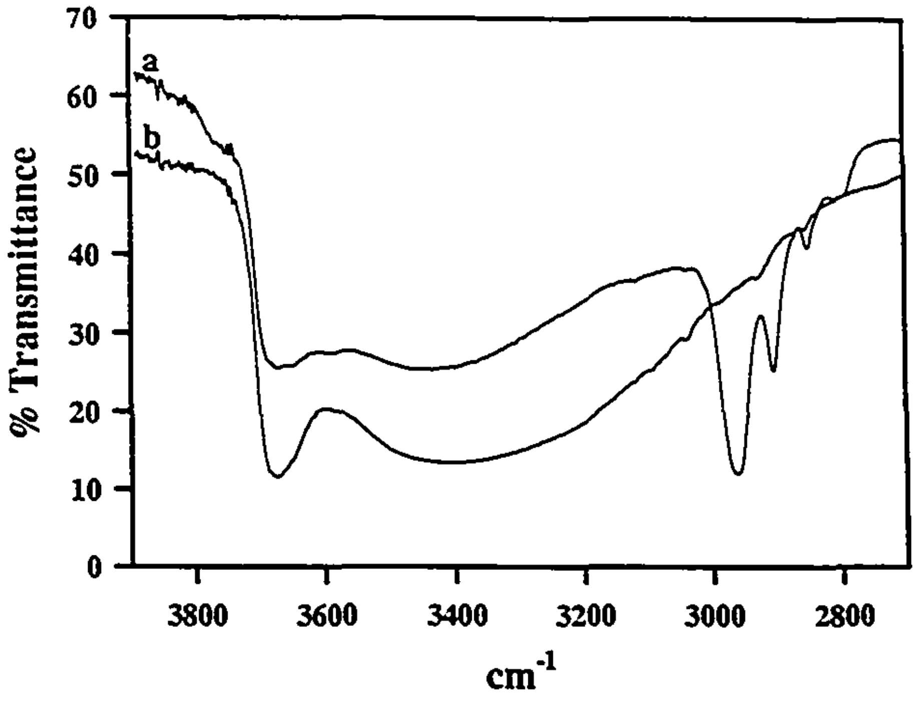

Figure 5.3 Infrared spectrum of (a) Cab-o-Sil TS-720 surface modified silica and (b) Cab-o-Sil M5 virgin silica.

(3400 cm^{-1} centered broad band). The same bands are observed in the spectrum of the surface modified silica which confirm the incomplete removal of surface hydroxyl groups. In addition, several bands are observed in the frequency range between 2800 and 3000 cm^{-1} which are the symmetric and asymmetric CH stretching frequencies associated with the polydimethylsiloxane substitution on the silica surface.[24]

5.3.1.2 Dispersion of the Surface Modified Silica in iPP

The size of the silica particles was monitored from the initial ball milling procedure to its dispersion in the silicone copolymer and finally into the iPP. A high magnification transmission electron micrograph of the surface modified silica particles obtained after the ball milling procedure is presented in Figure 5.4. As is apparent from this electron micrograph, the silica powder is composed of small primary particles. These particles appear fused to each other forming larger aggregates that range in size from less than 0.1 μm to as large as 1 μm. Since the shape of the particles varies throughout the sample, an accurate determination of the distribution in size of the silica particles is not possible. However, it is clear from the electron micrograph that the silica powder that is to be dispersed in the iPP is composed of sub-micron particles with a distribution in size.

A high magnification electron micrograph of the silica particles dispersed in the alkyl silicone is presented in Figure 5.5. In addition to a very good dispersion of the silica particles within the silicone oil, the size of the silica particles remains unchanged from that observed in Figure 5.4. A distribution in the size of the silica particles is noted with some indication of the existence of primary particles dispersed throughout the silicone. In addition, the bundles of particles that are observed in certain regions are consistent in size with the aggregates that were observed for the silica after it had been ball milled (Figure 5.4).

The level of dispersion of the silica particles that is obtained in the spun iPP fibers was also investigated by electron microscopy and is presented in Figure 5.6. The silica particles, seen as the black regions, are well dispersed within the iPP matrix and the size of the particles remains in the sub-micron range. Therefore, an important goal was realized in that the dispersion of the silica in the silicone prior to its incorporation into the iPP aided in maintaining the size of the fine particle silica.

5.3.2 Crystallization Kinetics

The effect of the silica/silicone additive on the crystallization kinetics of polypropylene was investigated by DSC and optical microscopy, both non-isothermally

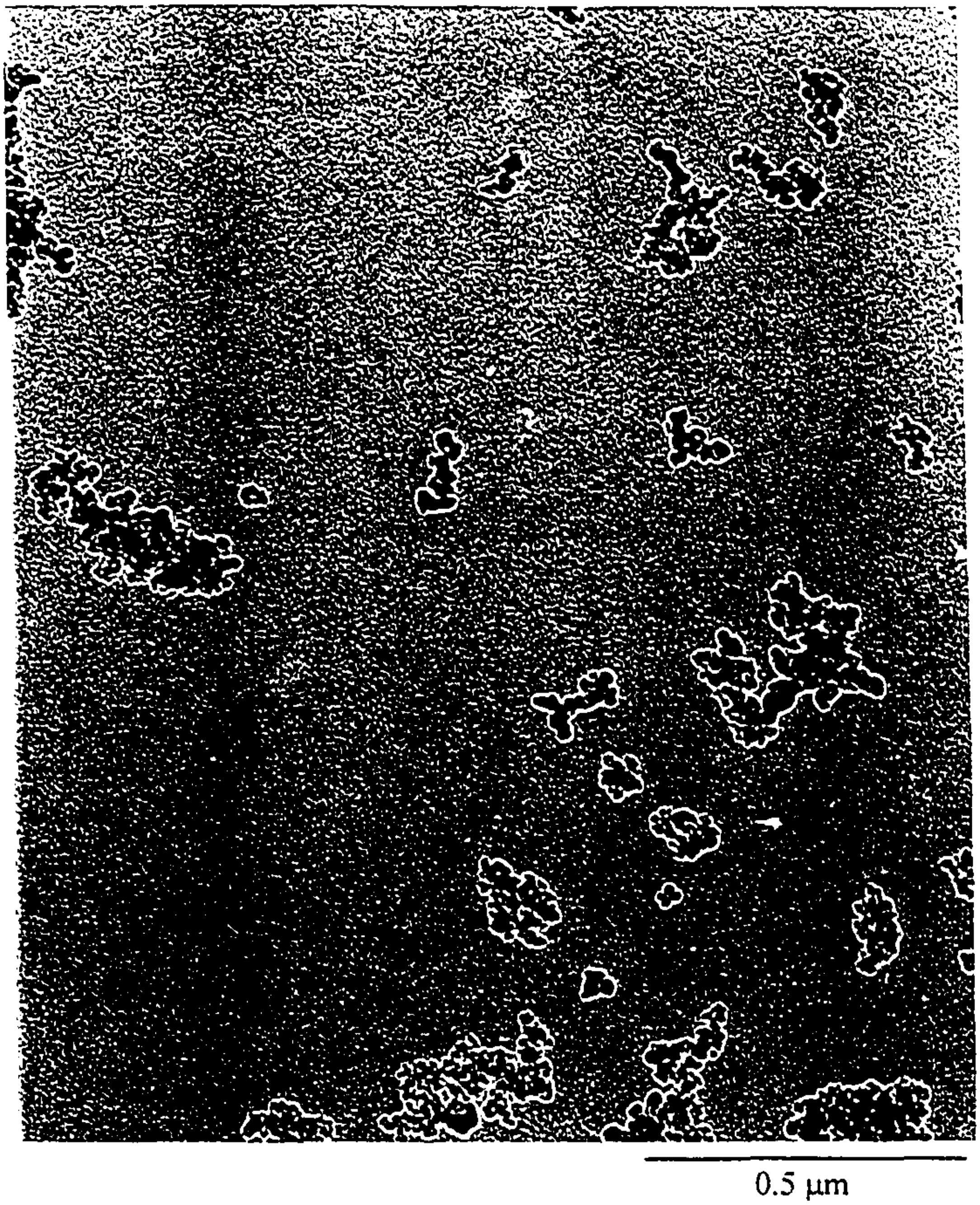

Figure 5.4 Electron micrograph of the silica particles at 100,000X magnification after ball milling for 3 hours at room temperature.

Figure 5.5 Electron micrograph of the silica particles dispersed in the alkyl silicone copolymer at a magnification of 300,000X. The silica particles were dispersed in an Eiger mill for 1 hour between room temperature and 80 °C.

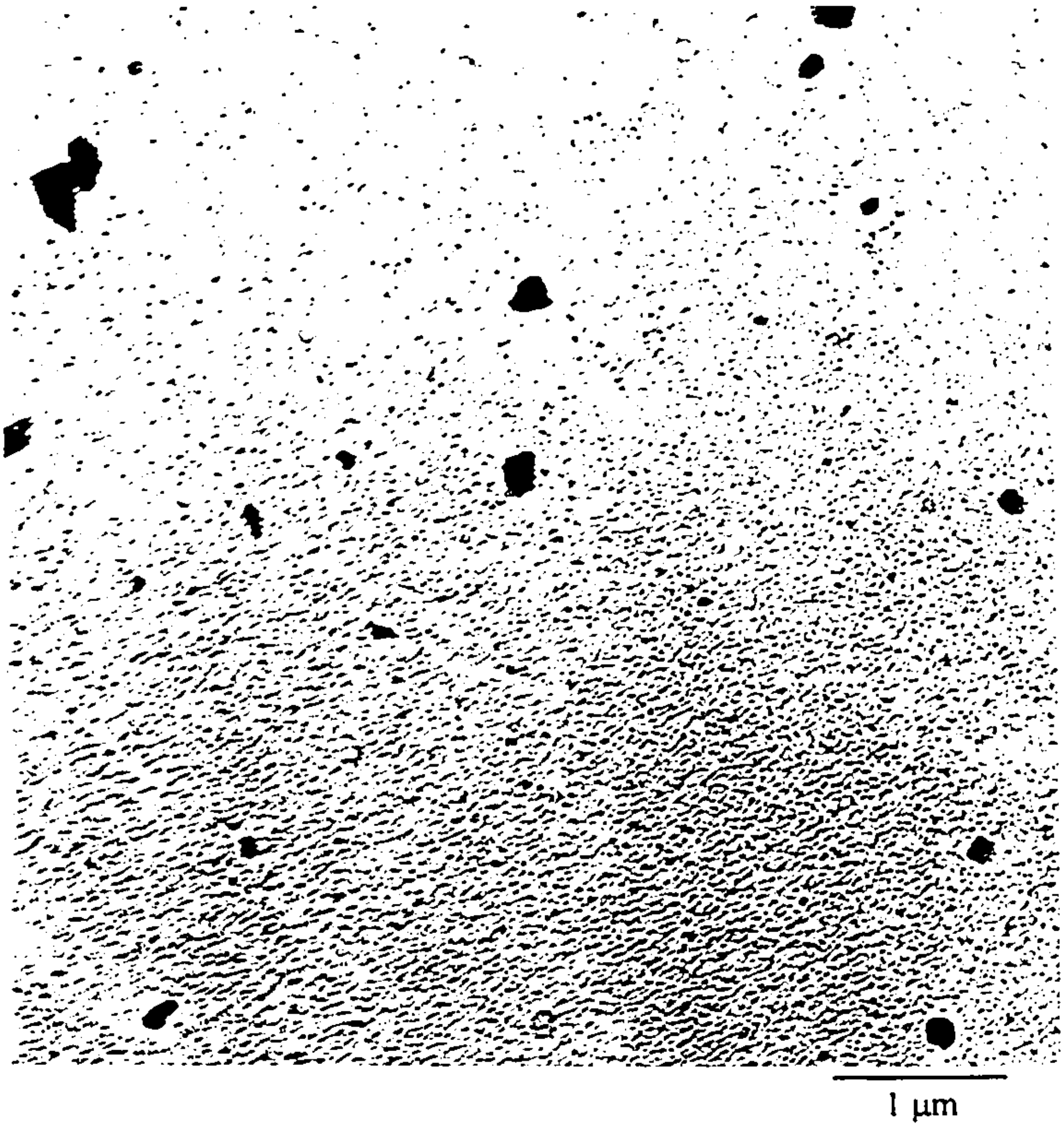

Figure 5.6 Bright field electron micrograph at a magnification of 20,000X of the silica particles dispersed in iPP.

and isothermally. The DSC thermogram for the cooling from 230 °C to room temperature, at a rate of 20 °C/min, is presented in Figure 5.7 for both PP34 and A60/40. The thermograms demonstrate a shift to higher temperature of both the onset temperature for crystallization and peak minimum. A 3 °C shift in temperature were recorded. The measured crystallinities of these samples were found to be essentially equal at *ca.* 68%.

The crystallization kinetics of the various iPP samples was also investigated by DSC under isothermal conditions and analyzed using the Avrami[25-27] treatment that was simplified by Evans[28] and put into polymer context by Meares[29] and Hay.[30] In general the progress of isothermal crystallization is expressed by

$$\ln(1-\chi_t) = -K t^n \qquad (5.1)$$

or

$$\log[-\ln(1-\chi_t)] = \log K + n \log t \qquad (5.2)$$

where χ_t is the volume fraction of crystalline material or degree of crystallinity, K, is the overall rate constant containing the nucleation and growth parameters, n, is an integer that depends on the mechanism of nucleation and on the form of crystal growth and, t, is time. The Avrami parameter, n, generally assumes values between 1 and 4 and describes the crystallization mechanism. The form of the crystal growth (*i.e.*, rods, discs, or spheres) as well as the type of nucleation (*i.e.*, predetermined or sporadic) are described by this Avrami parameter. The form of the overall rate constant, K, is dependent on the type of nucleation as well as on the form of the crystal growth due to different representations of the volume fraction of the crystalline phase.[30] However, in general, this rate constant is a combination of a nucleation density term and the growth rate of the crystalline entities. The Avrami parameters, n and K, are obtained from the slope and intercept, respectively, of the straight line that is generally obtained from plotting $\log[-\ln(1-\chi_t)]$ against $\log t$. It should be noted that linearity is frequently limited to low degrees of crystallinity.

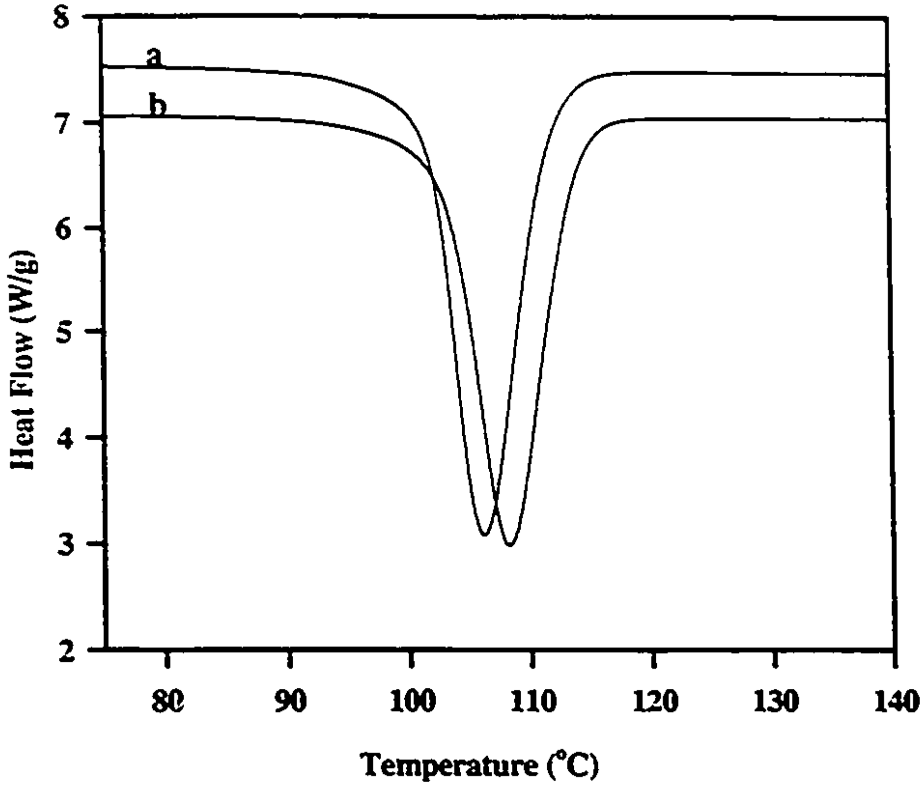

Figure 5.7 DSC thermograms for the cooling, at a rate of 20 °C/min, of (a) PP34 and (b) a 60%/40% blend of PP5/PP34 with the silica/silicone additive.

The crystallization kinetics of iPP with and without the silica/silicone additive were investigated under isothermal conditions in the temperature range between 120 and 126 °C. A typical DSC thermogram for the isothermal crystallization of PP34 is shown in the inset in Figure 5.8. Similar thermograms were obtained for all of the iPP samples that were investigated. To monitor the extent of conversion as a function of time, the

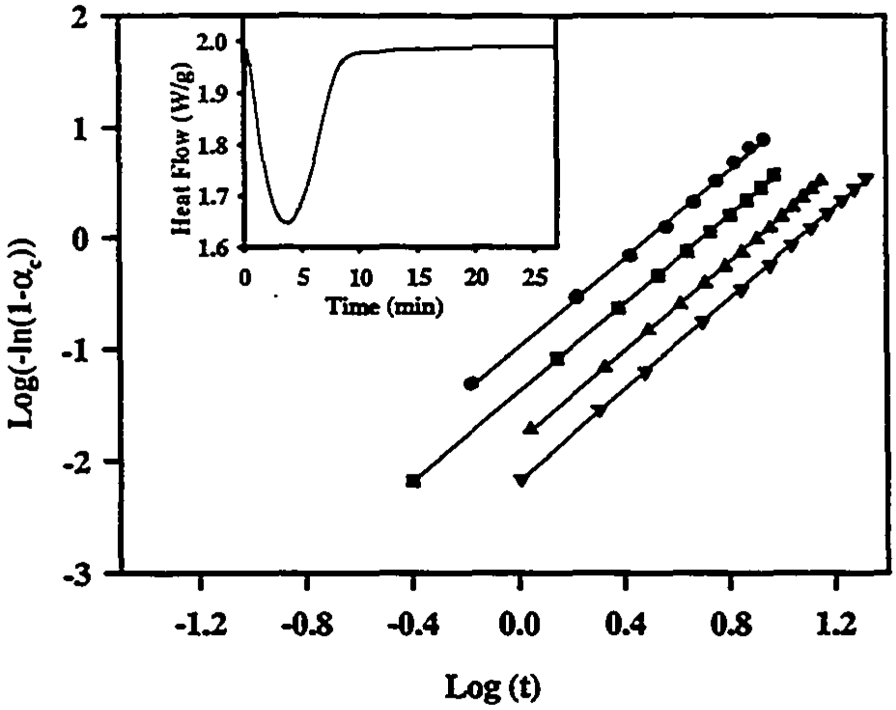

Figure 5.8 Plot of Log{-Ln[1-α(t)]} as a function of the Logarithmic of time for isothermally crystallized PP34 at (Circle) 120, (Square) 122, (Triangle) 124, (Inverted Triangle) 126 °C. The inset is a typical DSC thermogram obtained upon isothermally crystallizing iPP.

exotherm was sliced at various time intervals and the increase in ΔH, normalized to the total ΔH for complete isothermal crystallization, was plotted as a function of time. Sigmoid-shaped curves that ranged between 0 and 1 were obtained for all samples at all crystallization temperatures.

To obtain the Avrami parameters, K and n, the $\log[-\ln(1-\chi_t)]$ was plotted against $\log t$, as demonstrated in Figure 5.8. As is clearly evident from equation (5.2), the slope of the resultant straight line yields n while the intercept is equal to log K. These parameters were obtained for various iPP samples and at crystallization temperatures in the range between 120 and 126 °C. (The rate constant, K, that was obtained for these samples is presented in a subsequent section.) The Avrami index n was found to vary between 2 and 3 for both PP34 and PP5 as well as samples containing the silica/silicone additive for all of the investigated crystallization temperatures. For iPP, the Avrami index, n, has been reported in the range between 2.0 and 4.1.[8,31] The indices that were obtained in this study are in the lower portion of this range and are non-integral. As discussed by Meares,[29] a non-integral value for the Avrami index n suggests that more than a single nucleation process or form of crystal growth is occurring simultaneously. Since iPP is a polymorphic material and heterogeneous and homogeneous nucleation can occur simultaneously, the value of this index is unreliable in evaluating the nucleation and/or growth mechanism.

The overall rate of crystallization can be evaluated by noting the time for half of the crystallization to be completed, *i.e.*, the point of 50% conversion. By substituting $\chi_t = 0.5$ into equation (5.1), the following relation is obtained for the half-time of crystallization:

$$t_{1/2} = [\ln 2/K]^{1/n} \qquad (5.3)$$

Using the previously derived Avrami parameters, K and n, the half time of crystallization is easily evaluated. The overall rates of crystallization, $(t_{1/2})^{-1}$, are presented in Figure 5.9 for the isothermal crystallization, in the temperature range between 120 and 126 °C, of PP34, PP5, and A60/40. As expected, the rate of crystallization increases with an increase in the degree of supercooling. At all temperatures, essentially the same rates of crystallization are obtained for PP34 and PP5. However, the addition of the silica/silicone additive to

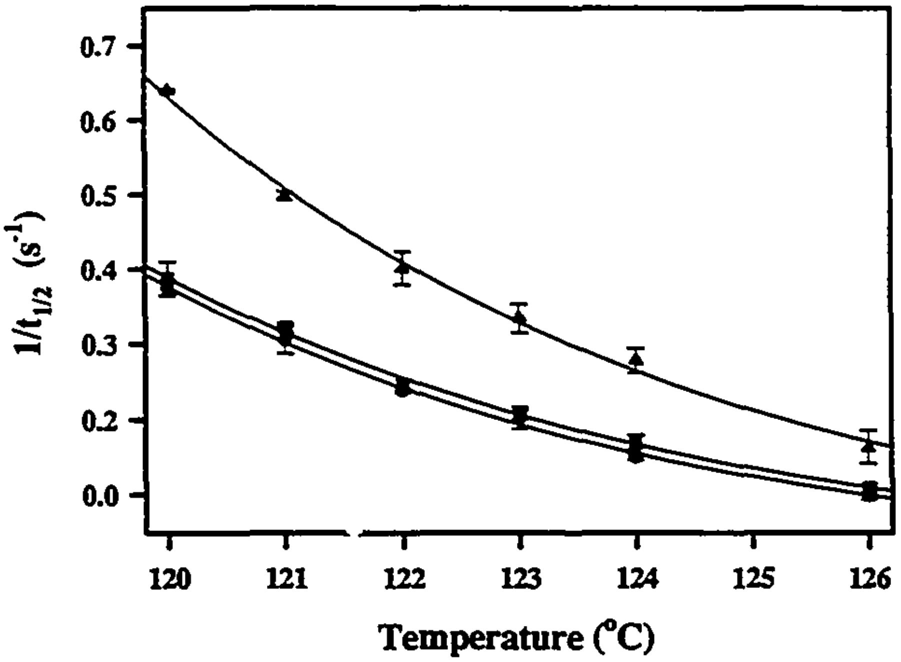

Figure 5.9 The inverse of the half-time of crystallization as a function of temperature for (Circle) PP34, (Square) PP5, and (Triangle) a 60%/40% blend of PP5/PP34 with the silica/silicone additive.

the 60%/40% blend of these two resins (*i.e.*, A60/40) increases dramatically the rate of crystallization at all crystallization temperatures. Identical behavior was also noted in the overall rate constant, K, obtained from the double logarithmic plot (Figure 5.10). Indeed, this rate constant is substantially larger for the polymer system containing the silica/silicone additive. Since this rate constant contains information concerning both nucleation and growth, the increased rate may be due to either of these parameters.

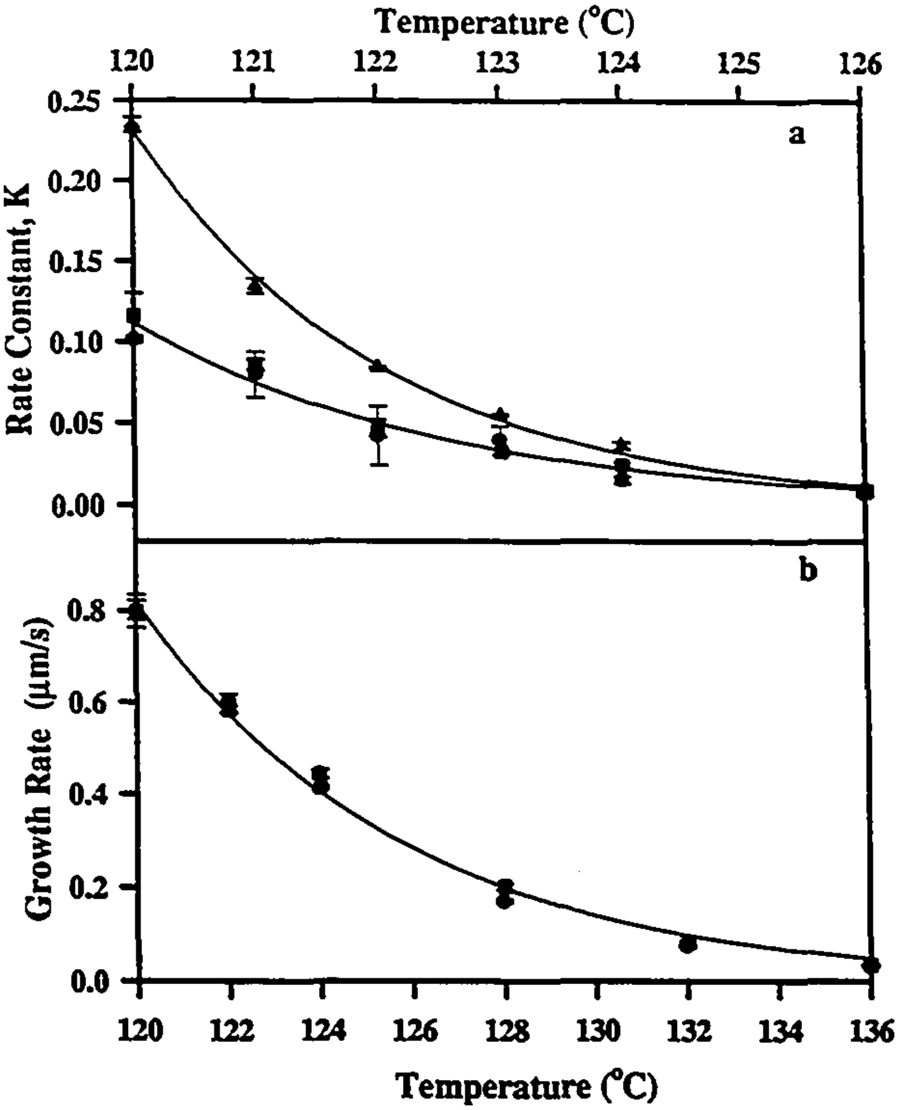

Figure 5.10 (a) Rate constant, K, obtained from the Avrami analysis of isothermally crystallized (Circle) PP34, (Square) PP5, and (Triangle) a 60%/40% blend of PP5/PP34 with the silica/silicone additive. (b) Temperature variation of the growth Rate of iPP spherulites of isothermally crystallized (Circle) PP5, and (Square) PP5 with the silica/silicone additive.

Radial growth rate measurements of individual spherulites were performed by optical microscopy in the temperature range between 120 and 136 °C for PP5 with and without the silica/silicone additive. The radial growth rates are presented as a function of the crystallization temperature in Figure 5.10. It is clear from this figure that the addition of this additive does not affect the growth rate of individual iPP spherulites. Therefore, the increase that is observed in the overall rate constant, K, as well as in $(t_{1/2})^{-1}$ must be due to an increase in the primary nucleation density. Thus, there is unequivocal evidence that under isothermal conditions the silica/silicone additive is acting as a nucleating agent for iPP spherulites.

5.3.3 Isotactic Polypropylene Fibers

5.3.3.1 Tensile Properties

In this investigation, the evidence for enhancement in the tensile properties of iPP single fibers is based on a comparison with the tensile properties of fibers prepared from PP34. However, the resin characteristics were changed in some samples by blending this resin with a low MFI resin (*i.e.*, PP5). The MFI as well as MWD data for PP34 and PP5 as well as a 60% / 40% blend of these two resins are presented in Table 5.2. As can be seen, the blending of the PP34 and PP5 resins results in an intermediate MFI, MWD and average molecular weights. Since the tensile properties of the fibers are compared to those prepared from PP34, a comparison between the resin characteristics of PP34 and C60/40 indicates a decrease in the MFI and an increase in the resin MWD through a decrease in M_n and an increase in M_w.

The tensile properties of iPP single fibers, 20 μm in diameter on the average, are presented in Table 5.3. The initial modulus, tensile strength and elongation-to-break are reported for three different iPP fibers; namely, PP34, C60/40 and A60/40. The first two samples examine the effect of changing the resin characteristics. Indeed, decreasing the MFI and simultaneously increasing the MWD within the range reported in Table 5.2 does not affect the tensile properties of the resultant fibers. The initial modulus, tensile strength and elongation-to-break are identical to that of the PP34 fibers.

Table 5.2: MFI and Average Molecular Weights for PP34, PP5 and C60/40.

Sample	MFI	M_n	M_w	M_z	M_w/M_n
PP34	34	50,000	144,600	300,000	2.9
PP5	5	45,200	212,200	562,000	4.7
C60/40	18-20	46,200	158,800	404,600	3.4

Table 5.3: Tensile Properties of iPP Single Fibers.

Sample	Diameter (μm)	Modulus (GPa)	Tensile Strength (MPa)	Elongation (%)
PP34	20.3±0.6	2.1±0.2	192±38	198±34
C60/40	19.2±0.1	2.0±0.2	162±18	184±22
A60/40	21±1	4.7±0.3	340±23	636±26

As discussed previously, the role of MWD and MFI of an iPP resin on the structure and properties of melt spun iPP fibers was investigated by Misra and co-workers.[13] They reported increases in the tensile properties of spun fibers upon decreasing the MFI while maintaining the MWD approximately constant and vise versa. However, those trends were noted as a result of large variations in the MFI and MWD, *i.e.*, 19 to 95 in the former and 2.8 to 4.8 in the latter. These ranges are substantially larger than the change in resin characteristics (Table 5.2) that were induced in this investigation through the blending of two iPP resins. However, of the nine iPP resins investigated by Misra and co-workers,[13] two resins have characteristics (*i.e.*, MFI and MWD) that are very similar to the ones investigated in this study. When the tensile properties of fibers prepared from those two resins are compared, a small increase of 60% is observed in the elongation-to-break while the modulus and tensile strength remained essentially unchanged.[13] The 60 % increase in elongation-to-break that was reported by Misra and co-workers[13] was not observed in this study, possibly due to differences in processing conditions. Therefore, within the MFI and MWD range listed in Table 5.2, decreasing the MFI and broadening the MWD does not appear to influence the tensile properties of iPP fibers.

As seen from Table 5.3, addition of the silica/silicone additive to the blend produces a significant increase in tensile properties. The initial modulus, tensile strength and elongation-to-break increase by 123, 77 and 221 %, respectively, compared to fibers prepared from PP34. This dramatic increase in tensile properties must be related to the nucleating effects of the additive that were observed under quiescent conditions.

Representative stress-strain curves for single fibers prepared from PP34 and A60/40 are presented in Figure 5.11. These curves clearly demonstrate a significant difference in tensile deformation properties of these two fibers. The stress-strain curve for PP34 shows a steady, almost linear increase in stress with elongation and does not pass through a maximum, nor does it attain a plateau. The general pattern indicates brittle fracture. The A60/40 fibers show an initial region of linear increase, a plateau region that persists for a period of time and finally an increase in the stress at high elongation prior to fracture. Following the initial region of linear increase, a yield point is observed at approximately 120 % elongation with no indication of "necking". The plateau region corresponds to permanent deformation at constant volume, or cold drawing. The increase

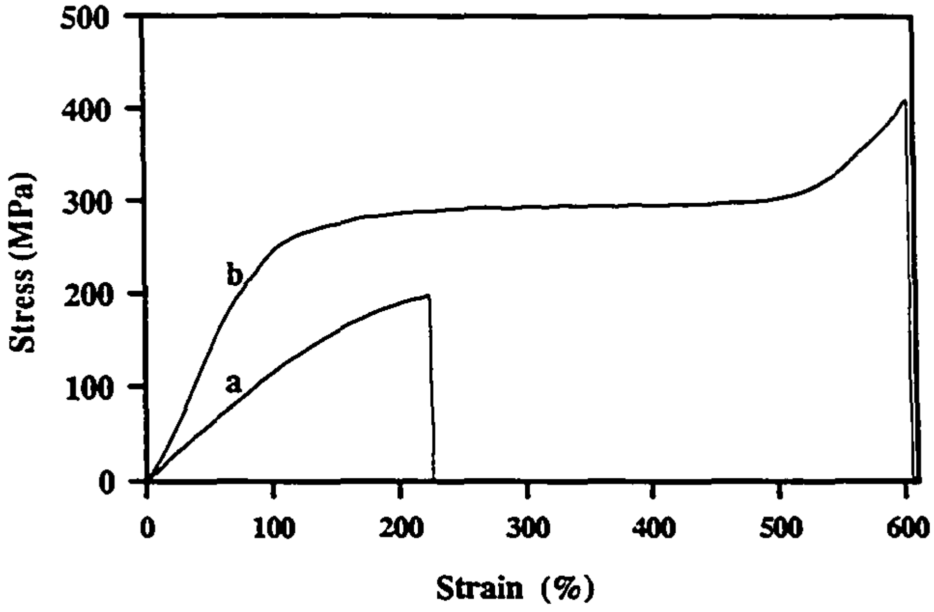

Figure 5.11 Stress-strain curves for iPP single fibers that were prepared from (a) PP34 and (b) A60/40.

in stress after this cold draw region is due to strain-induced crystallization, *i.e.*, it involves the alignment of elongated chains.[32] The general pattern of this sample is very much similar to that of a good elastomer. Therefore, the dispersion of the silica/silicone additive system as well as possible concomitant effects from the addition of a low MFI resin modifies the tensile properties of the resultant fibers from behavior characteristic of brittle fracture to that of a good elastomer. This change in mechanical behavior must be related to changes in the morphology of the fibers due to the addition of the silica/silicone additive, a nucleating agent for iPP.

5.3.3.2 Morphology of iPP Fibers

The crystalline phase of the spun iPP fibers was investigated by scanning transmittance electron microscopy (STEM) in cryo-microtomed sections that were sliced in both the longitudinal and cross-sectional directions. This investigation was performed on fibers prepared from PP34 as well as A60/40, which gave excellent tensile properties. STEM dark field images that present the crystalline phase of the iPP fibers in the longitudinal and cross-sectional directions are shown in Figure 5.12. A STEM dark field image of the crystalline morphology in the longitudinal direction of iPP fibers that were prepared from PP34 was presented previously in Figure 4.24. As can be seen from these micrographs, in the longitudinal direction the crystalline phase is oriented in the fiber direction, as is clearly seen by the long white regions. In the cross-sectional direction, small crystalline regions are noted throughout the micrograph. From a visual comparison of Figures 4.24 and 5.12, the level of orientation in the crystalline phase in the fiber direction appears to be higher for fibers prepared from A60/40 than PP34. The combination of the longitudinal and cross-sectional micrographs suggests that the crystalline morphology is consistent with a fibrillar or cylindritic type of supermolecular structure. A cylindritic morphology[33] is generally formed by crystallization of a melt under mechanical stress, as is the case in the fiber spinning process. The process involves ordering of extended chains into bands that can act as a nucleus for crystallization, the formation of row nucleation and the development of the cylindritic morphology.

The size of the crystals that are observed in the cross-sectional direction were measured at the surface, mid-radius and core of the fiber for both of the above mentioned samples. The crystalline entities in the fibers prepared from PP34 were found to be essentially constant in size from the surface to the core of the fiber. Crystal sizes ranged between 120 and 170 Å, with an average of 140 Å. However, in fibers prepared from A60/40, the crystal sizes were found to vary from the surface to the core of the fiber. At

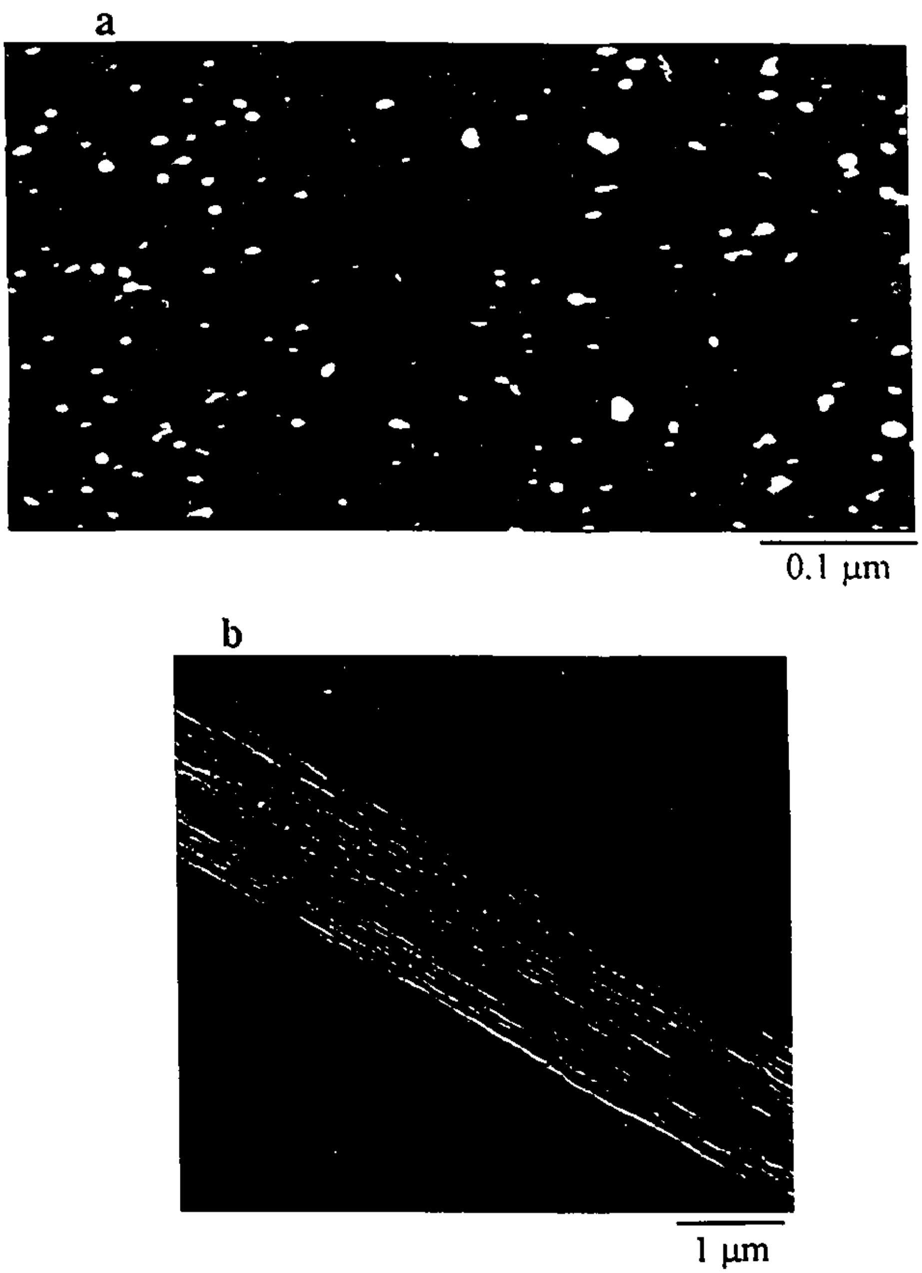

Figure 5.12 STEM dark field image of n-beam reflections of an iPP fiber prepared from a 60%/40% blend of PP5/PP34 with the silica/silicone additive. (a) Cross-sectional cut at a magnification of 300,000X. (b) Longitudinal fiber section that was cut close to the fiber surface at a magnification of 10,000X.

the surface, the size of the iPP crystals was found to be substantially smaller, ranging in size from 25 to 70 Å, with an average of 40 Å. The average crystal size increased from the 40 Å surface crystal size to 70 Å at the mid-radius and finally to 160 Å in the core. It is of interest that the crystal sizes in the core of the blend system that contains the silica/silicone additive are comparable to those observed in the fibers prepared from only PP34. The decrease in crystal size at the surface and mid-radius must be directly related to the nucleating ability of the silica/silicone additive that was presented previously. This additive induces a definite skin to core variation in morphology that is not apparent in PP34.

In an investigation of spider dragline elasticity, Termonia[34] introduced a comprehensive molecular model that incorporates most of the information known to date about the structure of these fibers. This model is based on previous analyses of the factors controlling the deformation of semicrystalline polyethylene fibers.[35-38] In this model, the fibers are viewed as a semicrystalline material that are composed of amorphous flexible chains reinforced by strong and stiff crystals. The crystalline phase is made of hydrogen-bonded β-pleated sheets which run parallel to the fiber axis while, in the amorphous region, the lengths of the chains are assigned a value comparable to the entanglement spacing in synthetic polyethylene. In addition, in this model a third region is described which is similar to the interfacial region in semicrystalline polymers. A thin layer surrounding the β-sheets is formed in the amorphous phase with a modulus of elasticity higher than in the bulk. Although hindered, the chains in this region do not lose their extensibility.

Among other discussions, Termonia[34] investigated the role of the size of the crystalline phase on the tensile strength of the fibers and on the formation of this thin, high modulus layer that surrounds the crystallites. A dramatic effect was noted on the tensile strength of the fibers due to changes in the size of the crystalline phase. Decreasing the size of the crystallites, while maintaining a constant volume fraction, leads to a substantial increase in tensile strength of the fibers. This increase in tensile strength resulting from a reduction in crystal size was found to be due to the concomitant increase in the volume fraction of the thin, high modulus layer surrounding the crystals, *i.e.*, the interfacial region. An increase in its volume fraction effectively reinforces the fiber and increases its tensile strength. This interfacial region generates a reinforcing effect similar to the thin interface of constrained mobility that is generated in the carbon black reinforcement of rubbers.[39]

The improved tensile properties that were obtained in this investigation appear to be due to a similar reduction in the size of the crystalline entities. The silica/silicone additive nucleates the iPP and effectively reduces the size of the crystals at the skin and mid-radius of the fibers. This decrease in crystal size increases the volume fraction of the interfacial phase and enhances the tensile strength of the fibers. However, the effect of the resin molecular weight must also be considered. The concomitant effect of a reduced crystal size and increased molecular weight is expected to promote the generation of a greater number and a more even distribution of "tie" molecules in the fiber. This will also enhance its tensile strength. Therefore, the lower MFI and broader MWD distribution, for the fibers that also contain the silica/silicone additive, may be playing a role in the enhancement of the tensile strength of the fibers.

In addition to the impact of these morphological changes on the tensile properties of the iPP fibers, reinforcement by the silica particles must also be considered. The surface of the silica particles was made hydrophobic by a derivatization of the surface silanol groups with poly(dimethylsiloxane) chains of unknown molecular weight. The poly(dimethylsiloxane) chains on the surface of the silica particles, when dispersed in the alkyl silicone, should extend off the silica surface and into the silicone oil. When this mixture is dispersed in iPP, the poly(dimethylsiloxane) chains should remain extended so that they can interact with the iPP through entanglements. Such dispersion into the iPP matrix would result, to a certain extent, in a degree of reinforcement and contribute to the increased tensile properties of the resultant iPP fibers.

5.3.4 Spunbonded Fabrics

5.3.4.1 Tensile Properties

The tensile properties of various spunbonded iPP fabrics are presented in Table 5.4. It should be noted that the properties of the spunbonded fabrics are greatly dependent on the processing and thermal bonding conditions. In the course of this investigation, several lots of fibers and spunbonded fabrics were prepared with PP34. The tensile properties of these fibers did not vary significantly and were found to always be in the range that is listed in Table 5.3. However, the tensile properties of the spunbonded fabrics were found to differ significantly from one sample to the next. This variation is due to the thermal bonding conditions which affect the quality of the bond points. This is clearly evident from a comparison of the tensile properties of the two PP34 spunbonded fabrics listed in Table 5.4. Consequently, a comparison of the fabric tensile properties must be performed with fabrics that were processed and thermally bonded under similar conditions. Therefore, the two sets of data that are separated in Table 5.4 cannot be compared directly with each other.

The dispersion of the silica/silicone additive system in the iPP blend systems results in a dramatic increase in the tensile properties of the spunbonded fabrics in both the machine and cross direction compared to the fabrics prepared from PP34 (Table 5.3). In addition, a gradual improvement in all properties is noted as the concentration of the lower MFI resin, PP5, is increased from 45% to 60%. It should be noted that it was not possible to fiber spin resins with higher concentrations of the lower MFI resin in the blend due to viscosity constraints. Increases as high as 82, 210 and 81 % in the peak load, peak energy and elongation-to-break, respectively, are noted for the A60/40 spunbonded fabrics. The addition of the silica/silicone additive to the iPP blend systems results in spunbonded fabrics of substantially higher tenacity.

Table 5.4: Tensile Properties of the Spunbonded iPP Fabrics.

Sample	Peak Load (kg)		Peak Energy (kg·m)		% Elongation	
	M.D.[a]	C.D.[b]	M.D.	C.D.	M.D.	C.D.
PP34	14±1	11±0.7	0.36±0.06	0.29±0.05	58±4	62±6
A45/55	18±0.9	16±0.6	0.85±0.08	0.72±0.09	96±7	98±7
A50/50	19±1.5	16±0.8	0.8g±0.1	0.71±0.09	97±4	101±8
A55/45	20±1.4	18±0.9	0.90±0.09	0.79±0.08	99±8	102±8
A60/40	21±1.5	20±0.8	0.99±0.09	0.90±0.07	105±8	108±9
PP34	10±0.6	8±0.3	0.26±0.03	0.29±0.02	44±4	44±4
A0/100	13±0.5	11±0.4	0.34±0.02	0.28±0.04	45±3	46±4
C60/40	15±0.8	12±1	0.30±0.02	0.29±0.01	45±3	47±4

[a] Machine Direction.

[b] Cross Direction.

As seen from the second set of data in Table 5.3, the dispersion of the silica/silicone additive in PP34 (*i.e.*, A0/100) results in a moderate increase in the tensile properties of the resultant spunbonded fabric compared to fabrics prepared from only PP34. Increases of 30 to 40 % are noted in the peak load and peak energy while the elongation-to-break remains essentially constant. Similarly, a comparison of the tensile properties of spunbonded fabrics that were prepared from C60/40 and PP34 indicates a moderate increase in peak load while the peak energy and elongation-to-break remain essentially constant (Table 5.3).

In the spunbonded fabrics prepared with PP34, the silica/silicone additive induces a moderate increase in its tensile performance. The increases in peak load and energy for these samples are substantially smaller than what is observed for the blend systems that contain the silica/silicone additive. Similarly, spunbonded fabrics prepared from C60/40 only indicate a small increase in peak load. This is consistent with the observations that were made for the C60/40 and PP34 single fibers. However, when the silica/silicone additive is dispersed in the blend of iPP resins, a dramatic increase in tensile properties is observed. In addition, these tensile properties are dependent on the concentration of the low melt flow index resin. It appears that the improvement in the tensile properties of the spunbonded fabrics are a consequence of the nucleating ability of the silica/silicone additive and the decrease in MFI and broadening of the MWD that was achieved from the blending of the two resins. While these two methods do not independently improve the tensile properties of the spunbonded fabrics, in conjunction, a dramatic improvement is obtained.

The tensile deformation of the PP34 and A60/40 spunbonded fabrics was recorded using a video camera. Photographs of the spunbonded fabrics were taken from the video images at different times during the tensile deformation and are presented in Figure 5.13. The spunbonded fabric on the left-hand side of each photograph is PP34 while the one on the right-hand side is A60/40. These photographs clearly demonstrate the enhancement in elongation-to-break that was achieved in the A60/40 fabrics. When failure has occurred in the PP34 spunbonded fabric (Figure 5.13C), extension continues in the A60/40 fabric.

A close inspection of the failure zone of the PP34 spunbonded fabric (Figure 5.13C) reveals that the bond points, seen as the small squares, remain intact during failure in the fabric. Therefore, the failure in the fabric must be accounted for by either failure in the fibers or at the bond point-fiber interface. However, the PP34 fabric fails at an elongation-to-break of approximately 60% (Table 5.4) which is substantially smaller than the 200% that is measured for iPP single fibers (Table 5.3). The deformation that has been induced in the fibers that are present in the spunbonded fabrics is not at an extent

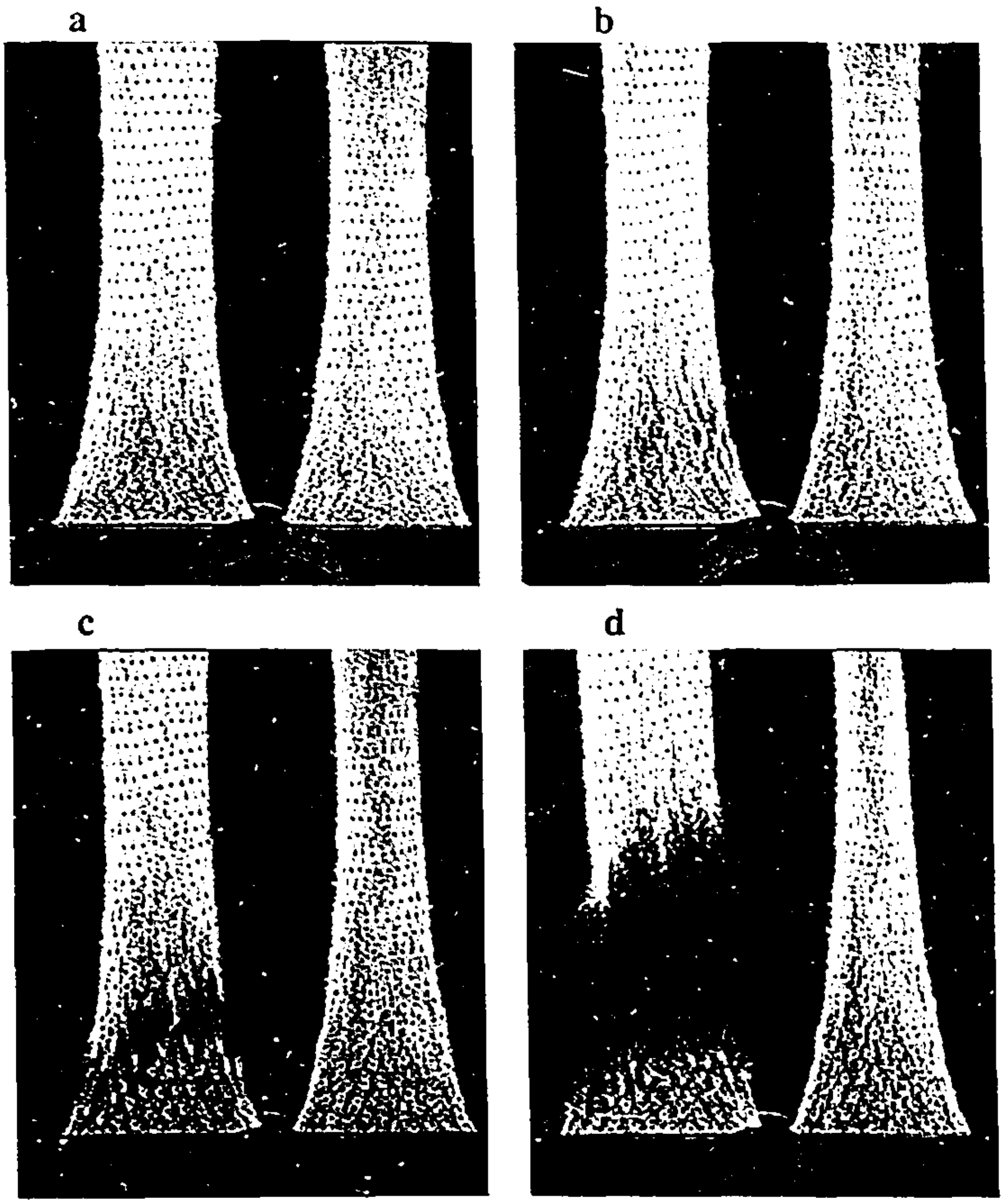

Figure 5.13 Photographs of the spunbonded fabrics at different times during tensile deformation. Left-hand side sample: PP34; Right-hand side sample: A60/40.

where failure is expected. Therefore, failure must be occurring at the bond point-fiber interface. This has been suggested previously[3-456] and appears to be generally accepted in the industry. The heat and pressure treatment that is used during thermal bonding may generate a large difference in morphology (*e.g.*, size of crystallites) at the interface between the bond point and fibers and cause the interface to become the weakest location on the fabric and most susceptible to failure. This is considered further in the next section.

5.3.4.2 Morphology of Spunbonded Fabrics

The crystalline phase of the bond points in the spunbonded iPP fabrics was investigated by scanning transmittance electron microscopy (STEM) in cryo-microtomed sections that were sliced in the cross-sectional direction. This investigation was also performed on spunbonded fabrics prepared from PP34 and A60/40. STEM dark field images that present the crystalline phase at various locations within the bond point are shown in Figures 5.14 and 5.15. Micrographs of cross-sectional cuts are presented for positions located at every 200 Å beginning from the bond point edge.

As for the iPP fibers, the addition of the silica/silicone additive to the blend of iPP resins results in a reduction in size of the crystalline entities that are observed within the bond points with a concomitant increase in the nucleation density. It should be noted that the size and density of the crystallites in both of these samples appears to remain essentially constant throughout the bond point. The reduction in crystal size and increase in nucleation density is consistent with the nucleating ability of the silica/silicone additive.

The formation of the bond points was performed by a hot calendering technique which involves heating and laterally compressing the fibers until they are bonded. The substantially smaller crystal sizes that are present at the surface of the A60/40 fibers should favor the bonding process. At a given bonding temperature, a greater fraction of these crystals will melt, due to the smaller sizes of the crystals that are located on the

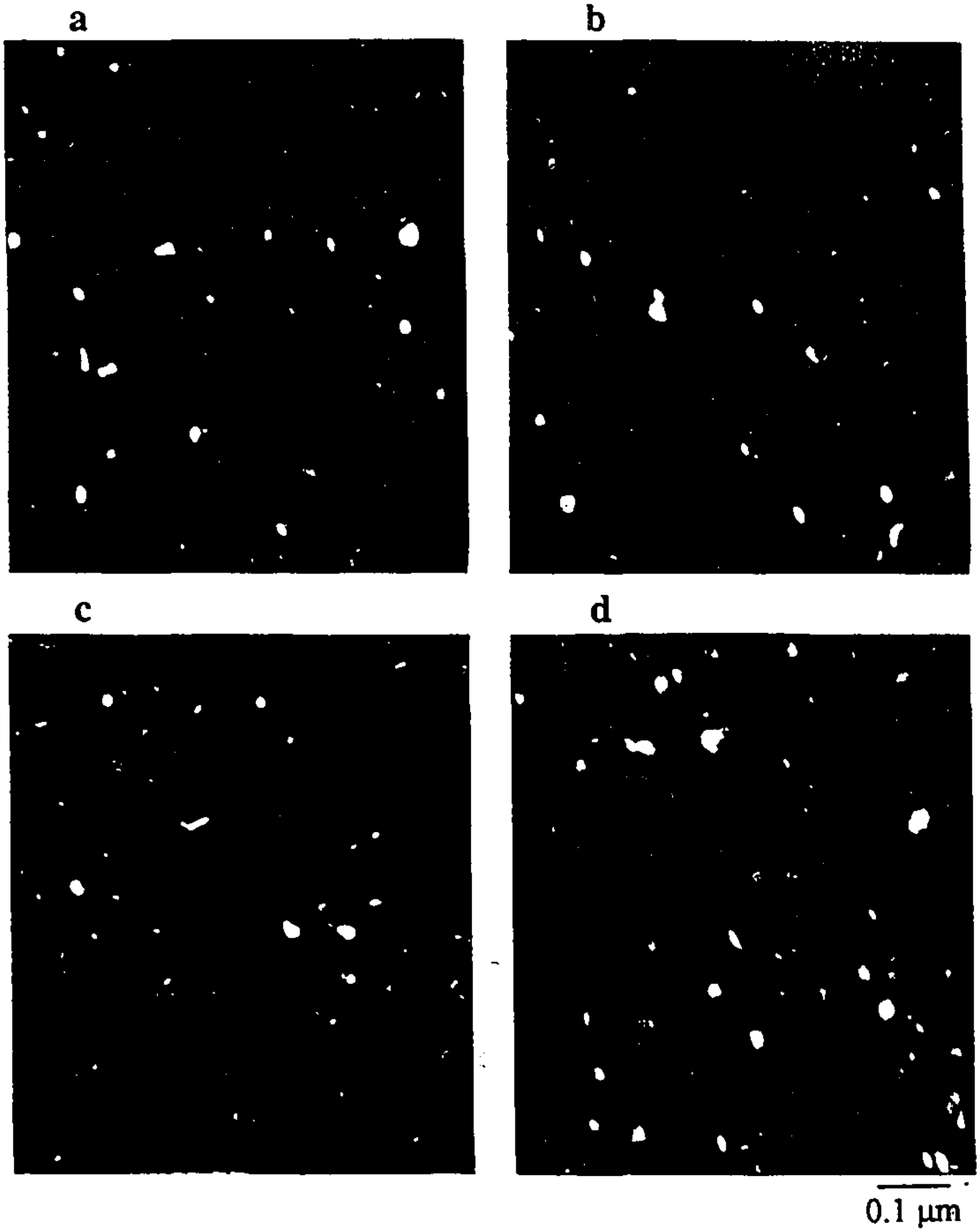

Figure 5.14 STEM dark field image of n-beam reflections, at a magnification of 100,000X, of a cross-sectional cut of the bond point of a spunbonded fabric prepared from PP34. The following locations are presented: (a) Edge of the bond point (b) 200 (c) 400 (d) 600 Å from the edge of the bond point.

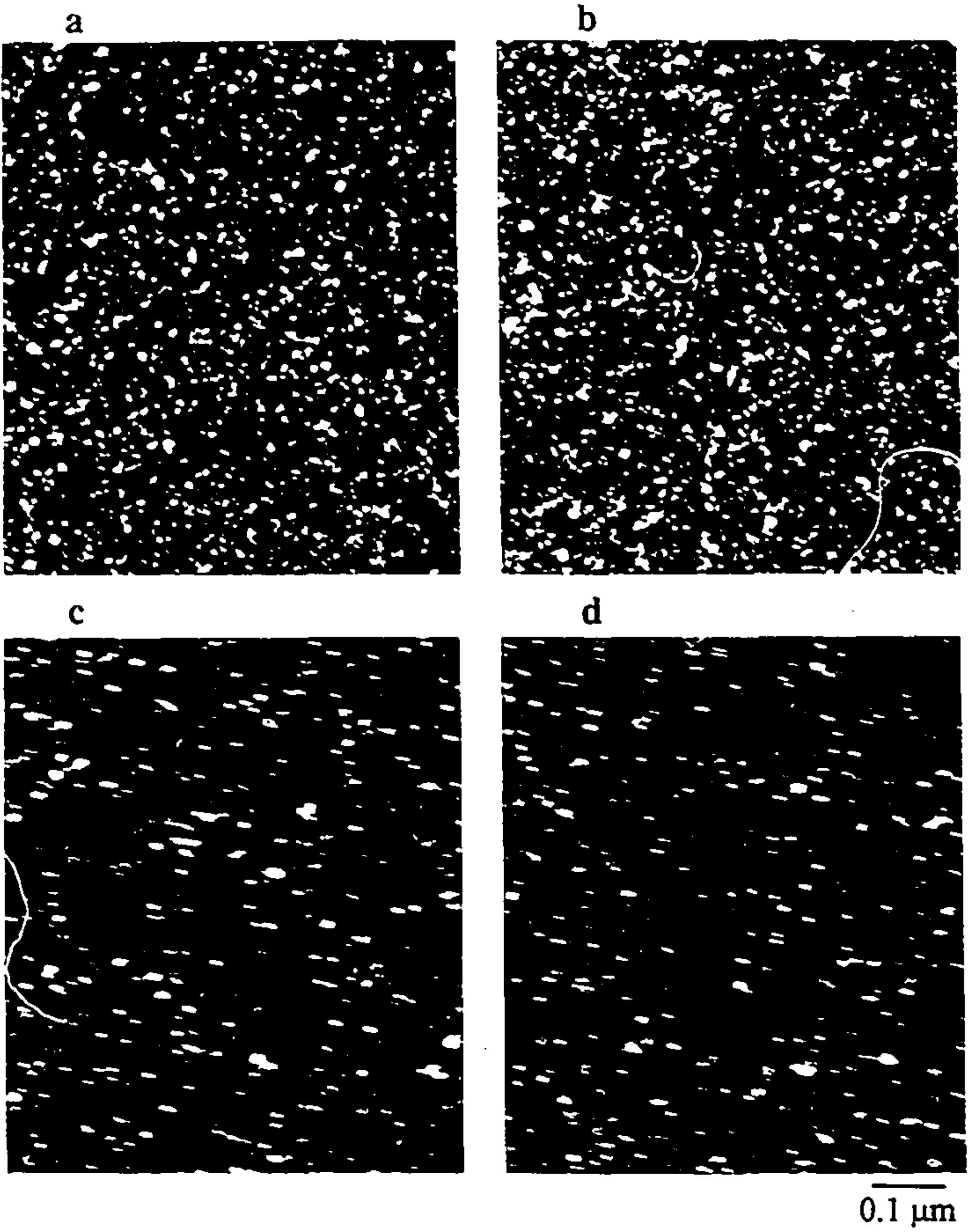

Figure 5.15 STEM dark field image of n-beam reflections, at a magnification of 100,000X, of a cross-sectional cut of the bond point of a spunbonded fabric prepared from A60/40. The following locations are presented: (a) Edge of the bond point (b) 200 (c) 400 (d) 600 Å from the edge of the bond point.

surface of the fibers. This melted fraction will recrystallize upon cooling and the nucleation density will increase due to the nucleating ability of the silica/silicone additive. The combination of these two effects should result in improved bonding of the iPP fibers. Furthermore, the morphology in the transition region between the bond point and fibers should be more homogeneous which would reduce the likelihood of failure occurring at this interface and improve the elongation-to-break properties of the fabric.

5.3.5 Annealing and Melting Behavior of iPP Spunbonded Fabrics

As discussed in previous sections, the addition of the silica/silicone additive influences the crystalline phase in both the iPP fibers and in the bond points by reducing the size of the crystalline entities. These morphological changes are expected to induce a change in the melting and annealing behavior of these spunbonded fabrics compared to those prepared from PP34.

DSC thermograms are presented in Figure 5.16 for the heating, at a rate of 20 °C/min, of iPP spunbonded fabrics prepared from PP34 and A60/40. The double melting endotherm of the spunbonded fabrics prepared from PP34 was discussed previously in Chapter 4. The addition of the silica/silicone additive to the blend of iPP resins affects the melting behavior of the resulting spunbonded fabrics. Unlike the fabrics prepared from PP34, the fabrics that were modified by the additive melt with a single endotherm. As seen from Figure 5.16, the melting endotherm appears almost coincident with the high temperature peak of the double melting endotherm prepared from PP34. This change in melting behavior must reflect morphological changes (*i.e.*, smaller crystal sizes and higher nucleation density) that occurred within the iPP fibers and bond points.

In the previous chapter, the double melting endotherm of spunbonded fabrics prepared from PP34 was investigated by monitoring the changes induced in the crystalline phase of iPP by annealing treatments. In particular, a sudden change in the rate of

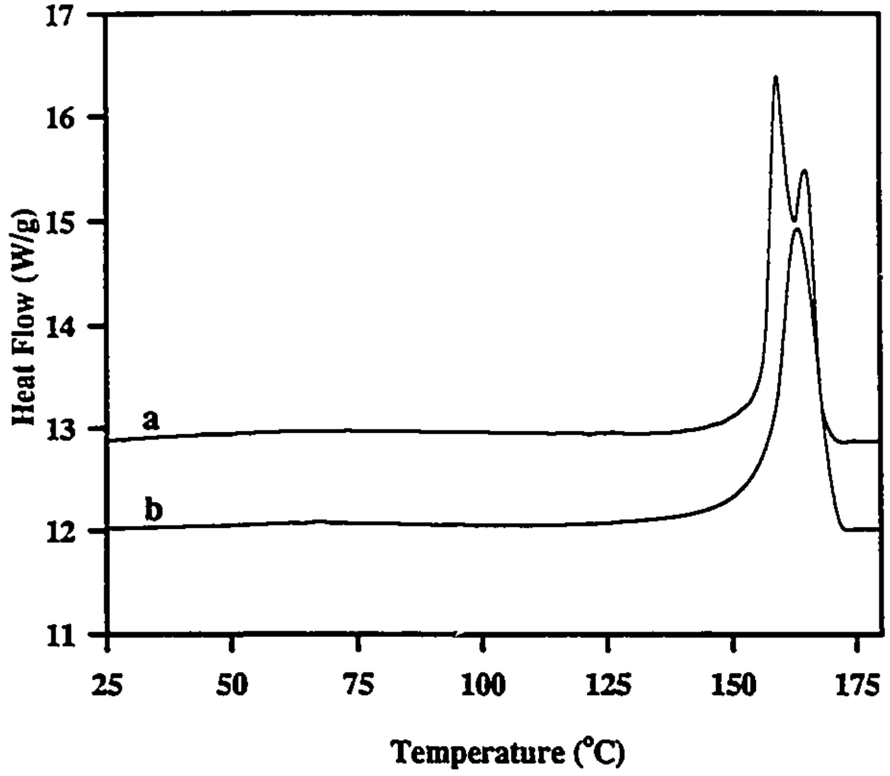

Figure 5.16 DSC thermograms for the heating, at a rate of 20 °C/min, of spunbonded iPP fabrics prepared from (a) PP34 and (b) a 60%/40% blend of PP5/PP34 with the silica/silicone additive.

increase of the long component of the spin-lattice relaxation time, $T_{1\rho}$ (^{1}H), was noted at a temperature coincident with the low temperature melting endotherm. This acceleration in the rate of increase was shown to be due to a reorganization within the α-monoclinic crystalline phase of iPP which produced crystals of higher order, *i.e.*, due to the α_1 to α_2 conversion. The effect of thermal anneal on the long component of $T_{1\rho}$ (^{1}H) was also monitored for the A60/40 spunbonded fabric which melts with a single endotherm. This spin-lattice relaxation time is presented as an average of the individual $T_{1\rho}$ (^1H) values in Figure 5.17 for samples that were annealed for 0 minutes. The long component of the spin-lattice relaxation times of the spunbonded fabric prepared from PP34 is also presented in Figure 5.17 for purposes of comparison. It should be noted that identical behavior in the values of the short component of $T_{1\rho}$ (^1H) as well as the percent of this short component were observed for both of these spunbonded fabrics.

An increase in the long component of $T_{1\rho}$ (^1H) when annealed at progressively higher temperature is noted for the A60/40 spunbonded fabrics. However, unlike the spunbonded fabric prepared from PP34, a change is not observed in the rate of increase. For this spunbonded fabric, a smooth increase in $T_{1\rho}$ (^1H) is observed over the investigated temperature region. The lack of any abrupt change in $T_{1\rho}$ (^1H) values is consistent with the observation of a single melting endotherm by DSC.

The relaxation times at all anneal temperatures for the A60/40 spunbonded fabrics are always longer than the ones for the fabrics prepared from only PP34. Therefore, for the crystalline phase of the fabric prepared with the silica/silicone additive, at all anneal temperatures, the motions are more hindered than those of a fabric prepared from only PP34. This suggests that its crystalline phase is more ordered compared to PP34 fabrics.

The values of the long component of the $T_{1\rho}$ (^1H) for the above samples prior to any annealing treatment are listed in Table 5.5. Indeed, for both the as-spun fibers and spunbonded fabrics, a consistently longer relaxation time is measured when the system contains the silica/silicone additive. A longer relaxation time implies more hindered motions in the crystalline phase, which suggests that on the average the crystalline phase is more ordered. The $T_{1\rho}$ (^1H) values indicate a morphology that is more consistent with a higher order α-monoclinic crystal form than with a quench-cooled phase.

The double endothermic transition of the spunbonded fabrics prepared from PP34 was found to be due to a restriction of the conversion from the α_1 to the α_2 monoclinic

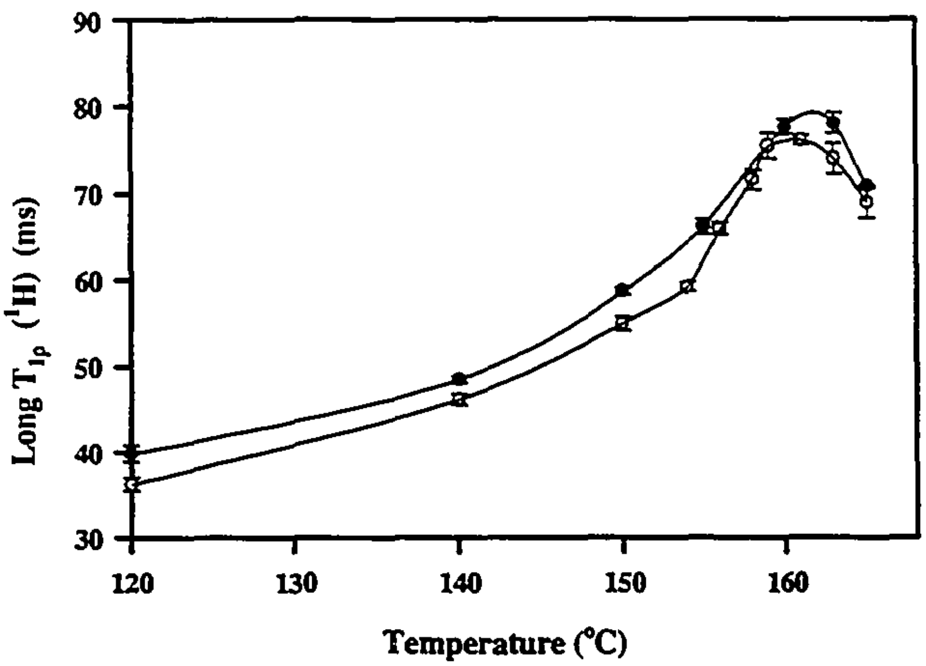

Figure 5.17 The effect of a 0 minute sample anneal on the long component of the spin-lattice relaxation time, $T_{1\rho}$ (^{1}H) of spunbonded iPP fabrics prepared from PP34 (Open Circles) and a 60%/40% blend of PP5/PP34 with the silica/silicone additive (Filled Circles).

crystal form during the heating of the sample. This restriction is thought to be due, in part, to the orientation that is present in the iPP fibers. Conversion from the α_1 to the α_2 monoclinic crystal form follows the softening and, thus, loss of orientation in the iPP fibers. The spunbonded fabrics prepared from the blend of iPP resins with the silica/silicone additive are also composed of fibers that have a definite orientation (Figure 5.12). However, the α-monoclinic crystalline phase of the A60/40 spunbonded fabrics have been shown to be of higher order at all anneal temperatures until final melting. This order is consistent with a greater fraction of the α_2 crystal form within the overall crystalline morphology. A higher melting temperature is expected for this crystal form. In addition, the amount of high temperature reorganization, *i.e.*, at T ≥ 156 °C, should be reduced. The combination of these two effects is consistent with the observation of a single melting endotherm. However, it may be possible that at lower heating rates a double melting endotherm would also be observed for this spunbonded fabric.

Table 5.5: The Long Component of the Proton Spin-Lattice Relaxation Times, $T_{1\rho}$ (^1H), Obtained at Room Temperature, for iPP Spun Fibers and Spunbonded Fabrics.

Sample Description	Relaxation Times (ms)		
	CH_2	CH	CH_3
Fabrics - PP34	29	29	27
Fabrics - 60%/40% blend with silica/silicone	34	34	33
Fibers - PP34	25	25	25
Fibers - 60%/40% blend with silica/silicone	31	30	30

5.4 Summary

In this chapter the effects of a silica/silicone additive on the tensile properties and morphology of iPP fibers and spunbonded fabrics were evaluated. The additive consisted of a poly(dimethylsiloxane) surface modified silica that was reduced in size to the sub-micron range. The silica particles were dispersed in a silicone fluid which is composed of a polydimethylsiloxane polymer onto which alkyl side-chains of varying molecular weight (*i.e.*, 2 to 11 methylene carbons) were randomly incorporated. The silica/silicone additive was dispersed in a 34 MFI resin as well as in blends of this polymer with a 5 MFI resin. The effect of decreasing the MFI of the iPP resin, achieved through the blending procedure, was also considered.

The effect of the silica/silicone additive on the quiescent crystallization kinetics of iPP was investigated to establish a possible influence on the crystalline morphology of the iPP fibers during their formation. It was shown that, under isothermal conditions, the silica/silicone additive increases the overall rate of crystallization of iPP by acting as a nucleating agent for iPP spherulites. The number of primary nuclei was found to increase while the radial growth rate of individual spherulites was not affected by the silica/silicone additive. This nucleating ability also increased the onset temperature to crystallization, obtained by DSC, under non-isothermal conditions.

The addition of the silica/silicone additive to the blend of iPP resins resulted in increased tensile properties in both the iPP fibers and spunbonded fabrics. At the highest concentration of the low MFI resin in the blend, *i.e.*, 60%, an increase of 82, 210 and 81 % in peak load, peak energy and elongation-to-break, respectively, was achieved in the spunbonded fabrics compared to fabrics prepared from PP34. Similarly, in the iPP fibers, an increase of 123, 77 and 221 % was achieved in the initial modulus, tensile strength and elongation-to-break, respectively, relative to fibers prepared from PP34. In addition, while the tensile deformation of the fibers prepared from PP34 indicates brittle fracture, the fibers prepared from A60/40 are consistent with the stress-strain behavior of a good elastomer. A yield point with no indication of necking was observed, at low strains, in the tensile deformation of A60/40 fibers. This yield point is followed by a region of plastic flow and strain induced crystallization.

The morphology of the iPP fibers and bond points was investigated by STEM. Due to the nucleating effect of the silica/silicone additive, a substantially smaller crystallite size and higher nucleation density was found in both the fibers and bond points compared to samples that were prepared with only PP34. In addition, through the measurement of

NMR relaxation times, it was found that the crystalline phase in the A60/40 fibers and fabrics is more ordered than in samples prepared from only PP34. This change in the crystalline morphology was also noted in the melting behavior of the spunbonded fabrics. Indeed, the A60/40 spunbonded fabrics were found to melt with a single melting endotherm. This is in contrast to the behavior of PP34 spunbonded fabrics which melt with a double melting endotherm as discussed previously in Chapter 4. The maximum melting temperature of the A60/40 spunbonded fabrics correlates with the high temperature peak of the PP34 fabrics.

The improved tensile properties of both the iPP fibers and spunbonded fabrics were found to be due to a combination of the nucleating ability of the silica/silicone additive and the lower MFI and broader MWD that were achieved in the iPP resin from the blending of two resins with different MFI. The smaller crystal sizes in the fibers and bond points induce a more homogeneously distributed crystalline phase within the amorphous phase. The combination of the smaller crystal sizes and the higher molecular weight should be favorable for the development of a greater number and better distribution of load-bearing "tie" molecules. This morphological change reflects in an increase in tensile strength, modulus and elongation-to-break. It was also suggested that the silica particles, due to the poly(dimethylsiloxane) surface modification, may be acting as a reinforcing agent and contributing to the improved properties.

5.5 References

[1] J.G. Tomka, in 'Comprehensive Polymer Science, The Synthesis, Characterization, Reactions & Applications of Polymers', G. Allen (Ed.), Permagon Press, Oxford, p. 487 (1989).

[2] J. Zimmerman, in 'Comprehensive Polymer Science, The Synthesis, Characterization, Reactions & Applications of Polymers', G. Allen (Ed.), Permagon Press, Oxford, p. 249 (1989).

[3] S.B. Warner, *Text. Res. J.* 59, 151 (1989).

[4] P.E. Gibson and R.L. McGill, *Tappi.* 82 (1987).

[5] F. Harris, *IMPACT 85* V1-V38, Ft. Lauderdale, (1985).

[6] S.B. Warner, *ANTEC* paper 33-137, Atlanta (1988).

[7] F.M. Lu and J.E. Spruiell, *J. Appl. Polym. Sci.* **49**, 623 (1993).

[8] G. Turturro, 'The Role of Extraneous Solids in Nucleation Transport in Polymer Crystallization', Ph.D. Thesis, McGill University, Montreal, Quebec (1981).

[9] G. Turturro, G.R. Brown and L.E. St-Pierre, *Polymer* **25**, 659 (1984).

[10] G. Turturro and L.E. St-Pierre, *J. Colloid and Interface Sci.* **67**, 349 (1978).

[11] J.H. Cole, 'The Effect of Interfacial Energy on the Crystallization and Melting Behavior of Poly(ether)-Silica Composites', Ph.D. Thesis, McGill University, Montreal, Quebec (1977).

[12] J.H. Cole and L.E. St-Pierre, *ACS Symposium Series* **6**, 58 (1975).

[13] S. Misra, F.-M. Lu, J.E. Spruiell and G.C. Richeson, *J. Appl. Polym. Sci.* **56**, 1761 (1995).

[14] F. Lu and J.E. Spruiell, *J. Appl. Polym. Sci.* **34**, 1521 (1987).

[15] F. Lu and J.E. Spruiell, *J. Appl. Polym. Sci.* **34**, 1541 (1987).

[16] Q. Fan, D. Xu, D. Zhao and R. Qian, *J. Polym. Eng*. **5**, 95 (1985).

[17] K. Albert and E. Bayer, *J. Chromatog*. **544**, 345 (1991).

[18] D.W. Sindorf and G.E. Maciel, *J. Am. Chem. Soc.* **105**, 4263 (1981).

[19] G.E. Maciel, D.W. Sindorf and V.J. Bartuska, *J. Chromatogr*. **205**, 438 (1981).

[20] D.W. Sindorf and G.E. Maciel, *J. Am. Chem. Soc.* **105**, 3767 (1983).

[21] D.W. Sindorf and G.E. Maciel, *J. Phys. Chem.* **87**, 5516 (1983).

[22] L. Miller, R.W. Linton, G.E. Maciel and B.L. Hawkins, *J. Chromatogr.* **319**, 9 (1985).

[23] B. Pfleiderer, K. Albert and E. Bayer, *J. Chromatogr.* **506**, 343 (1990).

[24] K.I. Brebner, 'The effect of interfacial energies on the absorption of polydimethylsiloxane at the liquid/silica interface', Ph.D. Thesis, McGill University, Montreal, Quebec (1976).

[25] M. Avrami, *J. Chem. Phys.* **7**, 1133 (1939).

[26] M. Avrami, *J. Chem. Phys.* **8**, 212 (1940).

[27] M. Avrami, *J. Chem. Phys.* **9**, 177 (1941).

[28] U.R. Evans, *Trans. Faraday Soc.* **41**, 365 (1945).

[29] P. Meares, 'Polymers: Structure and Bulk Properties', Van Nostrand, New York, Ch. 5 (1965).

[30] J.N. Hay, *Br. Polym. J.* **3**, 74 (1971).

[31] P. Parrini and G. Corrieri, *Makromolec. Chem.* **62**, 83 (1963).

[32] I.M. Ward, 'Mechanical Properties of Solid Polymers' Wiley, New York, Ch. 11 (1971).

[33] J. Varga, in 'Polypropylene Structure, Blends and Composites, Volume 1, Structure and Morphology', J. Karger-Kocsis (Ed.), Chapman and Hall, London, p. 91-98 (1995).

[34] Y. Termonia, *Macromolecules* **27**, 7378 (1994).

[35] Y. Termonia and P. Smith, *Macromolecules* **20**, 835 (1987).

[36] Y. Termonia and P. Smith, *Macromolecules* **21**, 2184 (1988).

[37] Y. Termonia and P. Smith, *Macromolecules* **21**, 3485 (1988).

[38] Y. Termonia and P. Smith, *Macromolecules* **26**, 3738 (1993).

[39] J.B. Donnet and A. Vidal, 'Pharmacy, Thermomechanics, Elastomers, Telechelics', K. Dusek (ed.), Springer-Verlag, Berlin, pp 104-127 (1986).

CHAPTER SIX

Contributions to Original Knowledge and Suggestions for Future Work

6.1 Contributions to Original Knowledge

The research described in this thesis investigates three major topics: 1. The room temperature morphology of quench-cooled iPP films as well as the mechanism of its development from the glassy state; 2. The morphological changes that occur within the purely crystalline phase of iPP during thermal annealing of quench-cooled iPP films and spunbonded fabrics, as observed by solid state NMR spectroscopy; and 3. The use of a silica/silicone additive for the improvement of the tensile properties of iPP fibers and spunbonded fabrics with.

6.1.1 Morphology of Quench-cooled iPP Films and its Development

The scanning transmittance electron microscopy (STEM) investigation of the room temperature morphology of quench-cooled iPP films resulted in the first direct observation of this morphology. Using the micro-micro electron diffraction technique, the observed crystalline phase was successfully identified and found to be composed of three phases: 1. Microcrystalline regions that range in size between 100 and 200 Å having the α-monoclinic crystal form; 2. Regions of lower crystalline order that are also composed of a monoclinic crystal form but which have a substantially longer *b* crystallographic axis compared to the α-monoclinic crystal form of the microcrystalline region; 3. An amorphous phase.

The development of the room temperature morphology of quench-cooled iPP films was investigated by a series of detailed DSC studies. This study was the first to report on the development of crystallinity during the quench-cooling process and on re-heating to room temperature. The DSC studies indicate that *during* quench-cooling to the glassy state iPP samples attain a low degree of crystalline order to an extent that is dependent on sample mass. An amorphous glass is obtained in samples of low mass while a low degree of crystallinity (*i.e.*, up to 18 %) is observed in samples of higher mass. Furthermore, upon heating from the glassy state, an exothermic transition is observed following the glass transition temperature. It corresponds to the formation of the room temperature morphology.

6.1.2 NMR Studies of Morphological Changes During Annealing

Previous investigations have used solid state NMR spectroscopy to characterize the various polymorphs of iPP. This investigation is the first to employ this characterization technique to monitor morphological changes that are occurring within the crystalline phase of iPP during thermal annealing. Consequently, all observations that are reported in this NMR investigation contribute to original knowledge. The characterization of these morphological changes was performed through the use of a modified cross polarization (CP) pulse sequence that allows the crystalline phase to be observed exclusively. This modified CP pulse sequence incorporates a delay period with a reduced spin locking field prior to cross polarization which allows the elimination of the magnetization associated with the faster relaxing components of iPP This is not only the first investigation that made use of such a pulse sequence but also the first to successfully separate the spectra of the crystalline and more mobile phases of iPP by a subtraction procedure.

The NMR spectra reported in this study are the first unambiguous identification of a splitting pattern (0.2 ppm) in the methine carbon resonance. In addition, a third peak was identified in the methyl carbon resonance. NMR spectra of the purely crystalline phase of iPP indicate that, upon annealing, a redistribution of intensity is observed in all carbon resonances which produces doublets at the highest anneal temperature. The redistribution of intensity, for the methylene and methine carbon resonances, involves an increase in the intensity of the downfield peak with a concomitant decrease in intensity of the upfield peak. In the methyl resonance, the redistribution of intensity occurs through an increase in intensity of the midfield methyl peak with a concomitant decrease in intensity of the upfield methyl peak. The downfield methyl resonance shows the behavior of an intermediate environment which is formed during the initial stages of crystal reorganization and disappears when the final crystalline state is attained. In addition, a narrowing of the various NMR peaks was observed, consistent with a convergence to more singularly defined positions within the crystal structure. These changes in the NMR spectra of iPP outline the morphological changes that are occurring in the crystal structure of iPP.

This investigation permitted several conclusions in regard to the solid state NMR spectrum of the α-phase of iPP. The development of the splitting patterns in the NMR spectrum of iPP was found to characterize the conversion of the crystalline phase from the disordered α_1 modification to the more ordered α_2 modification. In particular, the midfield methyl peak was found to closely follow this conversion. This splitting pattern is due to inequivalent packing geometries that form in the α_2-phase due to the association of right- and left-handed helices that generate a bilayer with the same methyl orientation (*i.e.*, up or down). This bilayer is characterized by a smaller interlayer separation and a higher methyl packing density than is observed for the interlayer between helices of opposite methyl orientation. This distance and density variation generates two different environments at the interlayers yielding two peaks in the solid state NMR spectrum of the α_2 form.

In the analysis of the double endothermic transition that is observed for spunbonded iPP fabrics, an apparent transition temperature of 156 °C was identified by solid state NMR and DSC. The CP/MAS NMR spectra of the purely crystalline phase of iPP indicated a rapid re-distribution of peak intensity and a decrease in the width of the various peaks at temperatures above this apparent transitional temperature. These NMR observations are consistent with a rapid conversion from the α_1 to the α_2 modification which is occurring in the temperature region between 156 and 163 °C, *i.e.*, the area between the two peaks observed by DSC. In this temperature region, the melting endotherm is being modified by the exothermicity that is associated with this conversion. The orientation present in the iPP fibers is thought to restrict the reorganization in the crystalline phase until a temperature that is associated with the softening of the fiber form.

6.1.3 Tensile Properties of Spunbonded Fabrics

The improvement of the tensile properties of iPP fibers and spunbonded fabrics was achieved with a silica/silicone additive and by changing the iPP resin characteristics. The consequence of the addition of this additive to iPP was investigated not only on the morphology of the resultant fibers and bond points but also on the overall crystallization kinetics of iPP. To the knowledge of the author, this is the first study that investigates the effect of a surface modified silica on the iPP crystallization kinetics and on the tensile properties and morphology of iPP fibers and spunbonded fabrics.

Under isothermal conditions, the silica/silicone additive influences the overall rate of crystallization of iPP by acting as a nucleating agent for iPP spherulites. This nucleating ability also increases the onset temperature to crystallization, obtained by DSC, under non-isothermal conditions. Due to the nucleating effect of the silica/silicone additive, a substantially smaller crystallite size and higher nucleation density was found in both the iPP fibers and bond points. In addition, the crystalline phase of these fibers and fabrics is more ordered than in samples that do not contain the silica/silicone. This change in the crystalline morphology affects the melting behavior of the spunbonded fabrics in that a single melting endotherm is observed by DSC.

The addition of the silica/silicone additive to the blend of iPP resins results in increased tensile properties in both the iPP fibers and spunbonded fabrics. At the highest concentration of the low MFI resin in the blend, *i.e.*, 60%, an increase of 82, 210 and 81 % in peak load, peak energy and elongation-to-break, respectively, was achieved in the spunbonded fabrics compared to fabrics prepared from PP34. Similarly, in the iPP fibers, an increase of 123, 77 and 221 % was achieved in the initial modulus, tensile strength and elongation-to-break, respectively, relative to fibers prepared from PP34. The improved tensile properties of both the iPP fibers and spunbonded fabrics are attributed to the smaller crystal sizes that were achieved due to the nucleating ability of the silica/silicone additive and to the lower MFI and broader MWD that were induced in the iPP resin from the blending of two MFI resins. In addition, it was also suggested that the silica particles, due to the poly(dimethylsiloxane) surface modification, may be acting as a reinforcing agent and contributing to the improved properties.

6.2 Suggestions for Future Work

Although the experiments described in this thesis were designed to produce a systematic study, this does not mean that the research is exhausted. Suggestions for some further research follows:

(1) The room temperature morphology of quench-cooled iPP films has been shown to be composed of microcrystalline region that range in size between 100 and 200 Å. This should be confirmed by atomic force microscopy (AFM). The quench-cooled films can be embedded in epoxy resin and cryo-microtomed as described in this thesis. Using transmittance electron microscopy with the minimum dosage device, the thin section of the film can be located on a copper grid and then imaged with AFM to confirm the existence of the microcrystalline regions and possibly the intercrystalline region of lower order.

(2) In the investigation of the annealing and melting behavior of quench-cooled iPP films and spunbonded fabrics by solid state NMR spectroscopy, excellent correlations were noted with observation made by DSC and WAXD analysis. An investigation should be undertaken which duplicates this analysis with iPP resins of different molecular weights and isotacticities. The iPP samples should be isothermally crystallized and their melting behavior properly characterized. The correlation that will be achieved with the solid state NMR analysis will contribute to the understanding of the relationship between the level of order in the crystalline phase and the melting behavior of the sample. The effect of isotacticity and molecular weight on this relationship will also be realized.

(3) The effect of the silica/silicone additive on the overall crystallization kinetics of iPP and tensile properties of iPP fibers and spunbonded fabrics was investigated. This research should be continued to develop a better understanding of the role of each of the components of the additive. iPP fibers and spunbonded fabrics that contain only silica and only silicone should be prepared and their tensile properties and morphology evaluated to ascertain the effect that each has on the overall performance of the fiber. In addition, the effect of each of the components on the overall iPP crystallization kinetics should be addressed.

(4) The concentration of the silica in the silicone fluid as well as the silica/silicone additive in the iPP was maintained constant in this investigation. These concentrations should be varied and the effect on the tensile properties of the fibers and fabrics as well as on the overall iPP crystallization kinetics should be evaluated.

(5) The importance of the poly(dimethylsiloxane) surface modification of the silica should also be considered with respect to effects on the crystallization kinetics of iPP as well as on the tensile properties of iPP fibers and spunbonded fabrics. A hydrophobic silica whose surface silanol groups were replaced with only methyl groups would be a

good candidate. This surface modified silica is available from Cabot Corporation (Cab-O-Sil TS-610).

Appendix A

Program #1

This Fortran computer program was obtained from Dr. Brisse of the University of Montreal. Through a least squares analysis, this program determines the unit cell dimension of the iPP crystals by entering the measured reflection spacings (i.e., in diffraction angles) and suggested Miller indices.

```
C    X=H, Y=K, Z=L, TT=THETA
C    NAXE   = 1  POUR MONOCLINIQUE (AXE-B UNIQUE)
C    NAXE   = 2  POUR MONOCLINIQUE (AXE-C UNIQUE)
C    ALPHAV = Longeur d'onde en angstrom de la raie K alpha moyen
C    ALPHA1 = Longeur d'onde en angstrom de la raie K alpha 1
C    ALPHA2 = Longeur d'onde en angstrom de la raie K alpha 2
C    BETA   = Longeur d'onde en angstrom de la raie K beta
C
      DIMENSION TT(100),INDEXE(100),A(5,5),B(5)
      DIMENSION SINT(100),SINC(100),DS(100),NOM(20),RADIA(5)
C
      CHARACTER TITL*80
      INTEGER IN,OUT,X(100),Y(100),Z(100)
      REAL RAD
C
      IN=5
      OUT=6
      RAD=0.01745329277
C
      WRITE(OUT,6005)
      WRITE(OUT,6010)
      READ(IN,5005) TITL
      WRITE(OUT,6015) TITL
      READ(IN,5010) NAXE,ALPHAV,ALPHA1,ALPHA2,BETA
      WRITE(OUT,6020) NAXE,ALPHAV,ALPHA1,ALPHA2,BETA
      WRITE(OUT,6025)
C
      DO 5 I=1,5
        B(I)=0.0
        DO 3 J=1,5
          A(I,J)=0.0
    3   CONTINUE
```

```
 5 CONTINUE
  I=1
  NREF=0
 10 CONTINUE
  READ(IN,5015,END=99) X(I),Y(I),Z(I),TT(I),INDEXE(I)
    IND=INDEXE(I)+1
C
    GOTO (25,26,28,29),IND
 25     CONTINUE
         WAV=ALPHAV
         GOTO 30
 26     CONTINUE
         WAV=ALPHA1
         GOTO 30
 28     CONTINUE
         WAV=ALPHA2
         GOTO 30
 29     CONTINUE
         WAV=BETA
         GOTO 30
 30   CONTINUE
C
    SINT(I)=(SIN(TT(I)*RAD)*ALPHA1/WAV)**2
    SNTT=(SIN(2.*TT(I)*RAD)*ALPHA1/WAV)**2
    WRITE(OUT,6030) X(I),Y(I),Z(I),TT(I),INDEXE(I),SINT(I)
C
    ALF=X(I)*X(I)
    BET=Y(I)*Y(I)
    GAM=Z(I)*Z(I)
    DEL=SNTT*SNTT
    XBT=X(I)*Z(I)
    XGM=X(I)*Y(I)
    A(1,1)=A(1,1)+ALF*ALF
    A(1,2)=A(1,2)+ALF*BET
    A(1,3)=A(1,3)+ALF*GAM
    A(1,5)=A(1,5)+ALF*DEL
    A(2,2)=A(2,2)+BET*BET
    A(2,3)=A(2,3)+BET*GAM
    A(2,5)=A(2,5)+BET*DEL
    A(3,3)=A(3,3)+GAM*GAM
    A(3,5)=A(3,5)+GAM*DEL
    A(5,5)=A(5,5)+DEL*DEL
    B(1)=B(1)+SINT(I)*ALF
    B(2)=B(2)+SINT(I)*BET
    B(3)=B(3)+SINT(I)*GAM
```

```
        B(5)=B(5)+SINT(I)*DEL
C
        IF(NAXE.EQ.1) THEN
          A(1,4)=A(1,4)+ALF*XBT
          A(2,4)=A(2,4)+BET*XBT
          A(3,4)=A(3,4)+GAM*XBT
          A(4,4)=A(4,4)+XBT*XBT
          A(4,5)=A(4,5)+XBT*DEL
          B(4)=B(4)+SINT(I)*XBT
        ELSE
          A(1,4)=A(1,4)+ALF*XGM
          A(2,4)=A(2,4)+BET*XGM
          A(3,4)=A(3,4)+GAM*XGM
          A(4,4)=A(4,4)+XGM*XGM
          A(4,5)=A(4,5)+XGM*DEL
          B(4)=B(4)+SINT(I)*XGM
        ENDIF
C
        I=I+1
        NREF=NREF+1
        GOTO 10
  99 CONTINUE
      WRITE(OUT,6035) NREF
      A(2,1)=A(1,2)
      A(3,1)=A(1,3)
      A(4,1)=A(1,4)
      A(5,1)=A(1,5)
      A(3,2)=A(2,3)
      A(4,2)=A(2,4)
      A(4,3)=A(3,4)
      A(5,2)=A(2,5)
      A(5,3)=A(3,5)
      A(5,4)=A(4,5)
C
      M1=1
      CALL MATINV(A,4,B,M1,DETERM,ID)
C
      IF(NAXE.EQ.1) THEN
        COSB=-B(4)/(2.*SQRT(B(1)*B(3)))
      ELSE
        COSB=-B(4)/(2.*SQRT(B(1)*B(2)))
      ENDIF
      SNSQB=1.-COSB*COSB
      SINB=SQRT(SNSQB)
      IF(COSB.EQ.0.0) THEN
```

```
        BETA=90.0
      ELSE
        BETA=ATAN(SINB/COSB)/RAD
        IF(BETA.LT.0.0) THEN
          BETA=180.0+BETA
        ENDIF
      ENDIF
C
      IF(NAXE.EQ.1) THEN
        A1=ALPHA1/(2.*SINB*SQRT(ABS(B(1))))
        B1=ALPHA1/(2.*SQRT(ABS(B(2))))
        C1=ALPHA1/(2.*SINB*SQRT(ABS(B(3))))
        WRITE(OUT,6040) A1,B1,C1,BETA
      ELSE
        A1=ALPHA1/(2.*SINB*SQRT(ABS(B(1))))
        B1=ALPHA1/(2.*SINB*SQRT(ABS(B(2))))
        C1=ALPHA1/(2.*SQRT(ABS(B(3))))
        WRITE(OUT,6045) A1,B1,C1,BETA
      ENDIF
C
      WRITE(OUT,6050)
      SDS=0.0
      DO 70 I=1,NREF
        IF(NAXE.EQ.1) THEN
          SINC(I)=0.25*ALPHA1*ALPHA1*(X(I)*X(I)/(A1*A1*SNSQB)+
     &          Y(I)*Y(I)/(B1*B1)+Z(I)*Z(I)/(C1*C1*SNSQB)-
     &          2.*X(I)*Z(I)*COSB/(A1*C1*SNSQB))
        ELSE
          SINC(I)=0.25*ALPHA1*ALPHA1*(X(I)*X(I)/(A1*A1*SNSQB)+
     &          Y(I)*Y(I)/(B1*B1*SNSQB)+Z(I)*Z(I)/(C1*C1)-
     &          2.*X(I)*Y(I)*COSB/(A1*B1*SNSQB))
        ENDIF
        DS(I)=ABS(SINT(I)-SINC(I))
        SDS=SDS+DS(I)
        WRITE(OUT,6055) X(I),Y(I),Z(I),SINT(I),SINC(I),DS(I)
   70 CONTINUE
      R=SQRT(SDS/(NREF-1))
      WRITE(OUT,6060) R
      WRITE(OUT,6065)
      STOP
C
 5005 FORMAT(A80)
 5010 FORMAT(I5,4F10.6)
 5015 FORMAT(3I5,F10.5,I5)
C
```

```
6005 FORMAT(1X,'PROGRAMME CR09_NEW, REF> S.RAYMOND, AVRIL 95',//)
6010 FORMAT(3X,'AFFINEMENT D''UNE MAILLE MONOCLINIQUE',
  &' PAR MOINDRES CARRES',//)
6015 FORMAT(3X,A80,/)
6020 FORMAT(3X,'NAXE='I5,',  RADIATIONS=',4F10.5,//)
6025 FORMAT(7X,'H',4X,'K',4X,'L',6X,'THETA',4X,'INDEXE',2X,
  &'SIN SQ THETA',/)
6030 FORMAT(3X,3I5,2X,F10.3,2X,I5,4X,F10.6,/)
6035 FORMAT(3X,'NOMBRE DE REFLECTIONS',I5,//)
6040 FORMAT(3X,'A=',F10.6,2X,'B=',F10.6,2X,'C=',F10.6,2X,
  &'BETA=',F10.3,3X,'AXE-B UNIQUE',//)
6045 FORMAT(3X,'A=',F10.6,2X,'B=',F10.6,2X,'C=',F10.6,2X,
  &'GAMMA=',F10.3,3X,'AXE-C UNIQUE',//)
6050 FORMAT(7X,'H',4X,'K',4X,'L',11X,'SIN 2 T',11X,'SIN 2 T',10X,
  &'DIFFERENCE',/31X,'OBS',14X,'CAL',/)
6055 FORMAT(3X,3I5  ,8X,3(F10.6,8X))
6060 FORMAT(//,3X,'FACTEUR D ACCORD',F10.4,//)
6065 FORMAT(1X,'FIN DES CALCULS')
   END
C
C
C
   SUBROUTINE MATINV(A,N1,B,M1,DETERM,ID)
C
C   MATRIX INVERSION WITH ACCOMPANYING SOLUTION OF LINEAR
EQUATIONS
C   GENERAL FORM OF DIMENSION STATEMENT
C   DIMENSION A( , ),B( , ),INDEX( ,3)
C
   DIMENSION A( 5, 5),B( 5, 1),INDEX( 5,3)
   EQUIVALENCE (IROW,JROW),(ICOLUM,JCOLUM),(AMAX,T,SWAP)
C
C   INITIALIZATION
C
   M=M1
   N=N1
   DETERM=1.0
   DO 20 J=1,N
     INDEX(J,3)=0
 20 CONTINUE
C
   DO 550 I=1,N
C
C     SEARCH FOR PIVOT ELEMENT
C
```

```
      AMAX=0.0
      DO 105 J=1,N
        IF(INDEX(J,3)-1.NE.0) THEN
          DO 100 K=1,N
            IF(INDEX(K,3)-1) 80,100,735
 80          IF(AMAX-ABS(A(J,K)).LT.0) THEN
              IROW=J
              ICOLUM=K
              AMAX=ABS(A(J,K))
            ENDIF
 100        CONTINUE
        ENDIF
 105    CONTINUE
      INDEX(ICOLUM,3)=INDEX(ICOLUM,3)+1
      INDEX(I,1)=IROW
      INDEX(I,2)=ICOLUM
C
C      INTERCHANGE ROWS TO PUT PIVOT ELEMENT ON DIAGONAL
C
      IF(IROW-ICOLUM.NE.0) THEN
        DETERM=-DETERM
        DO 200 L=1,N
          SWAP=A(IROW,L)
          A(IROW,L)=A(ICOLUM,L)
          A(ICOLUM,L)=SWAP
 200      CONTINUE
        IF(M.GT.0) THEN
          DO 250 L=1,M
            SWAP=B(IROW,L)
            B(IROW,L)=B(ICOLUM,L)
            B(ICOLUM,L)=SWAP
 250        CONTINUE
        ENDIF
      ENDIF
C
C      DIVIDE PIVOT ROW BY PIVOT ELEMENT
C
      PIVOT=A(ICOLUM,ICOLUM)
      DETERM=DETERM*PIVOT
      A(ICOLUM,ICOLUM)=1.0
      DO 350 L=1,N
        A(ICOLUM,L)=A(ICOLUM,L)/PIVOT
 350    CONTINUE
      IF(M.GT.0) THEN
        DO 370 L=1,M
```

```
          B(ICOLUM,L)=B(ICOLUM,L)/PIVOT
 370      CONTINUE
        ENDIF
C
C       REDUCE NON-PIVOT ROWS
        DO 510 L1=1,N
          IF(L1-ICOLUM.NE.0) THEN
            T=A(L1,ICOLUM)
            A(L1,ICOLUM)=0.0
            DO 450 L=1,N
              A(L1,L)=A(L1,L)-A(ICOLUM,L)*T
 450          CONTINUE
            IF(M.GT.0) THEN
              DO 500 L=1,M
                B(L1,L)=B(L1,L)-B(ICOLUM,L)*T
 500            CONTINUE
            ENDIF
          ENDIF
 510    CONTINUE
 550  CONTINUE
C
C     INTERCHANGE COLUMNS
C
      DO 710 I=1,N
        L=N+1-I
        IF(INDEX(L,1)-INDEX(L,2).NE.0) THEN
          JROW=INDEX(L,1)
          JCOLUM=INDEX(L,2)
          DO 705 K=1,N
            SWAP=A(K,JROW)
            A(K,JROW)=A(K,JCOLUM)
            A(K,JCOLUM)=SWAP
 705        CONTINUE
        ENDIF
 710  CONTINUE
      DO 730 K=1,N
        IF(INDEX(K,3)-1.NE.0) THEN
          ID=2
          GOTO 740
        ENDIF
 730  CONTINUE
 735  ID=1
 740  RETURN
      END
```

Program #2

This Turbo Pascal computer program was written to list possible Miller indices for a given d-spacing based on an assumed unit cell dimension.

```
uses crt,printer;

var
  a,b,c,beta,d : real;
  h,k,l,i       : integer;
  dcalc         : real;
  p             : integer;
  n,o,q,r,s     : real;
  redo          : char;

begin
  clrscr;
  writeln ('Please enter Unit Cell dimension:');
  write ('       a=');
  readln (a);
  write ('       b=');
  readln (b);
  write ('       c=');
  readln (c);
  write ('beta angle=');
  readln (beta);
  writeln; writeln;
 repeat
  writeln ('Please specify d-spacing to be tested');
  write ('       d=');
  readln (d);
  p:=0;
  clrscr; writeln (lst);
  writeln ('a= ',a:4:2,'  b= ',b:4:2,'  c= ',c:4:2,'  beta= ',beta:5:2,'      d-spacing: ',d:6:3).
  writeln (lst,'a= ',a:4:2,'   b= ',b:4:2,'   c= ',c:4:2,'   beta= ',beta:5:2,'          d-spacing:
',d:6:3);
  writeln; writeln; writeln (LST); writeln (LST); writeln (LST); writeln (LST);
  writeln ('h  k  l  (d-spacing)      h  k  l  (d-spacing)      h  k  l  (d-spacing)');
  writeln (lst,'h  k  l  (d-spacing)      h  k  l  (d-spacing)      h  k  l  (d-spacing)');
  writeln (lst,'-------------------      -------------------      -------------------');
  writeln; writeln; writeln (lst); writeln (lst);
  for h:=0 to 16 do
    begin
      for k:=0 to 16 do
```

```
       begin
          for i:=0 to 16 do
            begin
              if (h=0) and (k=0) and (i=0) then
                l:=1
              else
                l:=i;
              n:=(h*h)/(a*a);
              o:=(l*l)/(c*c);
              q:=(2*h*l)/(a*c)*cos(beta*3.141592654/180);
              r:=sin(beta*3.141592654/180)*sin(beta*3.141592654/180);
              s:=(k*k)/(b*b);
              dcalc:=1/sqrt(((n+o-q)/r)+s);
              if (d>=dcalc-0.3) and (d<=dcalc+0.3) then
                begin
                 if (h+k) in [0,2,4,6,8,10,12,14,16,18,20,22,24] then
                   begin
                    p:=p+1;
                    if p=3 then
                      begin
                        p:=0;
                       writeln (h,'.',k,'.',l,' (',dcalc:5:3,'[',abs(dcalc-d):4:3,'])      ');
                       writeln (lst,h,'.',k,'.',l,' (',dcalc:5:3,'[',abs(dcalc-d):4:3,'])      ');
                       writeln; writeln (lst);
                      end
                    else
                      begin
                       write (h,'.',k,'.',l,' (',dcalc:5:3,'[',abs(dcalc-d):4:3,'])      ');
                       write (lst,h,'.',k,'.',l,' (',dcalc:5:3,'[',abs(dcalc-d):4:3,'])      ');
                      end
                   end
                end
            end
        end
    end;
  writeln; writeln; writeln;
  write ('These are all the possible indices');
  readln;
  clrscr;
  write ('Do you wish to enter another d-spacing (y/n): ');
  readln (redo);
  clrscr;
 until redo='n';
end.
```

Program #3

This Turbo Pascal computer program was written to suggest a possible unit cell dimension based on a given set of Miller indices and observed d-spacings.

```
uses crt,printer;

var
  beta          : real;
  a             : array [1..200] of real;
  b             : array [1..800] of real;
  c             : array [1..100] of real;
  h,k,l         : array [1..6] of integer;
  d             : array [1..6] of real;
  dcalc         : array [1..6] of real;
  diff          : array [1..6] of real;
  new_sum       : real;
  min_sum, dcalc1_min,dcalc2_min.dcalc3_min,dcalc4_min,
  dcalc5_min,dcalc6_min,diff1_min, diff2_min, diff3_min, diff4_min,
  diff5_min, diff6_min,a_min,b_min,c_min                  : array [1..10] of real;
  n,o,q,r,s     : real;
  i,j,e,f,g,z,y : integer;
  print_ok      : char;

begin
  clrscr;
  writeln ('Calculating......Please wait!!!');
  writeln; writeln;
  for e:=1 to 200 do
    begin
      if e=1 then
        a[e] := 6.0
      else
        a[e] := a[e-1] + 0.01;
    end;
  for f:=1 to 400 do
    begin
      if f=1 then
        b[f] := 19.5
      else
        b[f] := b[f-1] + 0.01;
    end;
  for g:=1 to 100 do
    begin
```

```
    if g=1 then
     c[g] := 6.45
    else
     c[g] := c[g-1] + 0.01;
  end;
     beta:=99.0;
     h[1]:=1; k[1]:=1; l[1]:=1 ; d[1]:=4.163;
     h[2]:=2; k[2]:=2; l[2]:=2 ; d[2]:=2.080;
     h[3]:=0; k[3]:=4; l[3]:=1 ; d[3]:=4.147;
     h[4]:=0; k[4]:=8; l[4]:=2 ; d[4]:=2.080;
     h[5]:=1; k[5]:=3; l[5]:=2 ; d[5]:=2.522:
     h[6]:=1; k[6]:=5; l[6]:=0 ; d[6]:=3.707;
for i:=1 to 10 do
  min_sum[i] := 10000;
for e :=1 to 200 do
  begin
    for f :=1 to 400 do
      begin
        for g :=1 to 100 do
          begin
           for i:=1 to 6 do
             begin
               n:=(h[i]*h[i])/(a[e]*a[e]);
               o:=(l[i]*l[i])/(c[g]*c[g]);
               q:=(2*h[i]*l[i])/(a[e]*c[g])*cos(beta*3.141592654/180);
               r:=sin(beta*3.141592654/180)*sin(beta*3.141592654/180);
               s:=(k[i]*k[i])/(b[f]*b[f]);
               dcalc[i]:=1/sqrt(((n+o-q)/r)+s);
               diff[i]:=abs(dcalc[i]-d[i]);
             end;
             writeln (e,' ',f,' ',g);
           new_sum := diff[1]+diff[2]+diff[3]+diff[4]+diff[5]+diff[6];
           if ((e=1) and (f=1) and (g=1)) then
              begin
                for i:=1 to 10 do
                  min_sum[i] := new_sum;
              end;
            for i:=1 to 10 do
              begin
                if i = 1 then
                  begin
                   if new_sum < min_sum[i] then
                     begin
                       y:=10;
                       repeat
```

```
       min_sum[y]:=min_sum[y-1];
        y:=y-1
      until y=i;
      min_sum[i] := new_sum;
      dcalc1_min[i] := dcalc[1];
      dcalc2_min[i] := dcalc[2];
      dcalc3_min[i] := dcalc[3];
      dcalc4_min[i] := dcalc[4];
      dcalc5_min[i] := dcalc[5];
      dcalc6_min[i] := dcalc[6];
      diff1_min[i] := diff[1];
      diff2_min[i] := diff[2];
      diff3_min[i] := diff[3];
      diff4_min[i] := diff[4];
      diff5_min[i] := diff[5];
      diff6_min[i] := diff[6];
      a_min[i] := a[e]; b_min[i] := b[f]; c_min[i] := c[g];
      writeln (i,'   ',min_sum[i]:10:8);
    end;
  end
else
  begin
   if ((new_sum > min_sum[i-1]) and (new_sum < min_sum[i])) then
     begin
       y:=10;
       repeat
        min_sum[y]:=min_sum[y-1];
         if i<10 then
           y:=y-1
       until y=i;
       min_sum[i] := new_sum;
       dcalc1_min[i] := dcalc[1];
       dcalc2_min[i] := dcalc[2];
       dcalc3_min[i] := dcalc[3];
       dcalc4_min[i] := dcalc[4];
       dcalc5_min[i] := dcalc[5];
       dcalc6_min[i] := dcalc[6];
       diff1_min[i] := diff[1];
       diff2_min[i] := diff[2];
       diff3_min[i] := diff[3];
       diff4_min[i] := diff[4];
       diff5_min[i] := diff[5];
       diff6_min[i] := diff[6];
       a_min[i] := a[e]; b_min[i] := b[f]; c_min[i] := c[g];
       writeln (i,'   ',min_sum[i]:10:8);
```

```
                    end;
                  end;
                end;
              end;
            end;
  end;
repeat
for z :=1 to 10 do
 begin
   writeln (lst,'Unit Cell Dimension : ',z); writeln (lst);
   writeln (lst,'  Index   Obs. d-spacing    Calc. d-spacing    Difference');
   writeln (lst,' -----   -------------   --------------   ----------');
   writeln (lst,'  ',h[1],k[1],l[1],'   ',d[1]:7:4,'   ',dcalc1_min[z]:7:4,'   ',diff1_min[z]:9:7);
   writeln (lst,'  ',h[2],k[2],l[2],'   ',d[2]:7:4,'   ',dcalc2_min[z]:7:4,'   ',diff2_min[z]:9:7);
   writeln (lst,'  ',h[3],k[3],l[3],'   ',d[3]:7:4,'   ',dcalc3_min[z]:7:4,'   ',diff3_min[z]:9:7);
   writeln (lst,'  ',h[4],k[4],l[4],'   ',d[4]:7:4,'   ',dcalc4_min[z]:7:4,'   ',diff4_min[z]:9:7);
   writeln (lst,'  ',h[5],k[5],l[5],'   ',d[5]:7:4,'   ',dcalc5_min[z]:7:4,'   ',diff5_min[z]:9:7);
   writeln (lst,'  ',h[6],k[6],l[6],'   ',d[6]:7:4,'   ',dcalc6_min[z]:7:4,'   ',diff6_min[z]:9:7);
   writeln (lst); writeln (lst);
   writeln (lst,'a = ',a_min[z]:6:3);
   writeln (lst,'b = ',b_min[z]:6:3);
   writeln (lst,'c = ',c_min[z]:6:3);
   writeln (lst,'beta =',beta:4:1);
   writeln (lst);
   writeln (lst,'Sum of the differences =',min_sum[z]:10:8);
   writeln (lst); writeln (lst); writeln(lst); writeln (lst);
 end;
 clrscr;
 write ('Is this a good printout (y/n)?  ');
 readln (print_ok);
 until print_ok='y';
writeln (lst); writeln (lst); writeln(lst); writeln (lst);
end.
```

Appendix B

Data for Figures

Chapter 2

Fig. 2.3

Temperature	LTP Onset	Temperature	Exo. Minimum
30	42.24	30	98.2
40	47.74	40	98.2
50	53.75	50	98.7
60	63.24	60	98.4
70	71.65	70	101.4
80	82.23	80	107.7
90	89.67		
100	104.01		
110	114.64		
120	124.88		
27.2	40.99		

Fig. 2.5

Sample Weight	Excess Energy	Sample Weight	ΔC_p
0.92	0.20	0.86	0.53
1.30	1.65	0.92	0.61
1.96	10.67	1.30	0.50
2.80	19.61	1.96	0.50
4.22	29.60	2.80	0.36
5.25	29.32	3.30	0.31
7.85	30.84	4.22	0.27
		5.25	0.24
		7.85	0.22

Chapter 3

Fig. 3.6

Temperature	Downfield	Midfield	Upfield	Peak Ratio
25	3.45		48.77	
40	3.50		48.57	
60	4.07		47.66	
80	5.13	0.35	46.51	0.007
90	8.38	0.75	41.96	0.018

100	11.21	2.06	37.52	0.055
115	12.22	4.99	33.35	0.149
130	10.11	10.37	30.21	0.343
140	7.95	14.61	28.09	0.520
150	3.58	24.22	23.66	1.024
155	2.28	27.42	21.55	1.272
157	2.22	27.70	21.54	1.286

Fig. 3.7

Temperature	Downfield	Midfield	Upfield
25	0.983		1.773
40	0.968		1.777
60	1.034		1.756
80	0.898		1.597
90	0.946		1.422
100	0.947	0.439	1.240
115	0.910	0.467	1.069
130	0.783	0.458	0.914
140	0.721	0.469	0.836
150	0.519	0.391	0.551
155	0.516	0.346	0.451
157	0.518	0.328	0.436

Chapter 4

Fig. 4.8

Temperature	LTP/0min	HTP/0min	LTP/60min	HTP/60min
120	156.78	163.10	156.76	164.36
130	157.60	163.47	157.40	164.55
140	157.13	164.22	157.07	164.18
150	157.69	163.85	159.49	163.43
152	158.79	163.85	161.41	
154	159.32	163.85	162.81	
156	161.19		164.40	
157	162.37		165.83	
158	163.00		166.13	
161			171.92	

Fig. 4.9

Temperature	ΔH/0min	Temperature	ΔH/60min
120	99.52	120	98.01
130	101.63	130	99.57
140	103.55	140	104.58
150	106.75	150	107.06
152	108.08	152	107.83
154	108.39	154	114.33
156	109.33	156	116.33
157	110.80	161	118.27
158	112.29		
159	112.79		

Fig. 4.11

For the 0 minute annealed samples

Temperature	Long $T_{1\rho}(^1H)$	Short $T_{1\rho}(^1H)$	%Short Component
120	38.70	7.13	19.83
130	40.32	6.01	17.65
140	45.64	6.16	17.73
142	48.48	6.73	18.28
145	50.42	7.32	20.54
148	54.34	7.29	18.89
151	57.23	7.43	19.80
150	56.85	6.34	18.74
152	60.30	6.92	18.95
154	63.63	8.22	19.76
153	62.01	7.55	19.16
155	65.26	7.71	20.29
156	68.31	9.59	21.53
157	73.73	8.87	22.48
158	76.32	9.80	23.53
159	79.38	10.17	25.97
159.5	80.12	9.84	25.32
161	80.98	11.47	28.29
163	78.51	12.20	28.95
165	73.43	12.28	29.78

Fig. 4.11 (Continued)

For the 60 minute annealed samples

Temperature	Long $T_{1\rho}(^1H)$	Short $T_{1\rho}(^1H)$	%Short Component
120	41.70	6.38	18.31
125	44.95	6.85	19.23

130	45.33	5.73	18.27
132	47.26	5.68	17.43
135	48.04	4.55	15.82
138	51.80	6.85	20.01
140	53.43	7.24	18.91
145	60.03	7.37	18.75
148	62.99	7.22	19.16
150	68.67	8.48	19.71
151	68.63	8.40	21.22
152	70.82	8.52	20.92
153	74.47	8.17	20.48
154	75.17	8.28	20.94
155	78.19	9.11	21.41
156	80.78	9.12	23.29
157	88.16	9.84	22.71
158	90.76	11.27	25.86
159	100.68	10.24	25.59
161	109.06	11.06	27.73
163	114.96	13.03	30.00
165	83.48	12.53	34.65

Fig. 4.14

Temperature	Downfield	Midfield	Upfield	Peak Ratio
120	14.82	2.94	33.05	0.089
130	12.98	4.14	34.20	0.121
140	12.14	6.38	32.47	0.196
150	11.80	9.31	29.60	0.315
152	9.78	11.00	30.11	0.365
154	9.93	11.32	29.53	0.383
156	8.84	13.42	29.06	0.462
158	6.55	17.15	27.54	0.623
159	6.29	19.28	25.27	0.763
159.5	5.89	19.57	25.45	0.769
161	5.33	21.16	24.53	0.862

Fig. 4.15

Temperature	Downfield	Midfield	Upfield	Peak Ratio
120	12.49	3.21	35.60	0.090
130	12.94	5.09	33.64	0.151
140	11.18	7.57	32.60	0.232
145	10.42	9.40	31.03	0.303
148	9.33	11.53	30.13	0.382
150	8.31	13.20	29.70	0.444

152	8.50	13.32	29.36	0.454
154	7.34	15.36	28.50	0.539
156	6.99	16.13	28.01	0.576
157	5.09	19.86	26.40	0.752
159	2.38	25.34	23.42	1.082
161	2.39	26.92	21.97	1.225
163	1.79	27.97	21.86	1.279

Fig. 4.16a

Temperature	Downfield	Midfield	Upfield
120	1.02	0.483	1.102
130	0.93	0.508	1.102
140	0.89	0.557	1.050
150	0.91	0.542	0.956
152	0.81	0.529	0.942
154	0.84	0.523	0.932
156	0.81	0.522	0.899
158	0.71	0.486	0.807
159	0.69	0.438	0.728
159.5	0.69	0.449	0.724
161	0.65	0.427	0.682

Fig. 4.16b

Temperature	Downfield	Midfield	Upfield
120	0.94	0.562	1.153
130	0.94	0.554	1.101
140	0.85	0.556	1.036
145	0.86	0.558	1.006
148	0.81	0.539	0.960
150	0.79	0.558	0.927
152	0.78	0.553	0.914
154	0.74	0.549	0.878
156	0.73	0.506	0.842
157	0.64	0.460	0.731
159	0.50	0.383	0.539
161	0.56	0.360	0.481
163	0.51	0.370	0.478

Fig. 4.18

Temperature	Methylene	Methine	Methyl
120	29.0	70.0	47.0
130	23.0	57.5	45.0

140	25.0	68.7	46.0
150	26.0	68.0	42.0
154	30.0	77.0	46.0
156	30.5	82.0	48.0
159	37.0	102.0	60.0
161	45.0	120.0	69.3
163	47.0	131.0	72.0

Fig. 4.21

Melting Temp.	Area/0min	Melting Temp.	Area/60min
157.69	9.31	157.07	7.57
158.79	11.00	159.49	13.20
159.32	11.32	161.41	13.32
161.19	13.42	162.81	15.36
163.00	17.15	164.40	16.13
165.70	19.28	165.83	19.86
		171.92	26.92

Fig. 4.24

Temperature	Size
140.00	21.00
141.00	21.00
142.00	21.00
143.00	21.00
144.00	21.00
145.00	21.00
146.00	21.00
147.00	21.00
148.00	21.00
149.00	21.00
150.00	20.90
151.00	20.70
152.00	20.50
153.00	20.25
154.00	20.00
155.00	19.70
156.00	19.40
157.00	19.00
158.00	18.00
159.00	17.00
160.00	14.00
160.17	13.00
160.33	12.10

160.50	11.20
160.66	9.50
160.83	8.00
161.00	6.00
161.17	4.00
161.33	2.50

Chapter 5

Fig. 5.8

120 °C

Log(t)	Log{-Ln[1-α(t)]}
-0.173	-1.315
0.222	-0.536
0.426	-0.163
0.564	0.097
0.669	0.320
0.753	0.508
0.824	0.678
0.884	0.811
0.938	0.892

122 °C

Log(t)	Log{-Ln[1-α(t)]}
-0.397	-2.176
0.146	-1.087
0.380	-0.631
0.531	-0.340
0.643	-0.122
0.732	0.053
0.806	0.204
0.869	0.336
0.924	0.454
0.973	0.565

124 °C

Log(t)	Log{-Ln[1-α(t)]}
0.046	-1.722
0.324	-1.173
0.493	-0.831
0.614	-0.598
0.708	-0.407
0.786	-0.256
0.852	-0.127
0.909	-0.008
0.959	0.094
1.004	0.194
1.045	0.280
1.083	0.365
1.117	0.441
1.149	0.515

126 °C

Log(t)	Log{-Ln[1-α(t)]}
0.008	-2.161
0.305	-1.549
0.480	-1.210
0.700	-0.756
0.846	-0.464
0.955	-0.245
1.042	-0.062
1.114	0.087
1.176	0.220
1.231	0.340
1.279	0.445
1.322	0.541

Fig. 5.9

Temperature	PP34	PP5	A60/40
120	0.375	0.388	0.640
121	0.305	0.322	0.498
122	0.238	0.245	0.402
123	0.200	0.209	0.335
124	0.151	0.171	0.278
126	0.099	0.108	0.164

Fig. 5.10

	Rate Constant, K			Growth Rate		
Temp.	PP34	PP5	A60/40	Temp.	PP5	PP5/Silica/Silicone
120	0.102	0.116	0.235	120	0.802	0.799
121	0.080	0.086	0.135	122	0.599	0.584
122	0.042	0.047	0.084	124	0.443	0.414
123	0.040	0.033	0.055	128	0.171	0.201
124	0.016	0.024	0.036	132	0.075	0.082
126	0.008	0.008	0.012	136	0.033	0.035

Fig. 5.17

Temperature	PP34	Temperature	A60/40
120	36.25	120	39.83
140	46.21	140	48.51
150	54.94	150	58.63
154	59.17	155	66.16
156	65.93	160	77.58
158	71.57	163	78.02
159	75.45	165	70.82
161	76.12		
163	73.98		
165	69.01		